ornl

NUREG/CR-3460
ORNL/TM-8890

OAK RIDGE
NATIONAL
LABORATORY

MARTIN MARIETTA

Experiment Data Report for Multirod Burst Test (MRBT) Bundle B-6

R. H. Chapman
A. W. Longest
J. L. Crowley

Prepared for the U.S. Nuclear Regulatory Commission
Office of Nuclear Regulatory Research
Under Interagency Agreements DOE 40-551-75 and 40-552-75

OPERATED BY
MARTIN MARIETTA ENERGY SYSTEMS, INC.
FOR THE UNITED STATES
DEPARTMENT OF ENERGY

Printed in the United States of America. Available from
National Technical Information Service
U.S. Department of Commerce
5285 Port Royal Road, Springfield, Virginia 22161

Available from

GPO Sales Program
Division of Technical Information and Document Control
U.S. Nuclear Regulatory Commission
Washington, D.C. 20555

NUREG/CR-3460
ORNL/TM-8890
Dist. Category R2, R3

Engineering Technology Division

EXPERIMENT DATA REPORT FOR MULTIROD BURST TEST (MRBT) BUNDLE B-6

R. H. Chapman A. W. Longest
J. L. Crowley

Manuscript Completed – June 11, 1984
Date Published – July 1984

Prepared for the
U.S. Nuclear Regulatory Commission
Office of Nuclear Regulatory Research
Under Interagency Agreements DOE 40-551-75 and 40-552-75

NRC Fin No. B0120

Prepared by the
OAK RIDGE NATIONAL LABORATORY
Oak Ridge, Tennessee 37831
operated by
MARTIN MARIETTA ENERGY SYSTEMS, INC.
for the
U.S. DEPARTMENT OF ENERGY
under Contract No. DE-AC05-840R21400

CONTENTS

LIST OF FIGURES

LIST OF TABLES

FOREWORD

Examination, analysis, and interpretation of a bundle test take place over a long period of time, and our practice has been to report progress and results as they become available. Dissemination of the information in this manner results in its being disjointed and scattered throughout several publications. This presents some problems to the users in that one is never sure if the information at hand is the most recent. Our intention has been to alleviate some of these problems by (1) publication of a data report on each bundle test and (2) publication of analytic and interpretative reports when sufficient information has been developed.

Consistent with this intention, the objective of this data report is to provide a reference source of information and results obtained during the B-6 test and from pretest and posttest examination of the test array. We believe the data presented herein, consisting of plots, tabulations, photographs, and some important observations, are necessary for analysis and interpretation of the test. A decision was made that the data should be presented with a minimum of interpretation and that analysis or "second-generation" data, such as comparative temperature vs time plots, should be excluded.

This report is derived from research performed by the (now completed) Multirod Burst Test (MRBT) Program at Oak Ridge National Laboratory (ORNL). This program was sponsored by the Division of Accident Evaluation of the Nuclear Regulatory Commission, and the results were published routinely in a series of progress reports, topical reports and papers, quick-look test reports, and test data reports.

Progress reports published by the MRBT Program include:

NUREG Report No.	ORNL Report No.	Period covered
	ORNL/TM-4729	July–September 1974
	ORNL/TM-4805	October–December 1974
	ORNL/TM-4914	January–March 1975
	ORNL/TM-5021	April–June 1975
	ORNL/TM-5154	July–September 1975
	ORNL/NUREG/TM-10	October–December 1975
	ORNL/NUREG/TM-36	January–March 1976
	ORNL/NUREG/TM-74	April–June 1976
	ORNL/NUREG/TM-77	July–September 1976
	ORNL/NUREG/TM-95	October–December 1976
	ORNL/NUREG/TM-108	January–March 1977
	ORNL/NUREG/TM-135	April–June 1977
NUREG/CR-0103	ORNL/NUREG/TM-200	July–December 1977
NUREG/CR-0225	ORNL/NUREG/TM-217	January–March 1978
NUREG/CR-0398	ORNL/NUREG/TM-243	April–June 1978
NUREG/CR-0655	ORNL/NUREG/TM-297	July–December 1978
NUREG/CR-0817	ORNL/NUREG/TM-323	January–March 1979
NUREG/CR-1023	ORNL/NUREG/TM-351	April–June 1979
NUREG/CR-1450	ORNL/NUREG/TM-392	July–December 1979
NUREG/CR-1883	ORNL/NUREG/TM-426	January–June 1980

NUREG/CR-1919	ORNL/NUREG/TM-436	July–December 1980
NUREG/CR-2366, vol. 1	ORNL/TM-8058	January–June 1981
NUREG/CR-2366, vol. 2	ORNL/TM-8190	July–December 1981
NUREG/CR-2911	ORNL/TM-8485	January–June 1982

Topical reports and papers pertaining to research and development carried out by this program are:

1. R. H. Chapman (comp.), *Characterization of Zircaloy-4 Tubing Procured for Fuel Cladding Research Programs*, ORNL/NUREG/TM-29 (July 1976).

2. W. E. Baucum and R. E. Dial, *An Apparatus for Spot Welding Sheathed Thermocouples to the Inside of Small-Diameter Tubes at Precise Locations*, ORNL/NUREG/TM-33 (August 1976).

3. W. A. Simpson, Jr., et al., *Infrared Inspection and Characterization of Fuel-Pin Simulators*, ORNL/NUREG/TM-55 (November 1976).

4. R. H. Chapman et al., *Effect of Creep Time and Heating Rate on Deformation of Zircaloy-4 Tubes Tested in Steam with Internal Heaters*, NUREG/CR-0343 (ORNL/NUREG/TM-245) (October 1978).

5. J. F. Mincey, *Steady-State Axial Pressure Losses Along the Exterior of Deformed Fuel Cladding: Multirod Burst Test (MRBT) Bundles B-1 and B-2*, NUREG/CR-1011 (ORNL/NUREG/TM-350) (January 1980).

6. R. W. McCulloch, P. T. Jacobs, and D. L. Clark, *Development of a Fabrication Procedure for the MRBT Fuel Simulator Based on the Use of Cold-Pressed Boron Nitride Preforms*, NUREG/CR-1111 (ORNL/NUREG/TM-362) (March 1980).

7. R. H. Chapman, J. V. Cathcart, and D. O. Hobson, "Status of Zircaloy Deformation and Oxidation Research at Oak Ridge National Laboratory," in *Proceedings of Specialists Meeting on the Behavior of Water Reactor Fuel Elements Under Accident Conditions, Spatind, Norway, September 13–16, 1976*, CSNI Report No. 13 (1977).

8. R. H. Chapman et al., "Zircaloy Cladding Deformation in a Steam Environment with Transient Heating," pp. 343–408 in *Zirconium in the Nuclear Industry (Fourth Conference)*, ASTM STP 681, American Society for Testing and Materials, 1979.

9. R. L. Anderson, K. R. Carr, and T. G. Kollie, *Thermometry in the Multirod Burst Test Program*, NUREG/CR-2470 (ORNL/TM-8024) (March 1982).

10. A. W. Longest, J. L. Crowley, and R. H. Chapman, *Variations in Zircaloy-4 Cladding Deformation in Replicate LOCA Simulation Tests*, NUREG/CR-2810 (ORNL/TM-8413) (September 1982).

11. A. W. Longest, R. H. Chapman, and J. L. Crowley, "Boundary Effects on Zircaloy-4 Cladding Deformation in LOCA Simulation Tests," *Trans. Am. Nucl. Soc.* 41, 383 (1982).

12. R. H. Chapman, J. L. Crowley, and A. W. Longest, "Effect of Bundle Size on Cladding Deformation in LOCA Simulation Tests," in *Zirconium in the Nuclear Industry: Sixth International Symposium*, ASTM STP 824, D. G. Franklin, R. B. Adamson, and B. Cox, eds., American Society for Testing and Materials, in press.

The following bundle test quick-look and data reports have been issued by this program:

1. R. H. Chapman (comp.), *Quick-look Report on MRBT No. 1 4 × 4 Bundle Burst Test*, Internal Report ORNL/MRBT-2 (September 1977).

2. R. H. Chapman (comp.), *Quick-look Report on MRBT No. 2 4 × 4 Bundle Burst Test*, Internal Report ORNL/MRBT-3 (November 1977).

3. R. H. Chapman, *Quick-look Report on MRBT No. 3 4 × 4 Bundle Burst Test*, Internal Report ORNL/MRBT-4 (August 1978).

4. R. H. Chapman, *Quick-look Report on MRBT B-4 (6 × 6) Bundle Test*, Internal Report ORNL/MRBT-6 (February 1981).

5. R. H. Chapman et al., *Quick-look Report on MRBT B-5 (8 × 8) Bundle Test*, Internal Report ORNL/MRBT-5 (July 1980).

6. R. H. Chapman et al., *Quick-look Report on MRBT B-6 (8 × 8) Bundle Test*, Internal Report ORNL/MRBT-7 (January 1982).

7. R. H. Chapman et al., *Bundle B-1 Test Data*, ORNL/NUREG/TM-322 (June 1979).

8. R. H. Chapman et al., *Bundle B-2 Test Data*, ORNL/NUREG/TM-337 (August 1979).

9. R. H. Chapman et al., *Bundle B-3 Test Data*, ORNL/NUREG/TM-360 (January 1980).

10. A. W. Longest et al., *Experiment Data Report for Multirod Burst Test (MRBT) Bundle B-4*, NUREG/CR-2968 (ORNL/TM-8509) (December 1982).

11. R. H. Chapman et al., *Experiment Data Report for Multirod Burst Test (MRBT) Bundle B-5*, NUREG/CR-3459 (ORNL/TM-8889) (in publication).

12. R. T. Bailey, *Steady-State Pressure Losses for Multirod Burst Test (MRBT) Bundle B-5*, NUREG/CR-2597 (ORNL/Sub/80-40441/1) (April 1982).

EXPERIMENT DATA REPORT FOR MULTIROD BURST TEST (MRBT) BUNDLE B-6

R. H. Chapman A. W. Longest
J. L. Crowley

ABSTRACT

A reference source of MRBT bundle B-6 test data is presented with minimum interpretation. The primary objective of this 8 × 8 multirod burst test was to investigate cladding deformation in the alpha-plus-beta-Zircaloy temperature range under simulated light-water-reactor (LWR) loss-of-coolant accident (LOCA) conditions. B-6 test conditions simulated the adiabatic heatup (reheat) phase of an LOCA and produced very uniform temperature distributions. The fuel pin simulators were electrically heated (average linear power generation of 1.42 kW/m) and were slightly cooled with a very low flow (Re ~140) of low-pressure superheated steam. The cladding temperature increased from the initial temperature (330°C) to the burst temperature at a rate of 3.5°C/s. The simulators burst in a very narrow temperature range, with an average of 930°C. Cladding burst strain ranged from 21 to 56%, with an average of 31%. Volumetric expansion over the heated length of the cladding ranged from 16 to 32%, with an average of 23%. The average burst strain and the average volumetric expansion for the interior simulators were only slightly greater than the averages for the exterior simulators. The coolant channel flow area reduction was modest, with a maximum of 39% for the entire 8 × 8 array, 43% if based on the interior 6 × 6 array, and 45% if based on the central 4 × 4 array. As expected, no evidence of rod-to-rod mechanical interaction effects was observed.

Keywords: Zircaloy, nuclear fuel cladding, tubes, bundle burst tests, loss-of-coolant accident, deformation, flow blockage, boundary conditions, rod-to-rod interactions, fuel pin simulators.

---

1. INTRODUCTION

This report presents in considerable detail, the experimental data for the B-6 test (the second of two 8 × 8 multirod burst tests) conducted by the Multirod Burst Test (MRBT) Program at Oak Ridge National Laboratory (ORNL). This work (now completed) was sponsored by the Division of Accident Evaluation of the Nuclear Regulatory Commission (NRC) and was designed to investigate Zircaloy cladding deformation behavior under

simulated loss-of-coolant accident (LOCA) conditions. Although preliminary versions of the data have been published in a quick-look report[1] and in periodic progress reports,[2-4] the data are collected in final form in this report to provide a reference source document for the B-6 test results. Interpretation of the data is limited to that necessary to understand pertinent features of the test. Because of this, this report should be used in conjunction with other published results and interpretations.[2-7] (The Foreword lists all publications issued by this program.)

The primary objective of the B-6 test, which was conducted on December 3, 1981, was to investigate cladding deformation in a large array in the alpha-plus-beta-Zircaloy temperature range. Single-rod burst tests have shown that deformation is rather insensitive to heating rate in this temperature range and that the magnitude of the deformation is considerably less than observed in the high-alpha and low-beta temperature ranges. Consistent with these observations, test conditions were selected to give a burst temperature of about 925°C with a heating rate of 3–4°C/s. These conditions are representative of predictions from LOCA licensing calculations for a range of postulated light-water-reactor (LWR) accidents.

Results of the earlier B-5 test,[5,6,8] which was conducted with an 8 × 8 array under conditions conducive to large deformation in the high-alpha temperature range, showed that temperature uniformity and rod-to-rod mechanical interactions (resulting from large deformation and lateral restraint in a large test array) have a significant effect on deformation behavior in large arrays. Therefore, a secondary objective of the B-6 test was to determine, if possible, the relative importance of these two parameters. Analysis of the test results should permit this determination because very uniform temperature conditions existed and rod-to-rod interactions were relatively nonexistent in the test.

Because test conditions used in this program simulate the adiabatic heatup (reheat) phase of an LOCA and are generally considered to be conservative, the B-6 test results are believed to provide an upper-limit estimate of the deformation that can be anticipated in most accidents with cladding failures in the alpha-plus-beta-Zircaloy temperature range. Similarly, the results of the B-5 test[2-6,8,9] are believed to be a reasonable upper-limit estimate of the deformation that can be expected for failures in the high-alpha temperature range. Based on the burst strains characteristic of these two temperature ranges, that is, 50–100% for the high-alpha and 25–50% for the alpha-plus-beta temperature range, the B-5 and B-6 deformation results taken together bracket the variation in the upper limit of expected deformation over a wide temperature range of interest.

Following the format of the other reports[8,10-13] in this series, a brief description of the test design and an overview of test operations are given first. These are followed, in turn, by a section giving a summary of the test results and a section giving detailed test results, including photographic documentation of the bundle before and after testing and of the 58 cross sections on which the deformation measurements were made. Since the transient test data and the posttest deformation data are voluminous, much of the data is presented (in computer-generated graphical and tabular formats) on microfiche enclosures inserted in the pocket attached to the inside back cover. Similar to the B-5 report,[8] a

final section is devoted to interpretation and important observations; however, the interpretation is limited to that we believe necessary to understand and explain the test results.

2. TEST DESCRIPTION

2.1 Assembly

Figure 1 shows a simplified drawing of the B-6 test assembly installed in the test vessel. An *unheated* (electrically) shroud surrounded the test array as indicated in Sect. A-A of the figure. The shroud was constructed of thin (0.13-mm-thick) stainless steel, with a highly reflective, gold-plated surface to minimize thermal capacity and radiative thermal losses. The stainless steel sheet was backed by a layer of insulating material to reduce heat losses and the insulating material by a strong structure to withstand radial forces during the test transient. The thin shroud was spaced 1.75 mm (i.e., one-half of a coolant channel distance) from the outer rod surfaces. This permitted some deformation of these simulators before contact with the shroud but prevented gross outward movement of the simulators.

The test array and shroud assembly were separately suspended from the test vessel cover flange to allow free and independent axial movement. Four Inconel-718 grids, typical of the type used in commercial pressurized water reactor (PWR) 15 × 15 fuel bundles, provided proper spacing (14.43 mm center-to-center) of the fuel rod simulators (10.92 mm diam) in a square array. Because grid tie-rods were not used, the grids were held in position only by grid-spring forces acting on the individual simulators and were free to move axially to compensate for growth or shrinkage of the bundle during the test.

The steam inlet configuration (above the upper end of the bundle heated zone) was modified from the single-entry nozzle used in the B-5 test to a double-entry arrangement as shown in Sect. B-B of Fig. 1. This modification, combined with additional insulation to reduce heat losses from the top of the test vessel, provided a more uniform radial temperature distribution in the bundle at the inlet than could be obtained in the B-5 test.[8]

Because the B-5 test showed that the outer ring of simulators (and the next inner ring to a lesser extent) acted as deforming guard heaters and their deformation behavior was atypical, a decision was made to omit the temperature measuring instrumentation in 20 of the 28 simulators in the outer ring of the B-6 array. However, all 28 of the simulators were instrumented with pressure monitoring instrumentation.

Design features of the fully instrumented fuel pin simulators are illustrated in Fig. 2, and as-built data are listed in Table 1. The fuel simulators (internal heaters) were anchored to the cladding tubes by the lower seal gland. Differential axial movement (thermal expansion, growth, and/or shrinkage) between the fuel simulator and the cladding tube was accommodated by a flexible section in the upper electrical lead. Different simulator lengths were required to accommodate the dimensions of the upper seal gland (see Figs. 1 and 2), but ceramic inserts were used in both types to adjust the free volume to the same nominal value. The average free volume of the B-6 simulators was 49.7 cm^3, with a standard deviation of 1.1 cm^3.

Although the simulator gas volume was reasonably typical, the distribution of the volume was not typical of a full-length fuel rod. Of the

total initial volume (at room temperature), about 13% was in the heated portion of the annulus between the fuel simulator and the inside diameter of the Zircaloy tube, 10% was in the unheated portion of the annulus, 33% was in the pressure transducer and connecting tube, and 44% was distributed in the end regions (mostly at the upper end) of the fuel pin simulator.

The fuel simulators (internal heaters) were produced in the ORNL Fuel Rod Simulator Technology Development Laboratory, using fabrication procedures[14] developed specifically for the needs of this program. Of the 64 simulators, 54 were previously used, 50 in the 8 × 8 B-5 test and 4 in single-rod tests; these were cleaned, straightened, and restored (within specifications) to their original condition. A thin plasma-sprayed ZrO_2 protective coating was applied to the outside surface (over the heated length) of all the simulators. The axial heat generation profile of the coated simulators was characterized (before assembly within the Zircaloy tube) under transient heating conditions, using a high-temperature infrared (IR) scanning technique.[15] The highest-quality simulators, as judged by heat generation uniformity, were selected for the array interior positions.

The Zircaloy-4 tubes (10.92-mm OD by 0.635-mm wall thickness) came from the master lot of well-characterized[16-18] tubing purchased for use in several NRC-sponsored cladding research programs. Tube serial numbers, given in Table 1, can be used to relate the individual tubes to their fabrication history.[16] The tubes were lightly oxidized in superheated steam for 50 min at 480°C on both internal and external surfaces prior to fabrication of the fuel pin simulators to better simulate the condition of fuel cladding after a period of reactor operation. Metallographic examination of typical specimens oxidized under these conditions showed the oxide film to be very uniform and thin (1 to 2 μm); this should not have materially affected the metallurgical conditions of the tubes.

Each fuel pin simulator was instrumented with a fast-response, strain-gage-type pressure transducer. The fully instrumented simulators were also instrumented with four Inconel-sheathed (0.71-mm-OD) type K (Chromel-Alumel) thermocouples with ungrounded junctions. These were spot-welded to the inside surface of the Zircaloy-4 tubes, using a device developed specifically for this purpose,[19] at the locations shown in Fig. 3. Tantalum wire was used in place of the thermocouples for centering the fuel simulators (internal heaters) in the Zircaloy tubes of the 20 simulators in the outer ring without temperature sensors. The figure also gives thermocouple identifications for use in subsequent figures and discussions (the nomenclature TE 10-4 identifies thermocouple 4 in simulator 10).

Axial locations of the thermocouples are shown more clearly in Fig. 4. As evident from the figures, the inner 6 × 6 array had 18 thermocouples (average of one for every two simulators) installed at each of the seven instrumented elevations of primary interest, with 12 thermocouples at the lowest instrumented elevation and 3 thermocouples at each of the two grid elevations. The thermocouples in the fully instrumented simulators in the outer ring of the array were located at elevations of greatest interest. A repeating pattern was selected for the orientations of the thermocouples (Fig. 3) at any given elevation to provide supplementary

temperature information of potential benefit for plotting radial temperature profiles and for detecting rod-to-rod thermal interactions.

Eight 0.13-mm-diam bare-wire type S (Pt vs Pt + 10% Rh) thermocouples were spot-welded directly to the outside surface of the thin shroud surrounding the test array. Two thermocouples were attached to each side of the shroud at locations shown in Fig. 3 to obtain information on both the axial and circumferential temperature distributions. The shroud thermocouple identifications are also given in the figure for use in subsequent temperature plots.

As noted in Fig. 3, five simulator thermocouples (TE 19-3, TE 35-4, TE 38-3, TE 42-4, and TE 55-3) and possibly a sixth (TE 14-3) became detached during fabrication of the simulators. Although it is not apparent from the data, the detached thermocouples might have indicated temperatures slightly higher than those they would have indicated if they had remained attached to the Zircaloy tubes. For this reason they were not considered reliable indicators of the burst temperature.

Eight thermocouples (TE 11-2, TE 20-2, TE 29-2, TE 31-2, TE 34-2, TE 38-2, TE 45-2, and TE 52-2) at the 38-cm elevation on interior simulators were averaged electronically (in real time) to represent the bundle average temperature. This average, identified as TAV-10, was recorded and displayed to provide on-line information as the test progressed.

Five thermocouples (TE-320 through TE-324) were located in the inner 6 × 6 matrix at the 107-cm elevation (centerline elevation of the steam inlet nozzles; see Fig. 1) to obtain inlet steam temperature measurements across the bundle. Similarly, five thermocouples (TE-325 through TE-329) were located in the tube matrix near the bottom of the heated zone (3-cm elevation) to obtain outlet steam temperature measurements. Unfortunately, two of the latter (TE-326 and TE-329) were damaged during assembly and were inoperative during the test. Figure 5 shows the identifications and locations of these sensors. These were 0.71-mm-diam, stainless-steel-sheathed, type K thermocouples with insulated junctions.

A detailed description of the temperature measurement systems and a comprehensive analysis of the errors and uncertainties associated with the measurements have been reported previously.[20]

Millivolt signals from the pressure transducers, thermocouples, and electrical power measuring instruments were recorded on magnetic tape by a computer-controlled data acquisition system (CCDAS) for subsequent analysis. Calibration corrections, preprogrammed into the computer system, were automatically applied to the millivolt signals before printout of the data.

Each fuel pin simulator was connected in parallel at the upper end through separately fused electrical circuits to a common dc, constant-voltage power supply and was attached to a current collector at the lower end of the array as indicated in Fig. 1. Because the electrical characteristics were nearly the same for all the simulators (the average value for the resistance data given in Table 1 is 1.97 Ω with a standard deviation of 0.02 Ω), means were not provided in the external circuits for redistribution of the current to improve distribution of the power generation in the bundle.

2.2 Operations

Heatup of the vessel containing the test assembly was initiated early in the afternoon of the day before the test; the temperature was ~200°C at the end of the work shift. Power adjustments to the vessel heaters were made to maintain the temperature near this value during the next 12 h to avoid temperature cycling the test assembly. Early on the day of the test, power to the vessel heaters was increased, and superheated steam was admitted to the vessel in the approach to the initial test temperature. Throughout this phase of operation, electrical power was not applied to the simulators; periodic leak checks indicated the simulator seals were performing very well (i.e., <10-kPa helium pressure loss per min at 7600 kPa and ~330°C).

After thermal equilibration (~322°C) of the test assembly was attained, the simulators were pressurized to ~2100 kPa, and a short powered run (13.0-s transient) was conducted to ascertain that the data acquisition system and all the instrumentation were functioning properly and that the performance of the test components was as expected. Examination and evaluation of the limited quick-look data from this short transient (the temperature of the simulators increased to ~380°C) indicated that slight adjustments were needed to achieve the desired heating rate.

Following the adjustments and restabilization of the bundle temperature at ~330°C, all the fuel pin simulators were pressurized simultaneously to ~3050 kPa (differential above the external pressure) and individually isolated from the supply header to provide a constant helium inventory in each one during the transient. The header was vented, and the leak rate of each of the simulators was checked over a 2-min period, with the pressure loss being ~1 kPa/min. With these initial conditions established, the test transient was initiated by applying dc voltage to the simulators. The applied voltage was maintained constant throughout the powered portion of the transient and resulted in an average linear power generation of 1.42 kW/m in the simulators.

During the powered portion of the transient, superheated steam entered the test array through two inlet nozzles located at the 107-cm elevation on the east and west sides of the bundle (Fig. 1) and flowed downward through the test assembly at the same mass flux used in the B-5 test —~288 $g/s \cdot m^2$. Inlet steam conditions of ~329°C and 309 kPa (absolute) resulted in a Reynolds number of 140. These inlet conditions remained essentially constant until disrupted by helium escaping from the ruptured tubes and by the opening of valves to admit posttest cooling steam. When power to the bundle was terminated, the steam flow was increased to an estimated minimum of 2000 $g/s \cdot m^2$ to effect rapid cooldown of the bundle.

Termination of the powered portion of the test could be initiated by any of four actions: (1) CCDAS action resulting from a signal that 60 of the 64 simulators had burst, (2) CCDAS action resulting from a signal that 115 simulator thermocouples had exceeded the high-temperature limit (50°C above the anticipated burst temperature) on each of three successive data scans, (3) a timer that limited the transient to ~145 s, and (4) operator override. The choice to program criterion (1) to terminate power to the bundle after 60 tube bursts (with the expectation that all 64 tubes would

burst) was made to minimize the temperature overshoot at the end of the test. Also, criterion (2), the high-temperature limit, was established close to the expected burst temperature for the same reason. The test was terminated by criterion (3) and all 64 tubes burst.

3. SUMMARY OF TEST RESULTS

Initial conditions of the test, obtained by averaging each data channel over the time interval (~25 s) from the start of scanning to the power-on time, are summarized in Table 2. There are no temperature data in this and subsequent tables for those 20 of the 28 simulators in the outer ring of the array that were not instrumented with thermocouples; however, measured pressure data are available. All the simulators were pressurized simultaneously from a common manifold and then individually isolated from the manifold for the test. After isolation the average simulator pressure was 3050 kPa differential above the external steam pressure. The initial cladding average temperature was 330°C; the temperature distribution in the bundle was unusually uniform in both the radial and axial directions. The average temperature indicated by the eight shroud thermocouples was 334°C. Superheated steam entered the bundle at an indicated average temperature of 329°C and a pressure of 309 kPa (absolute) and flowed downward through the bundle at a constant mass flow rate of 288 $g/s \cdot m^2$; the indicated average steam outlet temperature prior to initiation of the transient was 332°C. Based on the inlet steam conditions and flow rate, the Reynolds number at the top of the heated zone (91.4-cm elevation) was 140 throughout the powered portion of the transient.

Figure 6 shows the applied voltage and the bundle average temperature represented by TAV-10 (i.e., the average of ten thermocouples attached to the inside surface of the cladding at the 38-cm elevation on interior simulators) during the transient. Constant voltage was applied to the bundle for 141.74 s; power generation (1.42 kW/m) and the temperature rate of increase were nearly constant during this time as indicated in the figure. The average heating rate in the high-alpha temperature range (i.e., from ~35 to ~105 s after power-on) was about 4.5°C/s. As the temperature increased into the two-phase-Zircaloy range, the heating rate decreased because of greater heat losses and the higher heat capacity of the two-phase material and, perhaps, the effects of deformation. The average heating rate from ~115 to ~141 s after power-on (i.e., to about the power-off time) was 3.5°C/s. This value is considered the appropriate one for characterizing deformation behavior in the test because the deformation occurred during the latter time interval. The average temperature, as indicated by TAV-10, reached a maximum of ~958°C about 5 s after power was terminated.

The time at which maximum pressure occurred in each simulator is a measure of the onset of significant deformation (i.e., the time when the rate of pressure increase caused by thermodynamic heating equals the rate of pressure decrease caused by increasing volume) and is given in Table 3 with the corresponding cladding temperature and pressure conditions. The bundle average maximum differential pressure was 3245 kPa and occurred at an average time of 112.6 s after power-on. The observation that the maximum pressures and the times at which they occurred were approximately the same in all the simulators is indicative of very uniform heating and the absence of seal leaks.

Times (after power-on), temperatures, and differential pressures measured at the burst time of each tube are given in Table 4. The tube

bursts occurred in an unusually orderly manner, starting 133.14 s after power-on, because of uniform azimuthal conditions coupled with a small radial temperature gradient that was caused by external heat losses. Tube burst times are plotted in three groups in Fig. 7 to indicate radial positions in the bundle. With one exception, all the simulators in the central 4 × 4 array burst before any bursts occurred in the next ring (i.e., the outer ring of the inner 6 × 6 array), and all the simulators in the inner 6 × 6 array burst before any burst in the exterior ring. Power was terminated 0.60 s after the last burst in the inner 6 × 6 array; however, the temperature continued to increase (Fig. 6) for several seconds before it turned around and slowly decreased. The first simulator in the outer ring burst 0.40 s after power-off, and all the simulators except the four corner ones burst by the time the average temperature (represented by TAV-10) reached its maximum value. The corner simulators, with the greatest external heat losses, were subjected to near-isothermal creep conditions and failed 25 to 50 s later as indicated in Fig. 7. A histogram (in 1.0-s intervals) of the burst times (Fig. 8) shows two distinct distributions for the interior and exterior tubes. Excluding the four corner rods, the average burst time for the bundle was 139.40 s.

Our practice for tests without significant rod-to-rod interactions has been to select the burst temperature as the maximum measured temperature at the time of failure, without regard to the location of the measurement with respect to the burst. This definition rests on the premise that the temperature at the failure point is at least as high as the maximum measured value but does not preclude its being higher. We evaluated the measured data and revised the quick-look burst temperature data[2] to exclude from consideration temperatures indicated by detached thermocouples (see Fig. 3). The revised data, given in the summary of test results (Table 5), represent the best-estimate burst temperatures in the absence of more definitive analysis of the data. Excluding the uninstrumented simulators in the outer ring, the bundle average burst temperature was 930°C.

The bundle average burst pressure (Table 5) was 2879 kPa; no significant variation was observed in the burst pressures for a rather narrow burst temperature range. The data are plotted in Fig. 9, in which greatly expanded scales and different symbols are used to differentiate the data for the three radial zones of the bundle. Although one can detect a difference between the data for the exterior and interior simulators, the burst data for the interior simulators were independent of simulator position in the array. As expected, the simulators in the outer ring of the bundle burst at a pressure slightly higher than the average. The range of the burst pressures for the exterior simulators, excluding the four corner ones, is noted in the figures. The curve labeled "B-6 LSF" is a linear least-squares fit to the B-6 data points.

Prior to performing the B-6 test, three single-rod *heated* shroud tests were conducted[3] with heating rates in the range of 5 to 6°C/s to aid selection of the B-6 test parameters. The burst data for these three tests are included in the plot for comparison; the curve labeled "SR-LSF" is a linear least-squares fit of the three single-rod data points. While the two fitted curves have virtually identical slopes, the bundle curve is about 10°C lower than the single-rod curve. Some of this difference

may be a result of the slightly lower heating rate in the bundle test (3.5 vs 5.5°C/s), but most of the difference is attributed to our use of fewer thermocouples to measure temperatures in bundle simulators than in single-rod simulators (i.e., 4 vs 12), which creates a greater statistical probability for underestimating burst temperatures in bundle tests.

The initial-to-burst pressure ratio is a qualitative measure of the volumetric expansion and has been shown[3] to be a useful parameter for modeling average deformation in the absence of measured geometrical data. This parameter is given in Table 5 and is plotted in Fig. 10 for the three radial zones of the test array. Consistent with the burst pressure data from the previous figure, slightly greater volumetric expansion is indicated for the interior zones.

The test array was cast in an epoxy matrix and sectioned at a number of axial nodes 10 to 20 mm apart. Enlarged photographs of the sections were digitized and processed (by the procedure described in Sect. 4.2.4) to obtain geometric parameters describing the deformation of each tube at each axial node. The strain profiles were used to calculate the volumetric expansion of the cladding heated length (based on the outside perimeter of the tubes) by assuming circular cross sections at each node. This parameter is tabulated in Table 5 and is plotted in Fig. 11 in a format similar to the previous figure. The average and the sample standard deviation limits of the data are also indicated in the figure; the bundle average volumetric increase, excluding the four corner rods, was 22.9%. The average strain in each tube was also calculated, by assuming that the volumetric expansion was uniformly distributed over the heated length, and is given in Table 5. These data also show that the interior simulators deformed slightly more than the exterior ones; however, there were no significant differences between the central 4 × 4 array and the next outer ring.

The volumetric increase of the heated length obtained from the deformation profiles was assumed equal to the increase in total gas volume and used to calculate the fuel pin simulator volumetric increase (Table 5) appropriate for analysis with the measured temperature and pressure data. However, as discussed in Sect. 2.1, the major fraction of the gas volume was distributed in regions in which the temperature during the test ranged from room temperature to the initial temperature, with only a small fraction of the gas in the heated zone.

Tube burst strains are plotted in Fig. 12 for each of the three radial zones; the average and the sample standard deviation limits are also indicated for each zone. As mentioned earlier, the four corner simulators deformed and failed under near-isothermal creep conditions much later (see Fig. 7) than the other simulators. As a result, deformation of these simulators was greater and atypical, as indicated by the large burst strains (relative to the other simulators in the outer ring). For this reason, they were excluded from the average of this zone. The bundle average burst strain, excluding the four corner rods, was 30%. As evident, the average burst strain was approximately the same in each of the three zones, indicating that burst strain was not a strong function of position. This was an unexpected observation since azimuthal temperature gradients were presumably greater in the outer ring of simulators (as a result of heat losses to the relatively cold shroud surrounding the

array) than in the interior simulators. An explanation for this observation is given in Sect. 5.

As mentioned earlier, three single-rod heated shroud tests were conducted prior to the bundle test to aid definition of bundle test conditions. Burst strains[3] for the three tests (36, 36, and 37%) were consistent with the results of this test.

The measured tube areas were summed at each axial node and combined to obtain the flow area restriction data shown in Fig. 13 as a function of array size. The maximum loss in flow area was modest and amounted to 39% for the entire 8 × 8 array, 43% for inner 6 × 6 array, and 45% for the central 4 × 4 array.

Because definitive flow tests were performed on the B-5 bundle,[8,21] which was more severely deformed than the B-6 bundle, there was no need to perform similar tests on the latter bundle.

4. DETAILED TEST RESULTS

The previous section summarized the important test results; this section presents, in a number of subsections, detailed results of the B-6 test. The purpose of this presentation is to provide a fairly complete reference source of uninterpreted data that can be used for analysis and evaluation by those interested.

4.1 Transient Results

4.1.1 Bundle behavior

Information contained in this section was obtained during the course of the test transient. The data were recorded by the CCDAS in the continuous scan mode (i.e., each sensor was sampled every 0.025 s) over a period of ~10 min, starting ~25 s before power-on. All 64 simulators were instrumented with fast-response pressure transducers, and all of the interior simulators and 8 of those in the outer ring of the 8 × 8 array were each instrumented with 4 sheathed (0.71-mm-diam) thermocouples spot-welded to the inside cladding surface at various positions (Figs. 3 and 4). The temperature of the thin (electrically) unheated shroud was measured by eight small-diameter, bare-wire (0.13-mm-diam) thermocouples, located as indicated in Fig. 3, spot-welded to the outside surface of the shroud. Steam temperature measurements were made with sheathed thermocouples (0.71 mm diam) at the locations shown in Fig. 5. Also, the electrical power parameters were measured and recorded by the CCDAS.

Superheated steam entered the test array through two inlet nozzles located at the 107-cm elevation on the east and west sides of the bundle (see Fig. 1) at an average temperature of 329°C and a pressure of 309 kPa (absolute) and flowed downward through the array at a constant mass flux of 288 g/s•m^2. With these conditions the nominal Reynolds number at the top of the heated zone (91.4-cm elevation) was 140. These inlet conditions remained essentially constant until disrupted by escaping helium from the bursting tubes. When power to the bundle was terminated, the steam mass flux was increased to an estimated minimum of 2000 g/s•m^2 for rapid cooldown. Inlet and outlet steam temperatures measured 1.0 s before power-on and 1.0 s before the first tube burst are indicated in Figs. 14 and 15, respectively.

Figures 16–25 present cladding temperatures measured at the instrumented elevations 1.0 s before power-on and 1.0 s before the first tube burst. The data are presented in a format intended as a schematic layout of the thermocouple locations. If the thermocouple junction is at the elevation for which the particular map applies, the thermocouple number circle is filled in to denote the azimuthal position of the measurement, and the temperature measurement is given. The row average temperatures for the inner 6 × 6 array are printed on the left; the column average temperatures, at the bottom of the layout. The cross-section

and bundle (excluding the six thermocouples at the grid elevations) averages, based on the inner 6 × 6 array measurements, are also included in the format.

The overall radial temperature distribution may be visualized somewhat more easily using the temperature map depicted in Fig. 26. The temperature given for each simulator is the average of the thermocouple measurements for that simulator without regard to elevation. Because every other interior simulator had thermocouples near the upper and lower ends of the heated zone (see Figs. 3 and 4), the averages given for these simulators in Fig. 26(*b*) reflect the lower temperatures existing near the ends of the heated zone during the transient. The figure also shows that the temperatures of the exterior simulators were 10 to 20°C lower (at the time for which it applies) than the average of the interior ones, as would be expected from the boundary conditions.

The data given in Figs. 16–25 for the inner 6 × 6 array were used to obtain the axial temperature profiles plotted in Fig. 27; the average at each instrumented elevation, the range of the data, and the number of thermocouples on which the average is based are also noted in the plot. The profile 1.0 s before the first tube burst shows the end effects mentioned above. Also evident is a slight temperature increase toward the lower end of the bundle (in the direction of and caused by the steam flow), with the peak temperature elevation being nearest the lower grid.

The temperature maps provide considerable insight and greatly facilitate visualization, interpretation, and evaluation of local and overall temperature distributions. As evident, the initial radial and axial temperature distributions were very uniform, indicating uniform distribution of the steam. Compare, for example, the data in Fig. 16 for the 84-cm elevation with the inlet steam temperatures at the 107-cm elevation in Figs. 13 and 14. Also, compare Fig. 25 with these figures for the radial distributions at the lower end of the heated zone. The modifications made to the inlet steam nozzle and others made to control heat losses from the top of the test vessel effectively eliminated temperature gradients in the bundle like those experienced in the B-5 test.

Differential pressures measured 1.0 s before power-on and 1.0 s before the first tube burst are presented in a similar format in Fig. 28. Because the simulators were pressurized simultaneously from a common header and then isolated individually, the uniformity in initial pressure indicates the absence of seal leaks. The data in Fig. 28(*b*) are consistent with Fig. 26(*b*) and indicate that the interior simulators were slightly hotter and had deformed slightly more at this time than the exterior ones.

A number of data plots are presented below to illustrate significant features of the test as it progressed and to provide an indication of the general conditions prevailing at the times of important events. A parameter, TAV-10, is plotted in a number of these figures to represent the bundle average temperature. This parameter is in reality the average of eight thermocouples (TE 11-2, TE 20-2, TE 29-2, TE 31-2, TE 34-2, TE 38-2, TE 45-2, and TE 52-2) at the 38-cm elevation (see Fig. 3 for relative positions) that was electronically averaged and recorded during the test to facilitate characterization and visualization of the bundle temperature as a function of time.

Figure 6, presented earlier, showed this parameter and the applied voltage as a function of time after power-on. Constant voltage (dc) was applied to the simulators for 141.74 s; this point is noted in the figure (and subsequent plots) for reference purposes by an arrow on the time axis. Because the temperature coefficient of resistivity of the heating element material (Kanthal A-1) is very low (less than 0.005%/°C above 700°C), the power generation varied very little from the average of 1.42 kW/m. As a result the cladding temperature increased at a nearly constant rate as indicated in the figure. The average heating rate in the high-alpha-Zircaloy temperature range (i.e., from ~35 s to ~105 s after power-on, corresponding to TAV-10 temperatures of 498 and 813°C) was 4.5°C/s. As the temperature increased into the two-phase-Zircaloy temperature range, the heating rate decreased because of increased heat losses at the higher temperatures and the significantly greater heat capacity of the two-phase material; deformation feedback effects also may have contributed to the reduction of the heating rate. The cladding average heating rate from ~115 s to ~141 s after power-on (i.e., just before power-off) was 3.5°C/s. Because maximum pressure, indicating the onset of significant deformation, was encountered in the latter time frame (Table 3), the lower heating rate (i.e., 3.5 C/s) is considered to be the appropriate rate for characterizing deformation behavior in this test. The average temperature, as indicated by TAV-10, reached a maximum of 958°C about 5 s after power-off and then slowly decreased.

Figure 29 depicts the bundle characteristic temperature (TAV-10) and several pertinent pressures. In particular, the vessel gage pressure is shown by PE-301, and differential pressures are shown by PE-29 for simulator 29 (one of the four central simulators and the first simulator to burst), by PE-55 for simulator 55 (one of the corner simulators in the inner 6 × 6 array and the last simulator of this array to burst), and by PE-8 for simulator 8 (an outside corner simulator and the last simulator to burst). The vessel pressure remained constant until the first tube burst, at which time it increased because of the release of the hot, high-pressure gas from the ruptured simulators. About 3 s after power-off, the steam control valves opened to reduce the vessel pressure and to permit increased steam cooling; at this time the vessel pressure decreased rapidly to atmospheric. The sudden decrease in the external pressure caused a small (~200-kPa) increase in the differential pressure of those simulators (near the corners in the outer ring of the array) not yet burst, as typified by the PE-8 pressure trace in the figure; this small increase (~7%) in differential pressure may have slightly advanced the failures in the last nine or ten tubes to burst.

Typical steam temperatures measured (see Fig. 5 for thermocouple locations) at the inlet (TE-322) and at the outlet (TE-327) and the vessel pressure (PE-301) are shown in Fig. 30; TAV-10 is included to characterize the bundle temperature. Neither the inlet nor the outlet steam thermocouples indicated unstable temperatures during the time the simulators were bursting; however, the outlet steam thermocouples sensed a temperature increase after the sudden vessel pressure decrease. This temperature increase was probably an effect of increased steam flow, caused by opening the large bypass valve downstream of the vessel, on the heat transfer conditions at the lower end of the bundle. The small spike evident in the vessel pressure trace (PE-301) at ~137 s after power-on was

caused by a number of tube bursts during a short time interval (Fig. 8) about this time.

The tube bursts occurred in an unusually orderly manner, starting 133.14 s after power-on, as was indicated earlier in Fig. 7, because of uniform azimuthal conditions and a small radial temperature gradient that was caused by heat losses to the surrounding shroud. The cladding axial temperature distribution, averaged over the inner 6 × 6 array, was also very uniform at this time as shown in Fig. 31. Except for one, all the simulators in the central 4 × 4 array burst (Fig. 7) before any bursts occurred in the next outer row (i.e., the outer ring of the inner 6 × 6 array). The 16 simulators of the central 4 × 4 array burst in a 2.25-s time interval. All the simulators in the outer ring of the inner 6 × 6 array burst in a 6.00-s time interval, with the four corner simulators of this array bursting last. The axial temperature distribution (Fig. 31) was still very uniform when power was terminated 0.60 s later. The first simulator in the outer ring burst 0.40 s after power-off; all the simulators except the four corner ones in this ring burst by the time the axial temperature distribution became distorted ~10 s later (Fig. 31). The corner simulators, with the greatest external heat losses, were subjected to near-isothermal creep conditions over a major portion of their length and failed 25–50 s later. By the time of the last failure, the axial temperature distribution had become severely distorted (Fig. 31) as the result of the increased steam flow that was initiated at power-off. A histogram of the tube burst times, depicted in Fig. 8, shows that the frequency distribution of the interior simulator tube bursts was distinctly different from the distribution of the exterior simulators.

4.1.2 Shroud behavior

The need for electrical isolation between the test array and the closely fitted shroud precluded Joule heating of the shroud. Although the shroud had a highly polished, gold-plated surface to reflect thermal radiation, the temperature of the shroud increased significantly during the test. Figure 32 compares measured shroud temperatures on each of the four sides at the 76-cm elevation (see Fig. 3 for thermocouple identifications and locations) to the characteristic bundle temperature (TAV-10). Similar data are shown in Fig. 33 for the thermocouples at the 28-cm elevation and in Appendix A for all the shroud thermocouples. Differences of ~100°C were measured around the shroud at both elevations; this was probably caused by variations in contact resistance between the outside of the thin shroud and the backup thermal insulating material (see Sect. A-A of Fig. 1). About 135 s after power-on, the shroud thermocouples indicated significant and rapid temperature increases that were probably caused by the release of significant quantities of high-temperature gas from the rupturing tubes (the first tube burst 133.14 s after power-on). Figures 34 and 35 compare shroud temperature measurements at the two instrumented elevations on the north and south sides of the bundle, respectively, with simulator cladding temperature measurements in the vicinity (see Fig. 3 for measurement locations). The average of the eight shroud temperature measurements was ~165°C less than the bundle average temperature during the time deformation was occurring (i.e., 1.0 s before the first tube burst).

These figures, as well as similar data in Appendix A for the east and west sides, indicate small (2 to 3°C) steplike decreases in simulator cladding temperatures at approximately the same time the shroud temperatures increased significantly. These small cladding temperature decreases, which sometimes occur, cannot be attributed to failure of these simulators because all the exterior simulators failed after power-off. Noise spikes appear to be unlikely causes because the perturbations were all negative. Although the major cause of the shroud temperature increases can be attributed to heating by hot gas escaping from failed interior simulators, there is a possibility that some of the increase can be attributed to contact between the deforming simulators and the shroud.

4.1.3 Fuel pin simulator behavior

Although the temperature distributions presented in Sect. 4.1.1 characterize the bundle as a whole, the individual simulators behaved differently from these smoothed (averaged) profiles. This would be expected, because the simulator temperature distributions would be strongly influenced by the heat generation characteristics of the individual simulators and by their locations within the array.

As was discussed in Sect. 2.1, the simulators in the outer ring were considered as guard heaters for simulating the radial temperature and mechanical boundary conditions imposed on the interior simulators. Because the deformation behavior of the exterior simulators would be atypical, only 8 of the simulators were instrumented with thermocouples; however, all 28 of the exterior simulators were instrumented with pressure transducers. Each of the 36 interior simulators was instrumented with 4 thermocouples, spot-welded to the inside surface of the cladding at the locations shown in Fig. 3, and a pressure sensor to provide cladding temperature and pressure data during the test transient.

Plots of these data provide considerable insight and qualitative information that supplement the tabulated data for analytical purposes. However, to include plots and data tabulations of convenient sizes for reading would add considerable bulk to this report. Instead, typical examples are displayed to illustrate the type of information that is included for each simulator in the computer-generated microfiche enclosures inserted in the pocket on the inside back cover. Figure 36 shows a typical plot of pressure (differential above the external pressure in the test vessel) and temperature data for an interior simulator. This particular one (simulator 29) is in one of the four central positions in the array and was the first to burst. A reference arrow is located on the abscissa to mark the time power was terminated. The time of burst is indicated by the sudden drop in pressure and frequently by a perturbation in the temperature traces. Figure 37 is a similar plot for one of the fully instrumented simulators (simulator 3) in the exterior ring of the array. The small pressure increase just before the burst was caused by the opening of the large bypass steam valve (for rapid posttest cooldown) to reduce the vessel pressure. Both figures show that the temperature distribution was unusually uniform before the power was terminated; after power-off the individual temperature traces (for different measurement

elevations in the simulators) diverged as a result of the increased posttest cooling steam flow. Similar plots for all the simulators are presented in Appendix A.

Qualitative information on burst time, temperature, pressure, etc., can be obtained from the figures, but quantitative information is best obtained from the computer-generated summary tables presented in Appendix B for the conditions measured at the time each tube burst. An example, for simulator 29, is given in Table 6 to illustrate the format and type of information available in the appendix. The tables include (1) the times from power-on and power-off and the magnetic data tape record from which the tabulation was printed, (2) the simulator differential pressure, (3) the measured cladding temperatures (as indicated by each of the four thermocouples and their average) on those simulators instrumented with thermocouples, and (4) the times from other tube bursts (relative to that for which the table pertains). Pertinent miscellaneous measurements include (1) shroud temperatures (TE 91-1 through TE 91-4 and TE 92-1 through TE 92-4; see Fig. 3 for locations), (2) inlet steam temperatures (TE-320 through TE-324; see Fig. 5 for locations), (3) outlet steam temperatures (TE-325, TE-327, and TE-328; see Fig. 5 for locations), (4) vessel gage pressure (PE-301), (5) total current through bundle (EIE-10), (6) voltage drop across bundle (EEE-10), and (7) characteristic bundle average temperature (a posttest software-averaged version of TAV-10; see Sect. 2.1 for definition).

Similar tables are also given in Appendix B at selected time intervals for 200 s of the transient; these can be used to approximate the transient of either the individual simulators or the bundle as a whole.

4.2 Pretest and Posttest Results

The information contained in this section was obtained from the pretest and posttest examinations of the test array. Some information, such as the simulator IR scans, resulted from quality assurance efforts made to characterize the test components. Other information, such as bundle disassembly photographs, was obtained as a step in the posttest examination of the bundle. The results are presented in considerable detail, because we believe the data are extremely important to the interpretation of the test in terms of deformation behavior and distribution.

4.2.1 Bundle pretest photographic documentation

Although they are not directly applicable to the interpretation of the test, selected photographs of the bundle assembly are included in this section for general interest. Various details of the construction and monitoring instrumentation can be seen.

A view of test array before installation of the shroud is shown in Fig. 38. As described earlier, the design was essentially identical to the B-5 8 × 8 design. The array was supported from the top flange and was free to move axially during the test. A close-fitting shroud was also supported from the top flange and was used to simulate the radial restraint in a nuclear fuel assembly without restricting axial movement of

the grids. The shroud was constructed of thin stainless steel strips, having highly polished, gold-plated surfaces, backed by insulating material; construction details are illustrated in Fig. 39. The four shroud panels (Fig. 40) were assembled into a box around the test array as illustrated in Fig. 41. The completely assembled array is shown in Fig. 42.

Several modifications were made to the B-5 design to improve performance in the B-6 test. These included improving the steam distribution at the bundle inlet and outlet. Instead of one steam inlet on the north side of the shroud, the flow was directed to two sides (east and west), as can be seen in Fig. 42. Additionally, a flow distribution baffle (Fig. 38) with 12.3-mm-diam holes for the 10.92-mm-diam rods was positioned between the steam inlet and the uppermost grid. A steam deflector (Fig. 38) was added to minimize impingement of hot steam on the lower seal glands of the fuel pin simulators.

Figure 43 shows a typical shroud thermocouple attachment. Each thermocouple was formed by making a ball junction (~0.4-mm diam) on the end of 0.13-mm-diam type S wires. The ball was then spot-welded to the back side of the thin shroud reflector strip. The mass of the thermocouple was kept small to minimize thermal shunting, that is, cooling of the reflector strip at the point of attachment by the thermocouple itself. An even smaller (0.076-mm-diam) type S wire was used in B-5 but was found to be difficult to work with and too fragile for this particular application. The small thermocouple wires exited through an insulator at the center of a plug, as shown in Fig. 44, and were spliced to 0.25-mm-diam wires that exited the end of sheathed type S thermocouple extension material through a glass end seal to prevent ingress of moisture. A protective cover was installed over the area where the thermocouple wires exited the shroud panel (Fig. 42).

A view of the lower end of the bundle showing the outlet steam thermocouples is shown in Fig. 45. All the steam thermocouples were 0.71 mm diam, stainless steel sheathed type K with insulated junctions. The junction end was centered within the flow channel with a ceramic spacer.

4.2.2 Bundle posttest photographic documentation

Following the burst test, the test assembly was removed from the test vessel and partially disassembled for observation and examination. After posttest instrumentation checks were performed, the shroud assembly was removed to permit visual observation and dimensional checks of the test array. Further disassembly (including successful removal of the internal heaters from all except four of the simulators in the outer ring) was then accomplished, and photographs were made to document the appearance in detail.

Figure 46 shows the west face of the assembly after removal of the shroud and internal heaters. The meter stick (suspended from the bundle with zero at the bottom of the heated zone) serves as a convenient reference to the discussion throughout this report. The west face panel of the shroud box is also shown in its relative axial position; the polished reflector strip shows discoloration and distortion patterns that reflect the image of the test array. A different perspective of the array is shown in Fig. 47. Deformation is rather uniformly distributed except for

the corner tubes. As discussed earlier, these tubes were the last to fail (Fig. 8) and were subjected to near-isothermal creep conditions for relatively long times compared to the deformation time of the other tubes. As a result their deformation, being considerably greater and less uniformly distributed, was atypical. Enlarged frontal views of the north and east faces, showing the region between the two interior grids (Fig. 38), are presented in Fig. 48. A scale is included to measure distances from the start of the heated zone. Similar views of the south and west faces are shown in Fig. 49.

The thin, highly polished reflector strips used in the shroud panels were preloaded axially with high-temperature springs (Figs. 39 and 40) to compensate for differential thermal expansion and to keep the strips taut during the test. The design was not entirely successful, because the strips wrinkled (bowed inward) and contacted the simulators as illustrated by the irregular discoloration and distortion patterns in Fig. 50; the locations of the grids are noted (by marks on the polished surfaces) for reference. Evidently the two-dimensional temperature gradients in the thin strips and/or the restricted movement caused them to buckle and touch the simulators. Undoubtedly this influenced the distribution of the cladding deformation, as discussed in Sect 5. Interestingly, there is little evidence that the corner simulators, although they deformed more than their neighbors, touched the strips. Shroud box corner restraints probably prevented the transverse buckling patterns from bowing the strips inward, so they did not contact the corner simulators.

Because deformation occurred in the two-phase-Zircaloy temperature range, texture effects caused very little change in the axial length of the cladding heated zone. The average elongation, based on the data presented in Table 7, was 0.31%.

4.2.3 Bundle cross-section photographs

Following photographic and dimensional documentation of the test array, it was cast into an epoxy matrix and sectioned transversely at 10- to 20-mm intervals for measurement of the deformation in each tube. The sections were polished sufficiently to sharply define the tube wall boundaries and then photographed. Although the photographs facilitated measurement of the tube strain at the axial nodes, we believe careful study of them also provides considerable insight into the deformation behavior and temperature distributions during the deformation process. For these reasons, the section photographs are given in Figs. 51 through 108 for documentary purposes.

The photographs were taken looking down on the surface at the given elevation with simulator 1 in the northwest corner. This corresponds to the layout of Fig. 3, which can be used as a convenient reference for tube identification in each section photograph. All the figures have white arrow points in the upper left corner. The distance along the edge of the epoxy matrix between the arrow points is proportional to the elevation of the section and can be used to calculate the height (from the bottom of the heated zone) of the actual plane of the photograph. A scale was also cast into (and is readable from the north side of) the matrix adjacent to

tubes 4 and 5 to provide another convenient and permanent reference measurement. A 1-in. scale (subdivided into 50 divisions of an inch) is included on the north edge of the matrix to facilitate calculation of the actual magnification factor of the photograph. Certain tubes are identified by number in several of the photographs for discussion of interesting features.

The remains of the internal heaters that could not be removed from the inside of the cladding tubes of four of the simulators can be seen in the section photographs. Figure 51, a photograph of a section well below the heated zone, shows an undeformed region of the array. Sections through the lower grid are shown in Figs. 58 and 59; the band (Fig. 45) that slightly retained the outer ring of simulators within the grid was located between the cutting planes of the two sections. Some flattening of the tubes at the spring-loaded contacts is evident in Fig. 59; the strain in the tubes at this node was in the range of 5 to 7%.

Four of the six failures (tubes 11, 13, 17, and 18) that probably initiated at thermocouple spot-welds occurred at the 20.3-cm elevation shown in Fig. 65. Although the failure orientations of tubes 11 and 13 are slightly different from the specified thermocouple locations (Fig. 3), there is physical evidence that the failures were at the spot-welds. The other two failures at thermocouple locations can be seen in Fig. 71 (tube 30) and in Fig. 78 (tube 62). Sections made at other planes containing thermocouples are shown in Figs. 84, 89, 100, and 104.

Localized wall thinning other than in the immediate vicinity of the tube failures was observed at a number of locations; typical examples are tube 42 in Fig. 65, tube 35 in Fig. 67, tube 54 in Fig. 73, tube 46 in Fig. 74 [incipient failure (?), although the failure was at a much lower elevation (Fig. 65)], tube 20 in Fig. 76 (at two places), and tube 38 in Fig. 82. While some of the locally thinned areas (at least before the burst) were opposite neighboring tubes (tube 42 in Fig. 65 is an example), a number of the thinned areas were located $\sim\pi/4$ rad away (tube 20 in Fig. 76, for example) from neighboring tubes. Presumably, very small azimuthal temperature gradients, combined with the high sensitivity of the creep rate equation to temperature in the alpha-plus-beta phase region,[22] were responsible for the localized thinning.

The sections were carefully examined to define the tube burst locations given in Table 8. The axial locations were determined first by internal examination of the tubes with a borescope before the encapsulation with epoxy and confirmed later from measurements of the sections; the midpoint elevations and burst lengths are considered reasonably accurate (to within 3 to 5 mm). The azimuthal orientations were determined from angle measurements made on the sections near the end of each burst opening and are probably accurate to within 5 to 10° of arc length. Burst midpoint elevations and orientations are shown schematically in Figs. 109 and 110, respectively.

As evident in Fig. 109, the bursts occurred over a length of ~28 cm in the lower portion of the region between the two interior grids (centerline elevations of 10 and 66 cm); this is consistent with the axial temperature profiles shown in Fig. 31. Although the steam mass flux was the same as in the previous tests, the heating time was longer and a greater quantity of steam flowed through the bundle. This caused a relatively

greater cooling effect and displaced the deformation downward (i.e., in the direction of steam flow).

As evident in Fig. 110, burst orientations in the two outer rings of simulators had a preferred (and rather uniform) direction toward the center of the bundle, indicating the influence of small azimuthal temperature gradients and an unusually high sensitivity to temperature in the alpha-plus-beta-Zircaloy phase temperature range. Burst directions for the central 4 × 4 array were more randomly distributed, indicating negligible azimuthal gradients. The six bursts that probably initiated at thermocouple spot-welds are noted in the figure. However, the unusual consistency in burst times, temperatures, pressures, and deformation profiles indicates that the bursts were not premature. Also, the burst opening shapes and lengths (Table 8) suggested nothing unusual about these failures. (In previous bundle tests, failures at thermocouple spot-welds resulted in very small pinholes.)

4.2.4 Deformation data reduction methodology and results

Enlarged (~3X) photographs of the sections were digitized to facilitate computer reduction of the photographic data to geometrical parameters describing strains, areas, volumes, centroids, and displacements. From 25 to 50 points on both the outside and inside perimeters of each tube were digitized to provide x-y coordinates with respect to an arbitrary origin established at the same relative position on each section photograph. The digitized points were smoothed by forward-fitting a quadratic curve to four consecutive points and then using the curve to generate ten points between each successive pair of digitized points. Thus, the series of curves (equal to the number of digitized points) was used to smooth and expand the number of digitized points by a factor of ten for use in generating areas, centroids, and chord lengths.

The nodes containing tube bursts required special treatment because the software algorithms required closed perimeters. The endpoints of the burst lips were connected by straight line segments, drawn in such a way as to not enclose any of the adjacent tubes, to provide a continuous (but fictitious) perimeter for use in the fitting and integration algorithms. All the area enclosed by the fictitious perimeter was included as tube cross-sectional area at the burst node. Because the same line segments were used for completing both the inside and outside perimeters, the segments also represented fictitious tube wall regions (of zero thickness) in calculating the area of the deformed tube. Of course, the length of the line segments was not included as part of the perimeter in the strain calculations.

The photographic data for each section were thus reduced to a table of geometric parameters that were used for verification of the digitized data and as a source file for further processing to obtain desired output parameters. Because these tables transform and summarize the section photographs into geometric parameters for analysis, they are included in Appendix C; an example is shown in Table 9 for illustrative purposes. This table, for the section at the 32.4-cm elevation, gives for each tube the cross-sectional areas enclosed by the tube outside and inside perimeters and (by difference) the tube wall area, the lengths of the outside

and inside perimeters, the x- and y-coordinates of the outside and inside tube area centroids referenced to the arbitrary origin established at the same relative position on each section photograph, and the strains (total circumferential elongation) based on the outside and inside perimeters.

One of the data verification procedures used the digitized data and the computer graphics software to reconstruct the section image for comparison with the original photograph. An example of this procedure is illustrated by Fig. 111, which shows the tube identification number, the strain based on outside tube perimeter, and the tube centroid and outline correctly located on the arbitrary coordinate grid. Comparison with Fig. 74 shows that the reconstructed image is an excellent reproduction of the section photograph.

Another more quantitative data verification procedure involved comparing the measured inside and outside perimeter strains to the theoretical expression relating the two (assuming constant tube wall area) as illustrated in Fig. 112. The corresponding inside and outside tube strain data of Table 9 are plotted on the graph as a single data point for each tube. Assuming constant tube wall area, the data points should lie on the theoretical curve. For practical purposes the inside and outside strain values are derived from independent measurements, and if either is incorrect the data point will deviate significantly from the theoretical curve. As evident from the figure, the data are in excellent agreement with the curve and can be assumed to represent the true strains adequately.

After verification of the digitized data, the data tapes were reprocessed to generate a strain matrix (Table 10) of the strain in each tube at each axial node; the values in the table are given as percentage increases of original tube outside circumferences. Burst strains, underlined in the table, were summarized earlier in Table 5 and displayed graphically in Fig. 12 as a function of tube radial position. As was evident in the section photographs (Figs. 51–108), the axial lengths of some of the bursts were such that they appeared in two or three of the section photographs; thus, for a single tube, multiple values of the burst strain could result. We selected the value (underlined in the table) from the section nearest the burst midpoint as the most representative.

The strain matrix was used to plot the axial profile of the deformation in each tube. These profiles are presented in Appendix D; however, an example of an interior simulator (simulator 20, which had the largest burst strain) is shown in Fig. 113 to illustrate the type and format of the information available in this appendix. The centerline positions of the two interior grids and the axial location and length of the burst are noted on the deformation profile. The pretest IR characterization scan of the fuel simulator (internal heater), the pretest axial positions of the thermocouples, and the direction of steam flow are also shown for reference purposes. An illustrative plot of a corner simulator (simulator 1, with the largest volumetric expansion) is presented in Fig. 114.

All the deformation profiles have certain characteristics, more or less independent of the characteristics of the individual fuel simulators. These include strains of 4 to 8% in the region of the grids (centered about the 10- and 66-cm pretest elevations) and maximum strains of 3 to 8% in the region between the bottom of the heated zone and the lower grid. Most tubes exhibited maximum strains of 8 to 13% in the region

between the upper grid and the top of the heated zone. Strain in this region was strongly influenced by the cooling effect of the inlet steam.

Strains of the interior tubes in the region between the interior grids increased rather uniformly in the direction of the steam flow. Strains of the exterior tubes in this region were in general less uniform because of localized contact with the shroud. The more or less uniform increase in deformation along the length of the tubes was caused by the unusually high sensitivity of the creep rate equation to temperature in the two-phase-Zircaloy temperature range[22] and the small axial temperature gradient (Fig. 31).

The deformation profiles did not correlate as well with the pretest IR characterization scans as in previous tests. The characterization scans were made primarily for simulator manufacturing quality assurance purposes and used a heating rate of ~40°C/s. At the heating rate used in the test (~4°C/s), the perturbations in heat generation were much less pronounced. Consequently, the deformation profiles were more sensitive to other effects than to the minor variations in simulator heat generation.

The bursts in six of the tubes initiated at thermocouple welds, as noted in Fig. 110. The deformation plots in Appendix D suggest that other bursts may have initiated at thermocouples. However, these can be eliminated from consideration by comparison of the burst orientations in Fig. 110 with the thermocouple locations in Fig. 3.

Excessive ballooning over an extended length is a concern in LOCA analyses. For the tubes and spacing (1.32 pitch-to-diameter ratio) used in our tests, adjacent tubes will touch with 32% uniform expansion. As evident from the deformation profiles and Table 10, very few tubes exceeded this value and then only close to the bursts.

Another important characterization of tube deformation is the volume increase over the heated length. This parameter is closely related to flow resistance, because the volume increase takes into account deformation along the length of the tube. The volume increase was calculated for each of the tubes from the geometric data given in Appendix C. The calculation assumed that the tube cross section at each axial node was circular in shape and had a perimeter equal to the deformed tube outside perimeter; presumably, this represents the shape of the tube just before failure. The area of the tube was then calculated at each node and integrated over the tube heated length, using the trapezoidal rule, to obtain the volume occupied by the outside diameter. This value was expressed as a percentage increase over the original volume and was tabulated in Table 5 and displayed graphically in Fig. 11 as a function of tube radial position.

Individual tube overall deformation was also characterized by computing an average strain value from the volumetric expansion data. This calculation assumed that the expansion was uniformly distributed over the tube heated length; that is, no account was taken of local variations caused by grid and end effects. The average strains thus calculated were tabulated in Table 5.

The total expansion for all tubes at each axial node is also of interest because it determines the coolant channel flow area restriction. This parameter is normally expressed as an average value for an array

cross section and was calculated on the basis of a rod-centered unit cell, using the equation

$$B = 100 \times \frac{\sum_{n=N}^{n=N} (A_{d,n} - A_o)}{N(p^2 - A_o)}, \qquad (4.1)$$

where

B = percentage restriction in coolant channel flow area,
$A_{d,n}$ = outside area of deformed tube (mm^2),
A_o = outside area of original tube (mm^2),
p = tube-to-tube pitch in square array (mm),
N = number of tubes in square array.

With this definition, B is 0 for no deformation and 100% if all the tubes deform into a square whose sides are of length p (completely filling the open area). For the case of uniform ballooning such that the tubes just come into contact (i.e., 32% strain for the dimensions appropriate to this test), B is 61%.

In summing the deformed tube areas in Eq. (4.1) for those nodes that contain bursts, one must decide how to treat the burst lips. As in the past, we used two treatments that appear to be reasonable upper and lower limits for the flow restriction. The upper limit used the area enclosed by the fictitious tube outside perimeter discussed earlier. Tube areas obtained this way are tabulated in the tables of Appendix C. For the lower limit, the software compared the area enclosed by the fictitious perimeter to that enclosed by a circular tube having the same (actual) perimeter of the burst tube and used the latter if smaller to describe the deformed tube area, $A_{d,n}$, at the burst. Results from processing the data in this manner are tabulated in Table 11. The right-hand column of the fourth page of the table is the sum of the 64 tube areas at any elevation.

The percentage flow area restriction was calculated at each axial node, using the above equation and appropriately defined values for the parameters, for the entire 8 × 8 array, the inner 6 × 6 array, and the central 4 × 4 array. The results are tabulated in Table 12; values listed under "maximum" are based on outside tube areas given in Appendix C, and those listed under "minimum" are based on the data in Table 11. By definition the two values differ only at those nodes where tube bursts occurred. Even at these nodes the differences are small because the burst openings were small and the two definitions are not greatly different.

The minimum flow area restriction data of Table 12 were depicted graphically earlier in Fig. 13. It is noted that the lower limit of coolant channel flow area restriction, as defined above, was also used by Powers and Meyer in NUREG-0630 (Ref. 23).

Restraint conditions of a full-size fuel bundle were simulated in the B-6 test by surrounding the 8 × 8 test array with a closely spaced

shroud that limited outward movement of the simulators. The pretest spacing (1.75 mm) was such that contact would be made when the exterior simulators deformed 32% provided the simulators were neither displaced nor bowed outward. Posttest examination showed that contact forces during deformation and/or thermal bowing caused permanent displacement of the simulators.

Simulator displacements were estimated at each axial node by a least-squares fitting routine that simultaneously minimized all the displacements. The manner in which this was accomplished can be visualized by imagining placement of a rigid grid (with pretest tube centroids at the center of each grid cell) on the section photograph and then translating and rotating the grid on the plane of the photograph until the average displacement between the pretest and posttest centroids of the 64 tubes is minimized. Using the centroids of the areas enclosed by tube outside perimeter from the geometric data source file (Appendix C) and the pretest tube pitch, the data were processed to provide the displacements in both tabular and graphical form. An example of the tabular output (for the section displayed in Fig. 111) is presented in Table 13; tables for all the sections are given in Appendix E. Although the computations were performed with reference to the arbitrary coordinate system that was established relative to the north side of the epoxy matrix when the section photographs were digitized, the results were translated to a new coordinate system that has its origin at the pretest centroid of simulator 1 (see Fig. 3). This facilitates interpretation and use of the displacement data. As evident from the pretest centroid coordinates in Table 13, the coordinate system used for digitizing the data was not perfectly aligned with the epoxy matrix; instead, it was rotated slightly clockwise.

As an example, the graphical output for the section displayed in Fig. 111 is shown, referenced to the digitizing coordinate system, in Fig. 115 to illustrate tube displacements relative to an imaginary grid that defines the pretest unit cells at this elevation. Similar plots are presented in Appendix F for all the axial nodes. In the figure, dots are used to denote the tube pretest centroids at the midpoints of the unit cells and crosses to denote the posttest centroids of the tube outlines. The latter correspond to the shapes and sizes of the areas enclosed by the tube outside perimeters. Straight line segments, representing fictitious perimeters, are drawn in the burst regions of those tubes that have bursts at this elevation (see Fig. 74). The outside of the imaginary grid corresponds to the pretest dimensions and the position of the shroud.

The figure shows the permanent displacements of the tubes within the original unit cells and aids visualization of subchannel flow area restriction.

5. SOME OBSERVATIONS AND LIMITED INTERPRETATION OF RESULTS

Initial conditions for the test were unusually uniform in both the axial and radial directions. As a result of the uniform conditions and the low heating rate, the temperature distributions remained reasonably uniform until all the tubes in the inner 6 × 6 array burst. Table 14 gives the average and standard-deviation (σ) values of a number of characteristic parameters and can be used to investigate variations as a function of radial position in the test array. Heat losses from the exterior simulators to the unheated shroud caused slightly lower heating rates and slightly later burst times for these simulators. Also, the heat losses were nonsymmetrical and caused azimuthal temperature gradients to develop in these simulators and influence the failure patterns, as evident in the burst orientations shown in Fig. 110.

In addition to this general behavior, there were local perturbations, caused by contact between the shroud and the exterior simulators, that influenced the axial distribution of the deformation. As shown by Fig. 50, contact with the shroud occurred at more or less regular intervals along the length and caused these localized regions of the simulators to be colder and, thus, experience less deformation. The deformation profiles of the exterior simulators show a periodic variation in the amplitude of the deformation that correlates well with the shroud contact areas. Figure 116 illustrates the periodic behavior of the profiles for the simulators on the north face of the array (see Fig. 3 for relative positions); similar behavior was observed on the other three faces. Since the corner simulators (simulators 1 and 8 in the figure) did not contact the shroud as much and as frequently as the others, the peaks and valleys in their profiles are not as well aligned.

Figure 117 is a similar plot that compares the profiles of the first layer of simulators to those of the second layer. Although some cyclic behavior is evident in the latter, it is less pronounced, except for simulators 9 and 16, which were located on the west and east faces of the array and thus were in contact with the shroud. The cyclic effect is practically dissipated with two layers of tubes, as shown by the comparison in Fig. 118 of the deformation profiles of the second and third layers of simulators.

As shown in Fig. 110, there was a preferred direction for the orientation of the bursts in the two outer rings of simulators, indicating an influence of azimuthal temperature gradients in each ring. Burst directions for the central 4 × 4 array were more randomly distributed, indicating a rather uniform temperature field. Unlike the results from the B-5 test,[8] the data presented in Table 14 — particularly the data for volumetric expansion over the heated length, burst strain, and average strain of the region between the interior grids — can be interpreted to imply that a single row of guard heaters is sufficient to establish a uniform radial temperature profile in a small test bundle without a heated shroud. However, the preferred burst orientation (inward) for the simulators in the outer ring of the inner 6 × 6 array and the effect of local perturbations shown in Figs. 117 and 118 indicate that the azimuthal temperature gradient effects were sufficient to influence the direction and axial location of the bursts and, presumably, the magnitude

of the local flow restriction in the two outer rings of simulators. Altogether the data show, consistent with the B-5 test results, that the equivalent of two rows of deforming guard simulators is necessary in small bundles to duplicate temperature and mechanical boundary conditions of large bundles.

ACKNOWLEDGMENTS

Data presented in this report reflect the combined efforts of a number of people over an extended period of time, spanning fabrication, testing, pretest and posttest examination of the test array, and reducing and processing the test data.

We wish to acknowledge the contributions of W. A. Bird for his careful attention to all the instrumentation and control aspects of the test; E. L. Biddle, J. N. Money, and C. Cross for assembly of the test array and for the many other necessary support tasks; F. R. Gibson for programming and operating the CCDAS and for processing much of the data; C. M. Boles for excellent pretest and posttest photography; F. G. Childress for developing procedures and casting the array in a high-quality epoxy matrix; B. C. Leslie for the sectioning, polishing, and excellent photography of the bundle cross sections; L. Jung and co-workers for developing software and digitizing the photographic data; N. J. Price for developing software and processing much of the digitized data; the Fuel Pin Simulator Development Group, under the leadership of R. W. McCulloch, for development and procurement of the fuel simulators; and the many other groups and individuals who had a part in the test and in the preparation and publication of this report.

We would like also to express our appreciation for the support and guidance provided by the NRC Program Managers: Dr. M. L. ("Pic") Picklesimer for several years prior to his retirement and, afterward, Dr. R. Van Houten.

REFERENCES

1. R. H. Chapman et al., *Quick-look Report on MRBT B-6 (8 × 8) Bundle Test*, Internal Report ORNL/MRBT-7 (January 1982).

2. R. H. Chapman, *Multirod Burst Test Program Prog. Rep. January–June 1982*, NUREG/CR-2911 (ORNL/TM-8485).

3. A. W. Longest, *Multirod Burst Test Program Prog. Rep. January–June 1981*, NUREG/CR-2366, Vol. 1 (ORNL/TM-8058).

4. J. L. Crowley, *Multirod Burst Test Program Prog. Rep. July–December 1981*, NUREG/CR-2366, Vol. 2 (ORNL/TM-8190).

5. A. W. Longest, R. H. Chapman, and J. L. Crowley, "Boundary Effects on Zircaloy-4 Cladding Deformation in LOCA Simulation Tests," *Trans. Am. Nucl. Soc.* 41, 383 (1982).

6. R. H. Chapman, J. L. Crowley, and A. W. Longest, "Effect of Bundle Size on Cladding Deformation in LOCA Simulation Tests," *Zirconium in the Nuclear Industry: Sixth International Symposium*, ASTM STP 824, D. G. Franklin, R. B. Adamson, and B. Cox, eds., American Society for Testing and Materials, in press.

7. A. W. Longest, J. L. Crowley, and R. H. Chapman, *Variations in Zircaloy-4 Cladding Deformation in Replicate LOCA Simulation Tests*, NUREG/CR-2810 (ORNL/TM-8413) (September 1982).

8. R. H. Chapman, J. L. Crowley, and A. W. Longest, *Experiment Data Report for Multirod Burst Test (MRBT) Bundle B-5*, NUREG/CR-3459 (ORNL/TM-8889) (in publication).

9. R. H. Chapman, *Multirod Burst Test Program Prog. Rep. January–June 1980*, NUREG/CR-1883 (ORNL/NUREG/TM-426).

10. R. H. Chapman et al., *Bundle B-1 Test Data*, ORNL/NUREG/TM-322 (June 1979).

11. R. H. Chapman et al., *Bundle B-2 Test Data*, ORNL/NUREG/TM-337 (August 1979).

12. R. H. Chapman et al., *Bundle B-3 Test Data*, ORNL/NUREG/TM-360 (January 1980).

13. A. W. Longest, R. H. Chapman, and J. L. Crowley, *Experiment Data Report for Multirod Burst Test (MRBT) Bundle B-4*, NUREG/CR-2968 (ORNL/TM-8509) (December 1982).

14. R. W. McCulloch, P. T. Jacobs, and D. L. Clark, *Development of a Fabrication Procedure for the MRBT Fuel Simulator Based on the Use of Cold-Pressed Boron Nitride Preforms*, NUREG/CR-1111 (ORNL/NUREG/TM-362) (March 1980).

15. W. A. Simpson, Jr., et al., *Infrared Inspection and Characterization of Fuel-Pin Simulators*, ORNL/NUREG/TM-55 (November 1976).

16. R. H. Chapman (comp.), *Characterization of Zircaloy-4 Tubing Procured for Fuel Cladding Research Programs*, ORNL/NUREG/TM-29 (July 1976).

17. R. H. Chapman, *Multirod Burst Test Program Prog. Rep July–September 1976*, ORNL/NUREG/TM-77.

18. J. E. Lewis et al., "Texture Measurement Techniques for Zircaloy Cladding: A Round-Robin Study," pp. 39–62 in *Zirconium in the Nuclear Industry: Fifth Conference*, ASTM STP 754, D. G. Franklin, ed., American Society for Testing and Materials, 1982.

19. W. E. Baucum and R. E. Dial, *An Apparatus for Spot Welding Sheathed Thermocouples to the Inside of Small Diameter Tubes at Precise Locations*, ORNL/NUREG/TM-33 (August 1976).

20. R. L. Anderson, K. R. Carr, and T. G. Kollie, *Thermometry in the Multirod Burst Test Program*, NUREG/CR-2470 (ORNL/TM-8024) (March 1982).

21. R. T. Bailey, *Steady-State Pressure Losses for Multirod Burst Test (MRBT) Bundle B-5*, NUREG/CR-2597 (ORNL/Sub/80-40441/1) (April 1982).

22. C. A. Mann et al., *The Deformation of PWR Fuel in a LOCA*, UKAEA Report ND-4-701(S) (April 1982).

23. D. A. Powers and R. O. Meyer, *Cladding Swelling and Rupture Models for LOCA Analysis*, NUREG-0630 (April 1980).

Table 1. As-built data for B-6 fuel pin simulators

Bundle position No.	Zircaloy tube serial No.	Internal fuel simulator[a]		FPS[b] gas volume (cm^3)	Bundle position No.	Zircaloy tube serial No.	Internal fuel simulator[a]		FPS[b] gas volume (cm^3)
		Serial No.	Element resistance (Ω)				Serial No.	Element resistance (Ω)	
1	0886	MNL-066	1.94	47.5	33	0873	MNL-049	1.96	48.9
2	0244	MNL-003	1.97	50.7	34	0231	MNL-015	1.99	50.7
3	0869	MNL-054	1.96	48.9	35	0857	MNL-029	1.95	48.6
4	0245	MNL-038	1.98	50.3	36	0232	MNL-086	2.01	50.8
5	0870	MNL-031	1.96	48.9	37	0858	MNL-071	1.97	48.8
6	0246	MNL-060	1.98	50.4	38	0233	MNL-055	2.00	50.8
7	0888	MNL-074	1.96	47.3	39	0859	MNL-022	1.97	49.6
8	0247	MNL-023	1.94	49.9	40	0251	MNL-006	1.96	50.8
9	0248	MNL-032	1.96	50.6	41	0252	MNL-017	1.98	52.9
10	0845	MNL-026	1.96	49.6	42	0860	MNL-018	1.97	48.9
11	0219	MNL-076	1.99	49.5	43	0234	MNL-040	1.99	50.4
12	0846	MNL-004	1.96	49.3	44	0861	MNL-063	1.98	49.0
13	0220	MNL-079	2.00	50.1	45	0235	MNL-028	1.98	51.5
14	0847	MNL-024	1.96	49.0	46	0862	MNL-020	1.97	50.2
15	0221	MNL-016	1.98	51.1	47	0236	MNL-068	1.98	49.5
16	0889	MNL-067	1.97	47.4	48	0882	MNL-053	1.97	48.7
17	0871	MNL-044	1.95	48.6	49	0890	MNL-037	1.95	49.9
18	0222	MNL-078	2.01	50.1	50	0237	MNL-051	2.00	49.8
19	0885	MNL-062	1.97	49.5	51	0863	MNL-008	1.97	49.5
20	0223	MNL-081	2.00	50.6	52	0238	MNL-050	1.97	49.8
21	0849	MNL-064	1.95	48.5	53	0867	MNL-025	1.98	50.1
22	0224	MNL-027	1.98	49.7	54	0240	MNL-052	1.97	50.4
23	0850	MNL-021	2.01	49.6	55	0868	MNL-012	2.00	50.0
24	0249	MNL-005	1.95	48.7	56	0256	MNL-057	1.95	52.2
25	0250	MNL-045	1.96	49.6	57	0257	MNL-009	1.93	50.5
26	0851	MNL-048	1.96	49.1	58	0891	MNL-069	1.95	47.6
27	0225	MNL-092	2.00	50.5	59	0258	MNL-061	1.97	50.9
28	0855	MNL-070	1.96	48.9	60	0883	MNL-043	1.98	49.0
29	0226	MNL-073	2.00	50.7	61	0259	MNL-058	1.98	51.6
30	0856	MNL-080	1.98	50.0	62	0884	MNL-007	1.97	49.7
31	0227	MNL-034	1.95	50.9	63	0260	MNL-046	1.96	48.7
32	0872	MNL-014	1.97	49.9	64	0893	MNL-059	1.94	48.0

[a] All 64 fuel simulators were fabricated in the ORNL Fuel Pin Simulator Development Laboratory.

[b] Fuel pin simulator gas volume measured at room temperature before installation into bundle; the volume measured includes a pressure transducer and connecting tube identical to the facility hookup for each simulator.

Table 2. Summary of B-6 initial conditions

ROD NO.	INITIAL CONDITIONS: DIFFERENTIAL PRESSURE (KPA)	TEMPERATURES (DEG C) TE-1	TE-2	TE-3	TE-4	AVG
1	3052					
2	3050					
3	3051	327	328	329	329	328
4	3046					
5	3053	328	328	329	329	328
6	3051					
7	3053					
8	3052					
9	3053					
10	3048	327	329	329	329	328
11	3047	328	328	329	329	329
12	3048	326	329	329	329	329
13	3048	327	330	330	330	329
14	3053	328	330	330	328	329
15	3052	330	329	329	330	330
16	3046					
17	3052	330	329	329	330	330
18	3046	329	330	329	330	330
19	3047	329	329	330	329	329
20	3050	328	329	330	330	329
21	3049	327	330	330	330	329
22	3049	329	330	330	331	330
23	3044	329	330	331	330	330
24	3044					
25	3049					
26	3052	330	330	330	330	330
27	3049	330	330	330	330	330
28	3048	329	330	331	330	330
29	3042	329	330	330	330	330
30	3041	330	330	331	330	331
31	30[illegible]	332	331	330	331	331
32	3[illegible]35	332	329	330	331	331
33	3051	331	330	329	330	330
34	3054	330	330	330	331	330
35	3046	330	331	330	329	330
36	3046	330	331	330	331	330
37	3044	329	331	331	329	330
38	3049	331	331	331	332	331
39	3046	332	331	332	332	332
40	3051					
41	3054					
42	3055	330	330	331	330	330
43	3049	331	331	331	331	331
44	3043	329	330	331	330	330
45	3041	329	331	331	331	331
46	3038	330	331	331	331	331
47	3045	332	331	329	332	331
48	3047	332	332	329	330	331
49	3063					
50	3057	329	330	330	330	330
51	3055	329	330	330	330	330
52	3053	329	330	331	331	330
53	3055	327	330	331	330	330
54	3053	330	331	330	331	330
55	3049	330	330	331	330	330
56	3052					
57	3059					
58	3054					
59	3056					
60	3058	330	329	329	330	329
61	3047					
62	3058	329	329	330	331	330
63	3054					
64	3054					

Table 3. Summary of B-6 conditions at time of maximum pressures

ROD NO.	CONDITIONS AT TIME OF MAXIMUM PRESSURES: DIFFERENTIAL PRESSURE (KPA)	TEMPERATURES (DEG C) TE-1	TE-2	TE-3	TE-4	AVG	TIME[a] (SEC)
1	3308						147.09
2	3250						114.34
3	3236	821	836	824	821	826	115.64
4	3235						110.09
5	3241	794	810	811	801	804	110.04
6	3235						110.39
7	3227						115.19
8	3324						146.84
9	3253						115.19
10	3235	796	818	819	798	808	108.54
11	3240	814	821	829	820	821	108.34
12	3249	791	824	820	798	808	105.99
13	3229	814	830	833	826	826	108.94
14	3236	809	834	834	804	820	110.24
15	3244	823	829	832	827	828	110.64
16	3219						115.09
17	3234	817	814	828	833	823	113.24
18	3238	822	830	832	828	828	110.04
19	3253	806	827	827	801	815	108.49
20	3240	827	834	840	832	833	110.19
21	3245	799	829	825	803	814	107.79
22	3234	817	828	829	823	824	108.44
23	3244	784	812	814	783	798	105.54
24	3219						116.04
25	3235						114.24
26	3256	808	831	830	807	819	109.09
27	3249	812	821	822	816	818	105.74
28	3253	778	802	804	777	790	101.64
29	3242	809	820	822	813	816	106.29
30	3229	808	833	830	806	819	108.69
31	3230	818	828	825	820	823	107.49
32	3245	819	838	834	825	829	115.24
33	3227	816	823	820	818	819	112.29
34	3239	817	823	824	822	822	107.34
35	3238	816	844	840	818	830	111.09
36	3231	801	814	816	807	809	104.59
37	3248	791	819	816	794	805	105.74
38	3251	806	817	820	812	814	105.29
39	3241	800	823	816	796	809	106.44
40	3252						114.89
41	3232						117.49
42	3234	810	834	833	805	820	110.64
43	3242	805	817	817	809	812	105.24
44	3245	796	824	822	797	310	107.54
45	3230	818	830	831	826	827	108.84
46	3240	813	843	840	817	828	111.04
47	3244	816	823	818	814	818	107.49
48	3236	818	820	827	812	819	113.74
49	3256						114.94
50	3251	825	831	833	832	830	111.54
51	3259	781	806	800	779	791	103.84
52	3248	830	840	841	836	837	111.59
53	3248	786	812	812	788	800	105.84
54	3245	832	837	831	834	834	111.34
55	3252	806	827	824	798	814	110.14
56	3231						114.04
57	3299						146.99
58	3231						115.04
59	3241						114.09
60	3255	798	798	800	802	800	107.59
61	3225						116.04
62	3249	823	816	812	817	817	111.34
63	3213						116.24
64	3327						146.79

[a]Time after power-on.

Table 4. Summary of B-6 conditions measured at time of bursts

ROD NO.	APPROXIMATE BURST CONDITIONS: DIFFERENTIAL PRESSURE (KPA)	TEMPERATURES (DEG C) TE-1	TE-2	TE-3	TE-4	AVG	BURST TIME[a] (SEC)
1	2826						191.43
2	3128						146.14
3	3015	905	923	909	905	911	144.39
4	2987						142.24
5	2882	895	917	924	912	912	143.09
6	2997						143.54
7	3046						147.19
8	2861						192.08
9	3059						144.44
10	2785	901	924	929	898	913	139.94
11	2815	921	919	934	925	924	136.19
12	2744	898	932	927	901	915	135.59
13	2856	912	928	929	921	922	135.14
14	2748	903	924	938	894	914	137.14
15	2822	926	932	923	917	924	139.34
16	3079						148.54
17	2941	911	903	920	931	916	143.94
18	2797	911	919	929	927	922	136.84
19	2826	901	919	922	900	910	134.44
20	2759	923	927	934	929	928	135.04
21	2813	894	923	923	898	909	134.14
22	2847	914	932	923	925	924	135.14
23	2746	899	928	927	891	911	138.09
24	3087						145.94
25	2944						143.29
26	2799	900	937	932	903	918	135.74
27	2827	923	936	932	927	929	133.69
28	2797	895	924	934	891	911	133.39
29	2868	908	924	933	917	921	133.14
30	2811	901	937	926	897	915	135.14
31	2715	932	936	929	925	930	137.14
32	2920	904	929	909	902	911	142.54
33	2941	910	908	921	919	914	142.14
34	2835	919	928	936	931	928	136.14
35	2816	897	936	925	906	916	134.74
36	2731	912	929	939	930	927	134.94
37	2803	893	926	924	900	911	134.49
38	2720	912	927	939	926	926	134.59
39	2805	904	929	921	904	914	135.99
40	2934						142.64
41	2956						142.94
42	2815	901	918	934	897	912	137.09
43	2785	919	936	928	922	926	134.64
44	2846	897	934	923	892	911	135.14
45	2763	913	924	935	927	925	135.14
46	2770	897	933	936	908	918	135.39
47	2909	916	925	909	914	916	135.14
48	2982	905	916	923	898	911	143.64
49	2996						144.59
50	2810	914	913	916	932	919	139.04
51	2842	903	924	913	892	908	136.99
52	2837	916	920	923	927	922	137.04
53	2821	895	928	916	895	908	136.74
54	2710	923	934	911	926	924	137.14
55	2759	912	941	941	890	921	141.14
56	3127						145.79
57	2975						174.64
58	3014						147.29
59	2977						143.64
60	2933	918	907	903	913	910	142.84
61	3012						143.94
62	2995	925	915	903	912	914	143.64
63	3043						150.64
64	2865						189.23

[a]Time after power-on.

Table 5. Summary of B-6 test results

Rod	Burst conditions			Tube heated length[a]		Fuel pin simulator[b]		Rod	Burst conditions			Tube heated length[a]		Fuel pin simulator[b]	
	Pressure (kPa)	Temperature (°C)	Strain[g] (%)	Volume increase[c] (%)	Average strain[d] (%)	Volume increase[e] (ratio)	Pressure decrease[f] (ratio)		Pressure (kPa)	Temperature (°C)	Strain[g] (%)	Volume increase[c] (%)	Average strain[d] (%)	Volume increase[e] (ratio)	Pressure decrease[f] (ratio)
1	2826	g	49	31.9	15	1.576	1.080	33	2941	921	27	17.3	8	1.303	1.037
2	3128	g	24	19.8	10	1.335	0.975	34	2835	936	27	24.3	12	1.411	1.077
3	3015	923	31	20.6	10	1.361	1.012	35	2816	936	42	25.3	12	1.446	1.082
4	2987	g	25	16.4	8	1.279	1.020	36	2731	939	39	26.5	13	1.447	1.115
5	2882	924	31	21.5	10	1.376	1.059	37	2803	926	32	24.8	12	1.436	1.086
6	2997	g	28	18.0	9	1.305	1.018	38	2720	927	31	28.5	13	1.480	1.121
7	3046	g	32	18.9	9	1.342	1.002	39	2805	929	26	23.0	11	1.398	1.086
8	2861	g	47	28.9	14	1.497	1.067	40	2934	g	29	18.4	9	1.311	1.040
9	3059	g	25	19.5	9	1.331	0.998	41	2956	g	32	19.3	9	1.312	1.033
10	2785	939	27	26.8	13	1.463	1.094	42	2815	934	43	25.1	12	1.440	1.085
11	2815	934	26	25.1	12	1.436	1.082	43	2785	936	35	25.9	12	1.440	1.095
12	2744	932	32	29.1	14	1.507	1.111	44	2846	934	33	24.0	11	1.420	1.069
13	2856	929	27	24.4	12	1.417	1.067	45	2763	935	35	27.7	13	1.460	1.101
14	2748	924	47	28.6	13	1.501	1.111	46	2770	936	29	26.1	12	1.445	1.097
15	2822	932	26	23.9	11	1.401	1.082	47	2909	925	21	20.6	10	1.356	1.047
16	3079	g	24	18.0	9	1.326	0.989	48	2982	923	23	17.2	9	1.303	1.022
17	2941	931	31	23.2	11	1.409	1.038	49	2996	g	32	22.8	11	1.392	1.022
18	2797	929	26	24.3	12	1.415	1.089	50	2810	932	22	23.2	11	1.400	1.088
19	2826	919	26	25.3	12	1.438	1.078	51	2842	924	34	23.1	11	1.399	1.075
20	2759	934	56	27.3	13	1.462	1.105	52	2837	927	27	23.3	11	1.402	1.076
21	2813	923	30	21.9	10	1.386	1.084	53	2821	928	29	23.0	11	1.394	1.083
22	2847	932	29	22.7	11	1.391	1.071	54	2710	934	43	31.1	15	1.529	1.127
23	2746	928	36	25.6	12	1.443	1.109	55	2759	941	35	27.0	13	1.463	1.105
24	3087	g	26	18.0	9	1.317	0.986	56	3127	g	22	16.8	9	1.276	0.976
25	2944	g	26	20.6	10	1.356	1.036	57	2975	g	38	26.1	12	1.444	1.028
26	2799	937	33	26.0	12	1.454	1.090	58	3014	g	29	23.1	11	1.415	1.013
27	2827	936	30	25.8	12	1.439	1.079	59	2977	g	32	19.9	10	1.335	1.027
28	2797	934	31	25.8	12	1.452	1.090	60	2933	918	26	18.3	9	1.321	1.043
29	2868	933	26	23.4	11	1.396	1.061	61	3012	g	31	18.1	9	1.300	1.012
30	2811	937	26	24.5	12	1.419	1.082	62	2995	925	25	16 6	8	1.287	1.021
31	2715	936	44	31.4	15	1.529	1.124	63	3043	g	24	20.6	10	1.362	1.004
32	2920	929	21	16.8	8	1.289	1.040	64	2865	g	39	25.6	12	1.457	1.066

[a]Measurements based on tube outside perimeter.

[b]Includes fuel pin simulator, pressure transducer, and connecting tube.

[c]From deformation profiles assuming circular cross sections.

[d]Assumes volume increase is uniformly distributed over heated length.

[e]Ratio of final to initial volume (see note b).

[f]Ratio of initial pressure to burst pressure.

[g]Simulator not instrumented with thermocouples.

Table 6. Summary of B-6 test conditions at rod 29 burst time

ROD NO.	DIFFERENTIAL PRESSURE (KPA)	TEMPERATURE (DEG C) TE-1	TE-2	TE-3	TE-4	AVG	TIME FROM BURST (SEC)	ROD NO.	DIFFERENTIAL PRESSURE (KPA)	TEMPERATURE (DEG C) TE-1	TE-2	TE-3	TE-4	AVG	TIME FROM BURST (SEC)
															-13.00
1	3210						-58.29	2	3193						
3	3161	881	897	886	879	886	-11.25	4	3165						-9.10
5	3139	874	892	896	882	886	-9.95	6	3163						-10.40
7	3172						-14.05	8	3212						-58.94
9	3185						-11.30	10	3074	881	907	911	881	895	-6.80
11	3001	909	908	923	912	913	-3.05	12	2955	890	922	917	894	906	-2.45
13	2978	902	920	924	914	915	-2.00	14	3003	889	913	923	883	902	-4.00
15	3087	905	910	909	908	908	-6.20	16	3170						-15.40
17	3141	887	881	900	905	893	-10.80	18	3035	901	910	918	912	910	-3.70
19	2963	897	916	916	896	906	-1.30	20	2982	916	917	931	919	921	-1.90
21	2962	890	920	918	897	906	-1.00	22	2998	907	927	918	916	917	-2.00
23	3049	883	912	912	877	896	-4.95	24	3163						-12.80
25	3154						-10.15	26	3007	890	926	923	897	909	-2.60
27	2913	921	934	929	924	927	-0.55	28	2862	894	923	933	891	910	-0.25
29	2868	908	924	933	917	921	0.0	30	2981	895	927	920	891	908	-2.00
31	2995	916	921	926	919	921	-4.00	32	3161	880	897	893	886	889	-9.40
33	3149	887	897	898	891	893	-9.00	34	3030	910	925	923	919	919	-3.00
35	2974	892	932	919	900	911	-1.60	36	2977	906	921	934	923	921	-1.80
37	2950	889	921	918	896	906	-1.35	38	2930	907	921	931	920	920	-1.45
39	3000	895	919	911	896	905	-2.85	40	3165						-9.50
41	3165						-9.80	42	3039	888	908	919	885	900	-3.95
43	2962	914	930	924	916	921	-1.50	44	3000	890	926	915	887	904	-2.00
45	2969	906	917	928	918	917	-2.00	46	2975	890	924	927	901	910	-2.25
47	3023	909	918	904	906	909	-2.00	48	3158	884	888	898	878	887	-10.50
49	3170						-11.45	50	3097	898	902	904	911	904	-5.90
51	3057	889	911	907	880	897	-3.65	52	3047	904	910	914	915	911	-3.90
53	3045	883	916	910	887	899	-3.60	54	2998	910	922	902	913	912	-4.00
55	3096	884	915	911	873	896	-8.00	56	3178						-12.65
57	3208						-41.50	58	3158						-14.15
59	3168						-10.50	60	3160	888	888	888	890	889	-9.70
61	3157						-10.80	62	3174	897	893	888	889	892	-10.50
63	3169						-17.50	64	3221						-56.09

MISCELLANEOUS INSTRUMENTS

14	TE-328	867 DEG C	19	PE-301	209 KPA	24	TE-320	327 DEG C
25	TE-321	337 DEG C	26	TE-322	336 DEG C	27	TE-323	330 DEG C
28	TE-324	332 DEG C	29	TE-325	879 DEG C	31	TE-327	882 DEG C
40	TE-91-1	761 DEG C	41	TE-91-2	727 DEG C	42	TE-91-3	790 DEG C
43	TE-91-4	697 DEG C	44	TE-92-1	800 DEG C	45	TE-92-2	710 DEG C
46	TE-92-3	695 DEG C	47	TE-92-4	749 DEG C	472	EIE-10	1640 A
473	EEE-10	56 V	488	TAV-10	918 DEG C			

Table 7. Approximate axial elongation of tubes

Simulator No.	Heated length elongation		Simulator No.	Heated length elongation	
	mm	%		mm	%
1	3.2	0.35	33	3.2	0.35
2	4.0	0.43	34	2.4	0.26
3	3.2	0.35	35	2.8	0.30
4	3.2	0.35	36	2.4	0.26
5	3.2	0.35	37	2.4	0.26
6	3.2	0.35	38	1.2	0.13
7	2.0	0.22	39	3.2	0.35
8	2.4	0.26	40	3.2	0.35
9	3.2	0.35	41	3.2	0.35
10	3.2	0.35	42	2.4	0.26
11	3.2	0.35	43	2.8	0.30
12	3.2	0.35	44	2.4	0.26
13	3.2	0.35	45	2.4	0.26
14	2.4	0.26	46	1.2	0.13
15	3.2	0.35	47	2.4	0.26
16	3.2	0.35	48	3.2	0.35
17	3.2	0.35	49	3.2	0.35
18	3.2	0.35	50	2.4	0.26
19	3.2	0.35	51	2.8	0.30
20	3.2	0.35	52	2.4	0.26
21	3.2	0.35	53	2.4	0.26
22	2.4	0.26	54	2.4	0.26
23	2.4	0.26	55	2.8	0.30
24	3.2	0.35	56	2.8	0.30
25	3.2	0.35	57	3.2	0.35
26	3.2	0.35	58	3.2	0.35
27	3.2	0.35	59	3.2	0.35
28	3.2	0.35	60	3.2	0.35
29	3.2	0.35	61	3.2	0.35
30	2.4	0.26	62	3.2	0.35
31	2.4	0.26	63	3.2	0.35
32	3.4	0.35	64	2.8	0.30

Table 8. Burst locations in B-6 test array

Simulator No.	Burst location		Burst length (mm)	Simulator No.	Burst location		Burst length (mm)
	Axial[a] (mm)	Angle[b] (deg)			Axial[a] (mm)	Angle[b] (deg)	
1	374	115	14	33	213	100	25
2	179	158	12	34	243	55	19
3	343	200	26	35	225	350	31
4	337	180	23	36	200	305	17
5	338	190	23	37	265	0	36
6	266	180	24	38	456	45	21
7	268	180	21	39	219	290	29
8	189	238	8	40	383	295	21
9	190	120	13	41	217	102	24
10	329	173	22	42	208	100	31
11	203[c]	144[c]	6[c]	43	247	40	18
12	259	100	36	44	193	45	14
13	204[c]	152[c]	9[c]	45	296	145	13
14	332	113	19	46	199	62	19
15	218	240	20	47	381	317	23
16	388	260	18	48	383	270	32
17	205[c]	90[c]	14[c]	49	236	50	14
18	202[c]	135[c]	6[c]	50	213	45	14
19	346	80	24	51	235	57	14
20	349	318	16	52	391	45	14
21	302	95	37	53	238	355	38
22	304	315	17	54	301	315	21
23	278	5	40	55	322	333	17
24	328	275	23	56	401	310	18
25	313	90	25	57	234	45	7
26	259	60	13	58	317	0	27
27	256	45	20	59	392	350	25
28	227	75	30	60	387	350	22
29	309	45	24	61	389	315	15
30	285[c]	270[c]	16[c]	62	385[c]	0[c]	16[c]
31	264	320	25	63	314	350	26
32	329	265	22	64	423	277	15

[a]Posttest midpoint elevation above bottom of heated zone. The bottom of heated zone of the bundle (zero elevation) represents an average of all rods.

[b]Clockwise rotation looking down on top of bundle. Estimated angle of rupture initiation.

[c]Burst probably initiated at thermocouple attachment.

Table 9. Geometric parameters of B-6 section at 32.4-cm elevation

PHOTO TUBE	IDENTIFICATION OD AREA (MM**2)	ID AREA (MM**2)	BRBT-B6 32.4 CM ELEVATION WALL AREA (MM**2)	OD PERIMETER (MM)	ID PERIMETER (MM)	OD CX (MM)	OD CY (MM)	ID CX (MM)	ID CY (MM)	OD STR (%)	ID STR (%)
1	161.62068	140.36536	21.25332	45.14728	42.05252	15.46815	134.33694	15.57706	134.22527	31.6	38.7
2	126.26497	104.63988	21.62509	39.90234	36.31679	29.06886	134.38882	29.08669	134.35978	16.3	19.8
3	131.96893	113.68018	20.28876	40.77419	37.50618	43.32912	134.80861	43.31143	134.75504	18.8	23.7
4	138.68927	115.56116	21.12811	41.56618	38.20415	58.02293	134.32909	58.02895	134.25874	21.1	26.0
5	137.06032	116.04799	21.01233	41.56141	38.26468	72.84431	133.86049	72.84996	133.81866	21.2	26.2
6	124.34074	103.16188	21.17886	39.60107	36.06464	86.61870	133.32288	86.62332	133.25716	15.4	18.9
7	119.41550	98.45500	20.93050	38.79730	35.22845	101.13133	133.91492	101.11850	133.89133	13.1	16.2
8	140.43996	119.84376	20.89618	42.06917	38.82187	114.61507	133.40089	114.56993	133.86841	22.6	28.0
9	128.20007	106.07503	22.10504	40.20494	36.57664	15.34716	119.58307	15.34391	119.57236	17.2	20.6
10	192.71674	171.97990	20.73693	43.54462	41.05392	29.42009	119.41266	29.46577	119.22246	26.9	35.4
11	132.73587	112.08543	20.65044	40.89355	37.59297	43.03249	119.75520	43.04132	119.73409	19.2	24.0
12	155.03812	133.28777	21.75035	44.24336	41.06497	57.49654	119.46680	57.54466	119.46840	28.9	35.4
13	133.89311	112.68787	21.20525	41.07434	37.69383	72.54094	119.06215	72.55396	119.05853	19.7	24.3
14	195.91342	174.55612	21.35730	47.44461	45.18826	87.44610	118.12050	87.59218	118.08835	36.3	49.0
15	133.95645	113.12355	20.83250	41.08255	37.75992	101.64374	118.38438	101.62775	118.36491	19.7	24.5
16	138.67191	117.00595	21.66685	41.79716	38.40861	114.80000	119.22762	114.71251	119.16053	21.8	26.7
17	134.75586	113.34767	21.38799	41.19003	37.76746	15.45704	105.74594	15.50914	105.72263	20.0	24.6
18	128.42789	107.24644	21.18144	40.23009	36.76123	28.89478	105.60609	28.92561	105.58775	17.2	21.2
19	136.21980	115.50877	20.71103	41.42374	38.17868	41.61956	105.40555	41.66632	105.41013	20.7	25.5
20	142.54773	121.68206	20.86523	42.36111	39.13956	58.58090	104.75610	58.53642	104.75299	23.5	29.1
21	147.15279	126.01524	21.13754	43.08522	39.87413	72.30794	105.64984	72.40680	105.63771	25.6	31.5
22	135.61139	114.52206	21.08931	41.34878	37.93355	87.47925	104.03628	87.43518	104.03284	20.5	25.1
23	135.55624	114.39514	21.16110	41.32858	37.95940	100.60456	104.63518	100.60182	104.61841	20.4	25.2
24	206.63855	185.82181	20.82674	43.34898	40.91692	113.71194	104.85123	113.47842	104.85124	26.3	34.9
25	152.44992	131.05060	21.39932	42.22270	39.31381	15.29537	91.28246	15.40492	91.28267	23.1	29.7
26	147.94794	126.45456	21.49338	41.16682	38.89876	30.12474	91.67053	30.16544	91.71159	25.8	31.6
27	132.82127	111.77811	21.04317	40.89555	37.52657	43.71538	91.28254	43.71735	91.30780	19.2	23.9
28	154.71552	133.03450	21.68102	44.15356	40.93643	58.15508	89.42941	58.24033	89.97807	28.7	35.0
29	141.50408	120.16063	21.34345	42.27972	38.92398	71.89186	90.40053	71.96950	90.43796	23.2	28.4
30	126.51550	106.54564	21.96826	40.22163	36.64595	87.35825	90.12106	87.31363	90.07492	17.2	20.8
31	157.16178	136.02995	21.13181	44.76183	41.63809	100.66589	90.00391	100.66585	90.02037	30.5	37.3
32	169.77174	149.16193	20.60982	41.55592	38.89577	114.11105	89.73323	113.88966	89.72099	21.1	25.8
33	148.53963	95.02779	21.51184	38.95672	35.33595	15.32644	76.56189	15.33859	76.60249	13.5	16.5
34	140.16090	118.90912	21.25179	42.03032	38.68810	28.86002	77.20743	28.90675	77.22566	22.5	27.6
35	139.73169	118.86876	21.86313	40.56447	37.03946	43.22441	75.87709	43.29803	75.89584	18.2	22.2
36	142.51681	121.52292	20.99590	42.35519	39.11665	57.84427	75.84566	57.52280	75.89687	23.4	29.0
37	131.83054	110.47624	21.35429	40.73740	37.26333	72.19736	75.64156	72.21191	75.66493	18.7	23.0
38	132.16641	111.91336	21.25305	40.95604	37.53156	86.49187	76.08330	86.48006	76.09128	19.4	23.8
39	135.71364	114.39240	21.32074	41.32876	37.94963	100.73570	75.95161	100.72481	75.97566	20.5	25.2
40	131.26660	110.30342	20.96318	40.65031	37.26941	115.04047	75.81056	114.99490	75.80516	18.5	22.9
41	122.26163	100.94321	22.21841	39.29679	35.51109	15.41688	62.27577	15.40916	62.29608	14.4	17.1
42	130.25262	106.87895	21.37367	40.49167	37.04803	29.17728	62.14168	29.22955	62.13196	18.0	22.2
43	134.23029	112.70605	21.52423	41.12356	37.68315	43.71582	61.18745	43.74344	61.19719	19.9	24.3
44	126.35321	104.62939	21.72382	40.22069	36.65315	58.57638	61.80363	58.62469	61.83055	17.2	20.8
45	137.75500	116.90640	21.82860	41.65289	38.22185	71.82028	61.69136	71.81926	61.64142	21.4	26.0
46	156.19794	134.35376	21.84418	44.40639	41.11982	87.13898	62.66214	87.19695	62.69305	29.4	35.6
47	130.72916	109.43512	21.29404	40.56893	37.10497	100.98250	61.83730	100.93617	61.87805	18.3	22.4
48	124.40904	102.57271	21.83633	39.61198	35.94147	115.15363	61.61343	115.10735	61.60513	15.4	18.5
49	130.17384	107.34116	22.83269	40.53627	36.79657	15.52169	47.59082	15.54626	47.61774	18.1	21.3
50	129.34180	107.64009	21.70171	40.36144	36.82797	29.22691	48.20108	29.24326	48.21663	17.7	21.5
51	132.35402	110.96310	21.39091	40.83385	37.36155	43.20937	47.68422	43.22285	47.89897	19.0	23.3
52	129.21809	107.07693	22.14116	40.42467	36.74558	57.96173	47.98424	57.98270	48.00325	17.8	21.2
53	131.81027	109.79056	22.01971	40.78926	37.19366	72.66971	47.03072	72.67786	47.05716	18.9	22.7
54	164.55234	142.78880	21.76353	45.56768	42.42197	86.79564	48.15230	86.82025	48.23947	32.9	39.9
55	174.91637	154.08663	20.83574	46.42392	43.57110	100.82535	48.80339	100.77444	48.91701	35.3	43.7
56	140.38870	97.71272	22.67598	38.94489	35.09265	115.21106	47.11786	115.19170	47.14754	13.9	15.7
57	132.64065	111.19130	21.64955	40.49978	37.42587	15.63409	32.79013	15.63753	32.80127	19.2	23.4
58	142.75916	120.23776	22.52139	43.34576	40.75677	29.25361	34.39529	29.24759	34.62762	26.6	34.4
59	140.12317	118.64217	21.48100	41.98901	38.66083	43.74080	33.52948	43.78925	33.59091	22.4	27.5
60	128.92064	107.25394	21.66670	40.27650	36.73332	58.28053	33.45010	58.26557	33.49152	17.4	21.1
61	129.14798	106.89546	22.27252	40.32207	36.68222	73.00739	33.34834	72.98438	33.40448	17.5	21.0
62	130.30190	108.30498	21.99692	40.49225	36.92380	86.53954	33.25706	86.52907	33.31096	18.0	21.8
63	174.16200	151.83392	22.32808	42.67514	39.85880	100.22360	33.56993	100.18745	33.75037	24.4	31.4
64	147.66022	125.66623	21.99399	43.10246	39.76599	115.00237	33.11078	114.97015	33.14435	25.6	31.1

Table 10. Circumferential strain values (%) in B-6 tubes

(Burst strains are underlined)

ELEVATION (CM)	CIRCUMFERENTIAL STRAIN OF TUBE NO. (%)															
	1	2	3	4	5	6	7	8	9	10	11	12	13	14	15	16
0.0	0.8	1.1	0.8	0.7	0.2	0.9	0.6	0.1	0.6	0.7	0.6	0.1	-0.2	0.3	0.4	0.2
1.5	2.0	1.8	2.3	1.7	1.4	1.8	1.4	1.3	1.8	2.0	1.8	1.2	1.8	1.5	1.0	1.1
3.0	3.1	3.1	3.0	2.4	2.8	2.8	2.1	2.3	2.9	3.8	3.4	3.2	3.3	3.2	2.4	2.4
4.5	3.8	3.4	3.3	3.1	3.0	2.6	2.4	2.5	3.1	4.9	4.9	4.7	4.5	4.1	3.4	2.2
6.0	5.7	4.8	4.5	3.7	5.1	4.9	4.2	4.6	4.9	6.6	6.4	6.5	6.3	6.1	5.1	3.3
7.5	6.5	5.7	5.7	4.8	6.5	5.2	4.7	5.8	4.3	6.5	6.7	6.7	6.7	6.6	5.2	3.9
9.0	5.0	4.7	4.9	4.3	5.0	3.9	3.9	4.5	4.0	5.8	5.8	5.9	4.9	5.5	5.1	3.1
11.6	6.6	6.4	6.3	5.5	6.7	5.5	5.5	6.8	6.3	7.5	7.9	7.6	7.4	7.3	6.7	4.8
13.2	10.1	8.0	7.8	6.0	7.3	6.4	6.9	8.5	10.2	11.7	11.3	11.7	10.6	10.9	9.3	6.3
14.7	17.4	11.5	11.6	8.4	10.0	8.2	8.0	12.6	14.0	15.5	15.0	15.0	13.4	14.3	12.2	8.7
16.1	18.4	14.5	15.5	10.0	13.1	9.9	10.3	20.1	13.3	19.0	16.9	17.6	15.5	16.2	13.3	8.8
17.5	17.3	23.6	24.3	12.5	17.7	14.3	15.7	30.6	15.5	25.1	21.3	21.3	18.7	18.7	15.6	8.5
18.9	21.0	19.5	18.9	12.2	18.1	15.5	22.2	47.3	25.4	30.6	24.0	24.3	22.1	19.7	17.4	9.7
20.3	23.2	13.1	12.2	9.3	13.4	11.7	16.8	35.1	17.0	26.4	25.6	24.9	26.9	20.0	22.1	14.0
21.8	28.3	11.5	11.0	9.4	13.0	10.7	12.7	20.1	16.5	21.0	20.1	25.8	21.3	21.5	25.7	16.1
23.2	31.9	11.6	11.4	9.0	12.7	10.4	12.3	15.5	12.8	18.8	18.6	24.1	20.6	21.9	22.9	10.3
24.6	18.5	11.9	13.5	12.0	16.3	13.8	15.6	18.3	10.7	19.2	20.8	32.0	21.6	25.7	22.2	9.2
26.1	16.6	12.3	14.3	14.5	21.1	28.4	32.2	34.2	12.5	18.4	22.8	32.1	19.9	25.0	21.1	13.3
27.5	17.0	12.2	13.0	12.8	17.3	24.3	28.7	35.3	14.2	18.9	22.1	26.1	18.1	22.1	20.5	19.4
27.9	14.8	9.8	10.5	10.3	14.5	15.8	19.5	31.7	11.8	17.1	20.4	22.9	16.9	21.6	20.1	18.3
29.5	18.8	11.4	10.5	9.2	11.6	10.0	11.8	33.1	11.6	18.7	20.4	21.9	16.2	19.8	18.2	13.2
31.0	25.9	15.2	14.8	12.7	15.2	11.6	12.0	30.9	13.7	21.9	21.4	26.7	18.3	22.8	19.6	18.8
32.4	31.6	16.3	18.8	21.1	21.2	15.4	13.1	22.6	17.2	26.9	19.2	28.9	19.7	38.3	19.7	21.8
33.8	32.1	16.4	30.5	24.7	31.3	18.7	14.6	22.0	16.1	26.2	17.9	27.2	20.4	46.9	19.1	14.9
35.2	28.3	16.7	29.5	16.9	20.1	12.4	12.0	18.0	13.0	21.3	17.7	23.0	19.9	27.8	16.8	10.6
37.0	49.4	14.0	13.6	10.1	12.1	9.7	9.5	22.2	14.6	19.1	15.6	19.8	16.8	19.9	15.1	14.7
38.4	38.1	11.7	11.0	9.4	12.3	10.3	9.9	19.5	15.3	17.9	14.9	19.6	16.6	18.6	15.1	23.6
39.8	31.3	13.4	13.6	12.4	16.1	13.2	13.1	22.6	14.0	17.8	15.3	21.1	17.1	18.4	15.6	21.0
41.8	26.0	14.1	14.3	12.7	18.7	16.4	16.1	17.7	11.6	16.8	15.5	20.9	16.6	17.9	16.0	10.9
43.6	13.6	11.7	11.0	9.6	14.0	13.3	14.1	16.1	8.3	15.7	15.6	17.7	15.9	18.1	16.4	11.4
45.3	10.6	10.2	9.8	7.9	10.4	9.1	9.6	11.1	7.7	14.1	14.3	15.9	13.9	16.6	14.7	8.6
46.9	9.9	10.6	11.5	8.7	10.7	9.1	8.8	10.5	7.8	13.7	14.3	15.1	13.0	16.3	13.7	9.5
48.4	12.9	11.5	11.6	8.8	10.7	9.9	10.4	13.9	9.7	14.6	14.1	15.4	12.9	15.7	13.9	11.3
50.0	15.4	9.8	9.1	7.8	9.5	8.2	8.3	12.6	10.5	13.5	12.8	14.3	12.2	15.0	12.5	9.8
51.6	17.2	11.5	10.9	8.3	10.5	8.4	7.8	9.3	10.5	14.0	12.8	14.7	12.4	13.9	12.4	8.2
53.2	17.5	11.2	11.4	8.8	12.2	8.9	8.2	9.2	9.7	13.2	12.4	14.0	12.1	13.2	12.0	8.0
54.8	19.5	11.2	10.9	8.7	11.6	8.6	8.2	9.0	11.0	12.9	11.9	13.4	11.8	13.1	11.7	8.4
56.5	13.2	9.0	8.9	6.7	9.6	7.5	7.8	12.3	9.4	12.4	11.3	12.2	11.2	11.9	11.3	7.2
58.2	17.1	9.3	9.2	7.1	9.2	7.1	7.9	10.9	9.3	11.3	10.7	10.9	10.2	11.0	10.3	7.0
60.0	14.1	7.7	7.2	5.7	8.5	6.8	7.1	11.5	7.7	8.9	8.5	8.8	8.4	9.0	8.1	6.7
61.7	10.0	6.4	5.5	4.5	5.9	4.9	5.1	9.5	6.0	7.9	7.5	7.9	7.7	7.9	7.0	5.3
63.4	9.0	7.0	6.8	5.6	6.7	5.4	5.6	8.4	7.0	8.0	7.6	8.0	7.4	7.6	7.3	6.2
65.0	4.8	4.6	4.6	4.1	4.4	4.0	4.0	4.8	5.0	5.7	5.4	5.6	5.3	5.6	5.3	3.8
67.6	6.3	6.0	5.9	5.4	6.5	5.6	5.0	5.3	5.5	6.7	6.9	6.9	6.6	6.7	6.3	4.1
69.2	6.1	5.0	5.6	5.4	7.6	5.8	5.6	6.5	5.7	7.5	8.3	8.3	8.4	8.7	8.0	5.4
71.0	7.4	5.8	6.5	5.6	7.7	6.5	6.7	10.5	6.4	9.4	9.6	10.1	9.4	10.3	9.6	6.7
72.8	10.3	7.1	7.1	6.3	8.0	6.5	6.3	11.8	7.9	9.7	9.8	10.3	9.8	10.5	10.0	8.8
74.7	11.1	9.3	8.0	6.3	8.4	6.8	7.3	11.5	8.6	10.3	9.9	9.9	9.3	10.7	10.1	8.5
76.6	13.4	9.4	8.1	6.5	8.7	6.8	7.8	10.5	11.0	10.2	9.4	9.6	9.0	10.2	9.9	8.7
78.5	12.5	9.7	8.1	6.2	8.0	6.8	7.6	8.9	9.3	9.1	8.6	8.7	7.9	8.8	8.5	8.2
80.4	10.6	8.5	7.5	6.5	8.6	6.7	7.1	7.3	8.8	8.3	8.0	8.0	7.4	8.1	7.5	6.5
82.4	6.6	7.6	6.3	5.2	6.3	6.1	6.5	5.2	6.3	6.7	6.7	6.2	5.8	6.5	6.0	5.0
84.4	7.2	7.3	6.4	5.0	6.4	5.1	5.0	3.6	5.9	5.9	5.4	4.9	5.0	5.4	5.0	4.2
86.2	6.5	5.7	5.3	4.5	5.8	4.6	4.7	3.7	5.8	4.9	4.1	3.9	3.8	4.0	3.9	3.9
88.0	4.5	4.5	3.9	3.6	3.6	3.6	3.2	2.8	3.8	3.3	2.9	2.7	2.6	2.5	2.9	2.9
89.5	3.1	2.8	2.5	2.2	2.5	2.2	2.1	2.2	2.8	2.3	1.8	1.8	2.0	1.8	1.8	2.0
91.5	2.1	2.2	2.0	1.8	1.5	1.7	1.3	1.5	1.7	1.7	1.6	1.1	1.5	1.1	1.3	1.7
93.0	1.8	1.6	1.4	1.2	1.1	1.1	0.9	0.7	1.9	1.3	1.3	1.7	1.2	1.0	0.9	1.3

Table 10 (continued)

ELEVATION	CIRCUMFERENTIAL STRAIN OF TUBE NO. (%)															
(CM)	17	18	19	20	21	22	23	24	25	26	27	28	29	30	31	32
0.0	0.1	0.3	0.4	0.3	-0.1	-0.1	0.4	0.2	0.2	0.3	0.1	0.1	0.1	-0.3	0.1	-0.3
1.5	1.9	2.0	1.3	1.4	1.2	1.7	1.1	0.7	1.7	1.4	1.4	1.6	1.1	1.6	1.4	0.6
3.0	2.9	3.2	3.0	3.6	3.2	2.9	2.3	1.8	2.7	3.6	3.4	4.0	3.8	3.0	2.8	2.1
4.5	3.2	4.7	4.8	4.5	3.7	3.6	3.5	2.0	3.0	4.9	4.5	4.2	3.8	3.9	4.1	1.9
6.0	5.1	6.2	6.3	5.7	5.4	5.0	4.6	2.8	3.9	6.1	6.0	6.1	5.4	5.9	5.7	2.4
7.5	4.8	6.2	6.0	5.9	5.7	5.4	4.9	3.5	4.3	6.2	5.9	6.1	5.7	5.7	5.5	2.9
9.0	4.2	4.9	4.9	4.6	3.9	4.3	4.2	2.5	4.3	5.6	5.6	5.3	4.7	5.3	5.6	3.1
11.6	6.8	7.0	6.4	6.1	5.8	5.6	5.6	3.8	5.5	6.7	6.5	6.2	5.9	5.7	6.7	4.1
13.2	11.2	10.6	10.0	9.8	8.6	8.7	8.5	5.8	8.8	10.2	10.2	9.7	8.7	8.7	10.1	5.6
14.7	14.6	13.5	13.3	13.3	11.2	12.2	11.9	7.4	11.8	13.6	14.1	13.6	12.3	12.2	14.0	7.2
16.1	13.0	14.3	16.0	15.7	12.5	13.5	12.9	6.2	10.4	15.1	17.8	16.3	14.8	13.9	15.9	7.6
17.5	13.5	15.6	21.1	16.9	12.7	15.3	15.0	8.1	9.7	17.3	22.3	18.5	17.8	16.5	19.3	9.6
18.9	18.9	18.1	29.6	17.3	13.2	16.5	16.2	10.0	13.2	19.2	26.4	20.3	20.1	18.2	21.3	10.7
20.3	31.3	26.3	28.8	17.5	13.8	17.6	18.1	13.4	19.4	20.9	28.1	21.6	21.4	18.1	21.9	11.8
21.8	21.8	22.8	26.4	18.4	14.3	16.9	18.5	16.2	21.2	23.0	25.8	28.9	20.8	18.9	24.8	13.2
23.2	15.4	21.3	21.9	19.0	14.1	17.3	17.9	15.3	14.1	22.8	22.6	31.4	20.8	19.7	28.4	16.1
24.6	12.7	22.1	20.2	19.3	15.6	18.9	21.4	12.8	11.7	25.4	28.7	24.6	22.7	21.5	35.4	16.6
26.1	16.9	22.6	20.5	18.1	17.5	20.1	28.7	14.2	15.7	32.6	30.4	21.2	21.6	20.0	42.7	14.7
27.5	23.8	23.0	19.3	18.7	19.5	21.8	31.9	16.4	23.5	25.6	23.7	20.2	22.5	23.5	43.9	12.5
27.9	23.0	20.4	17.8	17.3	19.8	22.1	36.3	14.4	21.4	22.5	20.9	19.1	21.9	26.4	40.5	11.6
29.5	22.8	18.5	17.6	17.8	26.5	28.7	24.4	10.1	18.2	22.9	19.1	21.6	22.6	22.7	27.1	8.9
31.0	19.5	17.3	19.4	20.2	29.7	28.6	21.6	15.0	26.2	24.8	19.0	24.8	26.4	19.0	27.2	13.2
32.4	20.0	17.2	20.7	23.5	25.6	20.5	20.4	26.3	23.1	25.8	19.2	28.7	23.2	17.2	30.5	21.1
33.8	16.0	17.2	25.8	40.5	21.7	17.4	19.3	21.7	12.9	22.3	19.0	30.5	19.0	16.3	29.5	21.9
35.2	13.7	17.7	24.9	55.7	19.9	18.0	20.0	11.4	12.3	20.2	21.7	25.1	18.0	18.3	26.9	12.1
37.0	16.8	17.4	17.8	26.7	16.4	15.9	17.6	13.0	14.5	17.3	20.4	19.0	15.8	18.3	21.6	12.0
38.4	17.4	17.1	16.9	21.7	14.8	15.5	17.9	14.7	13.3	16.8	18.2	18.0	14.7	20.5	20.0	13.0
39.8	16.1	16.4	17.7	19.1	14.9	15.2	16.8	13.0	13.4	16.2	16.9	17.0	15.0	21.9	17.6	10.4
41.8	12.6	14.7	15.8	17.3	13.9	16.4	15.0	9.0	11.6	14.7	15.0	15.1	14.4	20.0	15.3	7.4
43.6	9.6	14.0	15.3	18.4	14.0	14.6	16.0	10.8	10.2	14.0	14.6	15.4	15.1	18.0	16.2	8.5
45.3	9.5	12.8	14.8	18.9	13.0	13.5	18.3	10.8	8.8	12.9	13.5	14.8	14.2	17.2	17.2	10.0
46.9	9.0	13.1	13.6	18.4	12.9	13.3	22.1	12.2	8.3	13.1	13.0	14.2	13.3	16.5	17.7	10.7
48.4	11.8	13.9	13.2	17.4	13.3	13.4	22.6	13.4	10.4	13.0	13.3	14.3	13.4	16.1	18.3	11.2
50.0	11.8	13.2	12.4	15.3	12.2	11.9	17.2	12.9	10.0	12.6	12.9	13.0	12.1	13.6	16.5	11.3
51.6	11.2	13.1	12.5	13.6	12.2	12.1	14.9	11.9	10.2	12.6	12.2	12.5	11.8	13.6	16.4	11.2
53.2	10.2	12.1	11.8	12.1	11.1	11.5	13.2	12.2	9.4	12.3	11.5	11.4	10.8	12.3	15.0	10.9
54.8	12.4	12.1	11.6	11.8	10.6	11.0	12.4	11.3	11.8	12.2	11.1	10.8	10.5	11.3	14.3	10.9
56.5	11.1	11.6	11.4	10.9	9.8	10.5	11.4	9.3	12.6	11.7	10.6	10.1	9.9	10.6	13.2	10.2
58.2	10.5	10.3	9.9	9.7	9.0	9.1	10.1	8.2	10.7	10.5	9.8	9.2	9.0	10.0	11.3	8.4
60.0	9.1	8.0	7.7	7.2	7.0	6.8	7.9	6.4	8.0	8.0	7.6	7.0	7.0	7.4	9.0	5.0
61.7	6.5	7.2	7.5	6.9	6.2	6.2	6.9	4.8	5.5	7.6	6.8	6.4	6.5	7.0	8.2	4.3
63.4	7.6	7.4	7.3	6.7	6.6	6.5	7.2	6.5	6.5	7.5	6.6	6.0	6.7	6.9	8.1	5.8
65.0	4.9	5.0	4.6	4.2	4.5	4.6	4.8	4.1	4.3	5.1	4.7	4.0	4.3	4.2	5.2	3.8
67.6	6.4	7.1	6.6	6.5	6.2	6.1	6.7	5.0	6.1	7.3	6.4	5.8	6.1	6.2	7.5	4.9
69.2	6.6	7.7	7.3	7.6	7.0	6.2	7.9	5.0	6.2	8.2	7.7	6.9	7.1	7.6	9.2	4.8
71.0	8.2	9.4	8.8	9.7	8.0	7.9	9.1	6.6	8.0	9.9	9.6	8.1	8.4	9.1	11.2	6.4
72.8	9.9	10.2	9.3	9.8	8.6	8.7	9.6	8.6	9.9	10.6	9.8	8.9	9.0	10.1	12.3	8.8
74.7	10.5	10.1	8.9	9.1	8.3	8.4	9.9	8.3	10.8	10.3	9.4	8.5	8.5	9.3	12.3	8.1
76.6	11.1	9.8	8.8	8.8	7.6	8.0	9.0	7.6	9.8	9.7	9.4	8.5	8.3	8.8	11.6	7.0
78.5	9.5	8.5	7.3	7.2	6.2	6.6	7.3	7.5	8.4	8.2	7.8	7.1	6.3	7.1	9.4	7.2
80.4	10.1	7.6	6.8	6.9	6.3	6.4	6.6	6.3	7.2	7.6	7.2	6.6	6.4	7.0	8.2	6.2
82.4	8.2	6.1	5.2	5.3	4.9	4.7	5.4	4.8	6.1	5.9	5.8	4.9	4.9	5.5	6.4	4.5
84.4	6.9	5.7	4.8	4.0	3.8	4.0	4.7	4.5	6.1	5.6	4.6	4.1	4.0	4.6	5.6	3.8
86.2	6.0	4.3	3.6	3.5	2.9	3.0	3.3	3.9	5.2	4.0	3.6	3.1	3.3	3.2	4.0	3.3
88.0	3.8	3.0	2.6	2.2	2.3	2.2	2.2	2.7	3.0	3.0	2.3	2.0	2.2	2.0	2.5	2.9
89.5	2.8	2.4	1.7	1.2	1.4	1.5	1.5	1.8	2.5	2.4	1.5	1.3	1.8	1.4	1.6	1.7
91.5	2.0	1.6	1.4	0.8	0.7	0.5	0.9	1.2	1.8	1.2	1.3	1.0	1.1	0.6	0.7	0.9
93.0	1.9	1.7	1.6	0.8	0.8	0.5	0.7	0.8	1.7	1.4	1.2	0.9	0.9	0.7	0.5	0.8

Table 10 (continued)

ELEVATION	CIRCUMFERENTIAL STRAIN OF TUBE NO. (%)															
(CM)	33	34	35	36	37	38	39	40	41	42	43	44	45	46	47	48
0.0	0.3	0.4	-0.0	-0.2	-0.3	-0.5	-0.6	0.1	0.7	1.4	1.0	0.6	0.7	0.5	0.6	0.9
1.5	1.8	1.8	1.9	1.7	1.5	1.2	1.6	1.7	2.4	2.3	1.9	2.0	1.9	1.4	1.1	1.4
3.0	2.5	2.6	2.4	2.5	2.6	2.2	2.0	1.8	2.0	2.7	2.8	2.5	2.5	2.1	2.1	1.6
4.5	2.7	3.9	3.9	3.6	4.4	3.9	3.4	2.0	2.8	4.2	4.7	4.3	4.4	3.8	3.2	2.6
6.0	3.6	5.2	5.1	5.2	5.4	5.5	4.4	2.7	3.3	5.2	5.6	5.7	5.4	5.0	4.3	3.6
7.5	3.8	5.3	5.3	5.9	6.1	6.2	5.0	3.8	4.4	6.2	6.6	6.5	6.5	6.0	5.6	4.8
9.0	3.6	5.2	4.9	4.9	5.1	5.8	4.5	3.1	3.2	4.7	5.2	4.3	4.8	4.7	4.2	2.6
11.6	5.2	6.2	6.4	6.5	5.8	6.2	5.9	4.6	4.8	6.2	6.8	6.3	6.1	6.6	5.6	4.8
13.2	8.6	9.7	9.5	10.1	9.0	9.4	8.4	5.5	8.3	10.2	11.1	9.9	10.1	10.3	8.4	5.9
14.7	12.0	13.0	12.8	13.5	13.6	13.2	12.4	7.1	10.8	13.2	13.9	13.7	14.0	14.5	11.3	7.9
16.1	12.9	15.0	16.0	17.1	18.2	15.7	14.0	8.6	10.8	15.1	16.2	17.5	17.6	17.8	12.3	9.8
17.5	10.2	16.2	20.0	21.2	23.9	18.0	16.3	9.9	10.2	17.7	18.6	22.5	19.8	21.3	12.9	9.9
18.9	12.9	19.8	26.1	33.9	26.0	21.7	18.3	9.3	12.9	24.7	20.2	32.9	21.4	27.4	13.3	8.6
20.3	25.0	22.9	28.5	39.4	21.4	24.3	22.5	10.7	21.1	42.5	21.9	32.5	24.5	29.0	14.1	10.2
21.8	27.0	24.5	39.7	28.7	20.8	24.2	25.5	13.1	32.2	35.8	23.6	25.4	24.4	22.4	14.2	11.7
23.2	14.5	25.7	41.6	23.1	21.7	25.2	27.1	14.5	19.3	23.5	25.8	23.4	23.9	19.0	13.7	10.1
24.6	12.2	26.7	26.0	21.8	23.9	23.6	22.4	13.8	15.4	21.0	34.5	23.2	24.1	19.3	13.7	8.9
26.1	15.6	23.0	21.0	21.0	31.8	20.6	20.7	13.8	17.7	20.1	27.6	21.1	26.8	21.7	14.5	11.0
27.5	16.6	21.0	20.3	21.7	31.9	20.9	21.2	13.7	17.1	20.9	25.5	20.1	28.7	22.9	15.0	12.6
27.9	12.2	18.1	18.2	19.8	28.7	20.3	22.2	13.4	13.2	18.2	23.4	18.2	28.0	22.7	14.6	11.5
29.5	10.3	18.2	17.6	22.9	21.4	19.6	21.3	11.5	11.2	18.4	22.2	18.2	34.7	24.8	18.0	12.0
31.0	12.5	20.3	17.6	26.3	19.8	19.9	21.7	15.6	12.2	17.8	20.5	17.8	25.5	26.1	19.3	14.6
32.4	13.5	22.5	18.2	23.4	18.7	19.4	20.5	18.5	14.4	18.0	19.9	17.2	21.4	29.4	18.3	15.4
33.8	11.9	21.3	16.9	20.0	17.1	19.8	19.1	21.4	13.5	18.3	18.6	16.2	18.8	24.8	17.0	13.5
35.2	12.9	21.5	17.7	21.5	18.3	22.9	18.2	19.6	15.8	20.3	19.2	18.4	20.5	21.7	17.6	16.3
37.0	12.4	18.3	17.2	22.8	17.5	27.4	16.2	22.6	13.2	17.9	18.7	17.3	21.6	20.7	20.5	20.2
38.4	9.9	16.1	17.3	22.8	16.4	29.1	16.3	29.4	11.0	16.4	20.1	16.6	22.1	21.0	21.1	22.7
39.8	10.0	15.2	17.3	20.6	17.1	23.0	15.4	17.8	11.1	15.9	19.0	17.1	21.0	19.9	19.0	20.5
41.8	9.0	13.4	16.4	16.8	15.5	20.1	12.7	9.2	10.9	14.1	16.5	14.6	19.3	16.7	14.5	11.3
43.6	7.5	13.4	15.7	15.3	15.0	23.4	12.6	10.2	8.6	13.4	15.4	14.2	18.6	15.3	14.1	9.6
45.3	5.9	12.3	14.0	13.7	14.6	31.2	12.5	9.6	6.8	11.7	13.8	13.0	16.6	14.5	12.4	8.8
46.9	6.5	11.9	13.0	13.1	14.5	23.8	11.9	7.9	7.1	11.9	13.3	12.0	15.6	13.7	11.8	8.3
48.4	8.0	12.1	12.5	13.4	14.2	20.0	11.5	7.3	9.7	12.3	13.1	12.7	16.5	14.2	11.6	7.0
50.0	7.2	11.4	11.1	12.0	12.5	16.2	10.9	7.1	8.5	11.9	12.7	10.9	15.1	12.3	11.4	7.3
51.6	8.5	12.2	11.5	12.4	12.6	15.5	11.8	7.7	11.0	12.4	13.0	11.0	14.5	13.0	11.4	7.6
53.2	7.9	11.3	11.0	11.7	12.2	14.7	11.3	7.7	11.4	12.1	12.3	10.6	13.3	12.7	11.5	9.4
54.8	9.2	11.2	10.4	11.1	11.3	13.7	11.0	9.0	11.0	10.8	11.0	10.0	11.7	11.4	10.3	8.3
56.5	8.2	10.3	9.4	9.8	9.6	11.7	9.2	10.1	8.2	9.3	9.9	9.0	10.4	10.1	8.7	7.8
58.2	8.3	9.9	9.0	8.8	9.1	11.2	8.6	9.6	8.5	9.2	9.4	8.9	9.7	9.1	8.0	6.4
60.0	6.3	7.5	7.2	7.2	7.1	8.6	6.8	5.6	8.1	8.0	7.6	7.4	8.5	7.5	7.0	5.6
61.7	4.6	6.8	6.7	6.8	6.5	7.7	6.3	5.7	5.0	7.0	6.8	6.4	7.0	6.5	5.8	5.9
63.4	5.3	6.3	6.0	5.9	6.0	6.9	5.9	5.0	5.3	6.2	6.1	5.9	6.1	5.8	5.6	4.9
65.0	3.6	4.6	4.3	3.9	4.0	4.7	4.3	3.9	3.6	4.8	4.4	4.1	4.3	4.2	4.4	3.2
67.6	4.9	6.4	5.4	5.1	5.0	5.7	5.3	4.5	5.6	6.8	6.4	5.7	6.0	5.7	6.1	5.0
69.2	6.0	8.0	7.3	6.9	6.8	7.9	7.0	5.0	6.4	7.4	7.8	6.9	7.4	7.0	6.9	5.3
71.0	6.3	9.8	8.9	8.3	8.1	9.7	8.6	7.8	6.7	9.0	9.6	8.2	9.0	8.4	8.3	7.6
72.8	8.2	10.9	9.2	9.0	9.0	10.6	9.5	8.9	8.9	9.6	9.4	8.1	9.7	8.7	8.3	7.3
74.7	9.7	10.6	8.6	8.7	8.3	10.2	9.8	8.7	10.3	9.5	9.2	7.7	9.3	8.7	8.3	9.0
76.6	8.2	10.1	9.1	8.7	7.8	9.7	9.6	8.0	9.3	9.1	9.1	8.0	9.2	8.5	8.6	9.0
78.5	6.5	8.4	7.6	7.1	6.5	7.9	7.8	8.7	9.0	8.5	8.4	7.6	8.0	7.8	7.8	9.5
80.4	5.8	7.3	7.0	6.8	6.6	7.7	7.4	7.5	9.2	8.1	7.9	7.2	7.3	7.3	7.1	8.7
82.4	5.1	5.9	5.3	5.5	5.0	5.8	5.2	6.0	7.7	6.5	6.1	5.6	5.7	5.6	5.7	6.5
84.4	6.0	5.4	4.5	4.4	4.3	4.7	4.4	5.3	6.4	5.6	5.0	4.2	4.5	4.3	4.4	5.3
86.2	4.5	3.7	3.6	3.5	3.2	3.3	3.2	4.5	5.2	4.4	4.2	3.6	4.0	3.7	3.7	5.1
88.0	2.5	2.4	2.5	2.2	1.9	1.9	1.6	3.1	3.6	3.2	3.0	2.9	2.7	2.3	2.5	3.3
89.5	2.3	1.8	1.8	1.5	1.5	1.4	1.6	2.2	2.2	2.0	1.8	1.8	1.7	1.3	1.5	2.0
91.5	1.5	1.3	1.2	0.8	0.9	0.2	0.6	1.2	1.3	1.4	0.8	0.9	0.9	0.4	0.8	1.2
93.0	1.9	1.4	1.1	0.9	0.8	0.5	0.6	1.0	1.8	1.6	1.3	1.3	1.1	0.7	0.8	1.3

Table 10 (continued)

ELEVATION (CM)	CIRCUMFERENTIAL STRAIN OF TUBE NO. (%)															
	49	50	51	52	53	54	55	56	57	58	59	60	61	62	63	64
0.0	0.8	0.7	0.9	0.7	0.7	0.6	0.3	0.3	0.8	0.7	0.9	0.7	1.3	0.5	0.9	0.7
1.5	2.2	2.1	1.4	1.4	1.2	1.5	1.4	1.9	1.9	1.8	1.7	1.4	1.4	1.1	1.0	1.1
3.0	2.2	2.7	2.9	2.4	2.4	2.4	2.2	2.1	2.2	1.9	1.8	1.7	1.9	1.4	1.4	1.7
4.5	3.0	4.2	4.5	4.2	3.9	4.3	3.9	1.9	2.8	2.6	2.8	2.5	2.1	1.7	2.0	1.6
6.0	3.6	4.9	5.4	5.2	5.0	5.8	5.1	2.8	4.7	4.6	4.2	4.4	3.6	2.7	3.2	3.4
7.5	4.5	6.2	6.7	6.6	6.3	6.9	6.2	4.3	5.1	5.3	4.7	4.8	4.1	3.7	4.6	4.8
9.0	3.1	4.9	4.7	5.0	4.2	5.3	4.9	2.7	3.5	3.7	3.0	3.1	3.1	2.5	3.0	2.7
11.6	4.8	6.7	6.4	6.4	5.8	7.5	6.9	4.1	5.3	5.3	4.7	4.5	4.6	4.5	4.7	5.1
13.2	8.6	10.2	10.1	10.0	9.5	11.2	10.8	6.3	8.8	8.7	6.9	6.8	6.5	6.5	7.7	7.9
14.7	11.2	12.7	12.8	12.7	12.3	15.1	14.0	7.8	10.7	9.0	6.9	7.4	7.1	6.8	9.0	11.8
16.1	9.9	13.3	13.6	13.5	13.1	17.0	15.8	7.7	10.6	10.3	8.0	8.3	7.9	8.3	11.2	13.6
17.5	11.8	16.1	15.9	17.4	16.1	21.3	17.8	8.3	15.4	14.8	11.2	11.9	11.0	11.5	13.2	15.0
18.9	14.6	17.2	16.3	18.9	16.7	21.6	17.1	6.3	21.7	14.0	11.3	12.2	11.3	10.0	11.4	13.0
20.3	18.9	21.0	18.0	19.3	18.9	20.9	17.0	7.9	20.2	12.7	11.4	13.2	11.1	8.5	10.3	15.0
21.8	23.3	22.0	22.0	18.4	24.6	21.4	17.7	10.2	19.6	12.1	11.0	11.5	11.3	10.2	13.6	18.2
23.2	32.2	20.0	33.5	16.4	28.1	24.0	16.9	7.7	38.0	14.4	12.5	12.7	12.4	11.0	13.4	14.7
24.6	24.9	19.0	26.7	15.9	29.0	27.1	17.7	6.1	24.6	16.3	13.2	13.6	13.2	10.5	11.5	10.6
26.1	20.9	17.2	18.4	14.9	21.6	26.3	18.1	8.3	16.3	14.2	10.1	10.7	9.8	8.1	10.1	13.6
27.5	19.5	16.4	17.8	15.4	18.5	27.9	19.1	10.2	16.0	12.7	9.9	10.2	10.2	9.0	12.4	19.3
27.9	16.5	14.3	15.9	14.2	17.2	28.3	19.9	9.6	14.6	11.2	8.5	8.7	9.2	9.0	12.4	19.8
29.5	13.7	16.3	17.6	16.7	18.9	42.2	23.8	11.5	19.0	17.8	13.9	13.5	13.8	13.2	17.3	28.2
31.0	14.8	17.2	19.2	17.5	18.7	42.9	28.6	15.0	19.1	29.4	21.4	17.1	17.9	16.1	24.1	33.6
32.4	18.1	17.7	19.0	17.8	18.9	32.9	35.3	13.5	19.2	26.6	22.4	17.4	17.5	18.0	24.4	25.6
33.8	18.9	17.9	16.8	16.3	18.5	27.5	24.2	9.4	16.1	15.9	14.0	12.6	12.9	14.5	16.2	16.3
35.2	19.1	19.0	17.1	17.5	18.9	24.9	23.2	11.9	13.6	13.1	12.3	11.8	12.1	12.6	15.0	15.0
37.0	17.2	17.1	17.0	20.1	19.7	24.1	24.0	15.0	15.3	17.1	16.9	17.0	18.3	17.6	19.4	20.3
38.4	13.7	16.2	17.5	27.1	19.4	23.4	22.4	17.3	14.4	20.3	31.6	26.1	30.9	25.1	18.0	23.0
39.8	13.6	16.1	17.0	23.8	18.1	22.2	20.9	21.9	14.9	17.6	31.5	23.4	24.3	16.7	15.9	26.0
41.8	13.2	15.2	14.5	17.4	15.0	18.2	17.3	15.8	18.6	17.1	16.1	13.7	14.1	14.7	18.4	38.7
43.6	10.4	14.1	13.9	15.5	13.5	16.9	16.7	12.0	14.2	12.7	10.1	9.7	9.8	10.4	16.6	32.6
45.3	8.3	11.8	12.3	13.3	12.2	15.6	15.4	11.9	9.7	9.2	7.6	7.3	7.8	7.6	12.2	22.8
46.9	9.1	11.7	11.7	12.4	11.8	15.5	15.2	11.4	13.4	11.0	8.3	6.7	8.1	8.6	13.0	19.6
48.4	12.4	12.5	11.6	12.7	12.1	15.4	15.4	11.6	16.2	12.0	9.2	7.7	9.0	9.4	13.6	19.4
50.0	11.3	11.8	11.2	12.3	11.0	15.1	14.7	11.6	17.1	12.5	9.0	7.5	8.6	8.2	11.8	16.9
51.6	12.6	13.2	12.2	13.2	11.6	15.3	14.6	11.4	20.7	18.4	13.0	11.7	12.0	10.8	14.6	15.5
53.2	13.6	13.2	12.0	13.1	11.3	14.5	14.1	11.1	21.7	17.2	12.8	11.5	11.3	10.6	13.3	12.7
54.8	12.8	11.9	11.3	12.5	10.9	13.6	13.5	10.0	18.7	15.3	13.4	12.0	10.9	9.2	11.3	12.7
56.5	9.6	10.7	9.7	10.6	9.3	12.4	12.2	7.4	13.9	12.6	11.7	10.9	10.5	9.8	11.9	13.0
58.2	10.0	9.9	9.4	9.4	8.8	11.8	11.1	8.2	13.4	9.1	8.0	8.0	8.5	8.6	10.9	12.2
60.0	10.0	8.5	7.8	7.9	7.1	9.5	9.0	7.7	12.4	9.3	6.6	5.6	5.5	4.9	8.3	9.2
61.7	6.7	7.4	6.6	6.7	5.9	8.2	7.3	6.1	9.5	8.9	7.0	6.2	5.4	4.5	5.7	5.5
63.4	6.7	6.7	5.9	6.3	5.9	7.5	6.7	5.2	8.7	7.9	6.2	6.0	5.7	5.2	5.8	5.1
65.0	4.3	5.1	4.4	4.5	4.4	5.2	4.8	3.8	5.7	5.5	5.3	4.7	4.5	3.6	4.3	3.7
67.6	6.0	7.5	6.3	6.2	5.6	7.1	7.2	4.9	6.2	5.9	5.5	5.0	4.8	4.4	4.6	3.0
69.2	7.9	8.2	6.9	7.2	6.3	8.6	8.8	5.1	9.1	6.9	5.4	5.2	4.9	5.1	6.9	5.4
71.0	8.6	10.5	8.4	8.8	7.8	10.8	11.1	6.4	13.4	11.2	7.6	6.6	6.3	5.2	6.8	6.8
72.8	11.6	11.3	9.1	9.7	8.1	11.5	11.8	5.9	14.2	14.6	10.0	9.8	8.4	7.9	9.1	5.8
74.7	12.9	11.3	9.3	10.1	8.3	12.3	12.4	8.3	13.2	13.4	9.7	10.7	9.0	8.3	9.2	6.4
76.6	11.5	10.4	8.5	9.7	8.3	12.3	12.2	9.3	12.9	10.6	8.1	8.4	8.5	9.7	10.0	7.5
78.5	10.4	9.5	8.0	8.5	7.2	10.7	10.2	9.0	12.2	10.8	8.4	7.8	6.3	6.2	9.0	5.8
80.4	10.4	8.6	7.2	8.0	7.0	9.3	9.1	7.8	9.8	9.4	8.4	8.3	6.7	5.1	6.3	6.1
82.4	8.2	6.7	5.8	6.3	5.6	7.3	7.2	6.6	5.8	7.9	6.4	6.3	5.3	5.5	6.0	4.5
84.4	6.9	5.3	4.6	4.8	4.2	5.9	5.7	5.1	6.0	6.3	5.0	4.6	4.1	4.5	4.6	3.2
86.2	5.3	4.4	3.8	4.1	3.5	4.6	4.3	4.4	4.7	4.7	3.4	3.5	2.6	2.8	3.6	2.7
88.0	2.9	2.4	1.8	2.4	1.8	1.9	2.2	2.3	2.6	2.4	2.3	2.3	1.8	1.7	2.0	1.6
89.5	2.2	1.9	2.1	1.8	1.2	1.7	1.6	2.2	2.0	1.9	1.8	2.0	1.8	1.7	1.6	1.6
91.5	1.4	1.1	1.0	0.9	0.8	1.0	0.7	1.0	1.3	1.2	1.1	0.9	0.9	0.4	0.8	0.9
93.0	2.1	1.7	1.3	1.3	0.8	1.1	0.6	0.8	1.7	1.8	1.2	1.2	1.2	1.3	0.9	0.8

Table 11. Outside areas of deformed tubes in 8-6 test array

ELEVATION (CM)	OUTSIDE AREA OF TUBE NO. (MM**2) 1	2	3	4	5	6	7	8	9	10	11	12	13	14	15	16
0.0	95	95	95	94	93	95	94	93	94	94	94	93	92	94	94	93
1.5	97	96	97	96	96	97	96	95	96	97	97	95	96	96	95	95
3.0	99	99	99	98	98	98	97	98	98	100	99	99	99	99	98	98
4.5	100	99	99	99	99	98	98	98	99	102	102	102	102	101	100	97
6.0	104	102	102	100	103	102	101	102	103	106	105	106	105	105	103	99
7.5	105	104	104	102	106	103	102	104	101	106	106	106	106	106	103	101
9.0	103	102	103	101	102	100	101	102	101	104	104	104	102	104	103	99
11.6	106	105	105	104	106	104	104	106	105	107	108	108	107	107	106	102
13.2	113	109	108	105	107	105	106	110	113	116	116	116	114	114	111	105
14.7	128	116	116	109	113	109	109	118	121	124	123	123	120	122	117	110
16.1	131	122	124	113	119	113	113	134	120	132	127	129	124	126	120	110
17.5	128	143	144	118	129	122	125	159	124	146	137	137	131	131	125	110
18.9	137	133	132	117	130	124	139	200	147	159	143	144	139	134	129	112
20.3	141	119	117	111	120	116	127	170	127	149	147	145	150	134	139	121
21.8	153	116	114	111	118	114	118	134	126	136	134	147	137	137	148	125
23.2	162	116	116	111	118	114	117	124	119	132	131	143	136	138	141	113
24.6	131	117	120	117	126	121	125	130	114	133	136	163	138	147	139	111
26.1	127	117	122	122	137	154	163	167	118	131	141	163	134	146	137	120
27.5	127	117	119	119	128	144	155	171	122	132	139	148	130	139	135	133
27.9	122	112	113	113	122	124	133	161	116	127	135	140	127	138	134	130
29.5	132	116	114	111	116	113	116	165	116	131	135	139	126	134	130	119
31.0	148	124	123	118	124	116	117	160	120	138	137	150	131	141	133	132
32.4	161	126	131	136	137	124	119	140	128	150	132	155	133	179	133	138
33.8	162	126	159	145	161	130	122	138	125	149	129	150	135	202	132	123
35.2	154	127	157	127	134	118	117	130	119	137	129	141	134	152	127	114
37.0	208	121	120	113	117	112	112	139	122	132	125	134	127	134	123	123
38.4	178	116	115	111	118	113	112	133	124	130	123	133	127	131	124	143
39.8	161	120	120	118	125	119	119	140	121	129	124	137	128	131	125	136
41.8	148	121	122	118	131	126	126	129	116	127	124	136	127	129	126	115
43.6	120	116	115	112	121	120	121	125	109	125	125	129	125	130	126	116
45.3	114	113	112	108	114	111	112	115	108	121	122	125	121	127	123	110
46.9	113	114	116	110	114	111	110	114	108	121	122	123	119	126	121	112
48.4	119	116	116	110	114	113	114	121	112	122	121	124	119	125	121	115
50.0	124	112	111	108	112	109	109	118	114	120	119	122	117	123	118	112
51.6	128	116	114	109	114	109	108	111	114	121	119	123	118	121	118	109
53.2	129	115	116	110	117	110	109	111	112	120	118	121	117	119	117	109
54.8	133	115	115	110	116	110	109	111	115	119	117	120	117	119	116	109
56.5	119	111	110	106	112	108	108	118	111	118	115	117	115	117	115	107
58.2	128	111	111	107	111	107	108	114	111	115	114	114	113	115	113	107
60.0	121	108	107	104	110	106	107	116	108	110	110	110	110	110	109	106
61.7	113	105	104	102	105	102	103	112	105	108	108	108	108	109	107	103
63.4	111	107	106	104	106	103	104	109	107	109	108	109	107	108	107	105
65.0	102	102	102	101	101	101	101	102	103	104	103	104	103	104	103	100
67.6	105	104	104	103	106	104	103	103	104	106	106	106	106	106	105	101
69.2	105	103	104	103	108	104	104	106	104	108	109	109	109	110	109	103
71.0	107	104	106	104	108	106	106	114	105	112	112	113	111	113	112	106
72.8	113	107	107	105	109	105	105	116	108	112	112	113	112	114	113	110
74.7	115	111	109	105	109	106	107	116	110	113	112	113	111	114	113	110
76.6	120	111	109	106	110	106	108	114	115	113	111	112	111	113	112	110
78.5	118	112	109	105	109	106	108	110	111	111	110	110	108	110	110	109
80.4	114	110	108	106	110	106	107	107	110	109	109	109	107	109	108	106
82.4	106	108	105	103	105	105	106	103	105	106	106	105	104	106	105	103
84.4	107	107	105	103	106	103	103	100	104	105	103	102	103	104	103	101
86.2	106	104	103	102	104	102	102	100	104	102	101	100	100	101	101	100
88.0	102	102	101	100	100	100	99	98	100	99	99	98	98	98	98	99
89.5	99	98	98	97	98	97	97	97	98	97	96	96	97	96	96	97
91.5	97	97	97	96	96	96	96	96	96	96	96	95	96	95	95	96
93.0	97	96	96	95	95	95	95	94	97	96	95	96	95	95	95	95

Table 11 (continued)

ELEVATION (CM)	OUTSIDE AREA OF TUBE NO. (KM**2)															
	17	18	19	20	21	22	23	24	25	26	27	28	29	30	31	32
0.0	93	94	94	94	93	93	94	93	93	94	93	93	93	92	93	93
1.[illegible]	97	97	96	96	95	96	95	94	96	96	96	96	95	96	96	94
3.0	99	99	99	100	99	98	97	96	98	100	99	100	100	99	98	97
4.5	99	102	102	102	100	100	100	97	99	102	102	101	100	101	101	97
6.0	103	105	105	104	103	103	102	98	100	105	105	105	103	104	104	97
7.5	102	105	105	104	104	103	102	100	101	105	104	105	104	104	104	99
9.0	101	102	102	102	100	101	101	98	101	104	104	103	102	103	104	99
11.6	106	106	105	105	104	104	104	100	103	106	105	105	104	104	106	101
13.2	115	114	113	112	110	110	110	104	110	113	113	112	110	110	113	104
14.7	122	120	120	120	115	117	117	107	117	120	121	120	117	117	121	107
16.1	119	122	126	125	118	120	119	105	114	123	129	126	123	121	125	108
17.5	120	125	137	127	118	124	123	109	112	128	139	131	129	126	133	112
18.9	132	130	157	128	119	127	126	113	119	132	149	135	135	130	137	114
20.3	161	149	154	129	121	129	130	120	133	136	153	138	137	130	138	116
21.8	138	140	149	130	121	127	131	126	137	141	147	155	136	132	145	119
23.2	124	137	139	132	121	128	130	124	121	141	140	161	136	134	154	126
24.6	118	139	135	133	124	132	137	119	116	147	155	145	140	138	171	127
26.1	127	140	135	130	129	135	155	122	125	164	159	137	138	134	190	123
27.5	143	141	133	131	133	138	163	126	142	147	143	135	140	142	193	118
27.9	141	135	129	128	134	139	174	122	137	140	136	132	137	149	184	116
29.5	141	131	129	129	149	155	145	113	130	141	132	138	140	140	151	110
31.0	133	130	132	135	157	154	138	123	149	145	132	145	149	132	151	119
32.4	134	128	136	142	147	135	135	149	141	147	132	154	141	128	157	137
33.8	125	128	148	184	138	128	132	138	118	139	132	159	132	126	156	139
35.2	121	129	146	223	134	130	134	116	118	135	138	146	130	130	150	117
37.0	127	129	129	150	126	125	129	119	122	128	135	132	125	130	138	117
38.4	128	128	127	138	123	124	130	123	120	127	130	130	123	135	134	119
39.8	126	126	129	132	123	124	127	119	120	126	127	128	123	138	129	114
41.8	118	123	125	128	121	126	123	111	116	123	123	124	122	134	124	107
43.6	112	121	124	131	121	122	125	114	113	121	122	124	123	130	126	110
45.3	112	119	123	132	119	120	130	114	110	119	120	123	122	128	128	113
46.9	111	119	120	131	119	120	139	117	109	119	119	122	120	126	129	114
48.4	116	121	119	128	120	120	140	120	113	119	120	122	120	126	131	115
50.0	116	120	118	124	117	117	128	119	113	118	119	119	117	120	126	115
51.6	115	119	118	120	117	117	123	117	113	118	117	118	116	120	126	115
53.2	113	117	116	117	115	116	119	117	112	118	116	116	114	118	123	115
54.8	118	117	116	116	114	115	118	115	117	117	115	115	114	115	122	114
56.5	115	116	116	115	112	114	115	111	118	116	114	113	113	114	119	113
58.2	114	113	113	112	111	111	113	109	114	114	112	111	111	113	115	109
60.0	111	109	108	107	107	106	108	106	109	109	108	107	106	108	111	103
61.7	106	107	108	106	105	105	106	102	104	108	106	105	106	107	109	101
63.4	108	107	107	106	106	106	107	106	106	108	106	105	106	106	109	104
65.0	102	103	102	101	102	102	102	101	101	103	102	101	101	101	103	100
67.6	105	107	106	106	105	105	106	103	105	107	105	104	105	105	108	102
69.2	106	108	107	108	107	105	108	103	105	109	108	106	107	108	111	102
71.0	109	112	110	112	109	109	111	106	108	113	112	109	110	111	115	106
72.8	113	113	111	112	110	110	112	110	112	114	112	111	111	113	117	110
74.7	114	113	110	111	109	110	113	109	114	113	111	110	110	111	118	109
76.6	115	112	110	110	108	109	111	108	112	112	112	110	109	110	116	107
78.5	112	110	107	107	105	106	107	108	109	109	108	107	105	107	112	107
80.4	113	108	106	106	105	105	106	105	107	108	107	106	105	107	109	105
82.4	109	105	103	103	102	102	104	102	105	105	104	102	102	104	105	101
84.4	107	104	102	101	100	101	102	102	105	104	102	101	101	102	104	100
86.2	105	101	100	100	99	99	99	100	103	101	100	99	99	99	101	99
88.0	100	99	98	97	97	97	97	98	99	99	97	97	97	97	98	98
89.5	98	98	96	95	96	96	96	96	98	98	96	96	96	96	96	96
91.5	97	96	96	94	94	94	95	95	97	95	96	95	95	94	94	95
93.0	97	96	96	95	95	94	94	95	96	96	95	95	95	94	94	95

Table 11 (continued)

ELEVATION (CM)	OUTSIDE AREA OF TUBE NO. (MM**2)															
	33	34	35	36	37	38	39	40	41	42	43	44	45	46	47	48
0.0	94	94	93	93	92	92	92	93	94	96	95	94	94	94	94	95
1.5	96	96	96	96	96	95	96	96	97	97	97	96	96	95	95	95
3.0	98	98	98	98	98	97	97	96	97	98	98	98	98	97	97	96
4.5	98	100	101	100	101	101	100	97	98	101	102	101	102	100	99	98
6.0	100	103	103	103	103	104	102	98	99	103	104	104	103	103	101	100
7.5	100	103	103	104	105	105	103	100	101	105	106	106	106	105	104	102
9.0	100	103	103	102	103	104	101	99	99	102	103	101	102	102	101	98
11.6	103	105	105	105	104	105	104	102	102	105	106	105	104	105	103	102
13.2	110	112	112	113	111	112	110	104	109	113	115	113	113	113	109	104
14.7	117	119	119	120	120	119	118	107	114	119	121	121	121	122	115	108
16.1	119	123	125	128	130	125	121	110	114	123	126	129	129	129	117	112
17.5	113	126	134	137	143	130	126	113	113	129	131	140	134	137	119	113
18.9	119	134	148	167	148	138	131	111	119	144	135	165	137	152	120	110
20.3	146	140	153	182	137	144	139	114	136	190	138	163	144	155	121	113
21.8	151	144	182	154	136	144	147	119	163	172	142	146	144	140	121	116
23.2	122	147	187	141	138	146	150	122	132	142	147	142	143	132	120	113
24.6	117	150	148	138	143	142	140	121	124	136	169	141	143	133	120	110
26.1	125	141	137	136	162	136	136	121	129	135	152	137	150	138	122	115
27.5	127	137	136	138	163	136	137	120	128	136	147	134	154	141	123	118
27.9	117	130	130	134	155	135	139	120	119	130	142	130	153	140	122	116
29.5	113	130	129	141	137	133	137	116	115	131	139	130	170	145	130	117
31.0	118	135	129	149	134	134	138	125	117	130	135	129	147	148	133	122
32.4	120	140	130	142	131	133	135	131	122	130	134	128	137	156	130	124
33.8	117	137	127	134	128	134	132	137	120	130	131	126	131	145	128	120
35.2	119	138	129	138	131	141	130	133	125	135	132	131	135	138	129	126
37.0	118	130	128	141	129	152	126	140	119	130	131	128	138	136	136	135
38.4	113	126	128	141	126	155	126	156	115	126	135	127	139	136	137	141
39.8	113	123	128	135	128	141	124	129	115	125	132	128	137	134	132	136
41.8	111	120	126	127	124	135	118	111	115	121	126	122	133	127	122	115
43.6	108	120	125	124	123	142	118	113	110	120	124	121	131	124	121	112
45.3	104	118	121	120	122	161	118	112	106	116	121	119	127	122	118	110
46.9	106	117	119	119	122	143	117	109	107	117	120	117	125	120	117	109
48.4	109	117	118	120	122	134	116	107	112	117	119	118	127	122	116	106
50.0	107	116	115	117	118	126	115	107	110	117	118	115	124	117	116	107
51.6	110	117	116	118	118	124	117	108	115	118	119	115	122	119	116	108
53.2	108	115	115	116	117	123	116	108	115	117	117	114	120	118	116	111
54.8	111	115	114	115	115	120	115	111	115	114	115	113	116	116	113	109
56.5	109	113	111	112	112	116	111	113	109	111	112	111	114	113	110	108
58.2	109	113	111	110	111	115	110	112	110	111	111	110	112	111	109	106
60.0	105	108	107	107	107	110	106	104	109	109	108	107	110	108	106	104
61.7	102	106	106	106	106	108	105	104	103	107	106	106	107	106	104	104
63.4	103	105	105	104	105	106	105	103	103	105	105	104	105	104	104	102
65.0	100	102	101	101	101	102	101	100	100	102	102	101	101	101	102	99
67.6	102	105	103	103	103	104	103	102	104	106	105	104	105	104	105	103
69.2	105	109	107	106	106	109	107	103	105	107	108	106	107	107	106	103
71.0	105	112	111	109	109	112	110	108	106	111	112	109	111	109	109	108
72.8	109	115	111	111	111	114	112	111	110	112	112	109	112	110	109	107
74.7	112	114	110	110	109	113	112	110	113	112	111	108	111	110	109	111
76.6	109	113	111	110	108	112	112	109	111	111	111	109	111	110	110	111
78.5	106	109	108	107	106	108	108	110	111	110	109	108	108	108	108	112
80.4	104	107	107	106	106	108	107	108	111	109	108	107	107	107	107	110
82.4	103	104	103	104	103	104	103	105	108	106	105	104	104	104	104	106
84.4	105	104	102	102	101	102	101	103	105	104	103	101	102	101	101	103
86.2	102	100	100	100	99	99	99	102	103	102	101	100	101	100	100	103
88.0	98	98	98	97	97	97	96	99	100	99	99	99	98	97	98	99
89.5	97	97	96	96	96	96	96	97	97	97	97	97	96	96	96	97
91.5	96	95	95	95	95	93	94	95	95	96	95	95	95	94	95	95
93.0	97	96	95	95	95	94	94	95	97	96	96	95	95	94	95	95

Table 11 (continued)

ELEVATION (CM)	OUTSIDE AREA OF TUBE NO. (MM**2)																
	49	50	51	52	53	54	55	56	57	58	59	60	61	62	63	64	TOTAL
0.0	95	95	95	94	94	94	94	94	94	94	95	94	95	94	94	94	6038
1.5	97	97	96	95	95	96	96	96	97	96	96	96	96	95	95	95	6171
3.0	97	98	98	98	98	98	97	97	97	97	96	96	97	96	96	96	6297
4.5	99	101	102	101	100	101	101	97	98	98	98	98	97	96	97	96	6411
6.0	100	102	103	103	103	104	103	98	102	102	101	102	100	98	99	99	6577
7.5	102	105	106	106	105	106	105	101	103	103	102	102	101	100	102	102	6657
9.0	99	102	102	103	101	103	102	98	100	100	99	99	99	98	99	98	6520
11.6	102	106	105	105	104	107	106	101	103	103	102	101	102	101	102	103	6709
13.2	110	113	113	113	112	115	114	105	110	110	106	106	106	106	108	108	7102
14.7	115	118	119	118	117	123	121	108	114	111	106	107	107	106	111	117	7492
16.1	112	120	120	120	119	128	125	108	114	113	109	109	108	109	115	120	7721
17.5	116	126	125	128	126	137	129	109	124	123	115	117	115	116	119	123	8120
18.9	122	128	126	132	127	138	128	105	138	121	115	117	115	113	116	119	8471
20.3	131	136	129	133	132	136	127	108	135	118	115	119	115	110	113	123	8637
21.8	141	139	139	130	144	137	129	113	133	117	114	115	115	113	120	130	8626
23.2	163	134	167	126	153	143	128	108	177	122	118	118	118	115	120	123	8570
24.6	145	132	149	125	155	151	129	105	145	126	120	120	119	114	116	114	8517
26.1	136	128	131	123	138	149	130	109	126	122	113	114	112	109	113	120	8614
27.5	133	126	129	124	131	153	132	113	125	118	113	113	113	111	118	133	8618
27.9	126	121	125	121	128	153	134	112	122	114	109	110	111	111	118	134	8371
29.5	120	126	129	127	132	189	143	116	132	129	121	120	121	119	128	153	8438
31.0	123	128	132	129	131	191	154	123	132	156	137	128	130	126	144	166	8721
32.4	130	129	132	129	131	164	171	120	132	150	140	128	129	130	144	147	8826
33.8	131	129	127	126	131	151	143	111	125	125	121	118	119	122	126	126	8649
35.2	132	132	128	129	132	145	142	117	120	119	118	116	117	118	123	123	8465
37.0	128	128	127	135	134	144	143	123	124	127	127	128	130	129	133	135	8368
38.4	120	126	129	151	133	142	140	128	122	135	162	149	160	146	130	141	8440
39.8	120	126	128	148	130	139	136	139	123	129	161	142	144	127	125	148	8319
41.8	120	124	122	128	123	130	128	125	131	128	126	121	121	123	130	180	8016
43.6	114	121	121	124	120	127	127	117	122	118	113	112	112	114	127	164	7797
45.3	109	116	118	120	117	125	124	117	112	111	108	107	108	108	117	141	7593
46.9	111	116	116	118	116	124	124	116	120	115	109	106	109	110	119	133	7563
48.4	118	118	116	118	117	124	124	116	126	117	111	108	111	112	120	133	7633
50.0	115	117	115	117	115	123	123	116	128	118	111	108	110	109	116	127	7496
51.6	118	119	117	119	116	124	122	116	136	131	119	116	117	114	123	124	7565
53.2	120	119	117	119	115	122	121	115	138	128	118	116	115	114	120	118	7506
54.8	119	117	115	118	115	120	120	113	131	124	120	117	115	111	115	118	7455
56.5	112	114	112	114	111	118	117	107	121	118	116	115	114	112	117	119	7297
58.2	113	113	111	112	110	116	115	109	120	111	108	109	110	110	115	117	7196
60.0	113	110	108	108	107	112	111	108	117	111	106	104	104	102	109	111	6958
61.7	106	108	106	106	105	109	107	105	112	110	107	105	103	102	104	104	6807
63.4	106	106	104	105	104	108	106	103	110	108	105	105	104	103	104	103	6796
65.0	101	103	101	102	101	103	102	100	104	103	103	102	102	100	101	100	6541
67.6	104	107	105	105	104	107	107	102	105	104	103	103	102	101	102	99	6710
69.2	108	109	106	107	105	110	110	103	111	107	103	103	102	103	106	104	6838
71.0	110	114	109	110	108	114	115	105	120	115	108	106	105	103	106	106	7037
72.8	116	115	111	112	109	116	116	104	121	122	113	112	110	108	111	104	7162
74.7	119	115	111	113	109	118	118	109	119	120	112	114	111	109	111	105	7183
76.6	116	113	110	112	109	117	117	111	119	114	109	110	110	112	113	108	7152
78.5	114	112	109	110	107	114	113	111	117	114	109	108	105	105	111	104	7014
80.4	114	110	107	109	106	111	111	108	112	112	109	109	106	103	105	105	6930
82.4	109	106	104	105	104	107	107	106	104	108	105	105	103	104	105	102	6724
84.4	106	103	102	102	101	104	104	103	105	105	103	102	101	102	102	99	6610
86.2	103	101	100	101	100	102	101	102	102	102	100	100	98	98	100	98	6486
88.0	99	98	96	98	96	97	97	97	98	98	97	97	96	96	97	96	6311
89.5	97	97	97	96	95	96	96	97	97	97	96	97	96	96	96	96	6218
91.5	96	95	95	95	95	95	94	95	95	95	95	95	95	94	95	95	6128
93.0	97	96	95	95	95	95	94	95	96	96	95	95	95	96	95	95	6128

Table 12. Flow area restriction in B-6 test array

Elevation (cm)	Entire 8 x 8 array		Inner 6 x 6 array		Central 4 x 4 array	
	Maximum (%)	Minimum (%)	Maximum (%)	Minimum (%)	Maximum (%)	Minimum (%)
0.0	0.6	0.6	0.4	0.4	0.1	0.1
1.5	2.4	2.4	2.3	2.3	2.3	2.3
3.0	4.1	4.1	4.6	4.6	4.7	4.7
4.5	5.7	5.7	6.8	6.8	6.8	6.8
6.0	7.9	7.9	9.1	9.1	9.1	9.1
7.5	9.0	9.0	10.0	10.0	9.9	9.9
9.0	7.2	7.2	8.2	8.2	8.0	8.0
11.6	9.7	9.7	10.6	10.6	10.1	10.1
13.2	15.1	15.1	16.9	16.9	16.4	16.4
14.7	20.4	20.4	23.1	23.1	23.0	23.0
16.1	23.6	23.6	27.1	27.1	28.2	28.2
17.5	29.2	29.0	32.8	32.8	34.3	34.3
18.9	34.1	33.8	39.0	38.7	43.3	42.5
20.3	38.1	36.1	45.3	42.6	46.5	44.6
21.8	40.0	35.9	46.9	42.0	48.3	43.5
23.2	38.1	35.1	46.4	41.4	47.8	42.5
24.6	36.7	34.4	46.3	42.3	42.7	41.9
26.1	39.9	35.7	47.1	41.8	46.4	41.1
27.5	38.9	35.8	45.3	40.9	44.5	41.1
27.9	33.8	32.4	40.9	38.4	40.9	38.9
29.5	35.2	33.3	42.5	39.3	45.5	40.8
31.0	40.8	37.2	42.8	40.8	45.4	41.0
32.4	42.1	38.6	42.6	41.1	39.1	39.1
33.8	39.4	36.2	40.8	39.8	40.5	38.8
35.2	34.6	33.7	39.9	38.9	43.7	41.6
37.0	32.8	32.4	34.4	34.3	35.2	35.2
38.4	37.6	33.4	34.3	33.6	34.2	34.2
39.8	32.7	31.7	32.3	32.1	32.6	32.6
41.8	27.8	27.6	28.4	28.4	29.1	29.1
43.6	24.6	24.6	27.5	27.5	28.5	28.5
45.3	22.3	21.8	26.8	26.0	29.6	27.8
46.9	21.4	21.4	24.9	24.9	25.7	25.7
48.4	22.4	22.4	24.9	24.9	25.3	25.3
50.0	20.5	20.5	22.5	22.5	22.3	22.3
51.6	21.4	21.4	22.6	22.6	22.1	22.1
53.2	20.6	20.6	21.3	21.3	20.6	20.6
54.8	19.9	19.9	20.2	20.2	19.3	19.3
56.5	17.8	17.8	18.3	18.3	17.5	17.5
58.2	16.4	16.4	16.7	16.7	16.1	16.1
60.0	13.1	13.1	13.2	13.2	12.4	12.4
61.7	11.1	11.1	11.8	11.8	11.3	11.3
63.4	10.9	10.9	11.2	11.2	10.6	10.6
65.0	7.4	7.4	7.7	7.7	7.1	7.1
67.6	9.8	9.8	10.5	10.5	9.9	9.9
69.2	11.5	11.5	12.8	12.8	12.1	12.1
71.0	14.2	14.2	15.6	15.6	14.8	14.8
72.8	15.9	15.9	16.6	16.6	15.8	15.8
74.7	16.2	16.2	16.4	16.4	15.0	15.0
76.6	15.8	15.8	15.9	15.9	14.6	14.6
78.5	13.9	13.9	13.5	13.5	12.2	12.2
80.4	12.7	12.7	12.5	12.5	11.7	11.7
82.4	9.9	9.9	9.7	9.7	8.9	8.9
84.4	8.4	8.4	7.9	7.9	7.2	7.2
86.2	6.7	6.7	6.1	6.1	5.6	5.6
88.0	4.3	4.3	3.9	3.9	3.8	3.8
89.5	3.0	3.0	2.7	2.7	2.4	2.4
91.5	1.8	1.8	1.5	1.5	1.3	1.3
93.0	1.8	1.8	1.6	1.6	1.5	1.5

Table 13. Tube displacements[a] at 32.4-cm elevation (in millimeters)

TUBE NO.	PRETEST CENTROID X-DIM. (MM)	PRETEST CENTROID Y-DIM. (MM)	POSTTEST CENTROID X-DIM. (MM)	POSTTEST CENTROID Y-DIM. (MM)	CTF DISPLACEMENT X-DIRECT (MM)	CTF DISPLACEMENT Y-DIRECT (MM)
1	0.000	0.000	0.900	-0.339	0.900	-0.339
2	14.427	-0.010	14.479	-0.391	0.051	-0.381
3	28.854	-0.020	28.741	-0.811	-0.114	-0.791
4	43.282	-0.030	43.435	-0.331	0.153	-0.301
5	57.709	-0.040	58.256	0.137	0.547	0.177
6	72.136	-0.050	72.030	0.675	-0.106	0.725
7	86.563	-0.060	86.544	0.083	-0.020	0.143
8	100.990	-0.070	100.027	0.097	-0.964	0.167
9	0.010	14.427	0.759	14.415	0.749	-0.013
10	14.437	14.417	14.832	14.585	0.394	0.168
11	28.864	14.407	28.444	14.243	-0.420	-0.165
12	43.292	14.397	42.908	14.531	-0.384	0.134
13	57.719	14.387	57.953	14.935	0.234	0.548
14	72.146	14.377	72.860	15.877	0.714	1.500
15	86.573	14.367	87.055	14.813	0.482	0.247
16	101.000	14.357	100.212	14.770	-0.789	0.413
17	0.020	28.854	0.869	28.252	0.849	-0.603
18	14.447	28.844	14.306	28.392	-0.141	-0.453
19	28.874	28.834	27.231	28.592	-1.643	-0.242
20	43.302	28.824	43.993	29.242	0.691	0.417
21	57.729	28.814	57.720	28.348	-0.009	-0.466
22	72.156	28.804	72.891	29.559	0.735	1.155
23	86.583	28.794	86.016	29.362	-0.567	0.568
24	101.011	28.784	99.124	29.147	-1.887	0.362
25	0.030	43.282	0.707	42.732	0.677	-0.549
26	14.457	43.272	15.536	42.327	1.079	-0.944
27	28.885	43.262	29.127	42.714	0.243	-0.547
28	43.312	43.251	43.567	44.068	0.255	0.817
29	57.739	43.241	57.304	43.597	-0.435	0.356
30	72.166	43.231	72.770	43.877	0.604	0.645
31	86.593	43.221	86.076	43.994	-0.516	0.773
32	101.021	43.211	99.523	44.264	-1.498	1.053
33	0.040	57.709	0.738	57.406	0.698	-0.303
34	14.467	57.699	14.272	56.790	-0.196	-0.908
35	28.895	57.689	28.696	58.115	-0.199	0.430
36	43.322	57.679	42.956	58.152	-0.366	0.473
37	57.749	57.669	57.609	58.356	-0.140	0.688
38	72.176	57.659	71.909	57.914	-0.267	0.256
39	86.603	57.649	86.147	58.046	-0.456	0.398
40	101.031	57.638	100.452	58.187	-0.579	0.549
41	0.050	72.136	0.828	71.722	0.778	-0.414
42	14.477	72.126	14.585	71.856	0.111	-0.270
43	28.905	72.116	29.128	72.810	0.223	0.694
44	43.332	72.106	43.990	72.194	0.658	0.088
45	57.759	72.096	57.232	72.306	-0.527	0.211
46	72.186	72.086	72.551	71.336	0.364	-0.750
47	86.613	72.076	86.394	72.160	-0.219	0.085
48	101.041	72.066	100.565	72.384	-0.475	0.319
49	0.060	86.563	0.933	86.407	0.873	-0.156
50	14.487	86.553	14.635	85.797	0.151	-0.756
51	28.915	86.543	28.621	86.113	-0.294	-0.430
52	43.342	86.533	43.373	86.014	0.032	-0.519
53	57.769	86.523	58.081	86.967	0.312	0.444
54	72.196	86.513	72.207	85.845	0.011	-0.668
55	86.623	86.503	86.237	85.194	-0.387	-1.308
56	101.051	86.493	100.623	86.880	-0.428	0.387
57	0.070	100.990	1.051	101.208	0.980	0.217
58	14.498	100.980	14.666	99.602	0.168	-1.378
59	28.925	100.970	29.152	100.468	0.228	-0.502
60	43.352	100.960	43.692	100.548	0.340	-0.413
61	57.779	100.950	58.419	100.649	0.640	-0.301
62	72.206	100.940	71.951	100.741	-0.255	-0.199
63	86.634	100.930	85.635	100.428	-0.998	-0.502
64	101.061	100.920	100.414	100.887	-0.647	-0.033

[a]Tube centroid locations based on area enclosed by OD perimeter with origin arbitrarily located at pretest centroid of tube 1 (note: positive X is left to right, positive Y is top to bottom).

Table 14. Test results as a function of radial

	Four exterior corner rods		Outer ring of 8 x 8 without corner rods		Outer ring of central 6 x 6		Outer r central
	Avg.	Dev.	Avg.	Dev.	Avg.	Dev.	Avg.
Number of simulators	4		24		20		12
Initial pressure differential (kPa)	3054	3	3051	5	3051	4	3046
Initial temperature (°C)	a		330[b]	1.2	330	0.9	330
Maximum pressure differential (kPa)	3314	13	3235	13	3243	8	3241
Pressure differential 1.0 s before first tube burst (kPa)	3216	5	3176	11	3062	34	3013
Temperature 1.0 s before first tube burst[c] (°C)	a		888[b]	7.1	911	6.3	919
Heating rate during deformation[d] (°C/s)	a		3.50[b]		3.53		3.69
Burst pressure (kPa)	2882	65	2999	65	2799	50	2799
Burst temperature (°C)	a		924[b]	4.2	931	4.6	932
Burst time (s)	186.8	8.2	144.5	3.9	137.2	1.6	134.8
Burst strain (%)	43.3	5.8	27.4	3.6	31.4	7.6	33.4
Volumetric expansion of heated length (%)	28.1	2.9	19.2	2.0	25.5	2.8	25.4
Average strain[e] (%)	20.5	2.1	13.4	1.4	18.3	2.1	18.5

[a]Simulators not instrumented with thermocouples.

[b]Based on eight simulators in outer ring instrumented with thermocouples.

[c]Based on thermocouples in region between interior grids.

[d]Based on average temperature of region between interior grids and 115 s and 132 s after power-on.

[e]Based on integration of strain profiles between 18.3-cm and 58.3-cm elevations in region between interior grids.

position — average and standard deviation values

ng of 4 x 4	Central 2 x 2 array		Central 4 x 4 array		Central 6 x 6 array		8 x 8 arrsy less corners		Entire 8 x 8 array	
ev.	Avg.	Dev.	Avg.	Dev.	Avg.	Dev.	Avg.	Dev.	Avg.	Dev.
	4		16		36		60		64	
4	3045	3	3046	4	3048	5	3050	5	3050	5
0.8	330	0	330	0.7	330	0.8	330[b]	0.9	330[b]	0.9
8	3239	18	3242	8	3243	8	3240	11	3244	21
17	2988	30	3007	23	3037	40	3093	75	3100	79
5.8	921	6.1	919	5.8	915	7.3	909[b]	13.0	909[b]	13.0
	3.72		3.70		3.61		3.58[b]		3.58[b]	
39	2800	56	2799	42	2799	46	2879	113	2879	110
5.9	933	5.4	932	5.6	932	5.0	930	5.6	930[b]	5.6
0.5	134.0	0.9	134.6	0.7	136.0	1.8	139.4	5.3	142.4	12.8
8.2	32.3	5.4	33.1	7.5	32.2	7.5	30.3	6.6	31.1	7.3
1.9	25.1	1.4	25.3	1.8	25.4	2.4	22.9	3.8	23.2	4.0
1.4	18.5	1.3	18.5	1.4	18.4	1.2	16.1	3.6	16.3	3.7

ORNL-DWG 82-6386 ETD

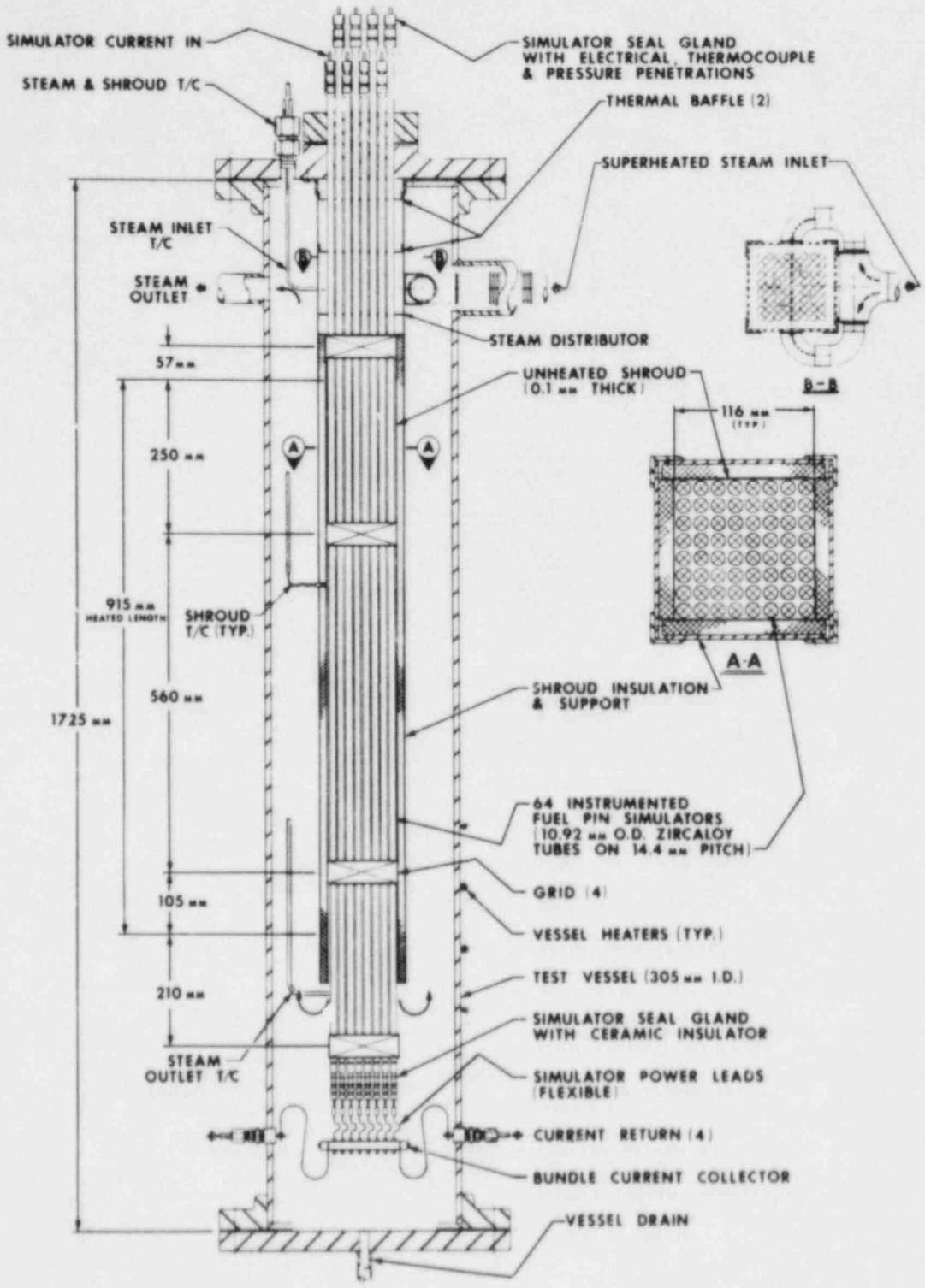

Fig. 1. Schematic of B-6 test assembly.

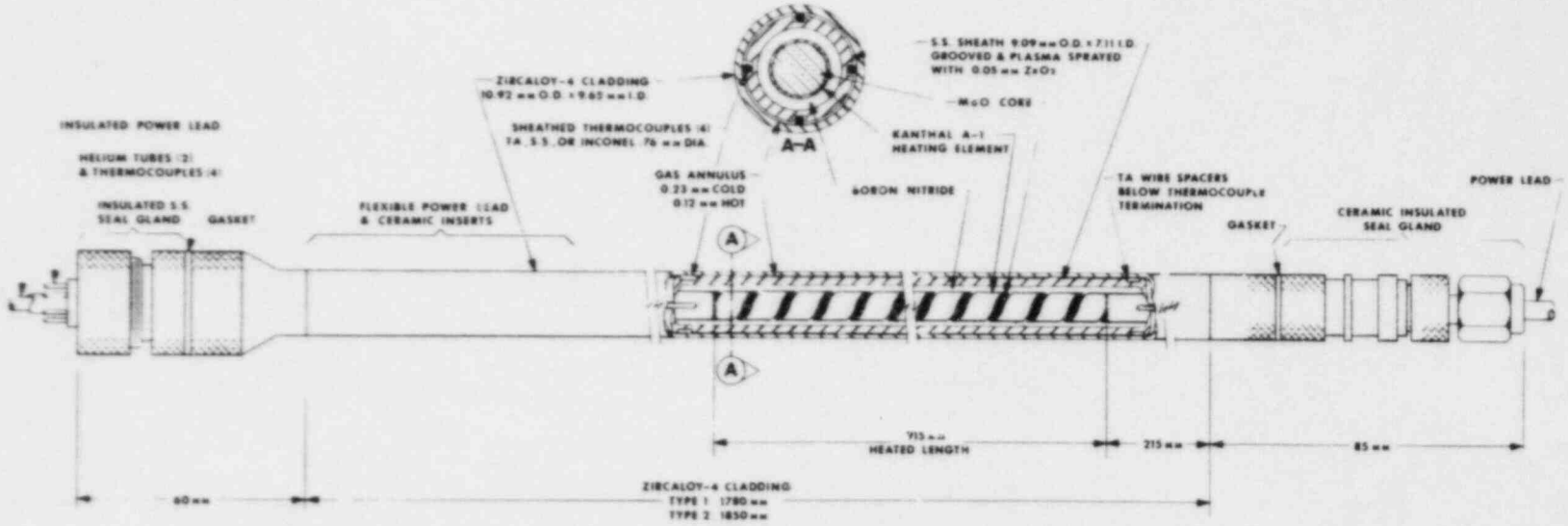

Fig. 2. Typical fully instrumented fuel pin simulator.

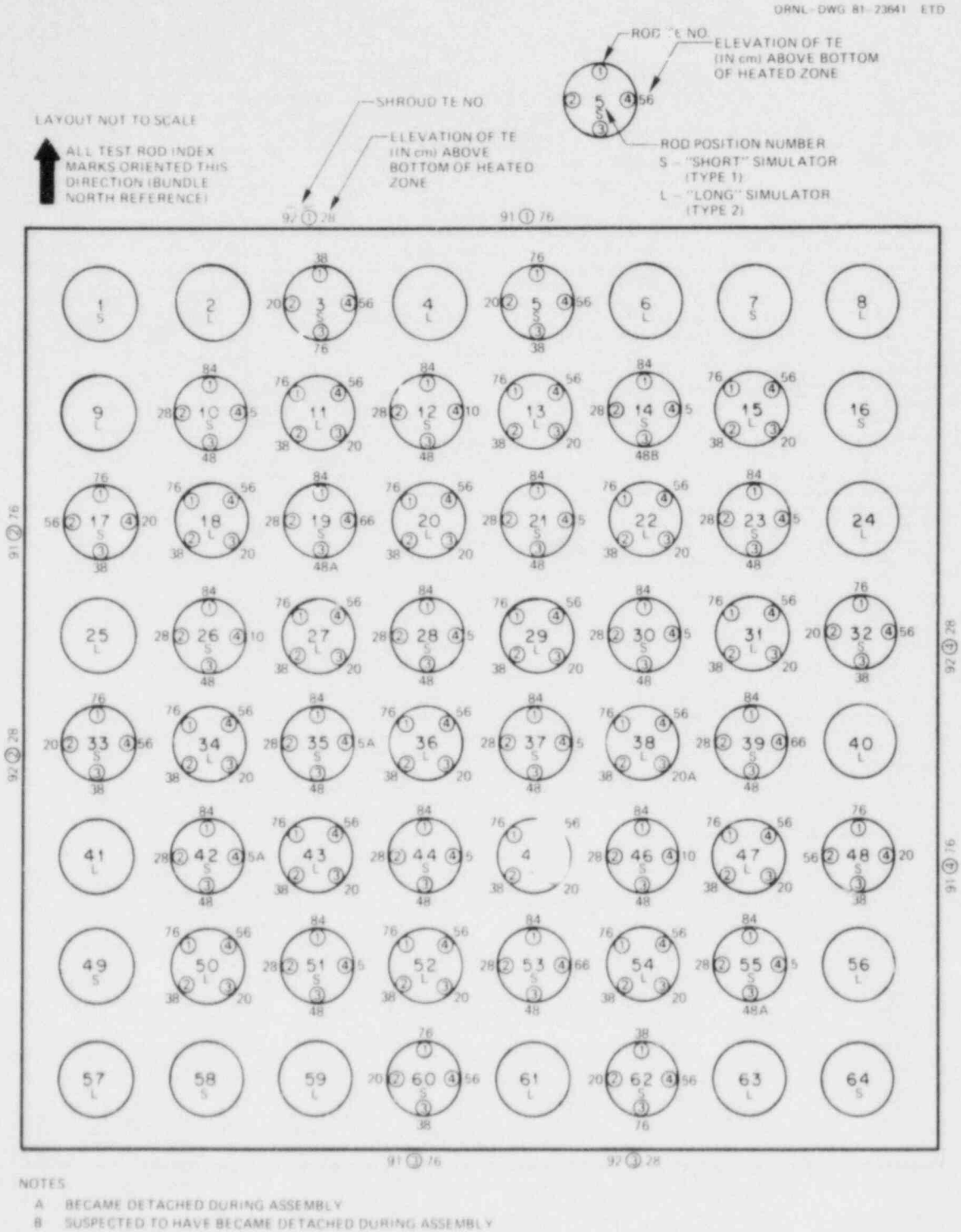

Fig. 3. Thermocouple identifications and as-built locations in B-6 test (plan view).

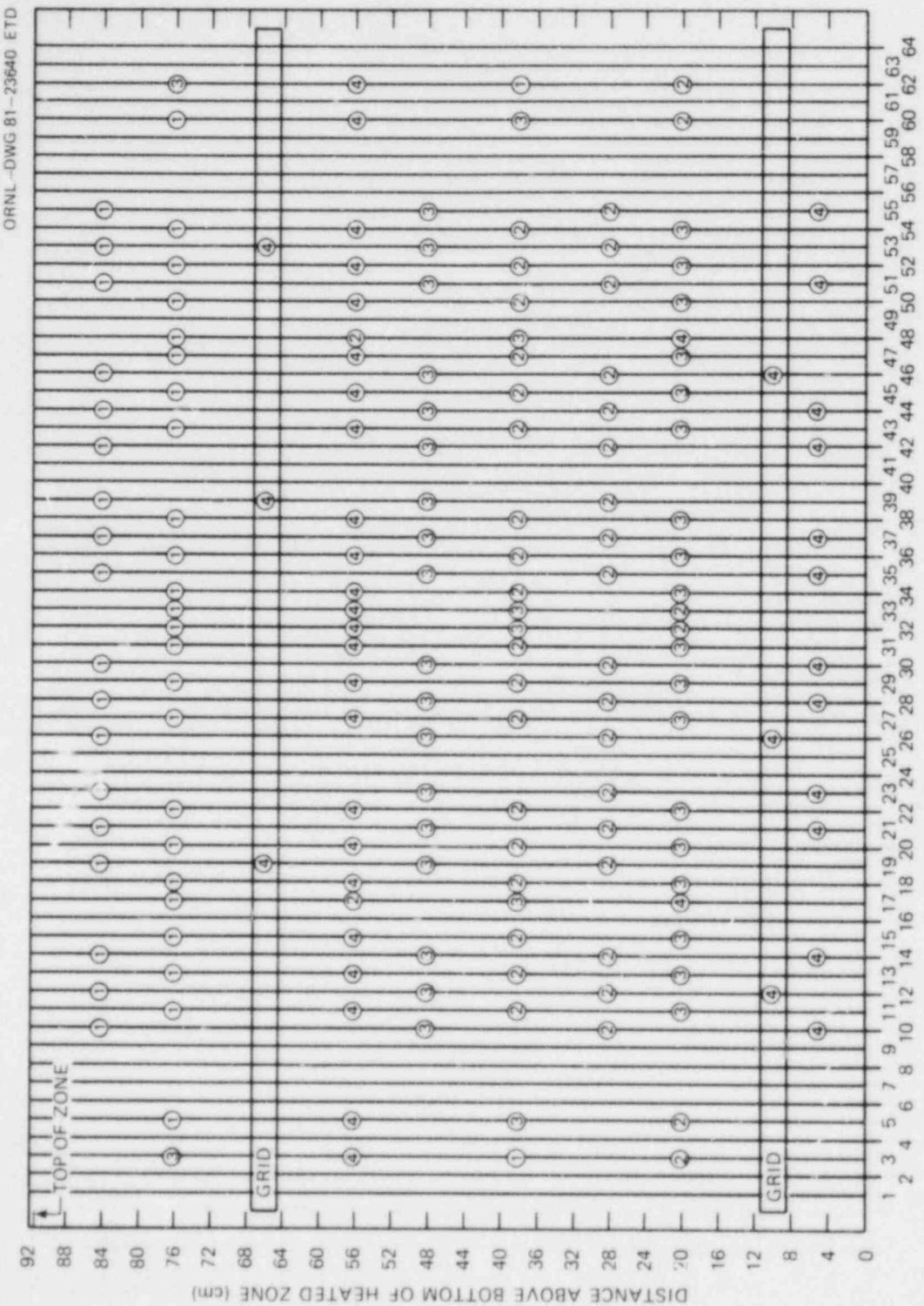

Fig. 4. As-built axial locations of simulator thermocouples in B-6 test (elevation view).

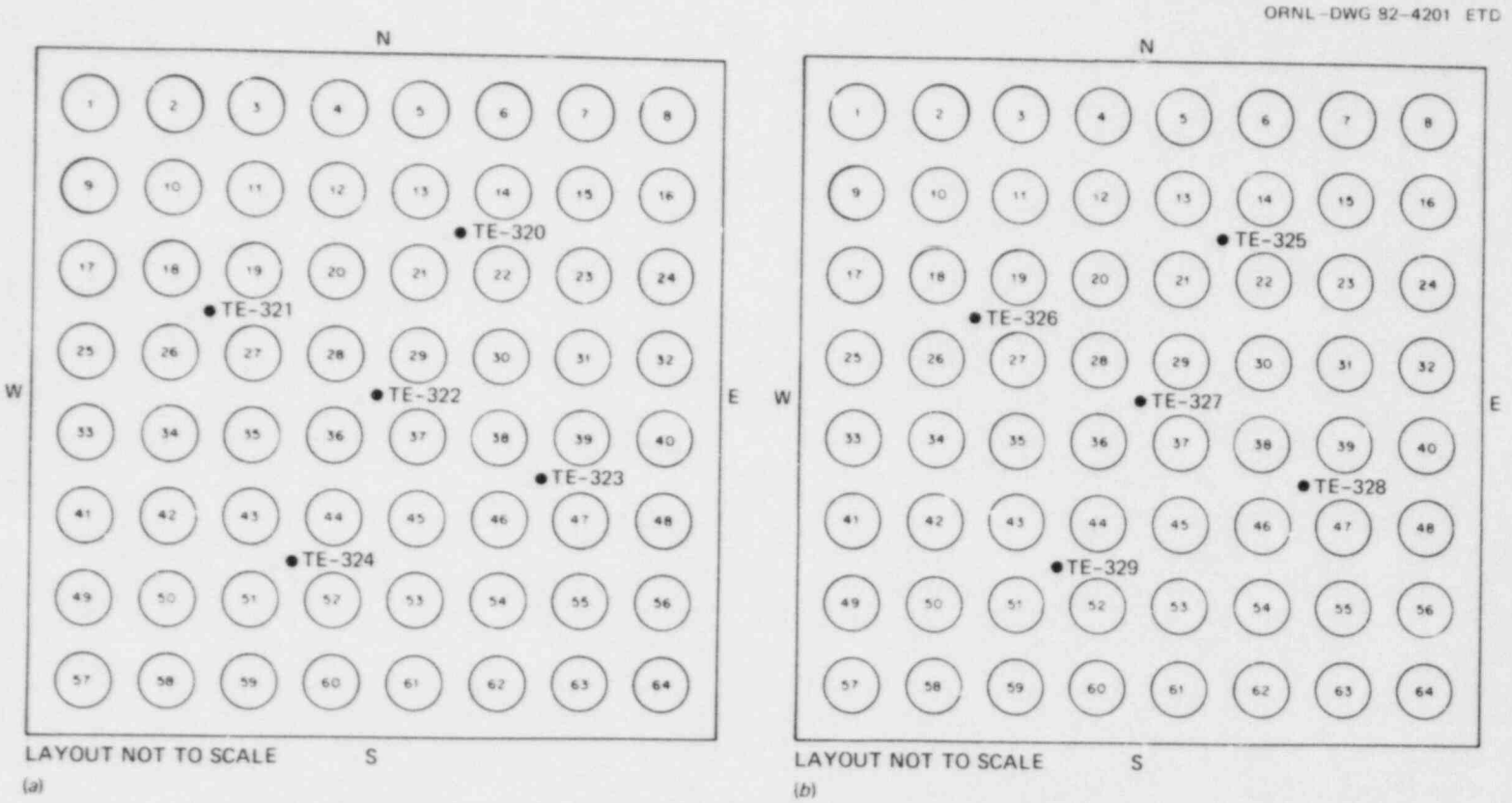

Fig. 5. Locations and identifications of thermocouples for measuring temperature of (*a*) inlet steam at 107-cm elevation and (*b*) outlet steam at 3-cm elevation in B-6 test.

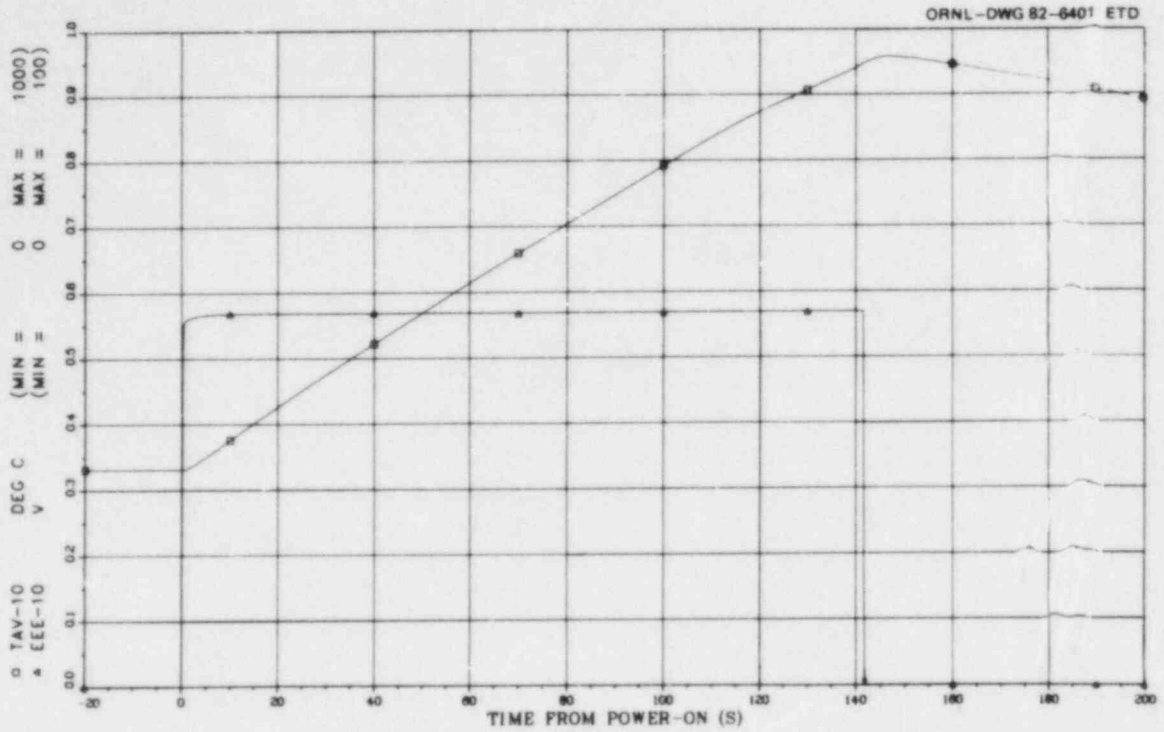

Fig. 6. B-6 applied voltage and bundle average temperature.

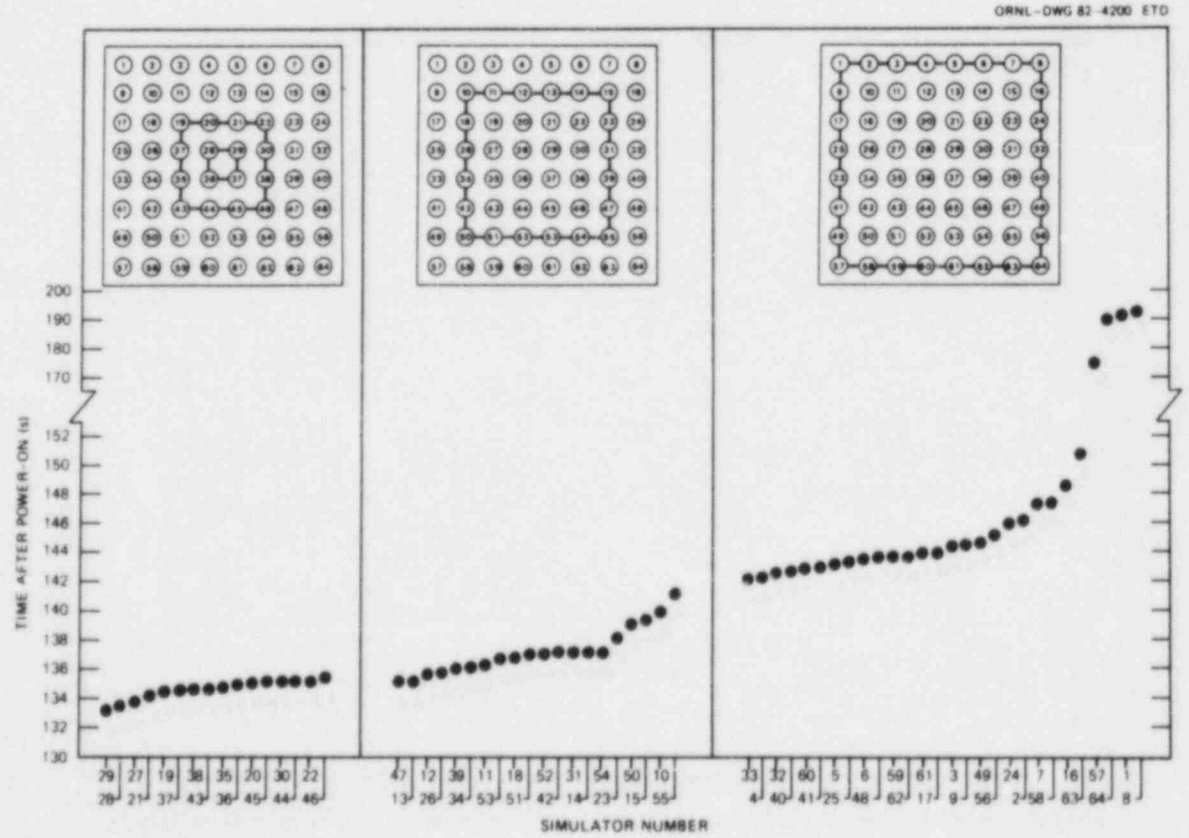

Fig. 7. Burst times in B-6 test.

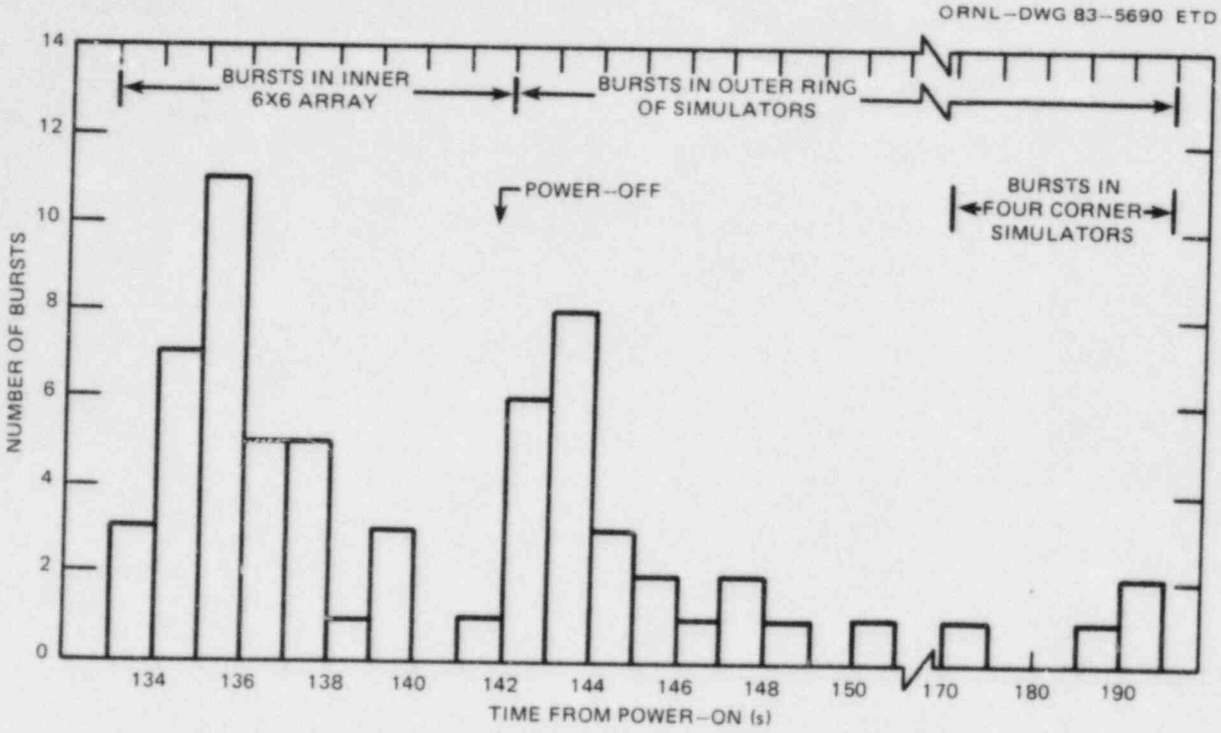

Fig. 8. Burst frequency in B-6 test.

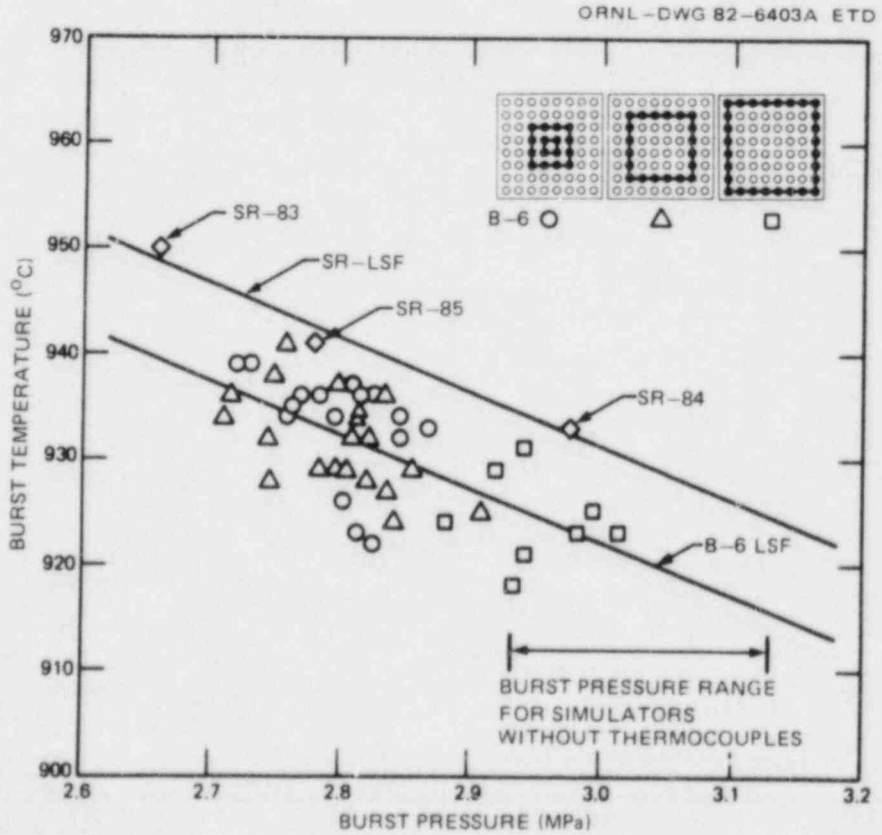

Fig. 9. Comparison of B-6 burst data with prediction from single-rod heated shroud test data.

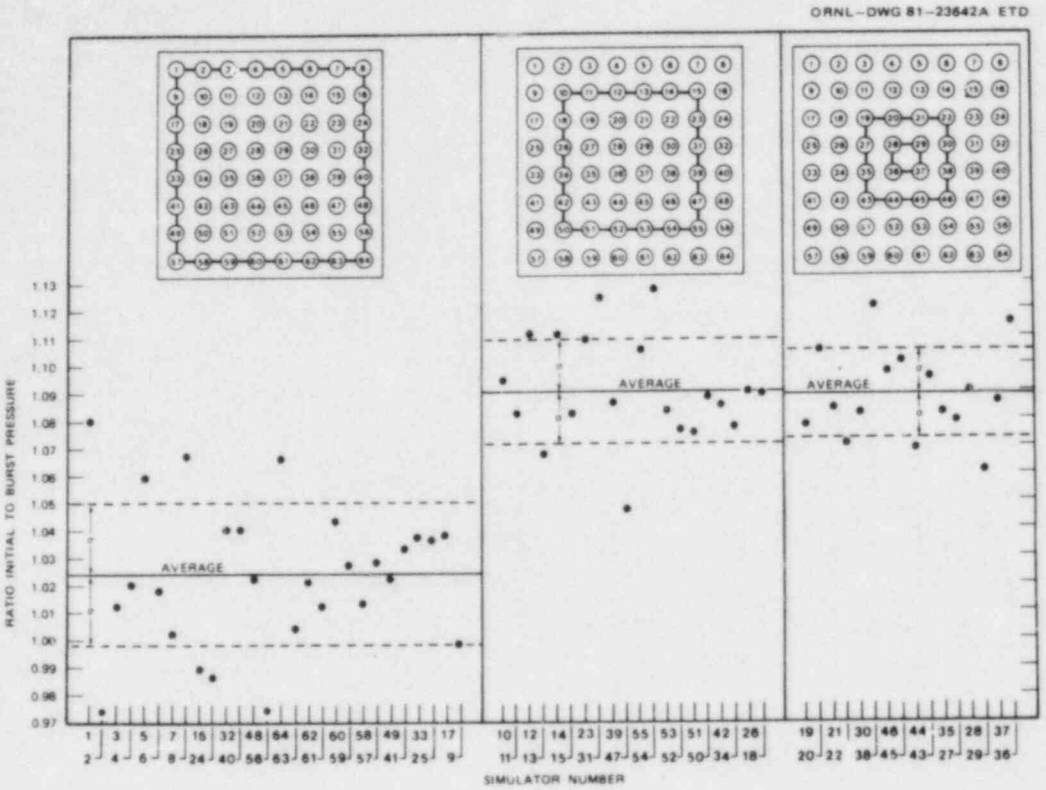

Fig. 10. Initial-to-burst pressure ratios in B-6 test.

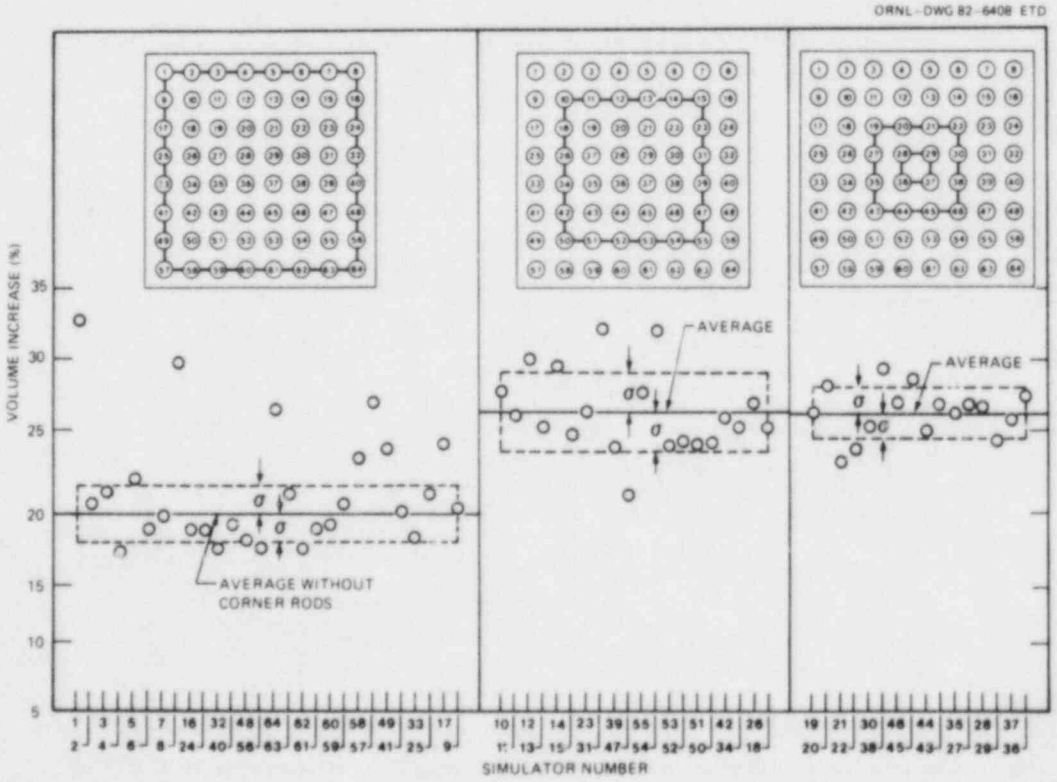

Fig. 11. Volume increase of B-6 tubes.

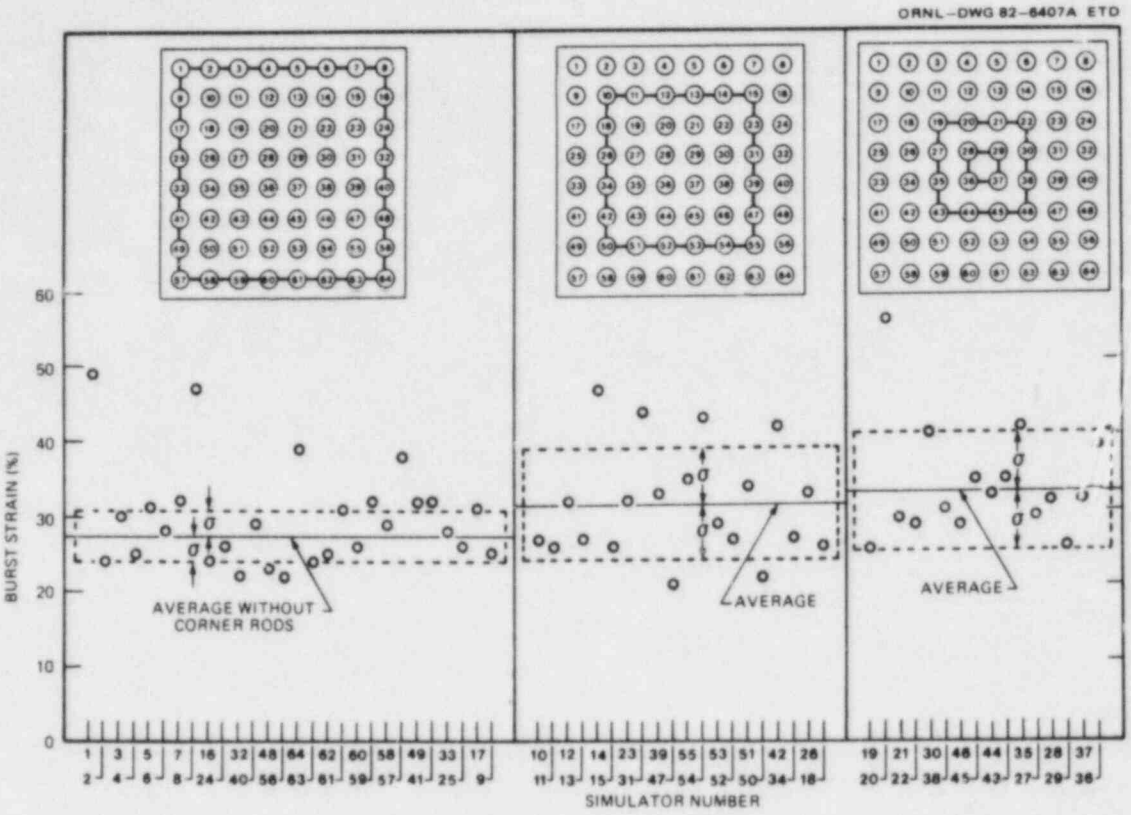

Fig. 12. Burst strain of B-6 tubes.

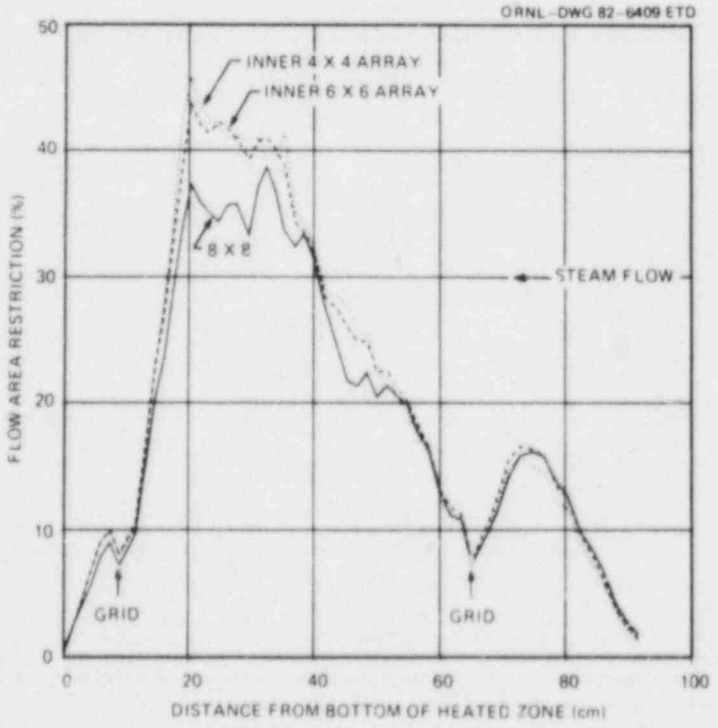

Fig. 13. Flow area restriction of B-6 central 4 × 4 array, inner 6 × 6 array, and entire 8 × 8 test array.

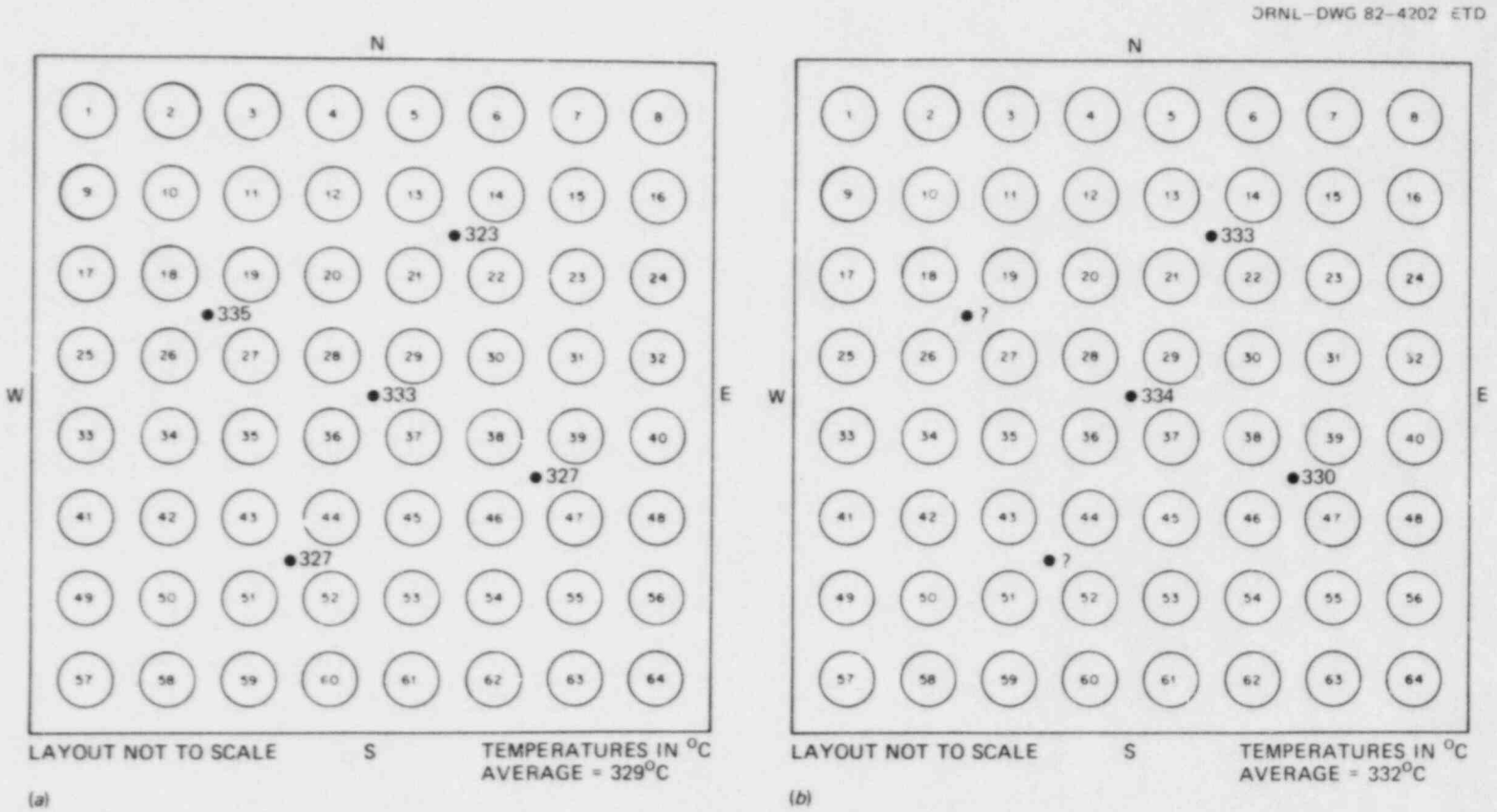

Fig. 14. Measured steam temperatures 1.0 s before power-on. (*a*) Inlet steam at 107-cm elevation and (*b*) outlet steam at 3-cm elevation.

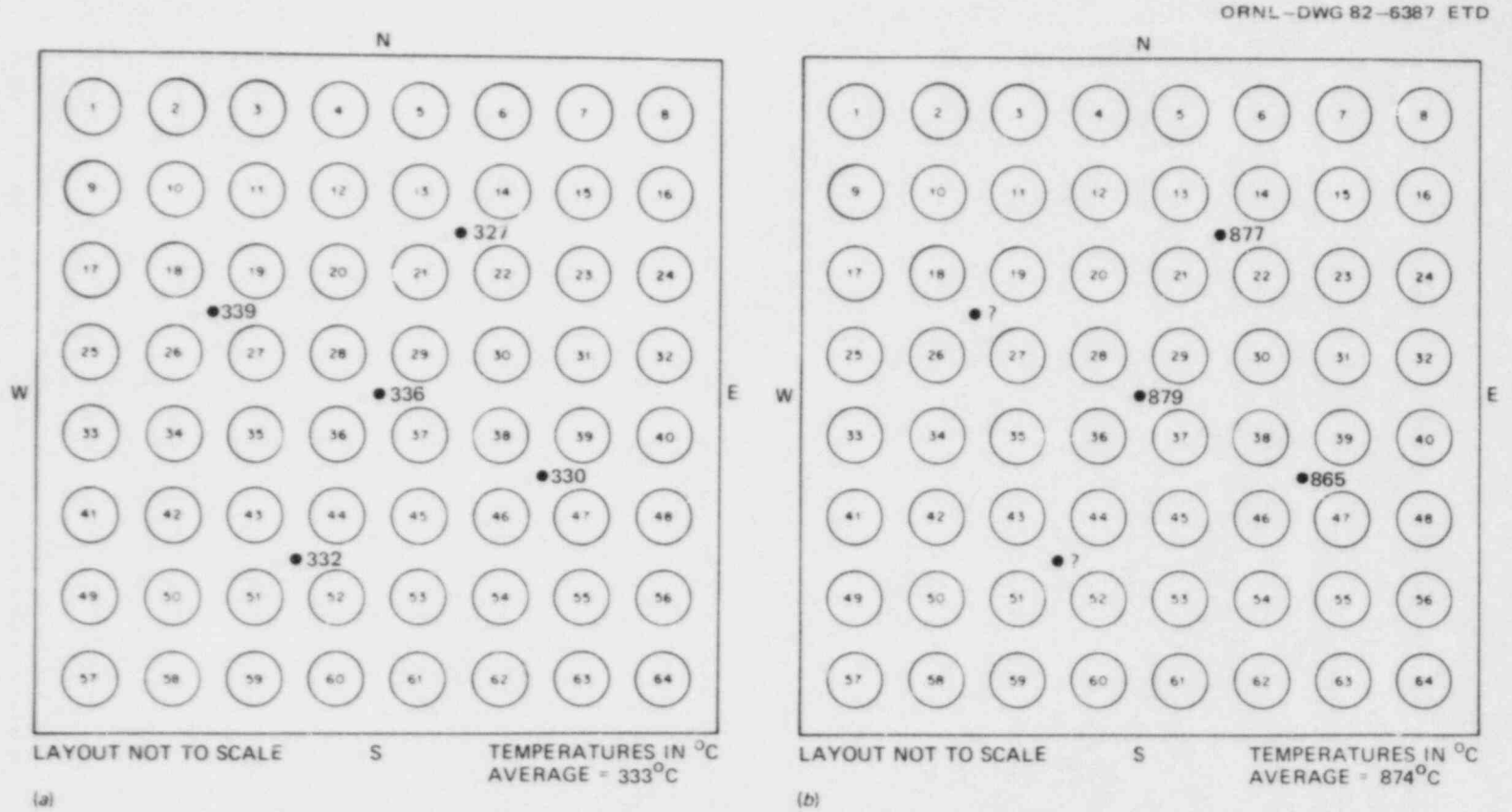

Fig. 15. Measured steam temperatures 1.0 s before the first tube burst. (*a*) Inlet steam at 107-cm elevation and (*b*) outlet steam at 3-cm elevation.

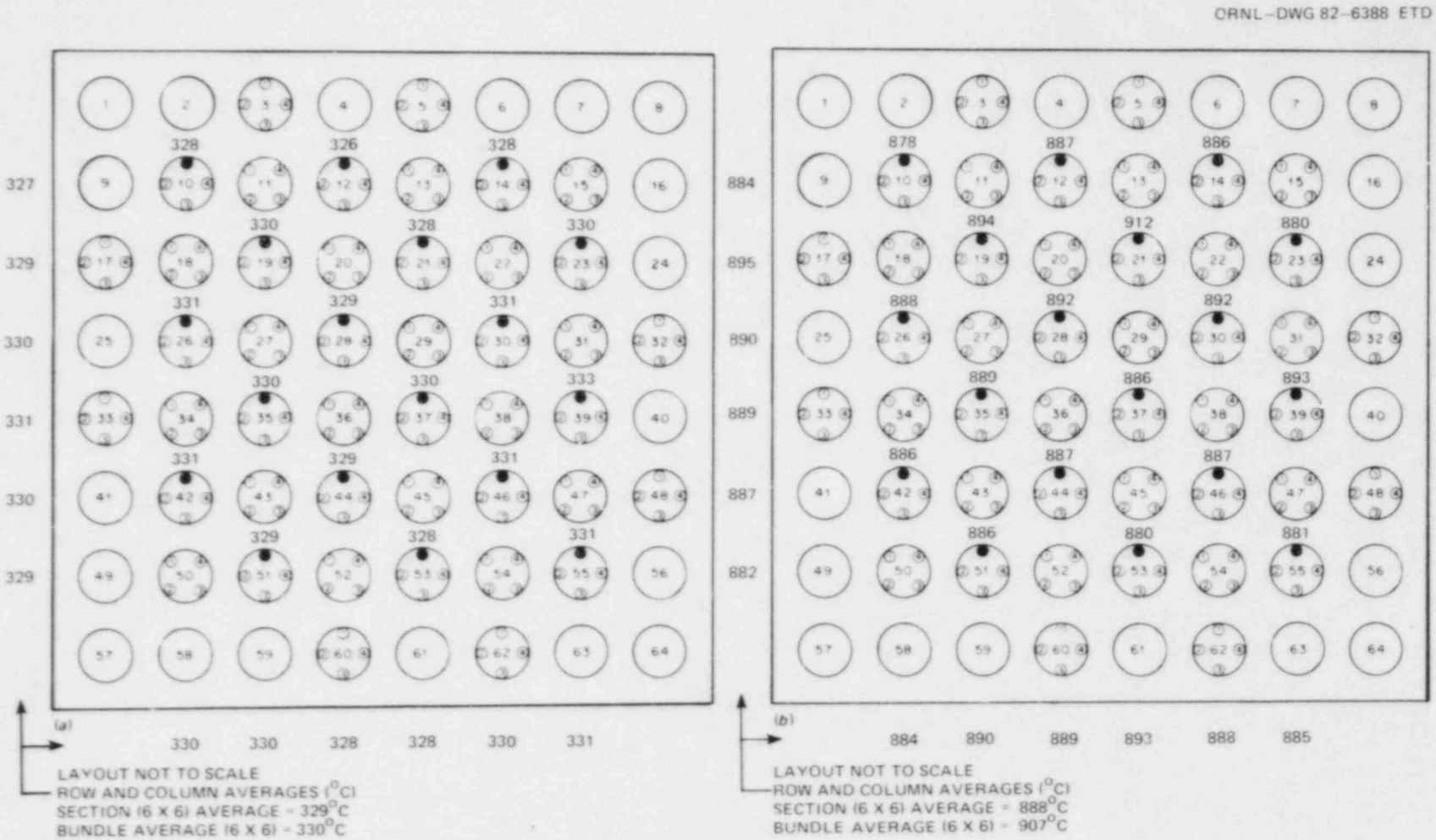

Fig. 16. Cladding temperatures measured at 84-cm elevation (*a*) 1.0 s before power-on and (*b*) 1.0 s before first tube burst.

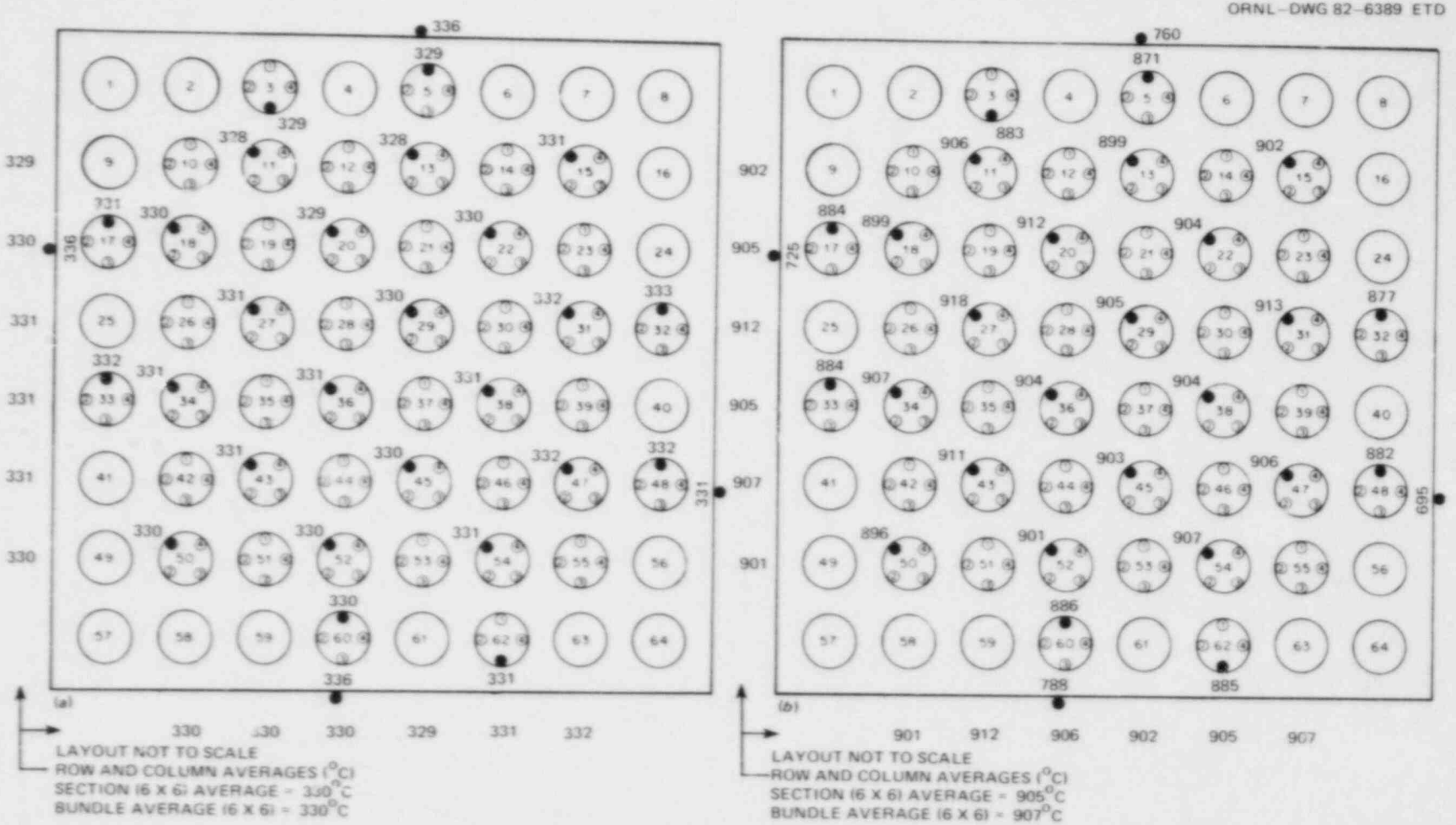

Fig. 17. Cladding temperatures measured at 76-cm elevation (*a*) 1.0 s before power-on and (*b*) 1.0 s before first tube burst.

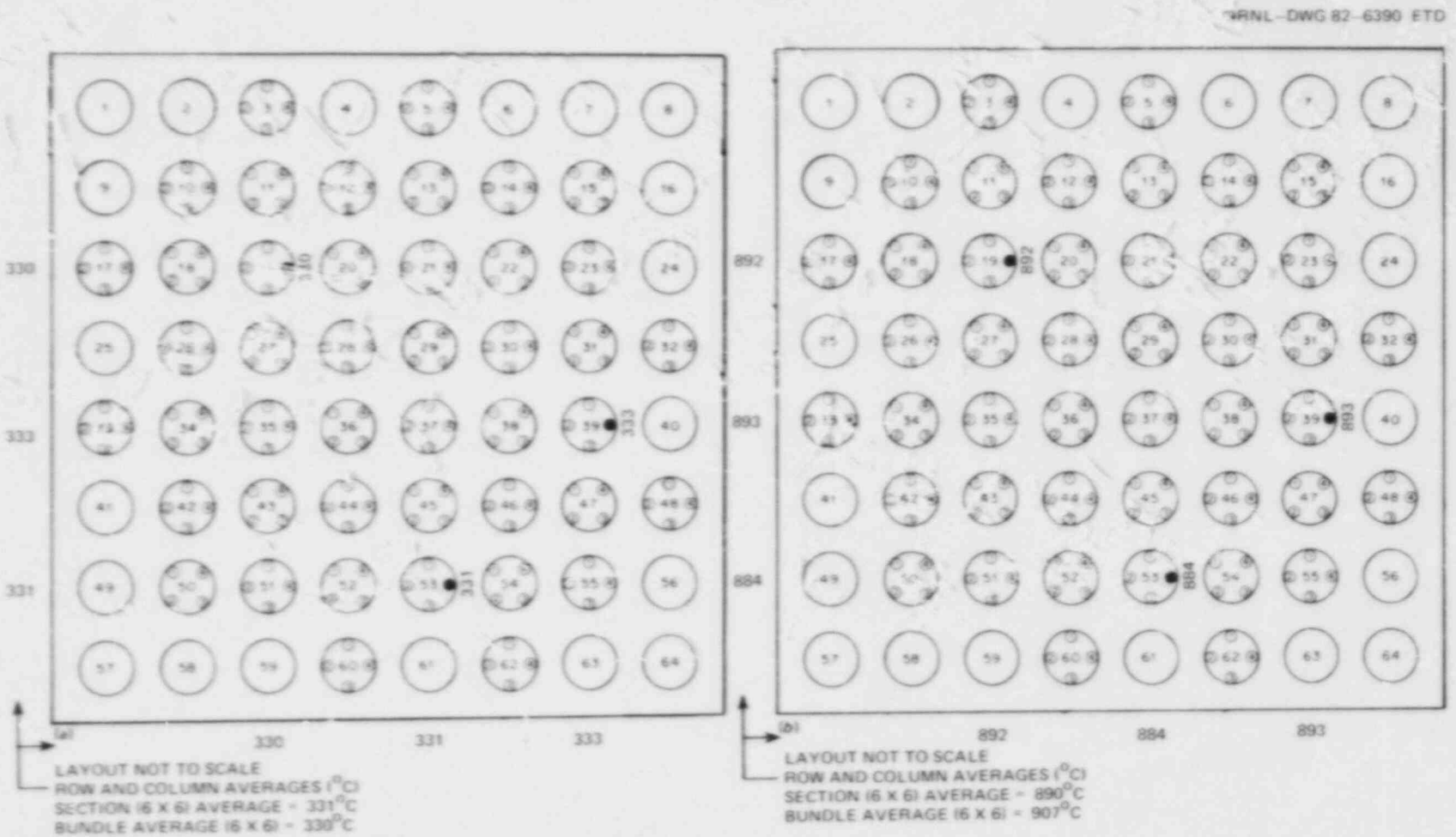

Fig. 18. Cladding temperatures measured at upper grid (66-cm) elevation (*a*) 1.0 s before power-on and (*b*) 1.0 s before first tube burst.

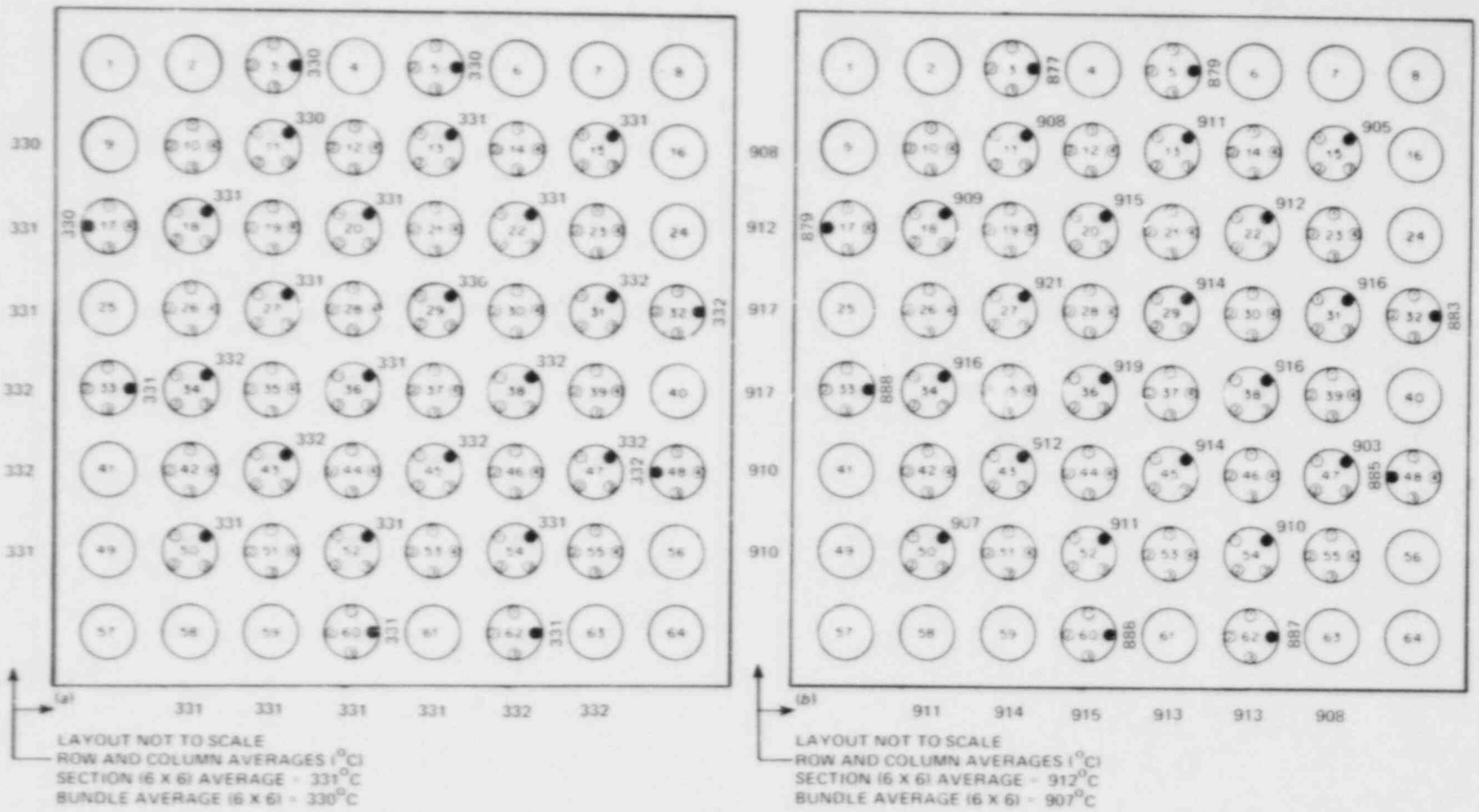

Fig. 19. Cladding temperatures measured at 56-cm elevation (*a*) 1.0 s before power-on and (*b*) 1.0 s before first tube burst.

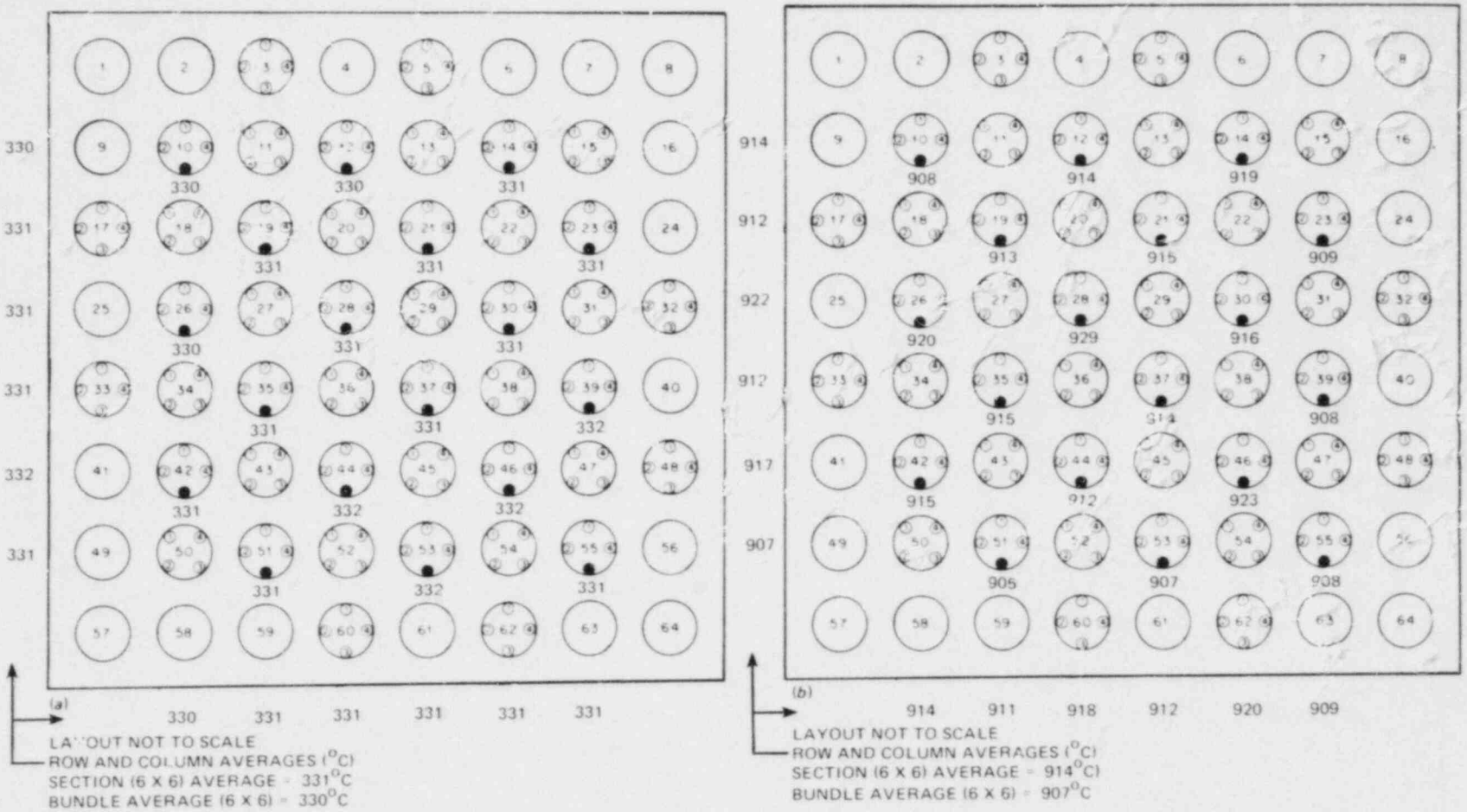

Fig. 20. Cladding temperatures measured at 48-cm elevation (*a*) 1.0 s before power-on and (*b*) 1.0 s before first tube burst.

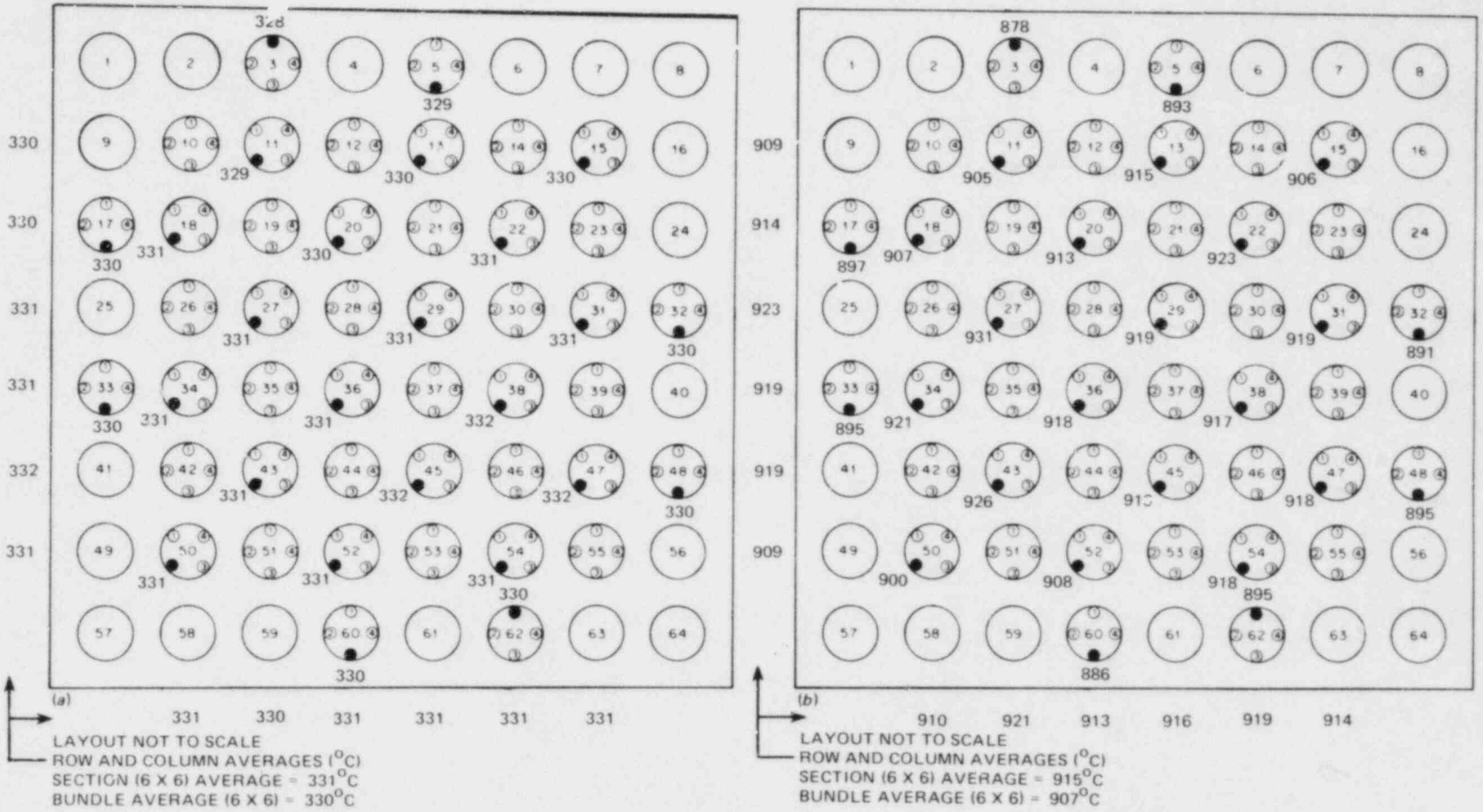

Fig. 21. Cladding temperatures measured at 38-cm elevation (*a*) 1.0 s before power-on and (*b*) 1.0 s before first tube burst.

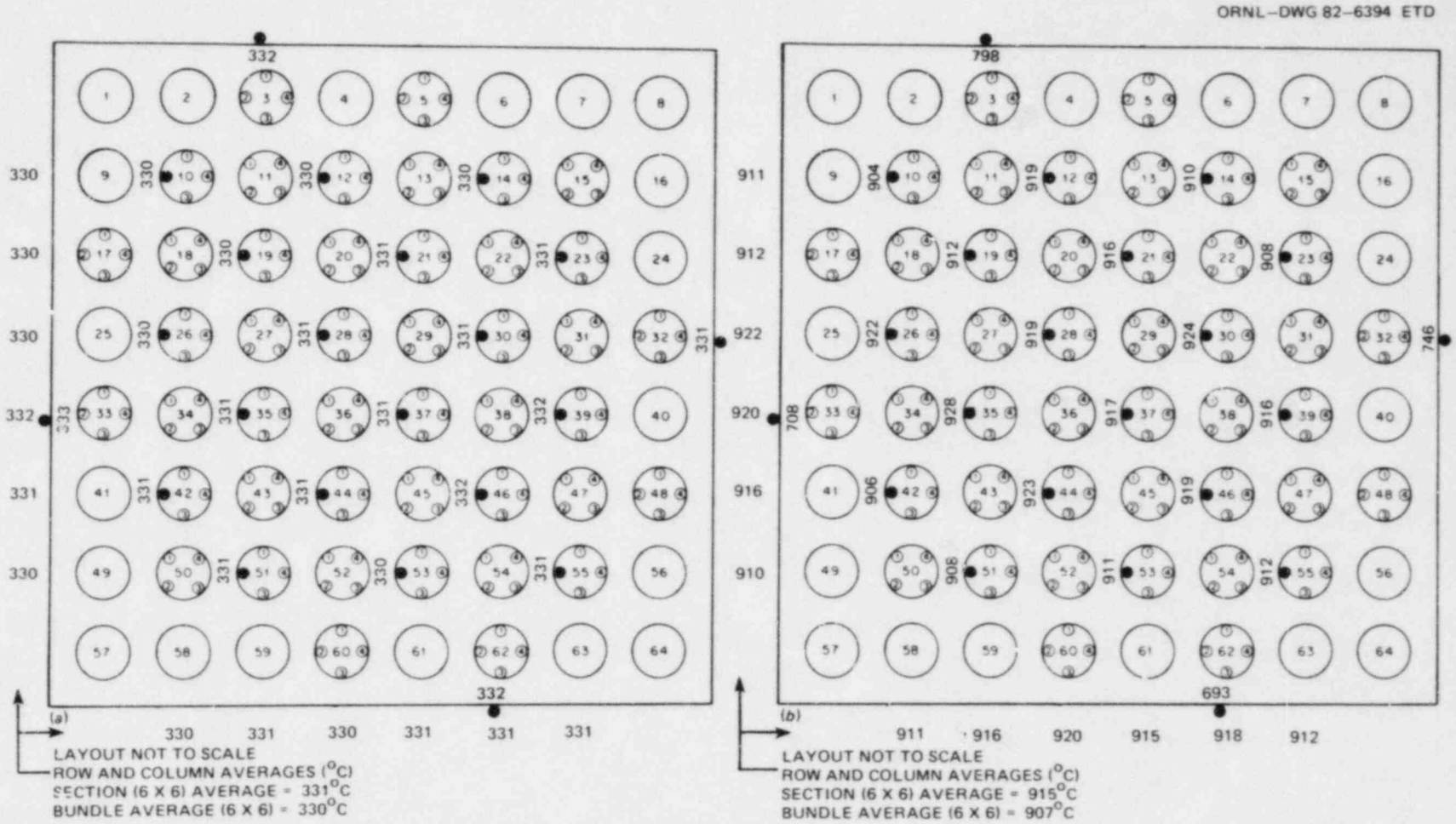

Fig. 22. Cladding temperatures measured at 28-cm elevation (*a*) 1.0 s before power-on and (*b*) 1.0 s before first tube burst.

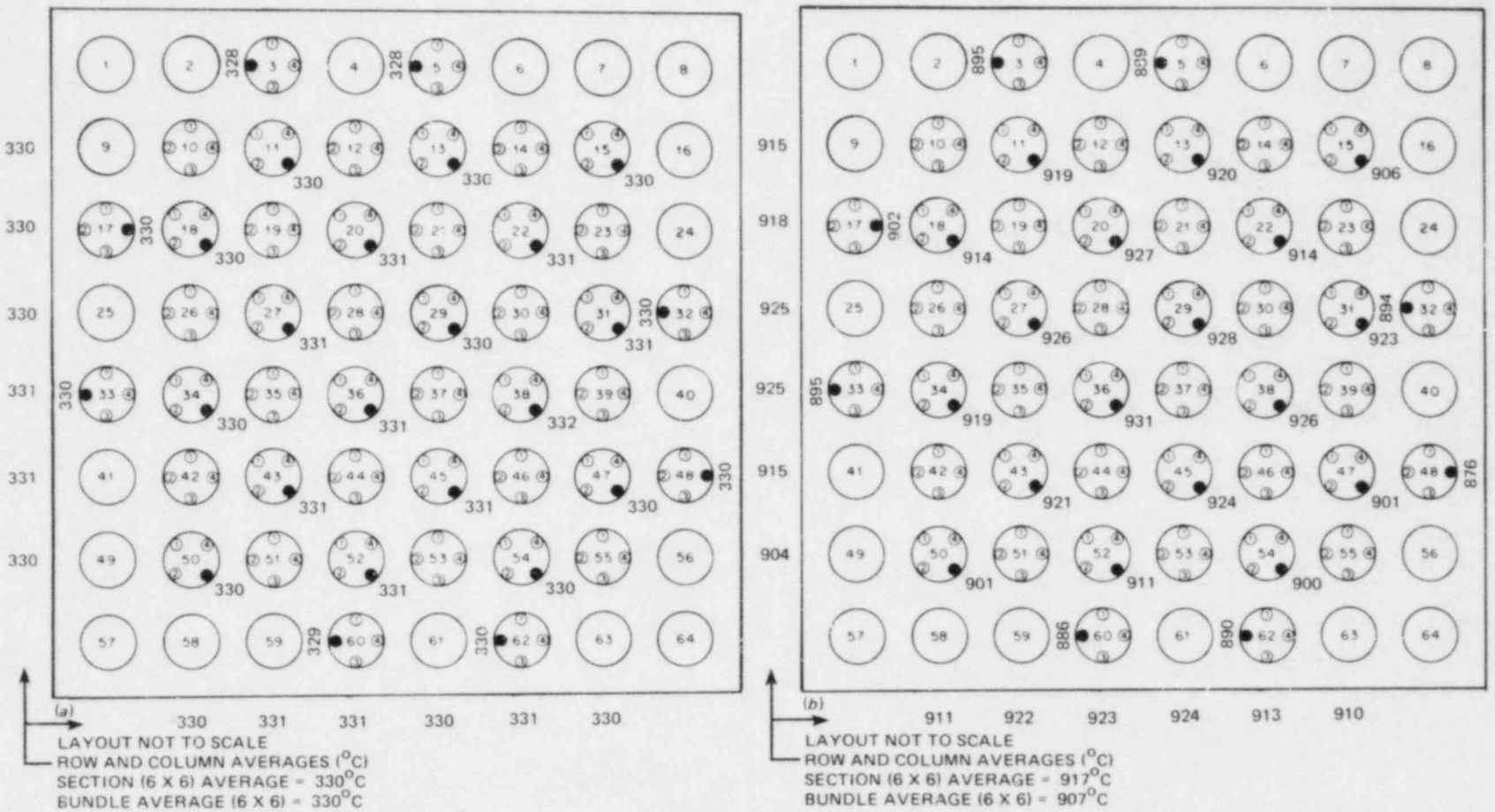

Fig. 23. Cladding temperatures measured at 20-cm elevation (*a*) 1.0 s before power-on and (*b*) 1.0 s before first tube burst.

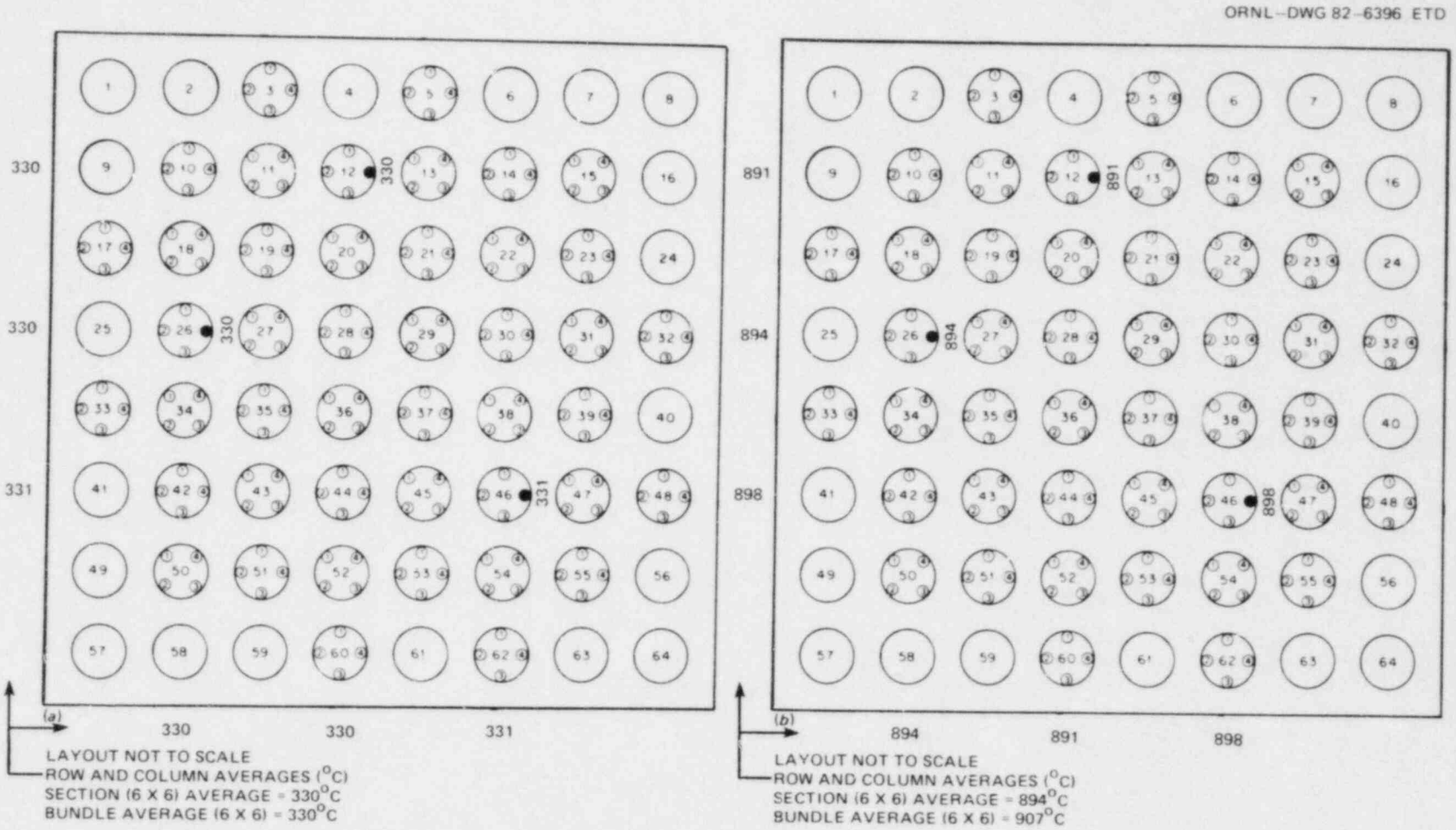

Fig. 24. Cladding temperatures measured at lower grid (10-cm) elevation (*a*) 1.0 s before power-on and (*b*) 1.0 s before first tube burst.

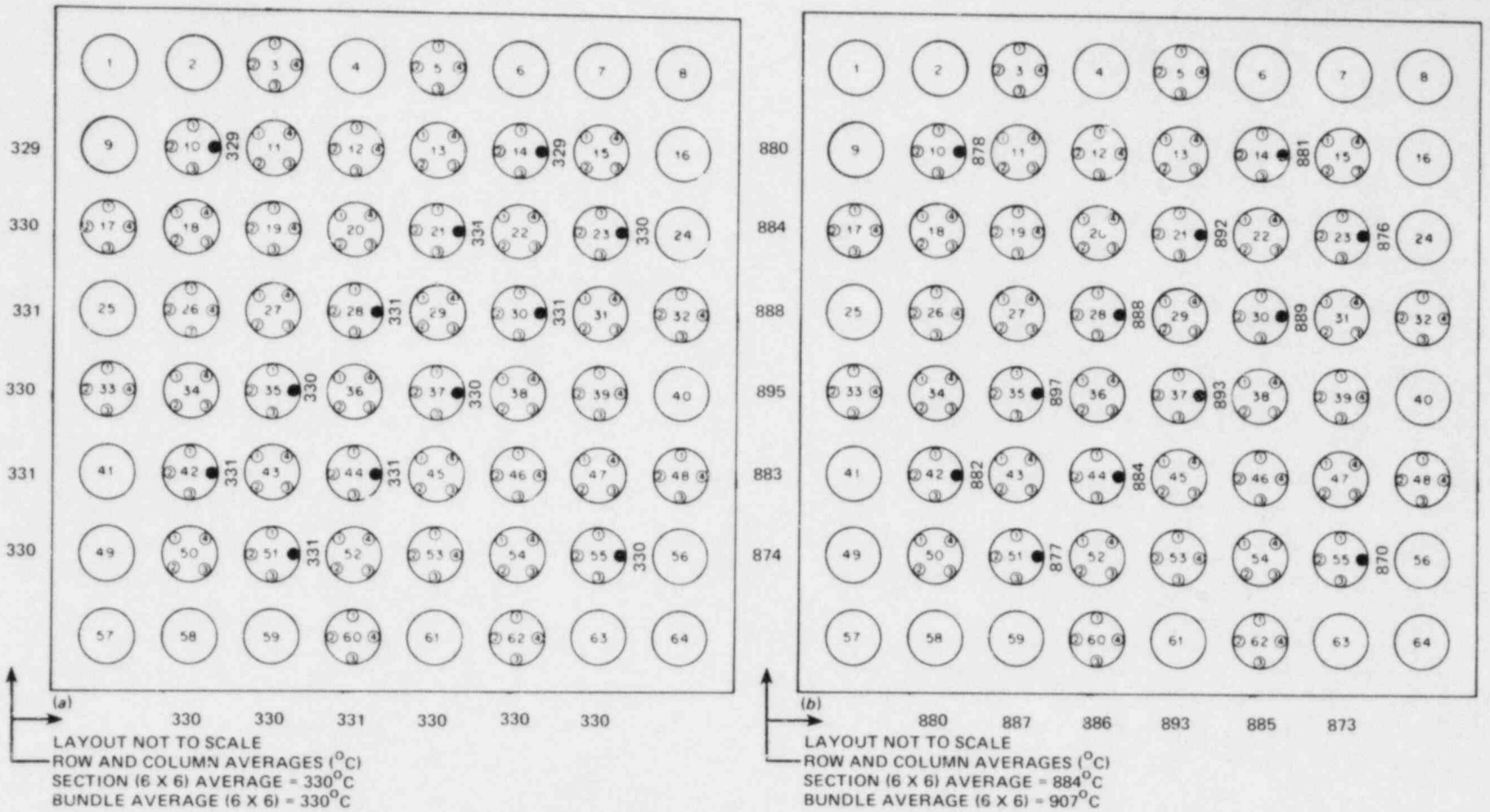

Fig. 25. Cladding temperatures measured at 5-cm elevation (*a*) 1.0 s before power-on and (*b*) 1.0 s before first tube burst.

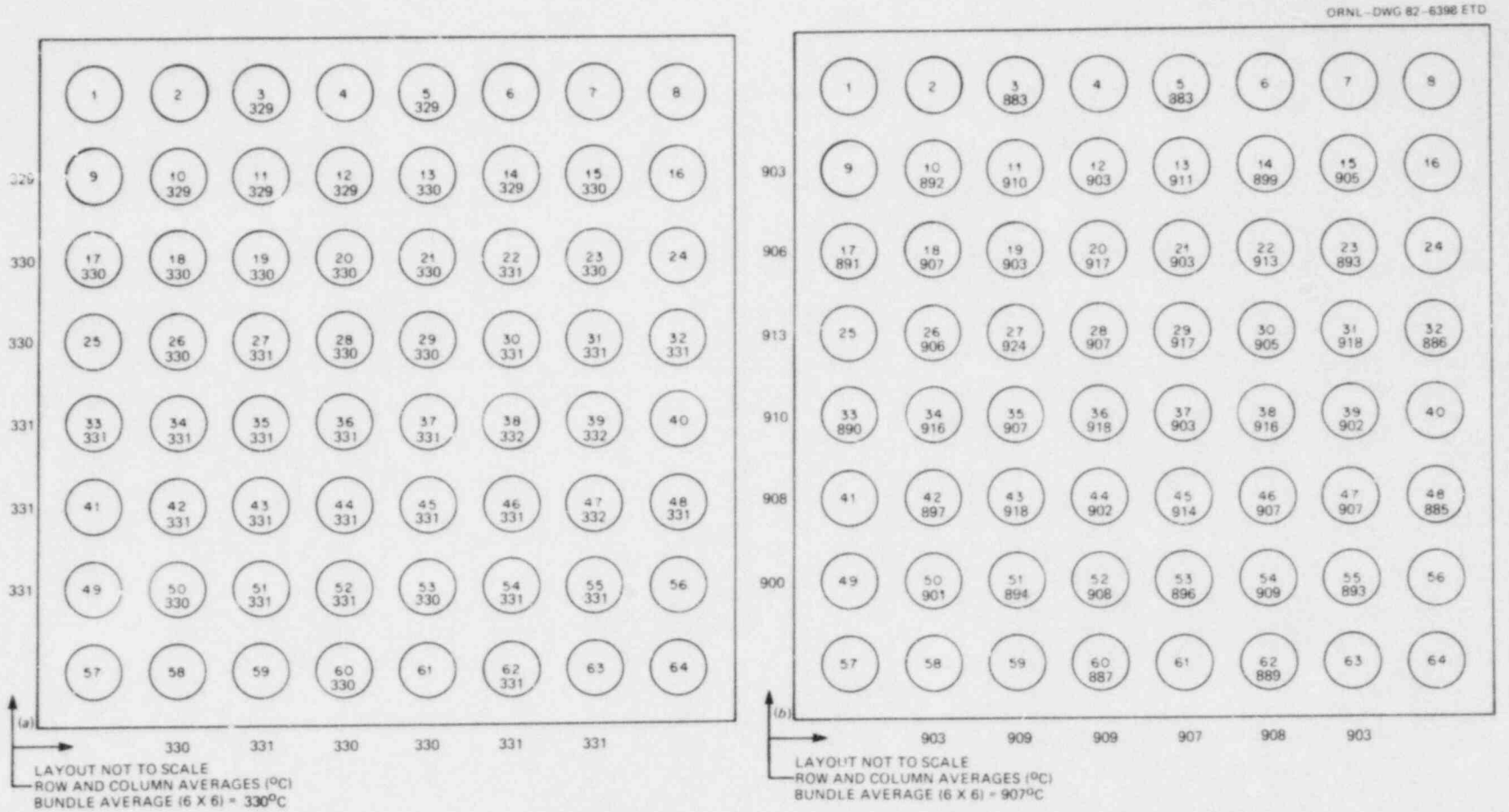

Fig. 26. Simulator-averaged cladding temperature measurements (*a*) 1.0 s before power-on and (*b*) 1.0 s before first tube burst.

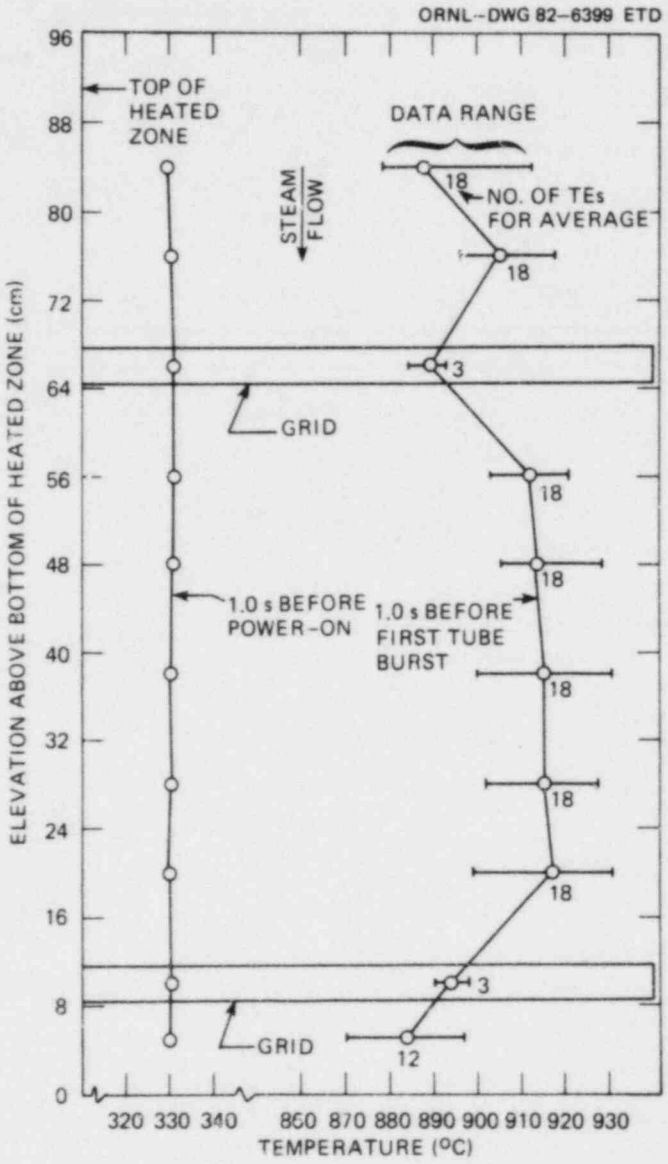

Fig. 27. Axial temperature profile of inner 6 × 6 array of B-6 measured 1.0 s before power-on and 1.0 s before first tube burst.

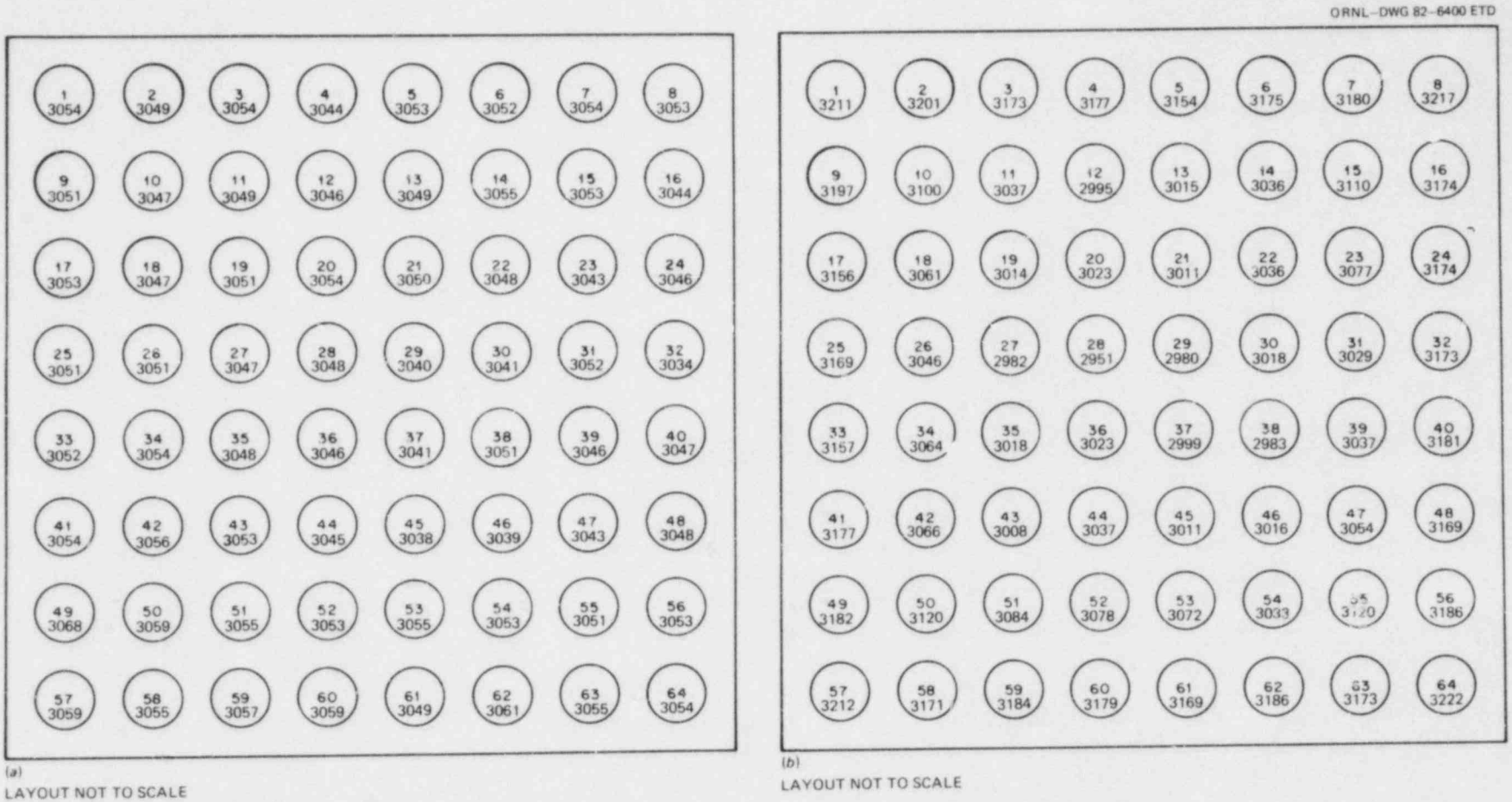

Fig. 28. Differential pressures (kPa) measured (*a*) 1.0 s before power-on and (*b*) 1.0 s before first tube burst.

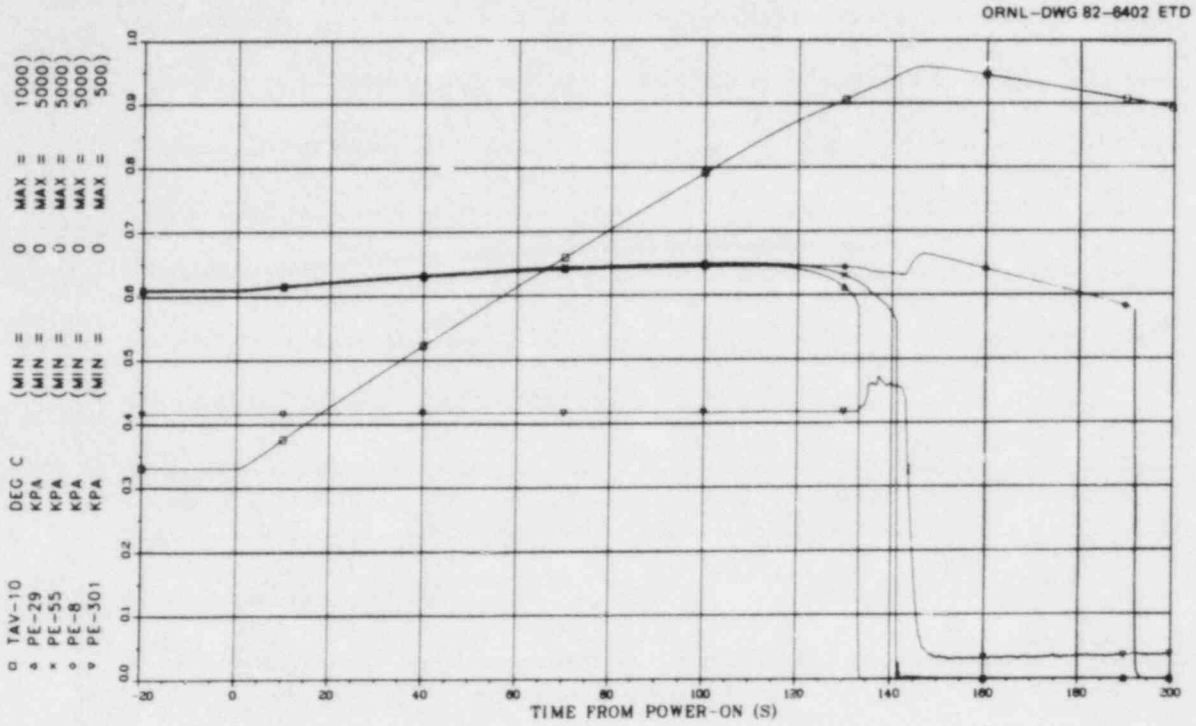

Fig. 29. Typical temperature and pressure behavior during B-6 test.

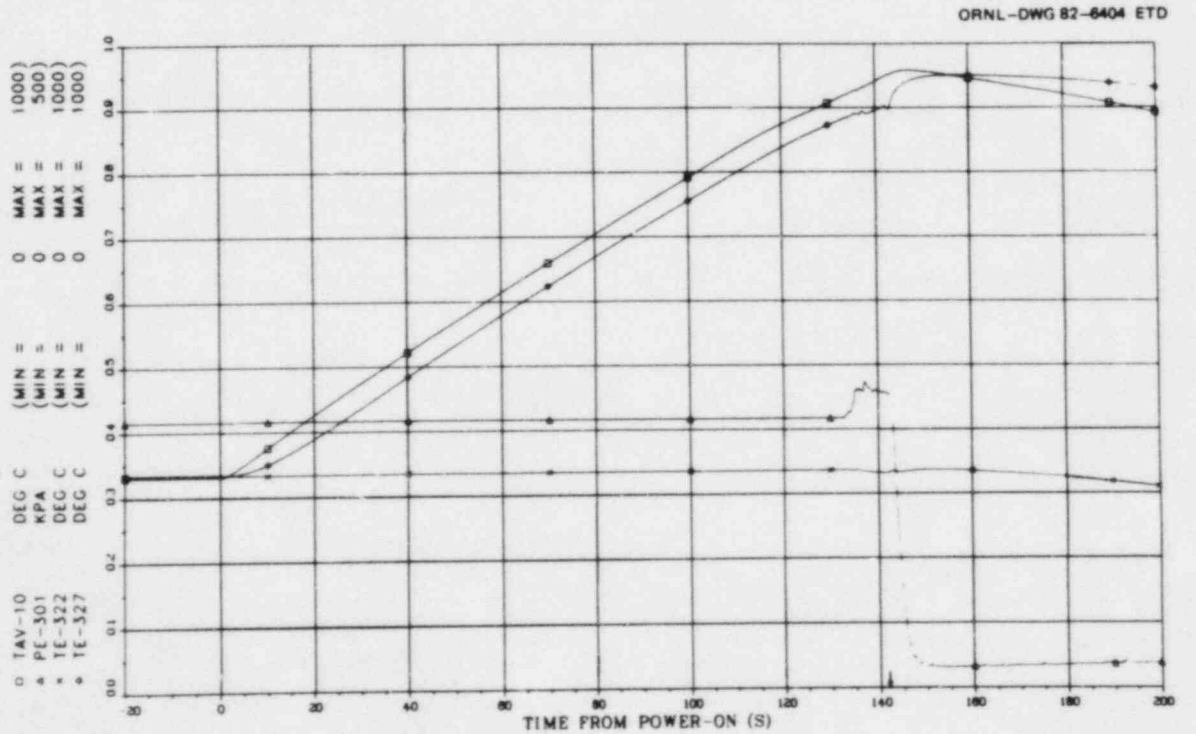

Fig. 30. Typical steam-related parameters measured during B-6 test.

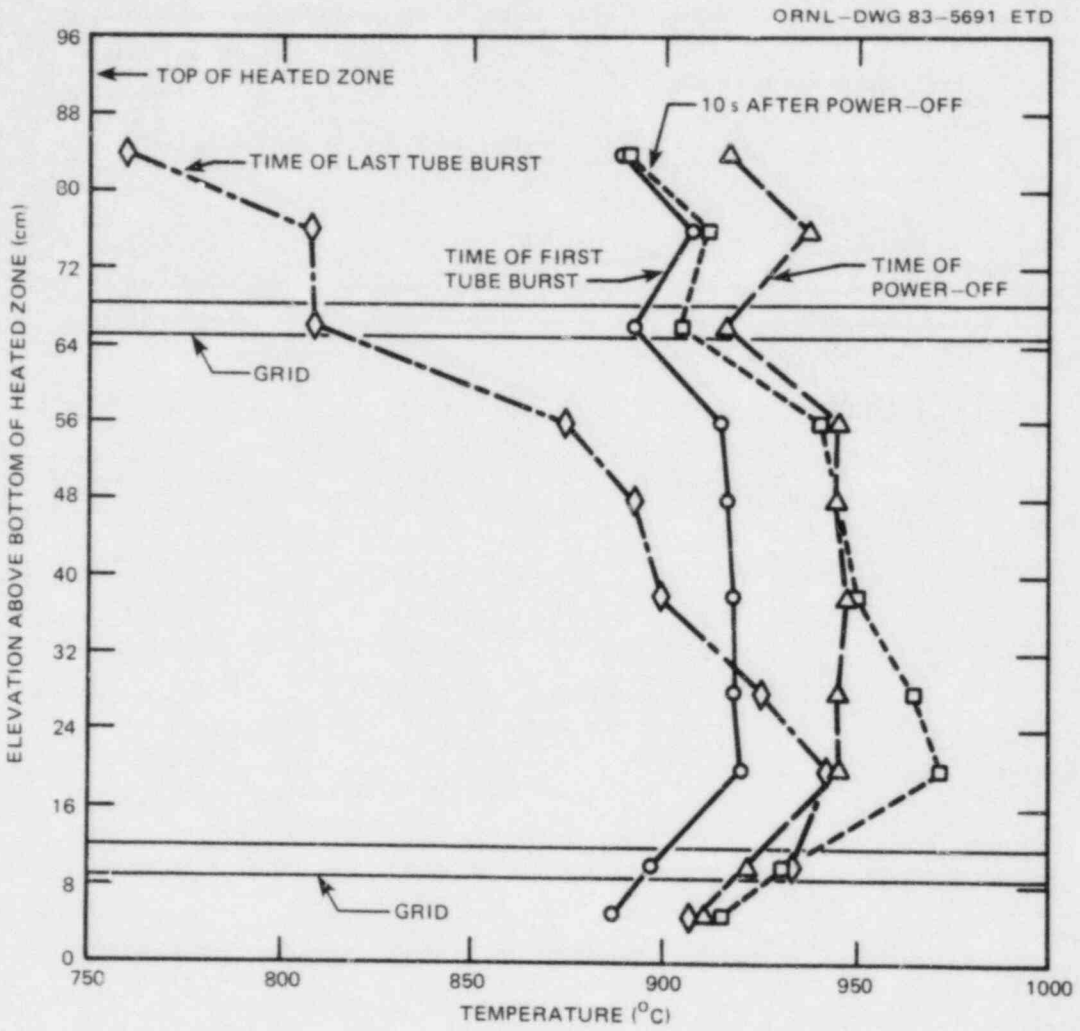

Fig. 31. Axial temperature profiles of inner 6 × 6 array of B-6 measured during time of tube bursts.

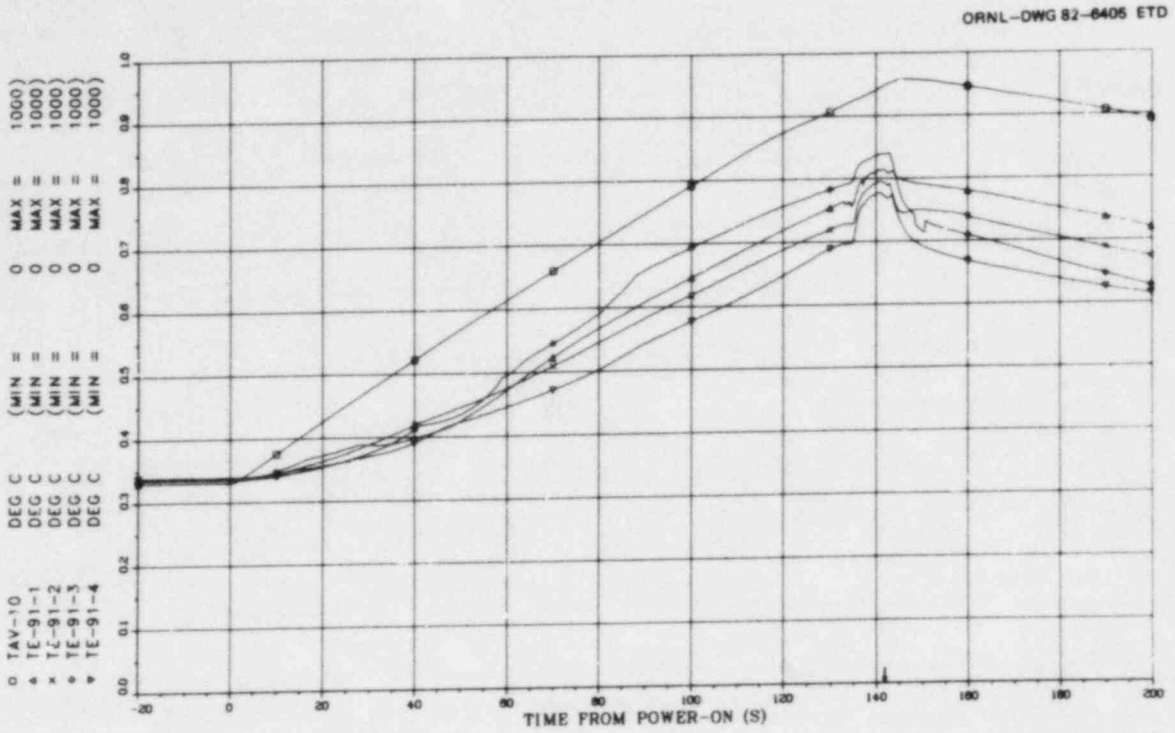

Fig. 32. Shroud temperature measurements at the 76-cm elevation.

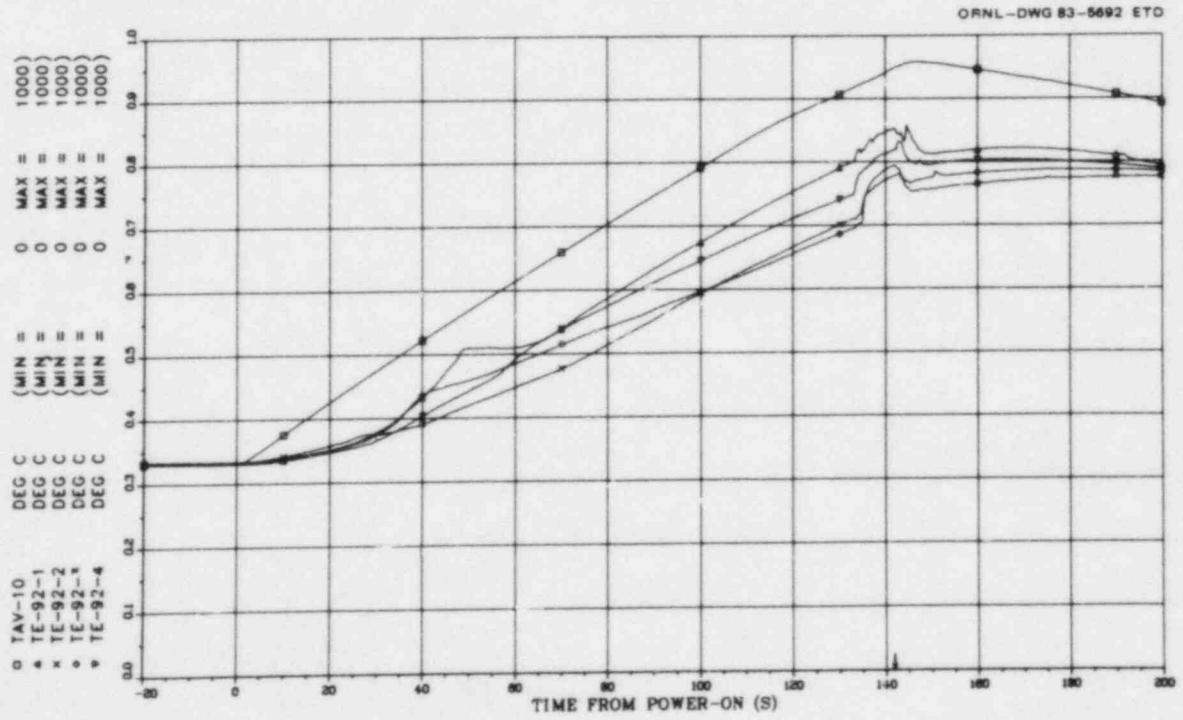

Fig. 33. Shroud temperature measurements at the 28-cm elevation.

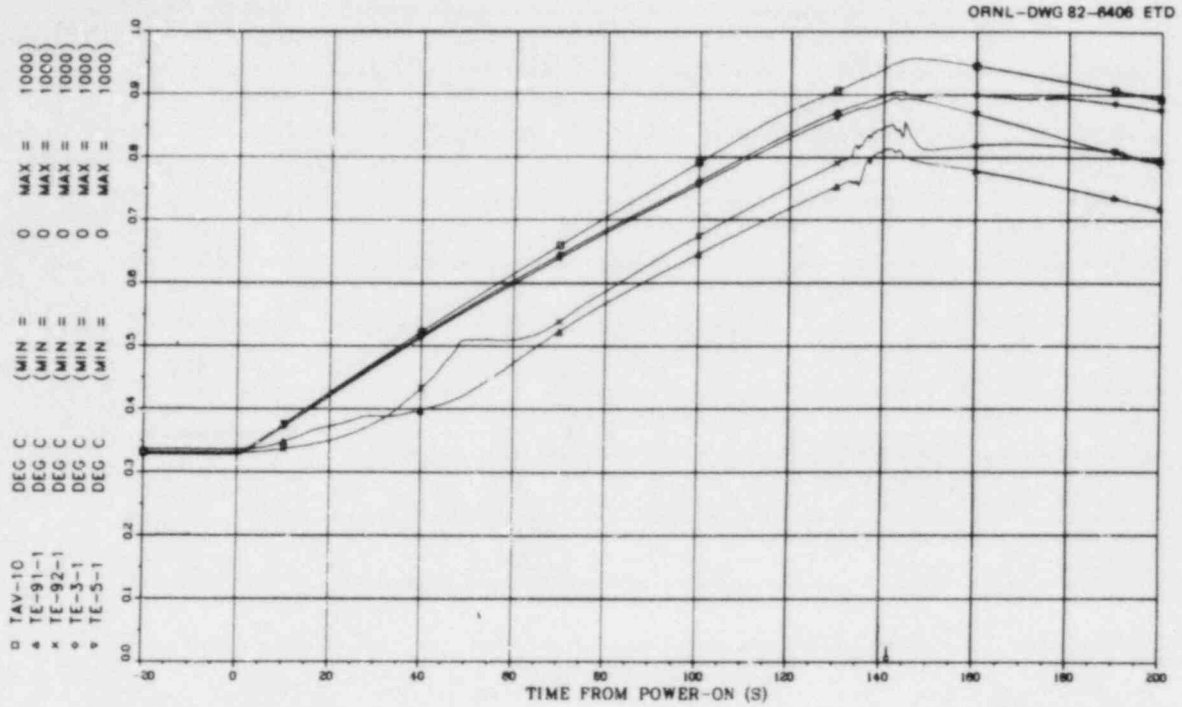

Fig. 34. Comparison of shroud and simulator temperature measurements on the north side of the array.

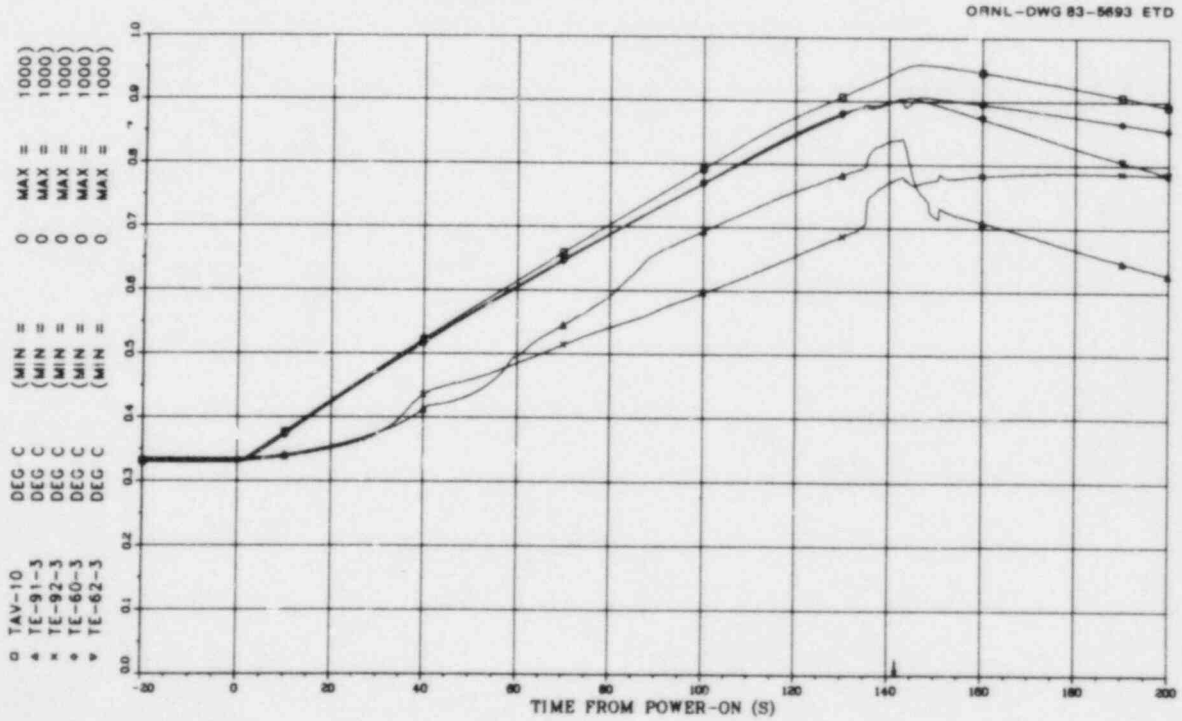

Fig. 35. Comparison of shroud and simulator temperature measurements on the south side of the array.

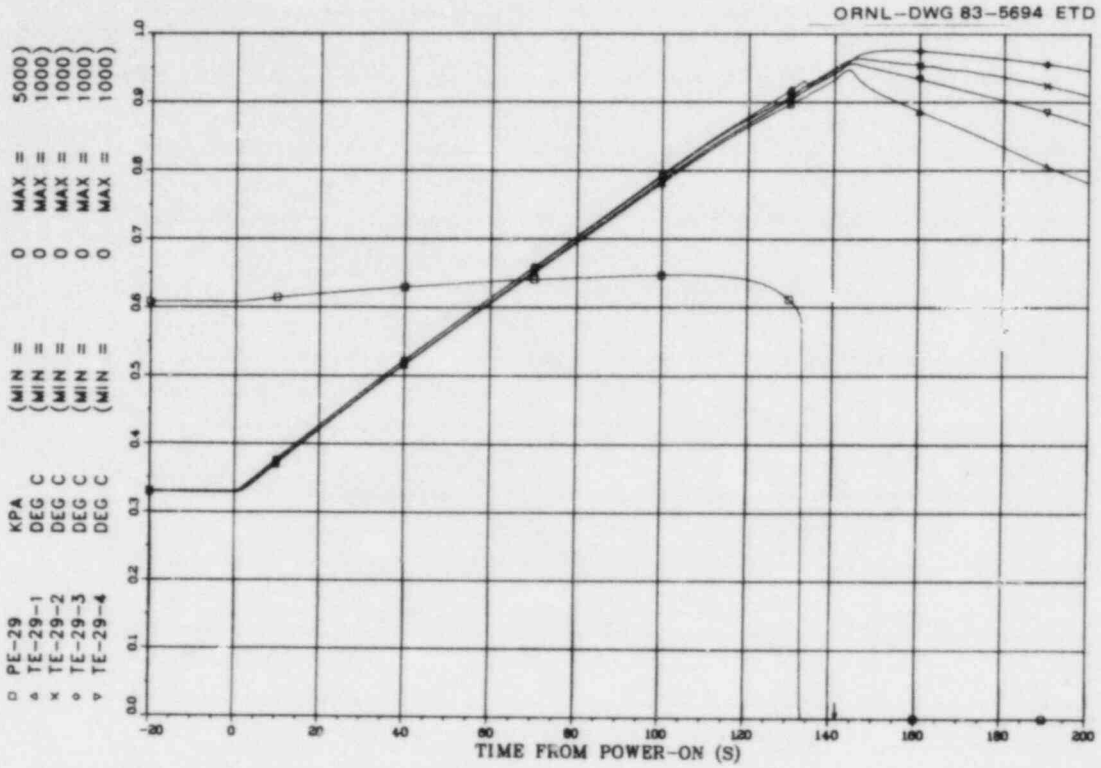

Fig. 36. Typical cladding pressure and temperature behavior for an interior simulator.

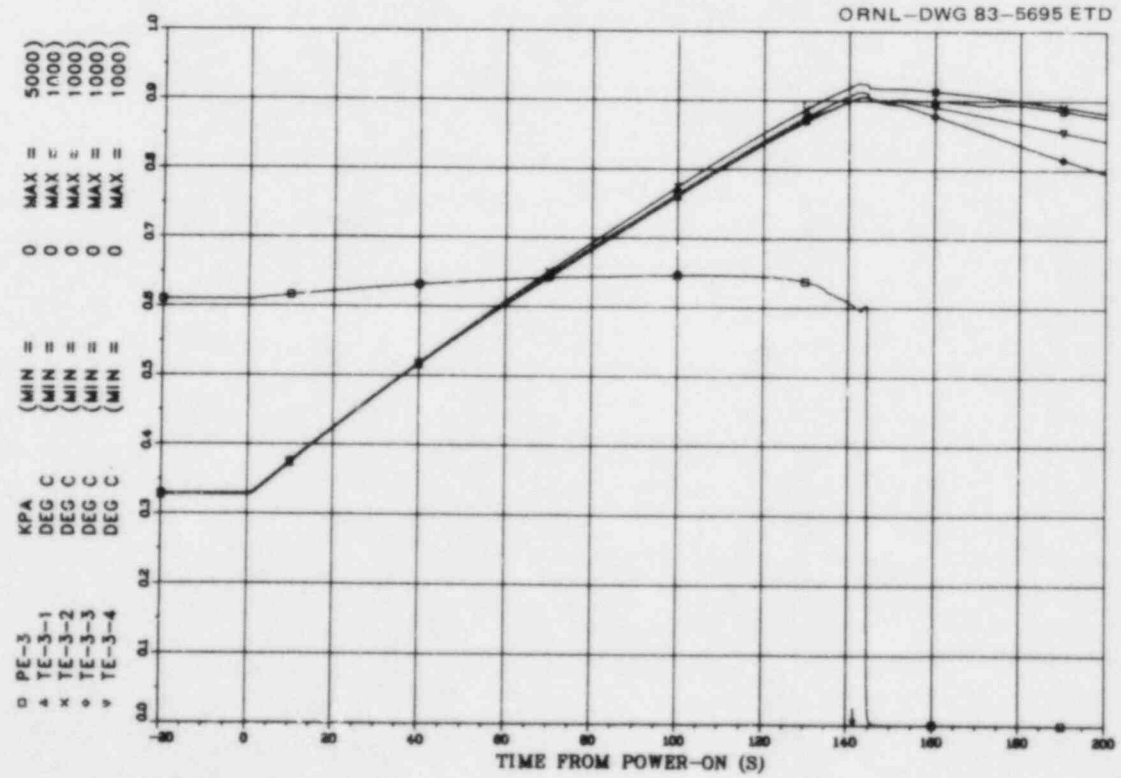

Fig. 37. Typical cladding pressure and temperature behavior for a fully instrumented exterior simulator.

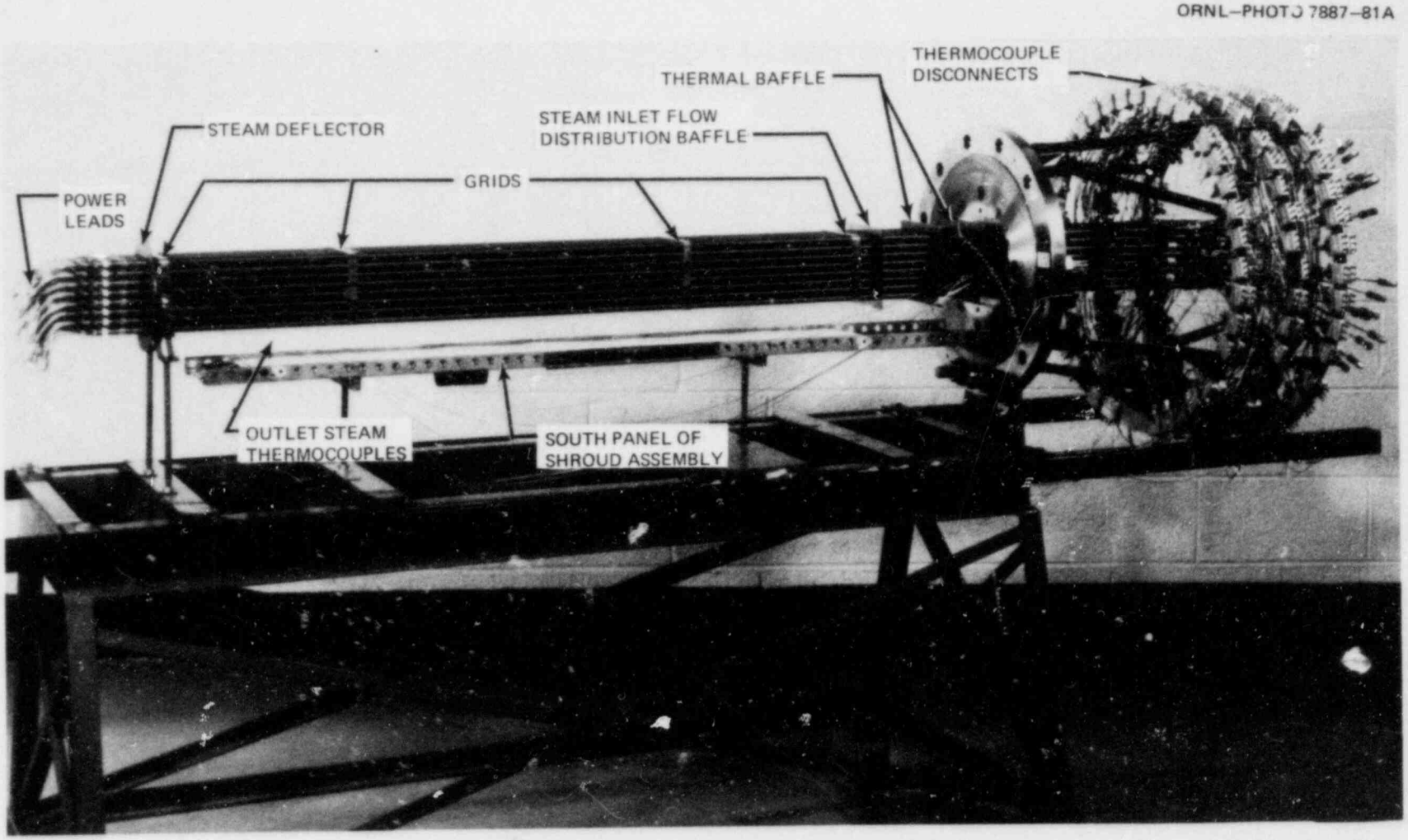

Fig. 38. Partially assembled B-6 test array.

ORNL-PHOTO 7467-80A

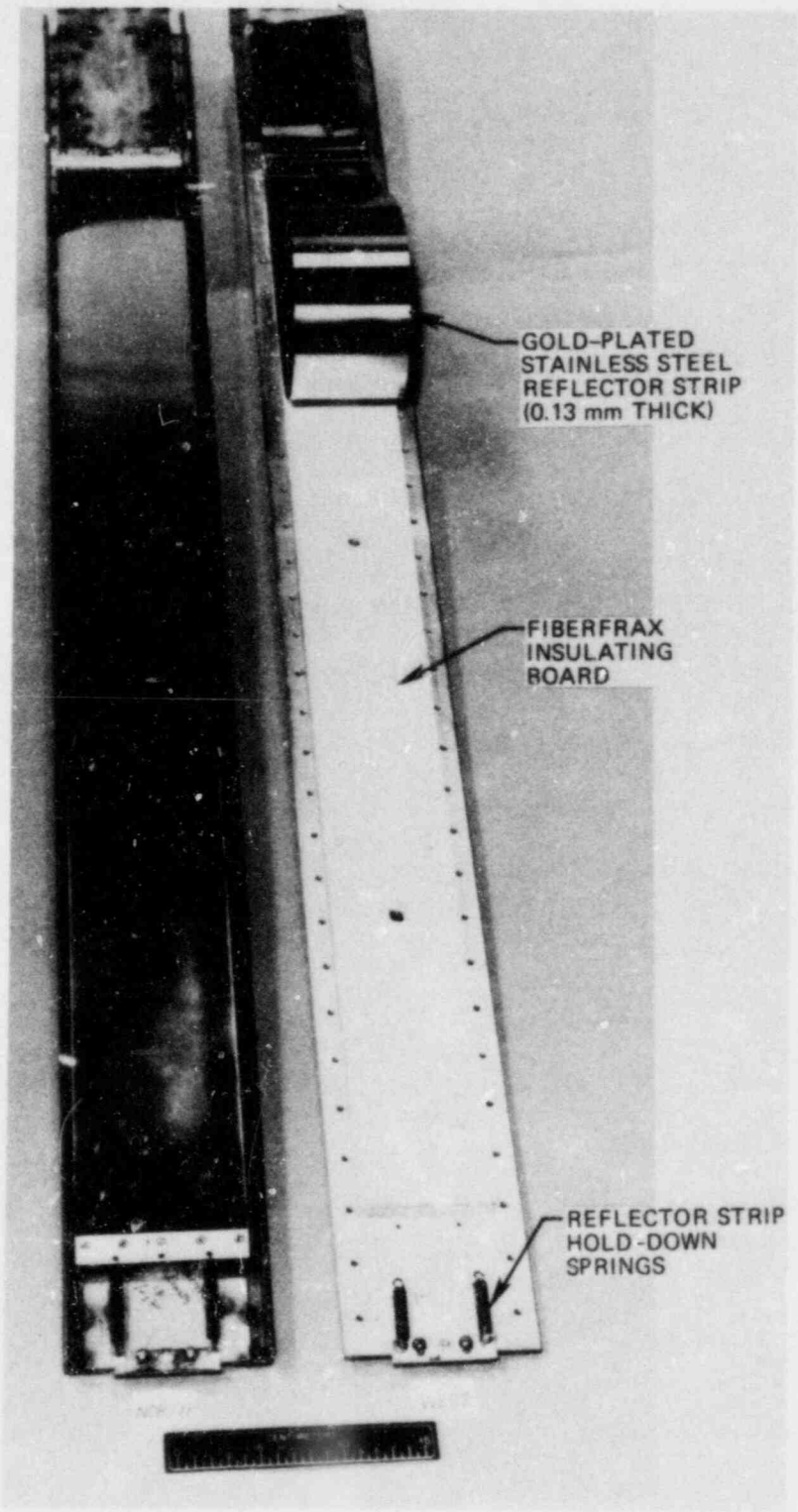

Fig. 39. Typical shroud panels from B-4 test shown with reflector strip folded back to illustrate construction details.

ORNL–PHOTO 7883–81A

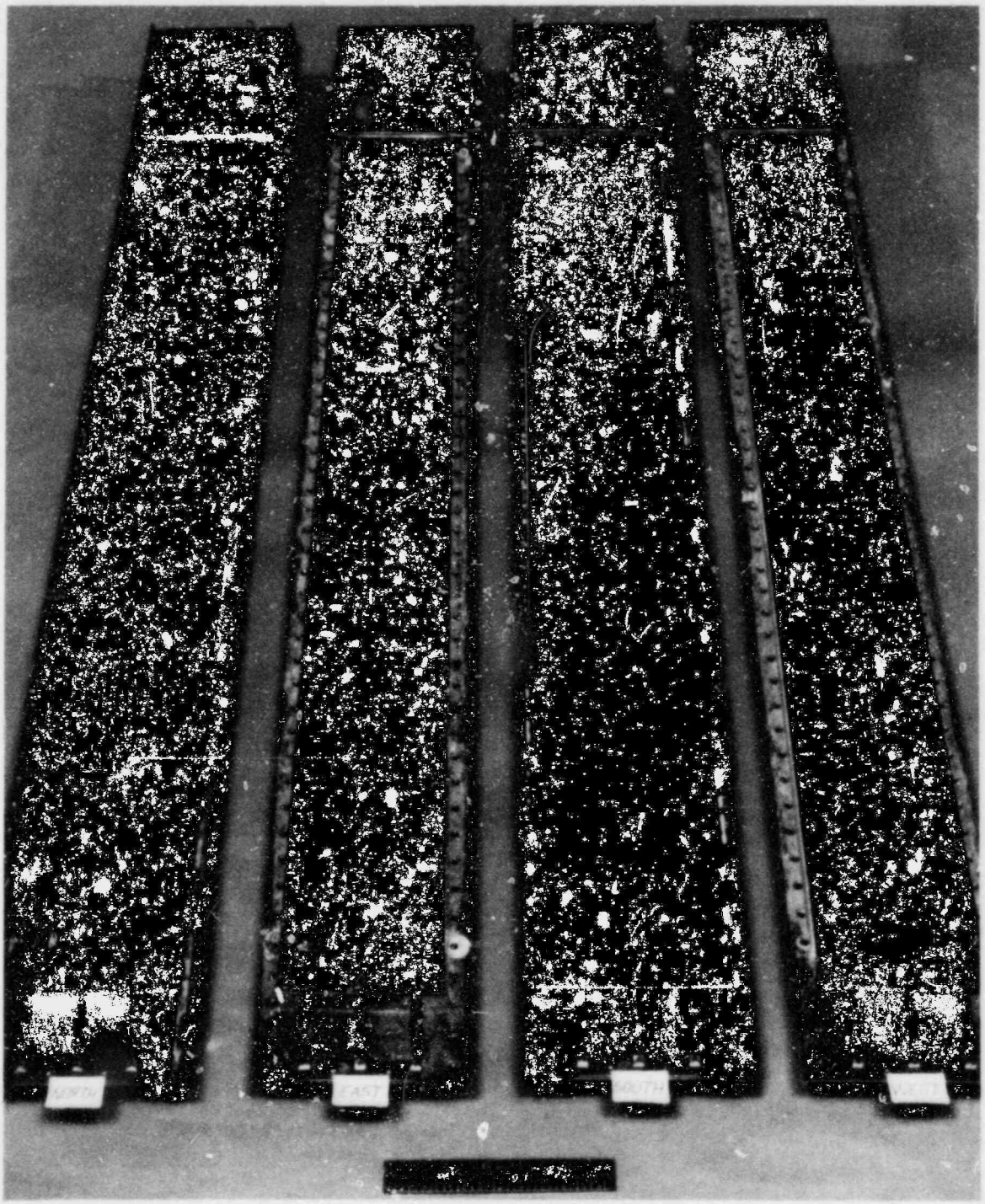

Fig. 40. Shroud panels with highly polished reflector strips in place prior to assembly around bundle.

ORNL–PHOTO 7886–81A

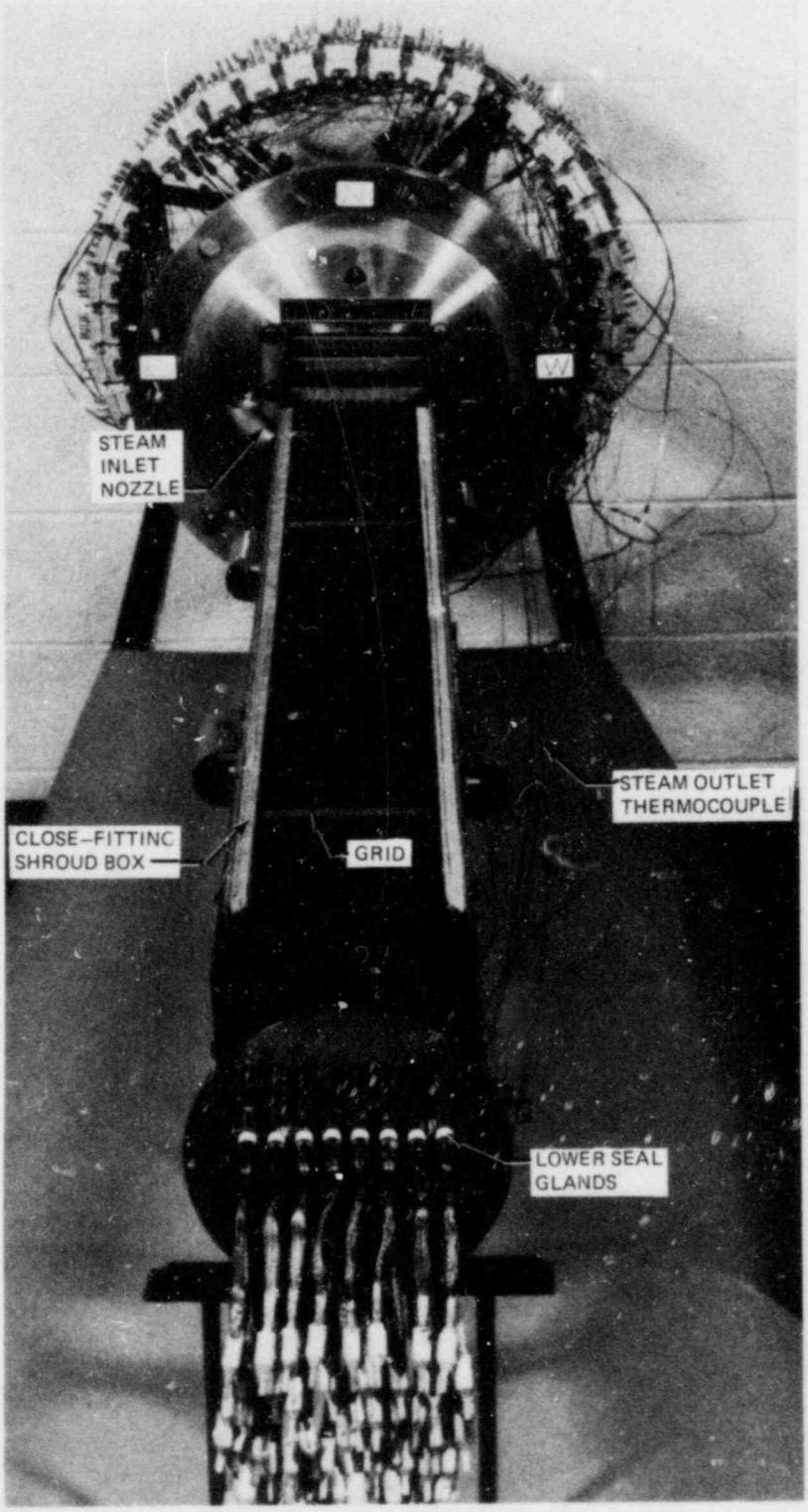

Fig. 41. Bundle before installation of north panel of shroud box.

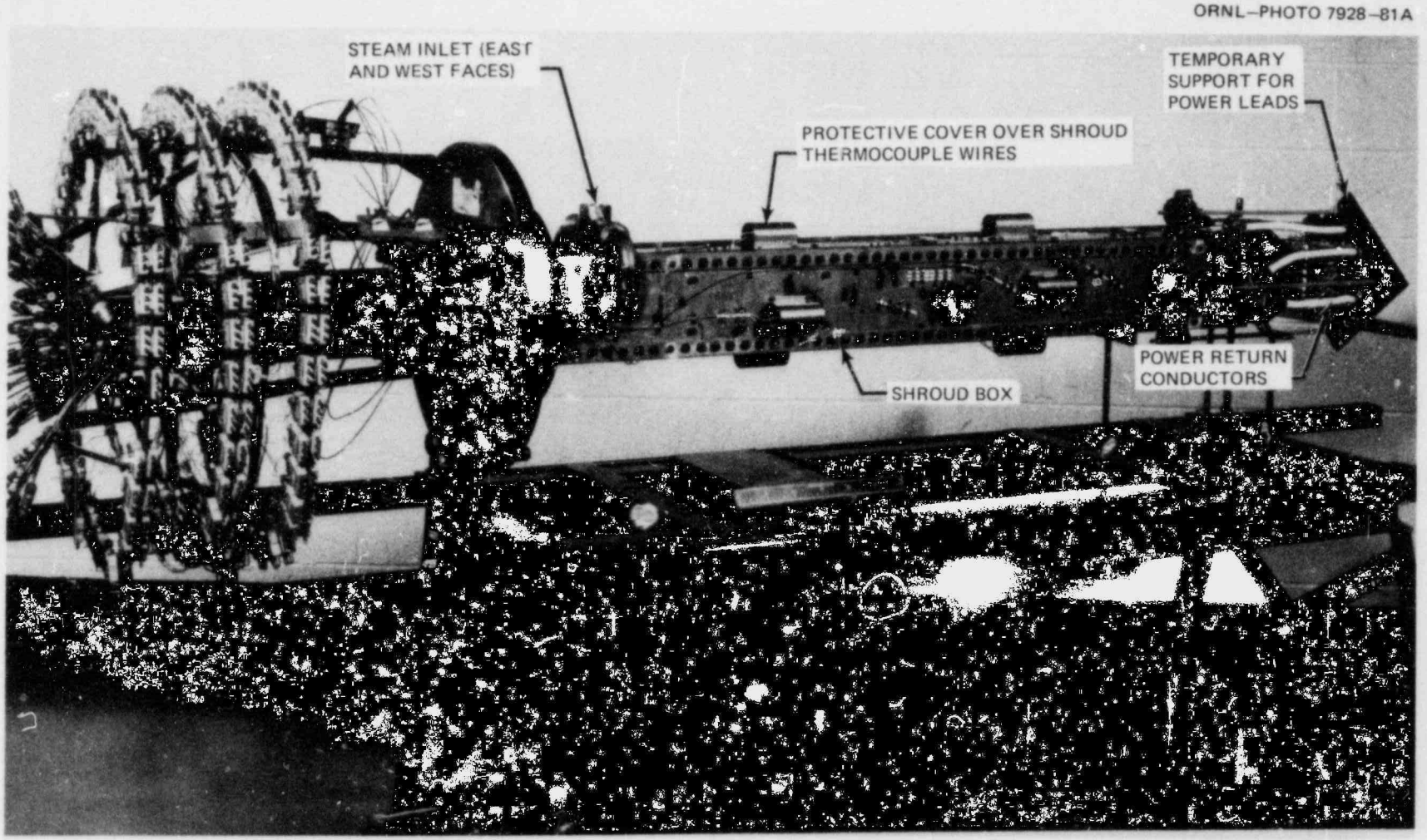

Fig. 42. Completely assembled B-6 test array.

ORNL-PHOTO 7463-80A

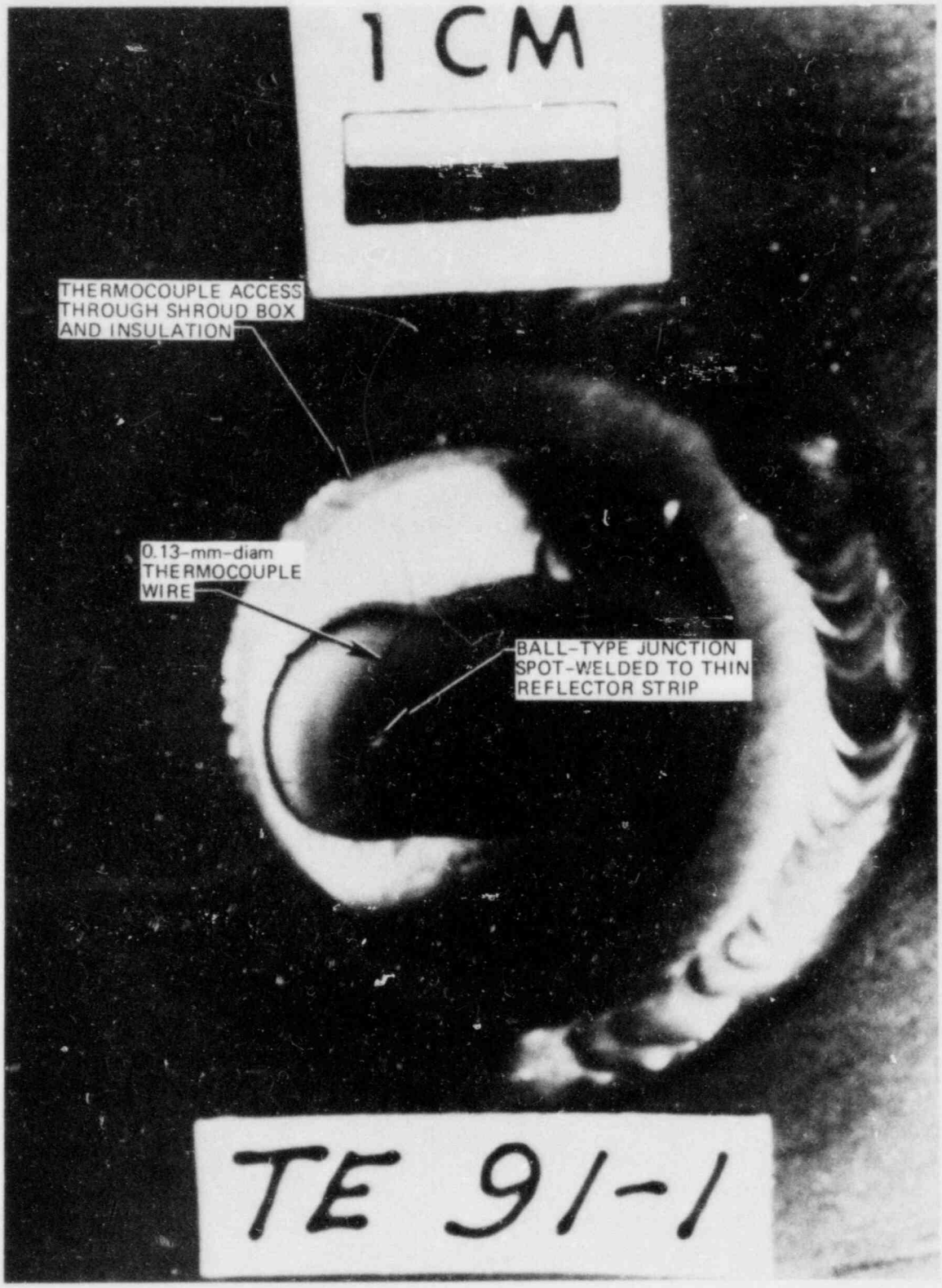

Fig. 43. Typical shroud thermocouple attachment.

ORNL–PHOTO 7931–81A

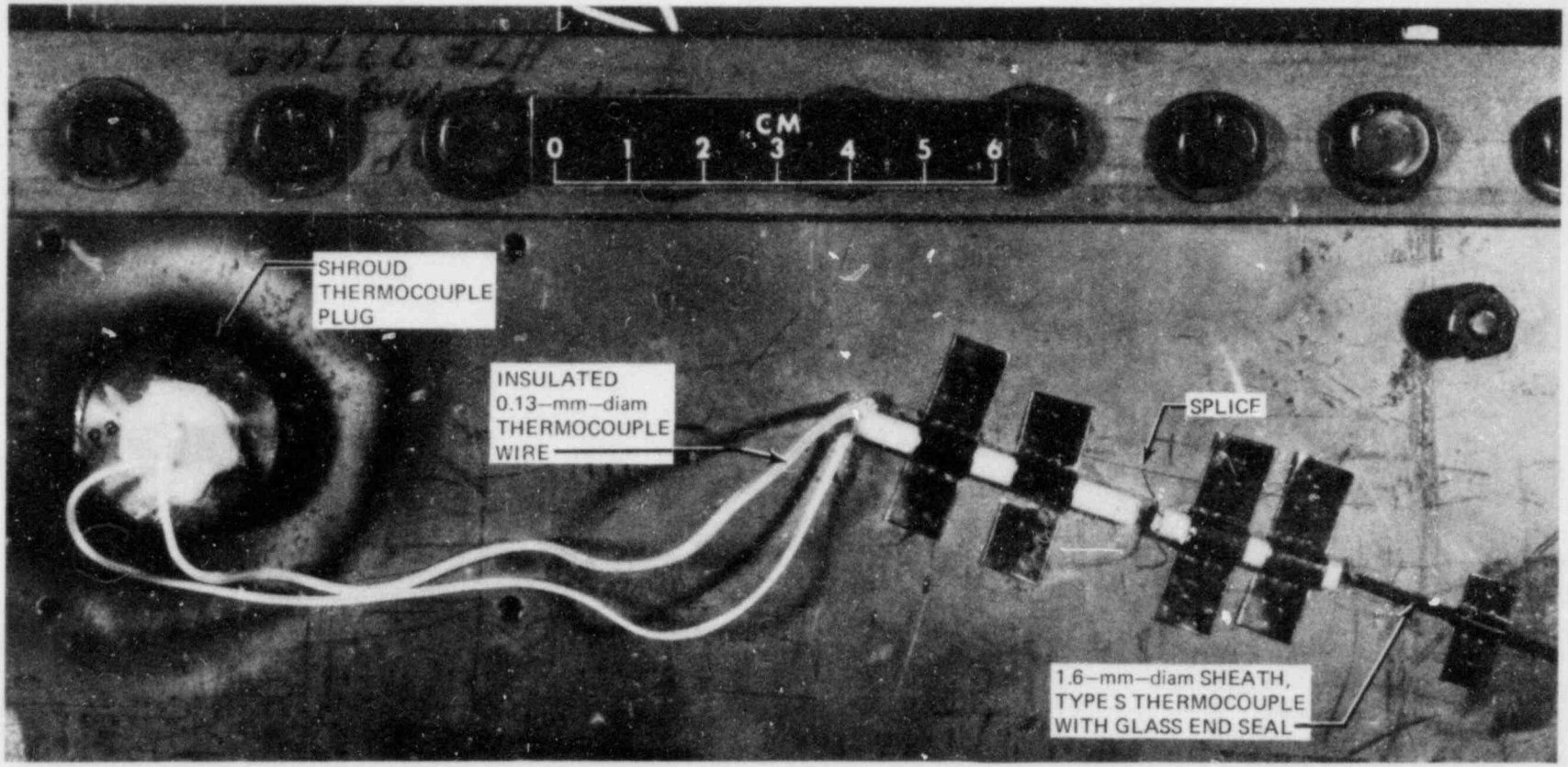

Fig. 44. Typical shroud thermocouple installation.

ORNL–PHOTO 7881–81A

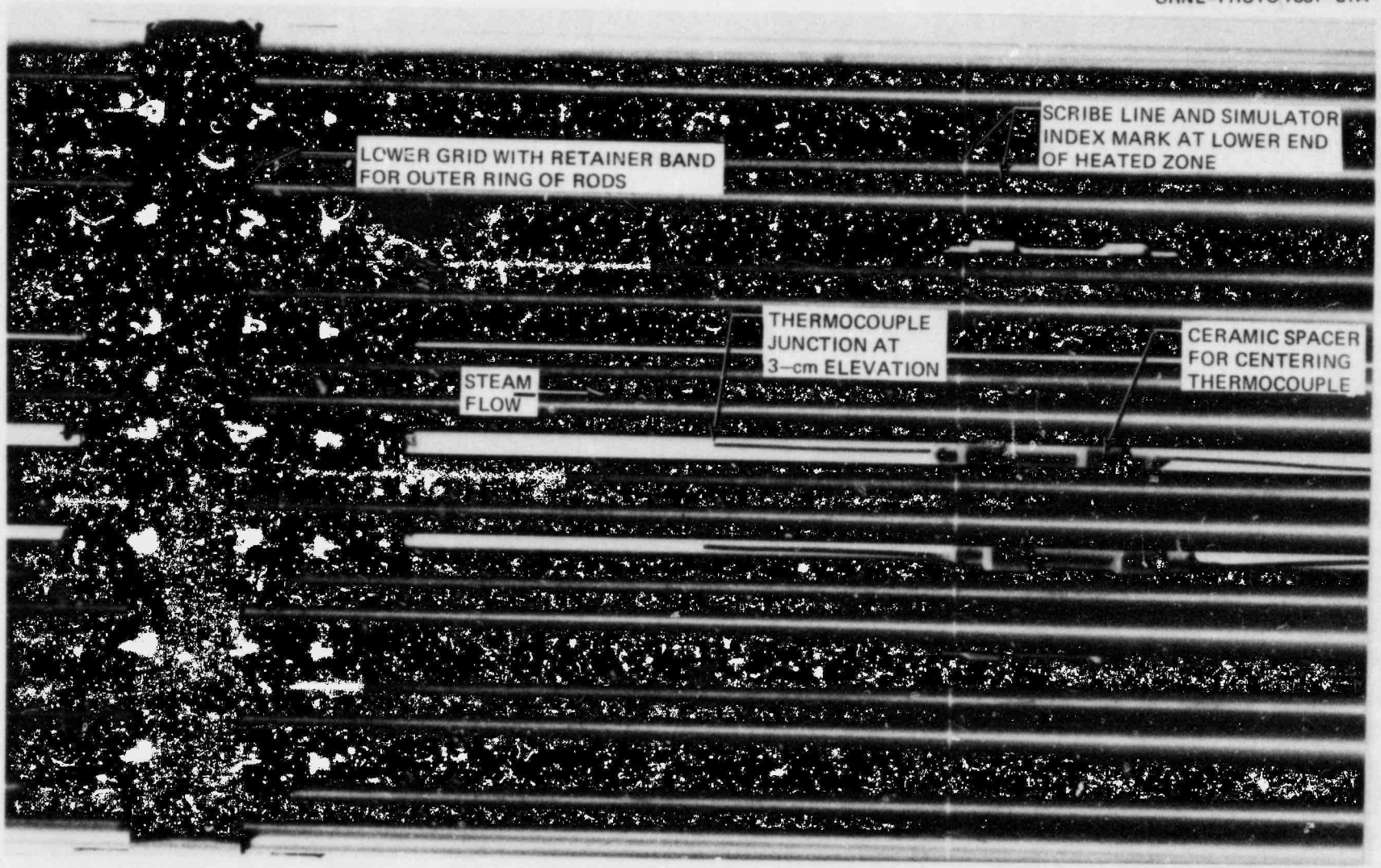

Fig. 45. Detail of outlet steam thermocouple installation.

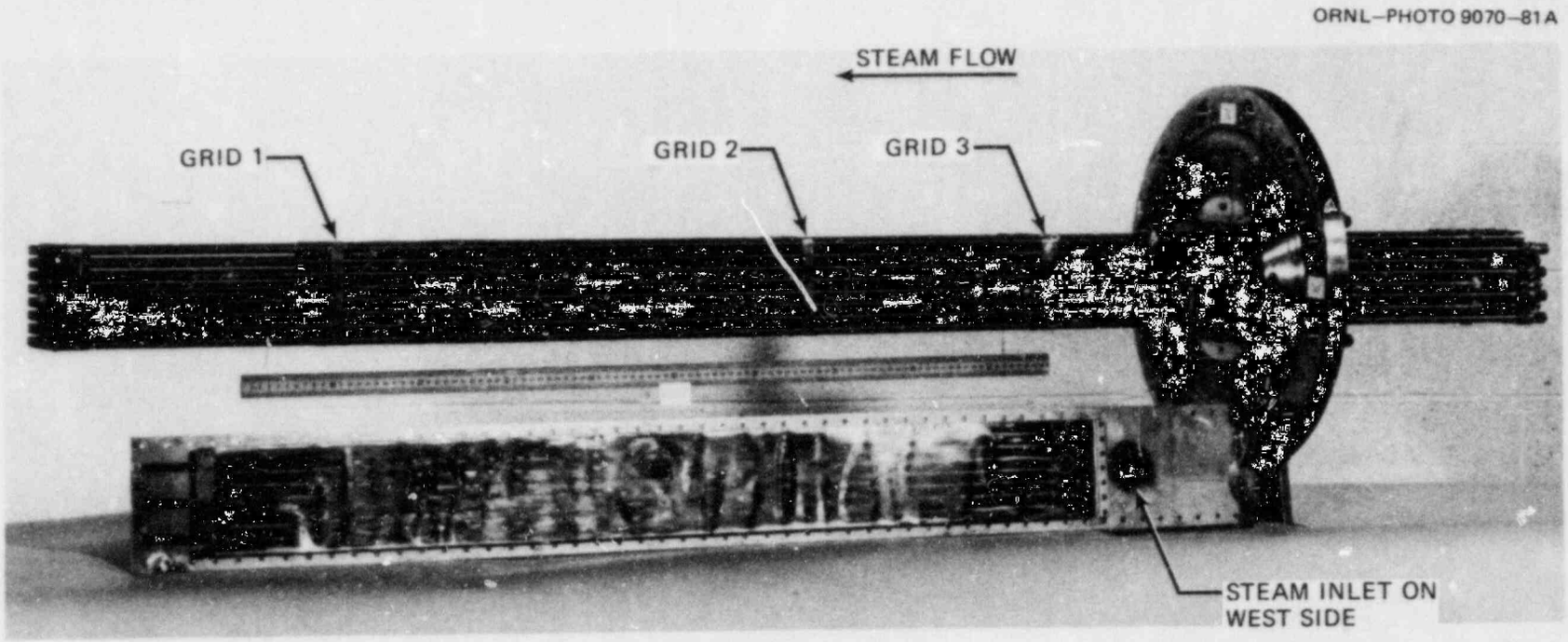

Fig. 46. Posttest view of west face of test array and shroud panel.

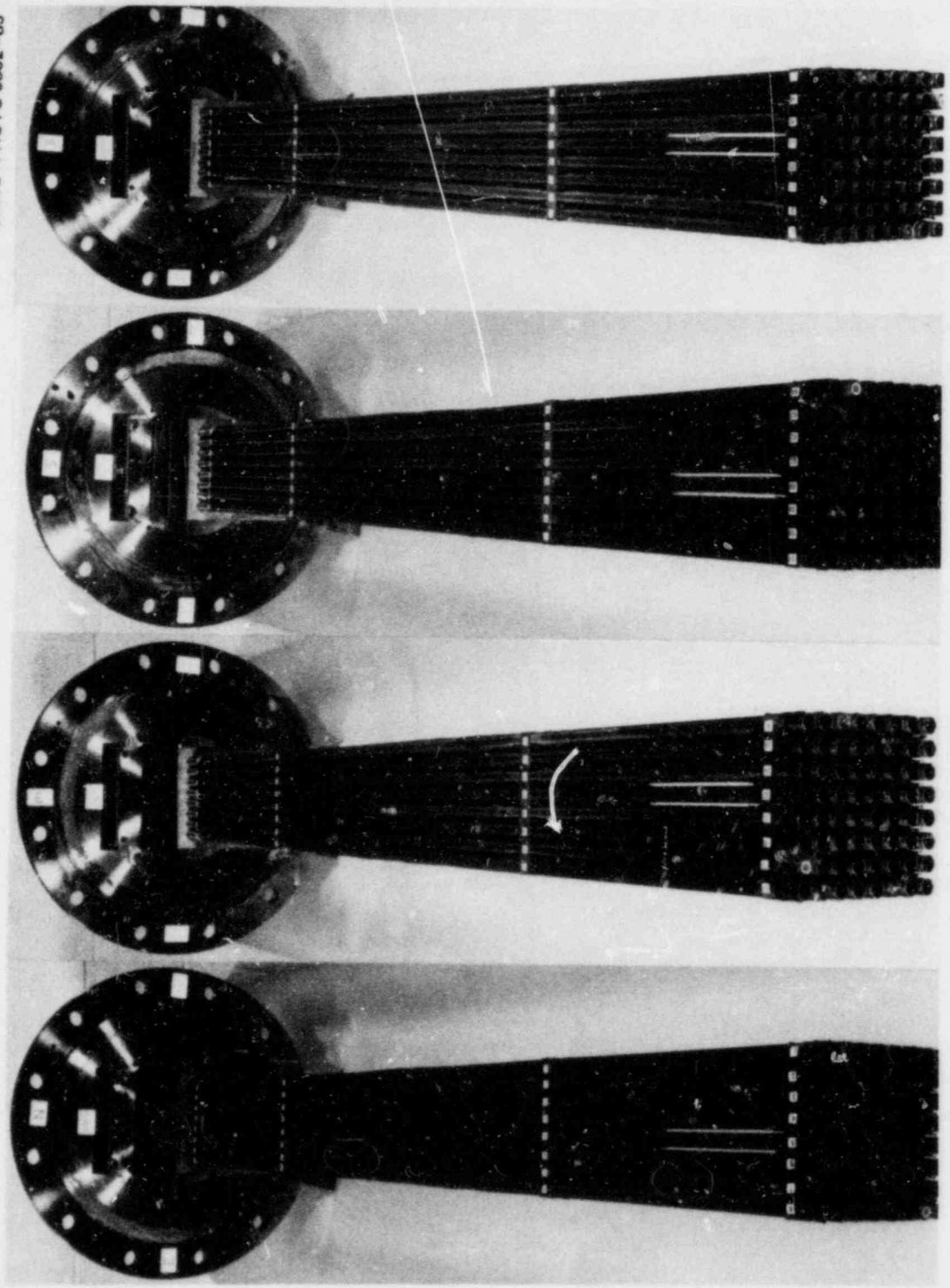

Fig. 47. Posttest views of four faces of test array.

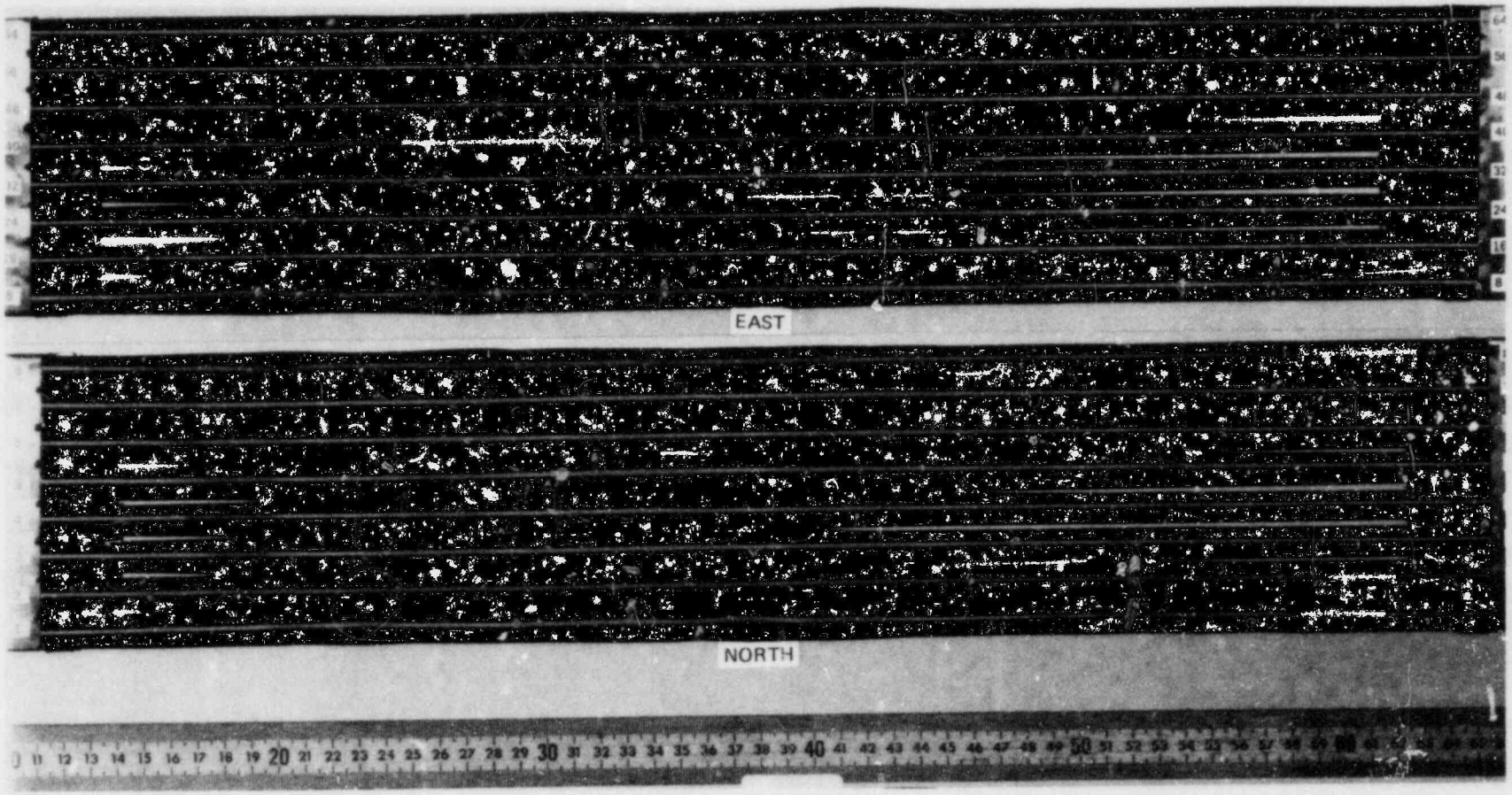

Fig. 48. North and east faces of bundle between interior grids.

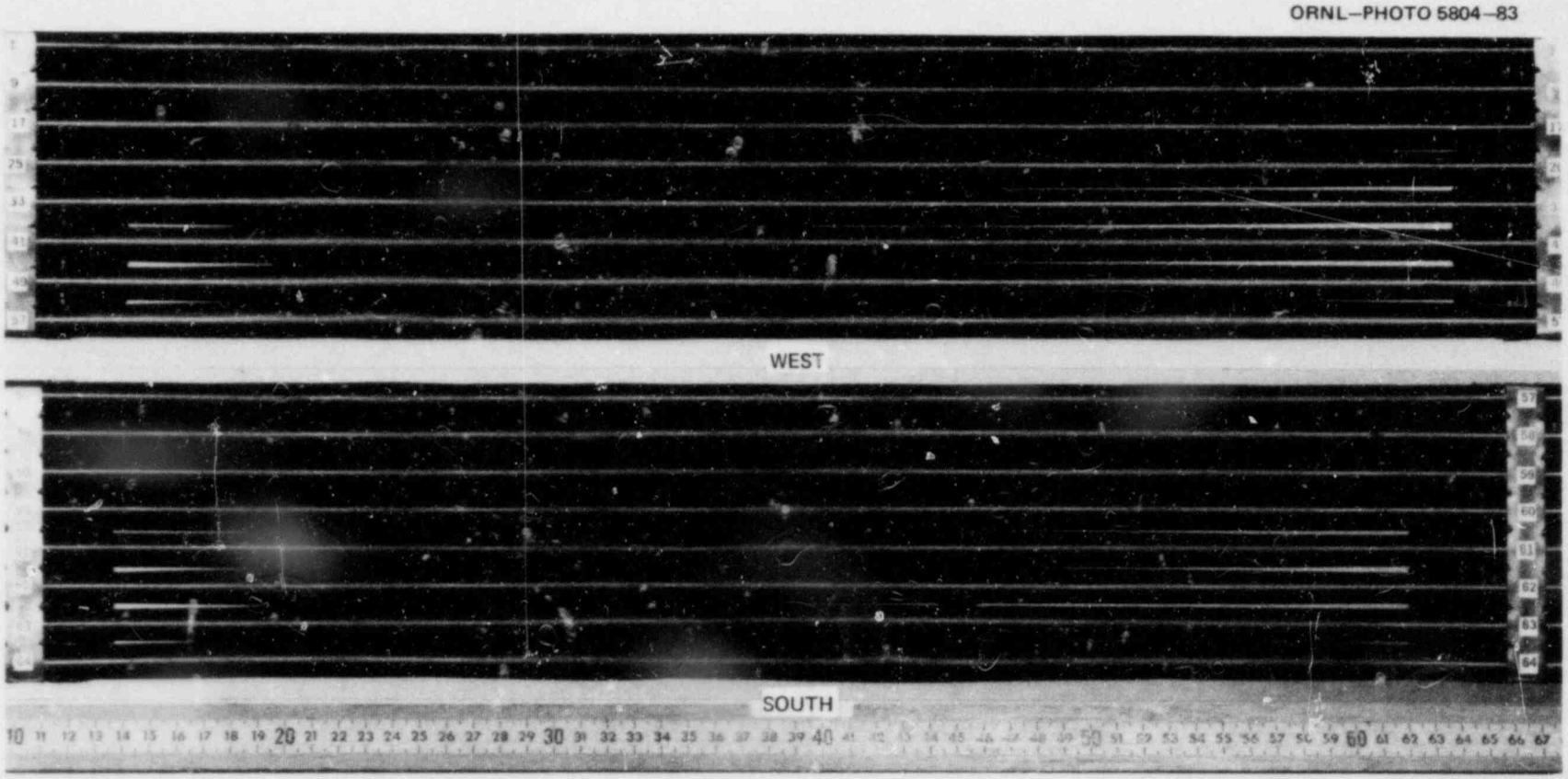

Fig. 49. South and west faces of bundle between interior grids.

ORNL–PHOTO 5805–83A

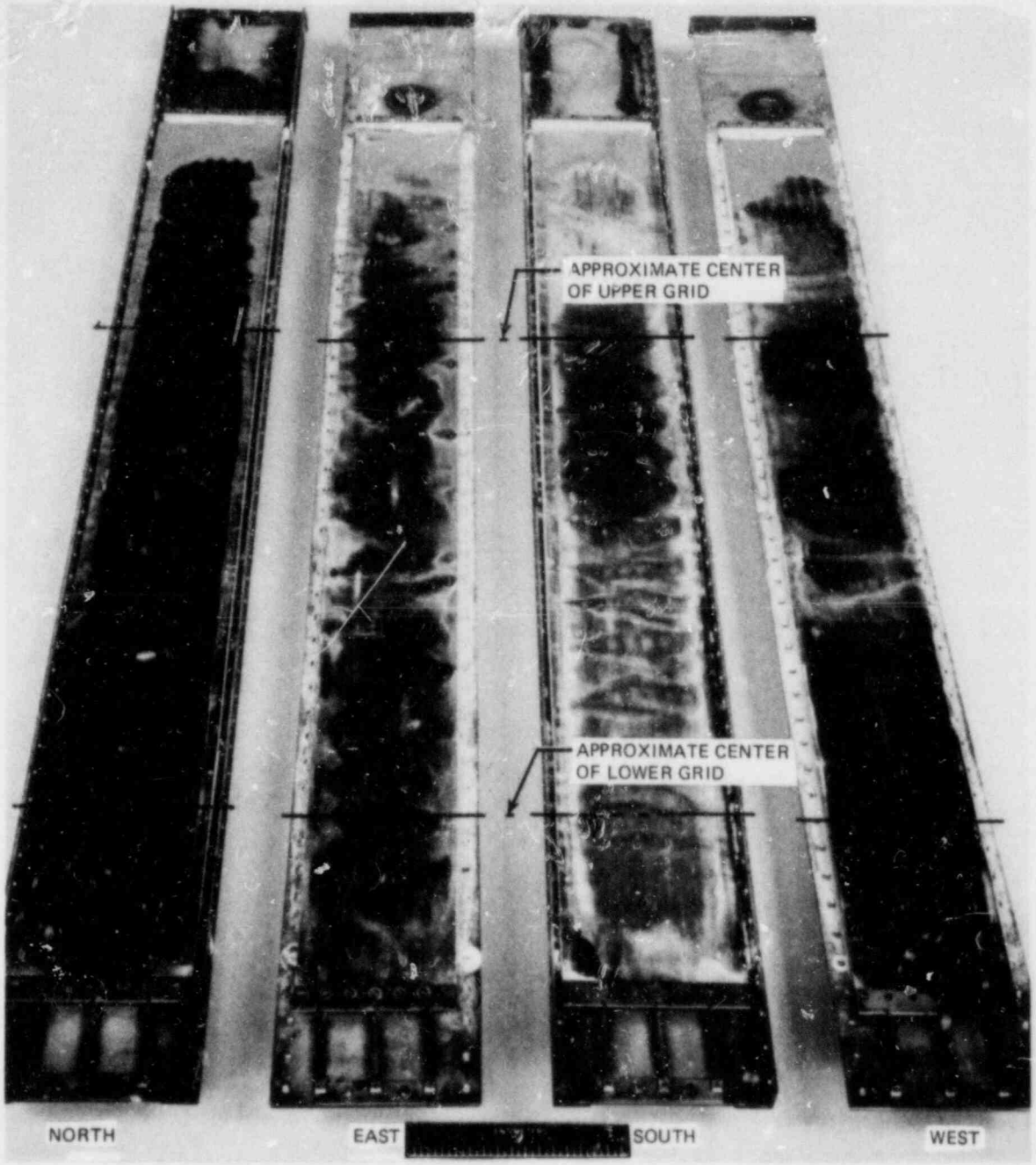

Fig. 50. Posttest views of shroud panels showing distortion and discoloration from contact with simulators.

M&C PHOTO Y183689

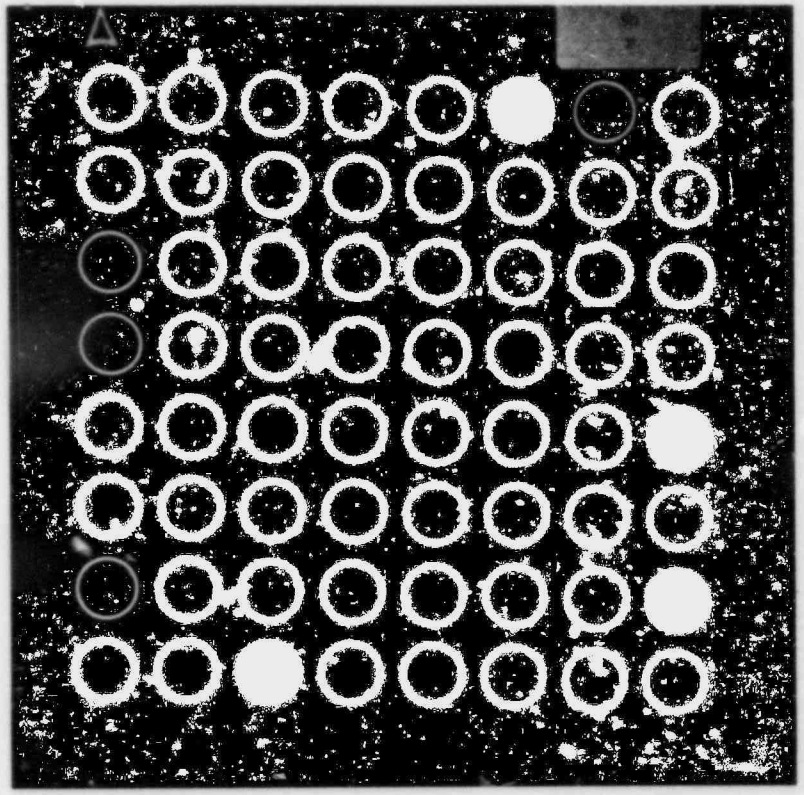

Fig. 51. Section in undeformed region at −6.0-cm elevation.

M&C PHOTO Y183690

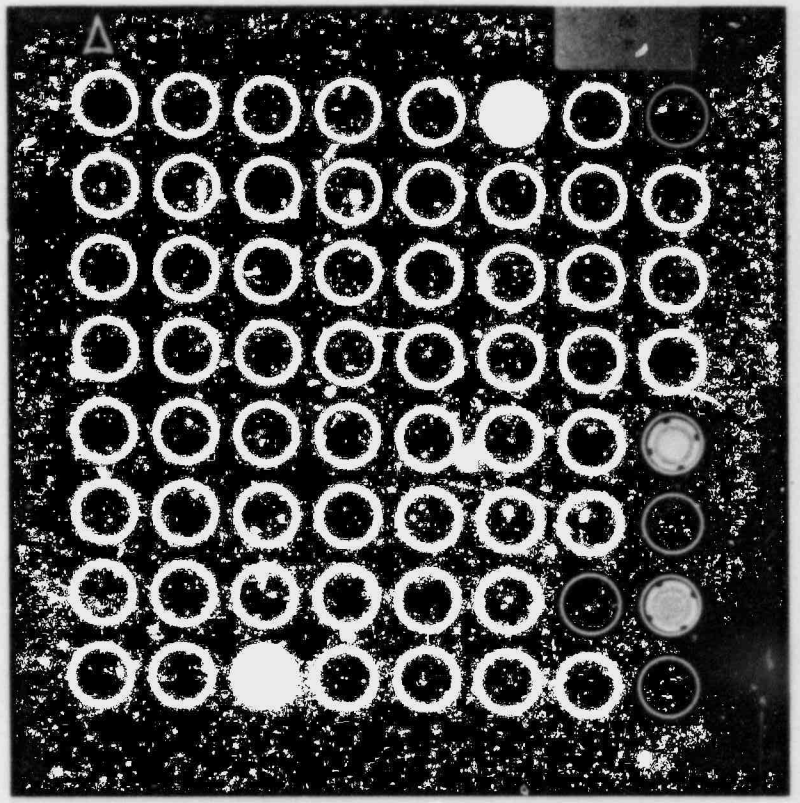

Fig. 52. Section at start of heated zone at 0.0-cm elevation.

M&C PHOTO Y183691

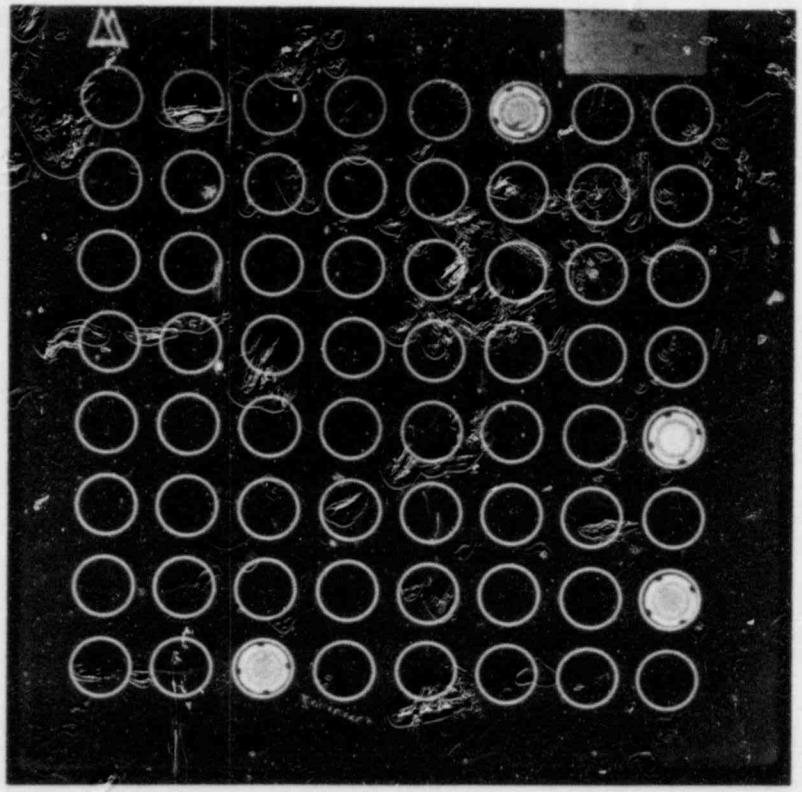

Fig. 53. Section at 1.5-cm elevation.

M&C PHOTO Y183686

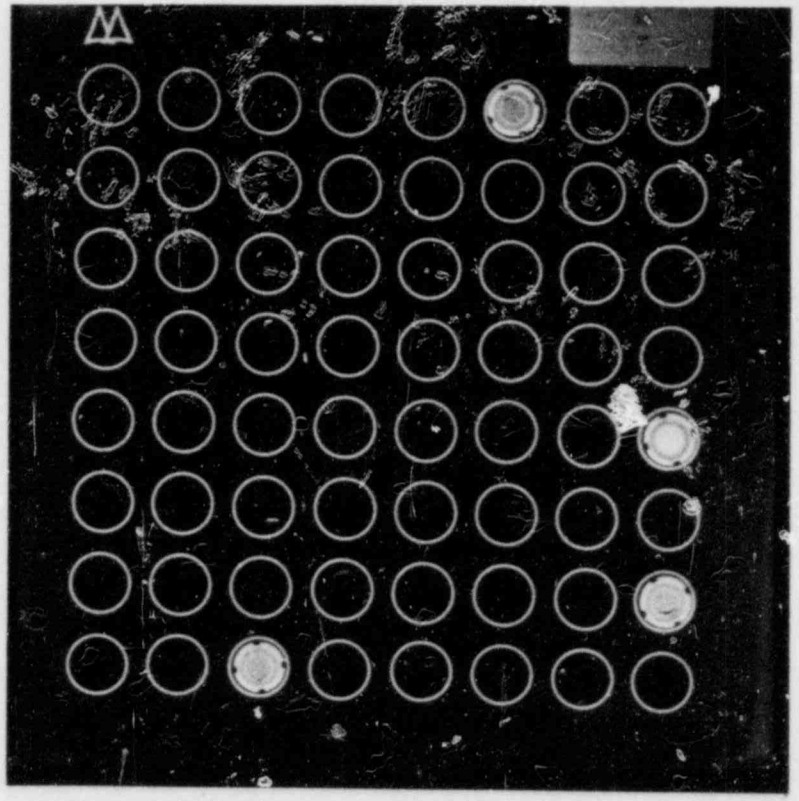

Fig. 54. Section at 3.0-cm elevation.

M&C PHOTO Y183850

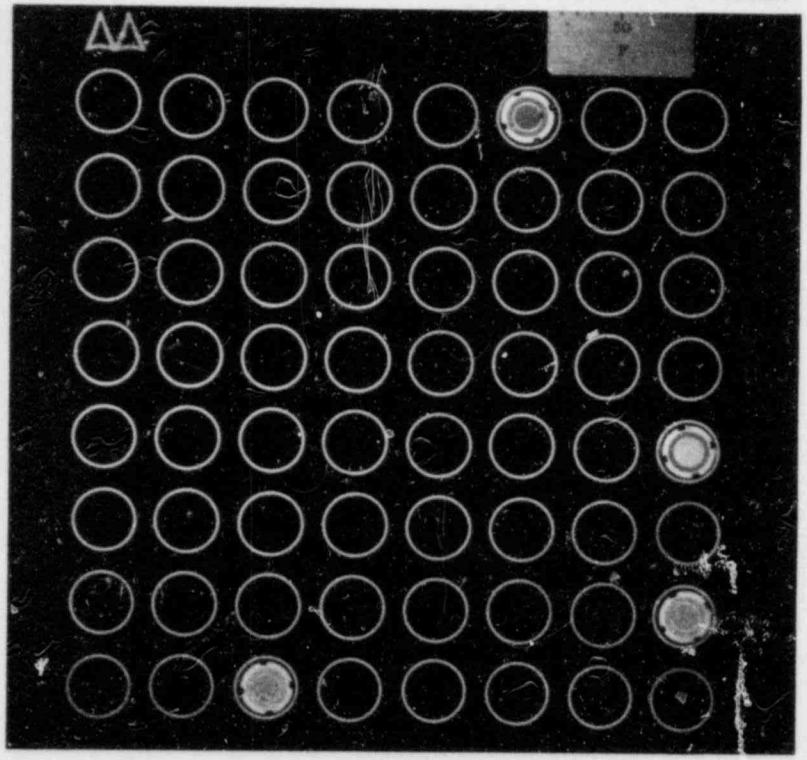

Fig. 55. Section at 4.5-cm elevation.

M&C PHOTO Y183851

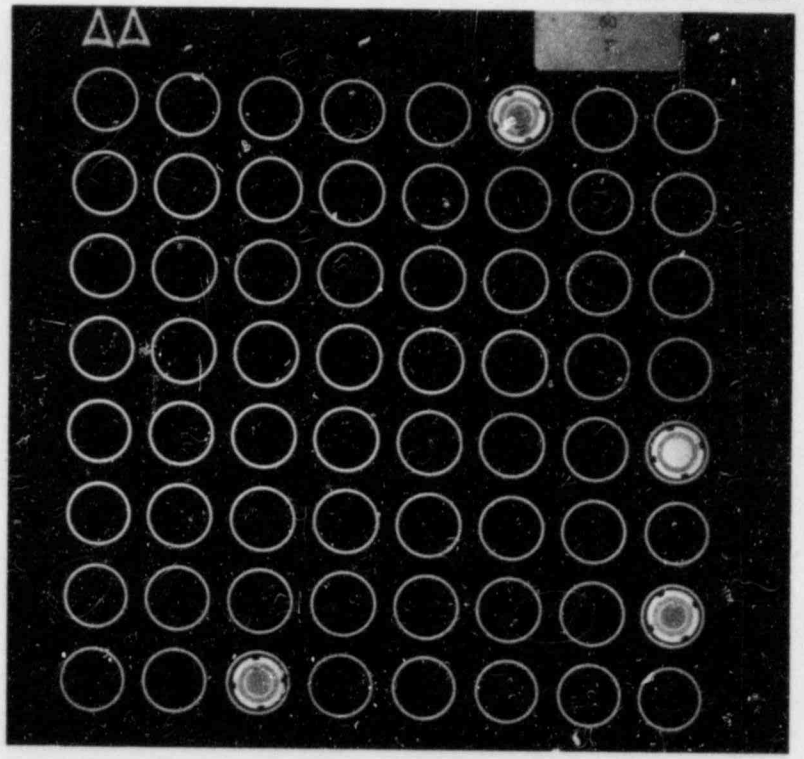

Fig. 56. Section at 6.0-cm elevation.

M&C PHOTO Y183852

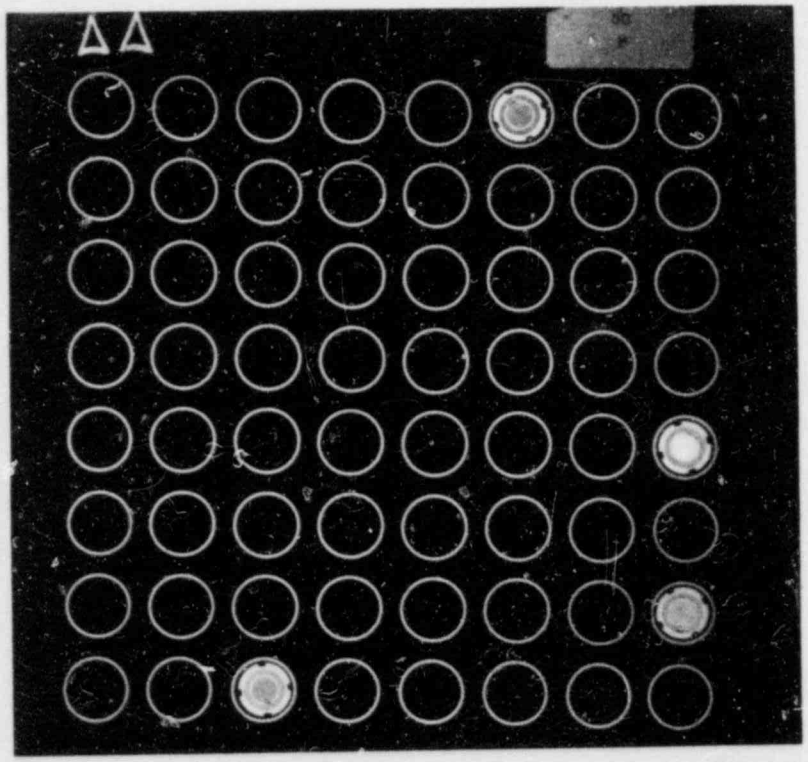

Fig. 57. Section at 7.5-cm elevation.

M&C PHOTO Y183853

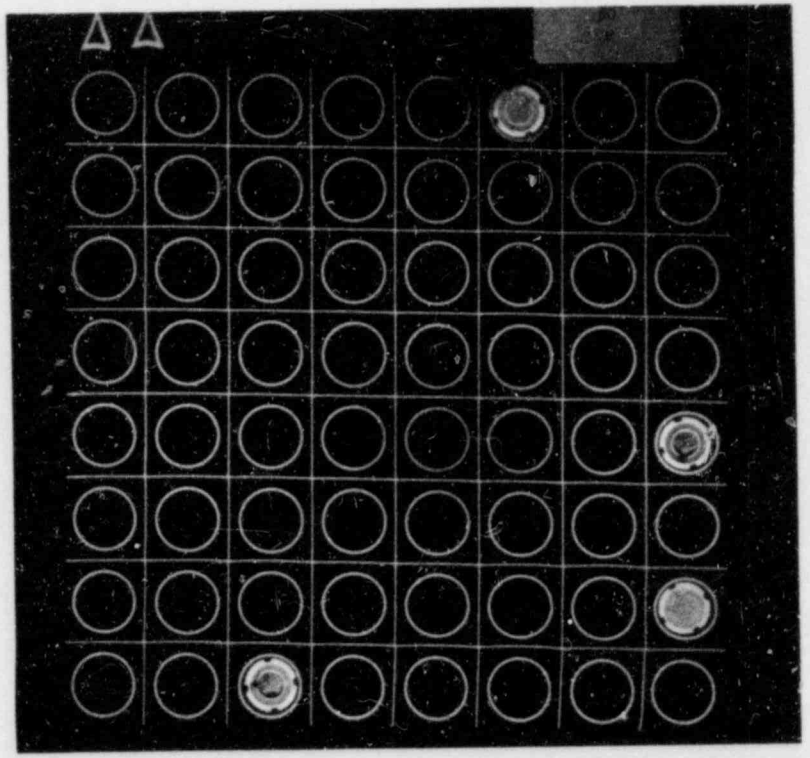

Fig. 58. Section through lower grid at 9.0-cm elevation.

M&C PHOTO Y183854

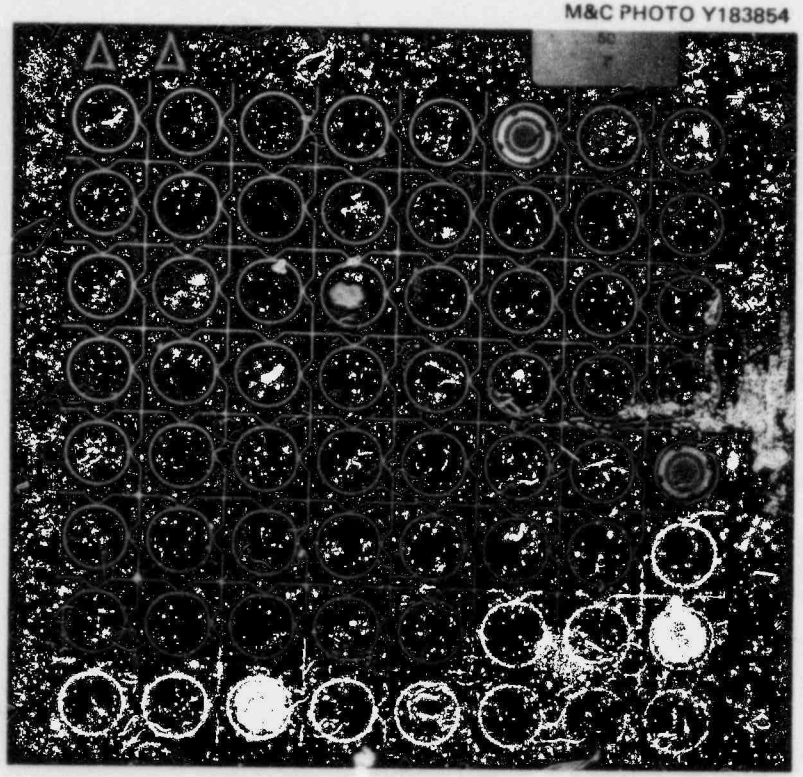

Fig. 59. Section through lower grid at 11.6-cm elevation.

M&C PHOTO Y183855

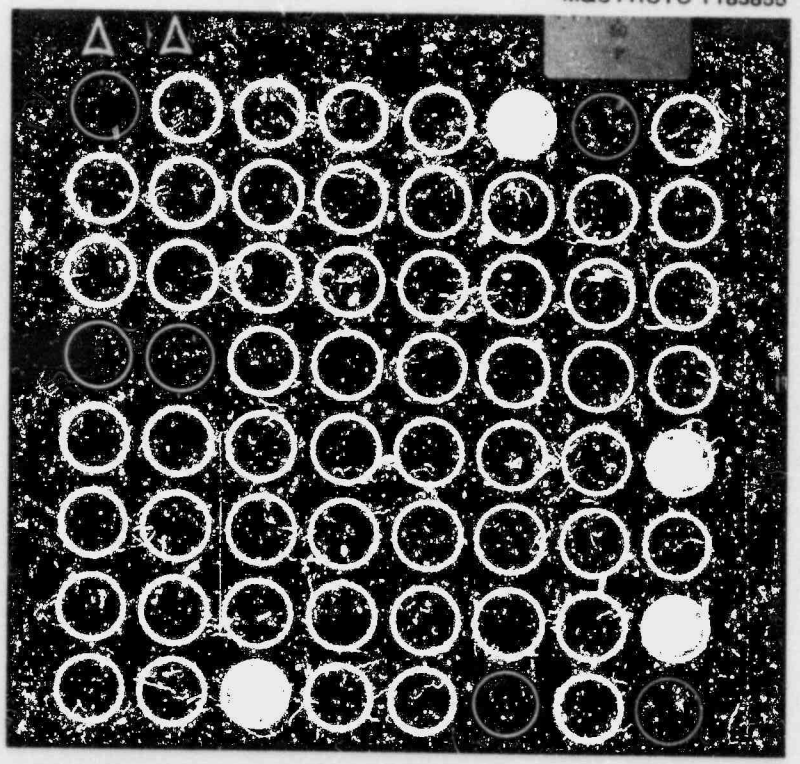

Fig. 60. Section at 13.2-cm elevation.

M&C PHOTO Y183856

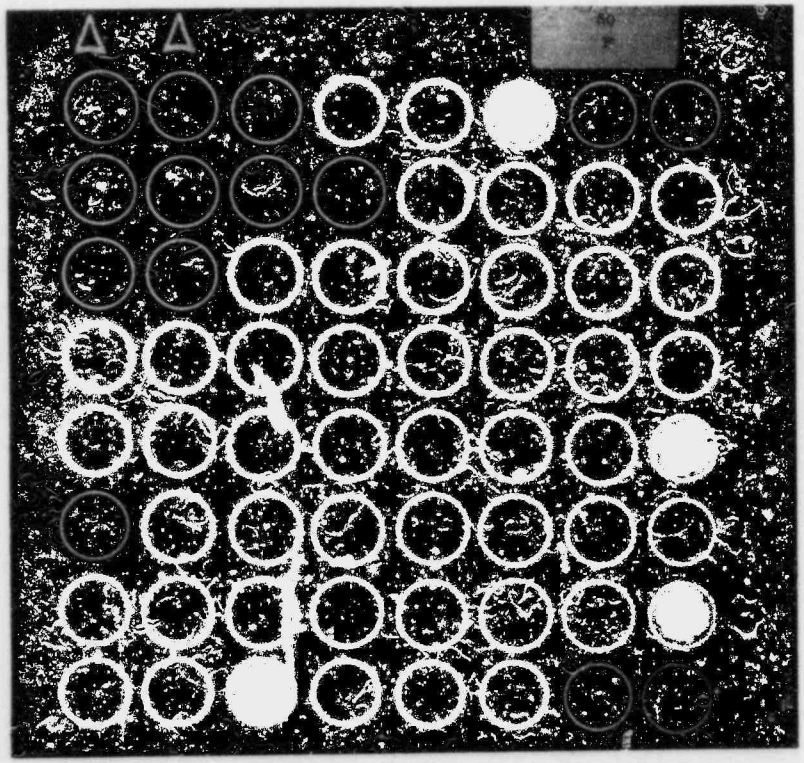

Fig. 61. Section at 14.7-cm elevation.

M&C PHOTO Y183857

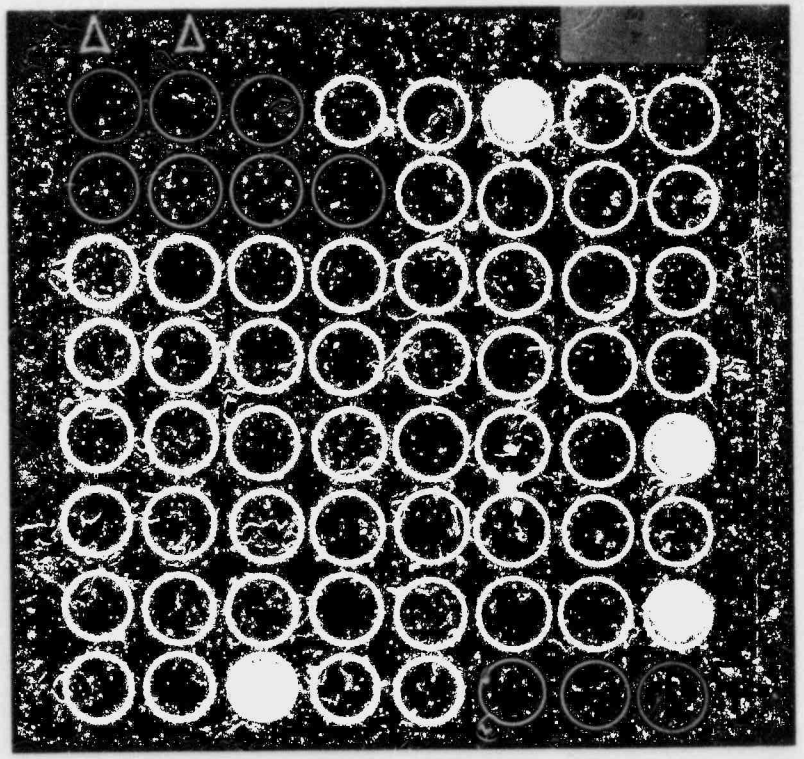

Fig. 62. Section at 16.1-cm elevation.

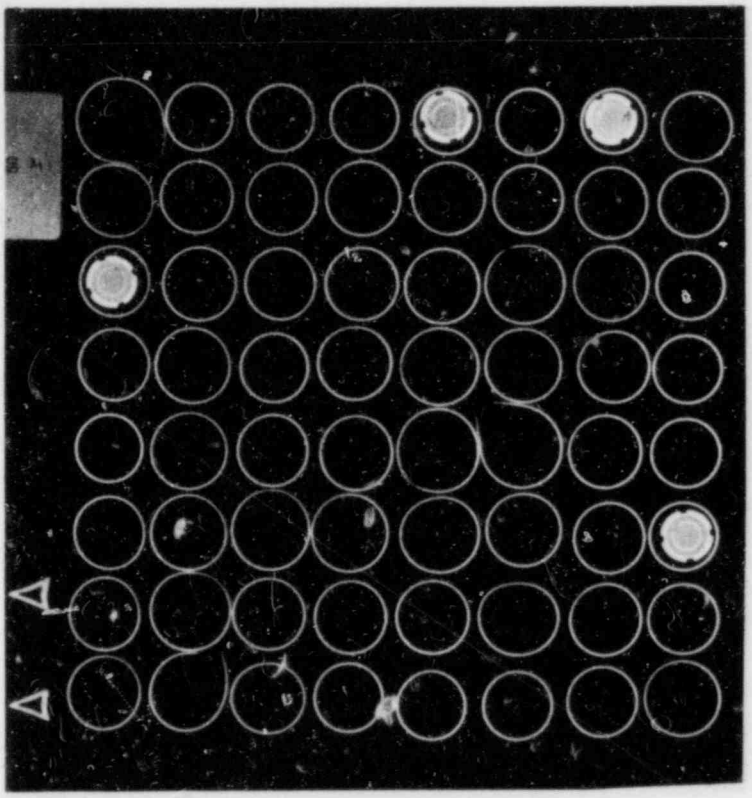

Fig. 64. Section at 18.9-cm elevation.

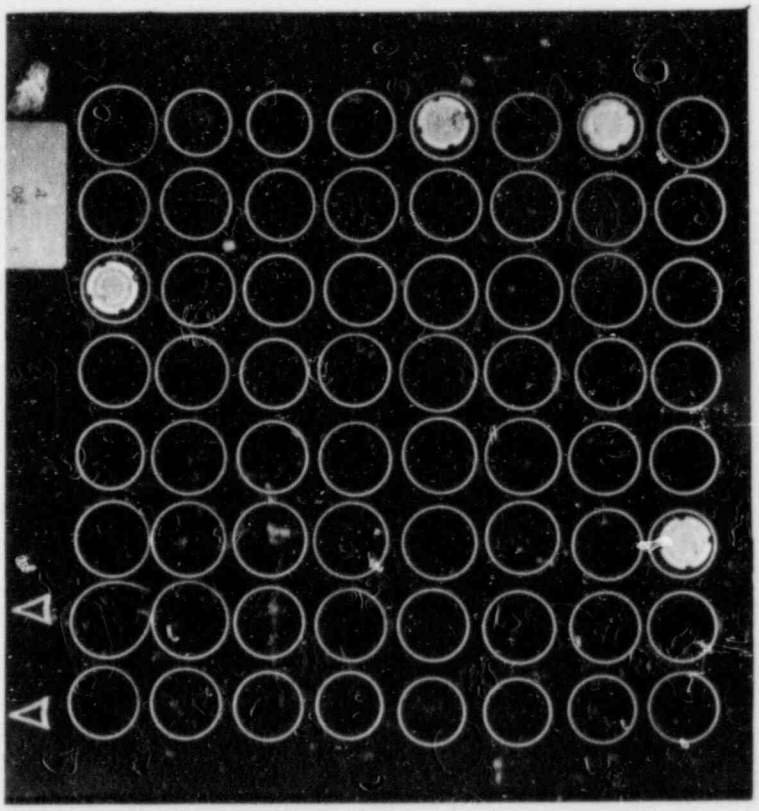

Fig. 63. Section at 17.5-cm elevation.

ORNL–PHOTO 3497–82

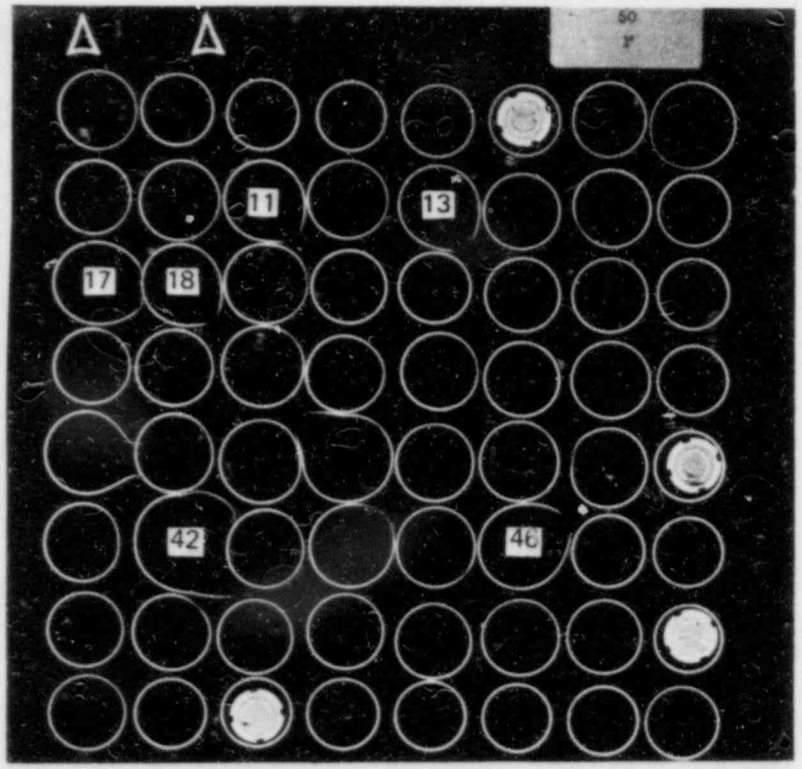

Fig. 65. Section at 20.3-cm elevation.

M&C PHOTO Y183843

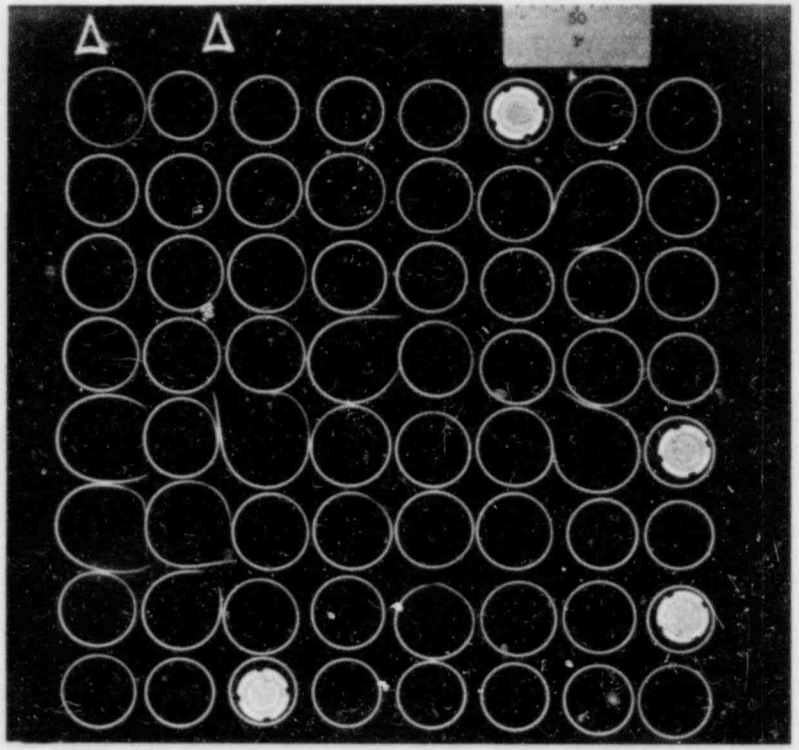

Fig. 66. Section at 21.8-cm elevation.

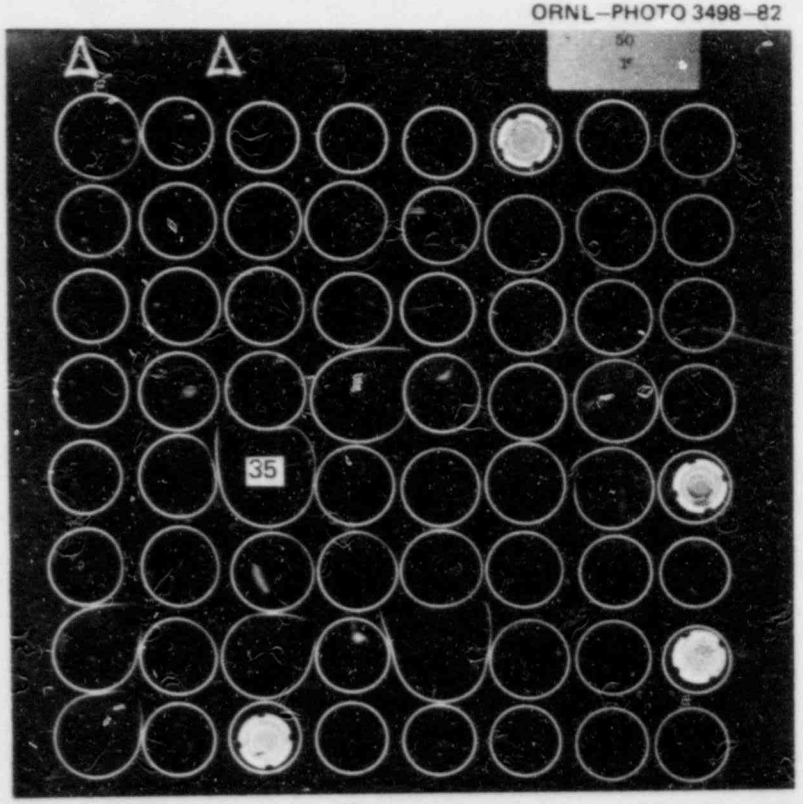

Fig. 67. Section at 23.2-cm elevation.

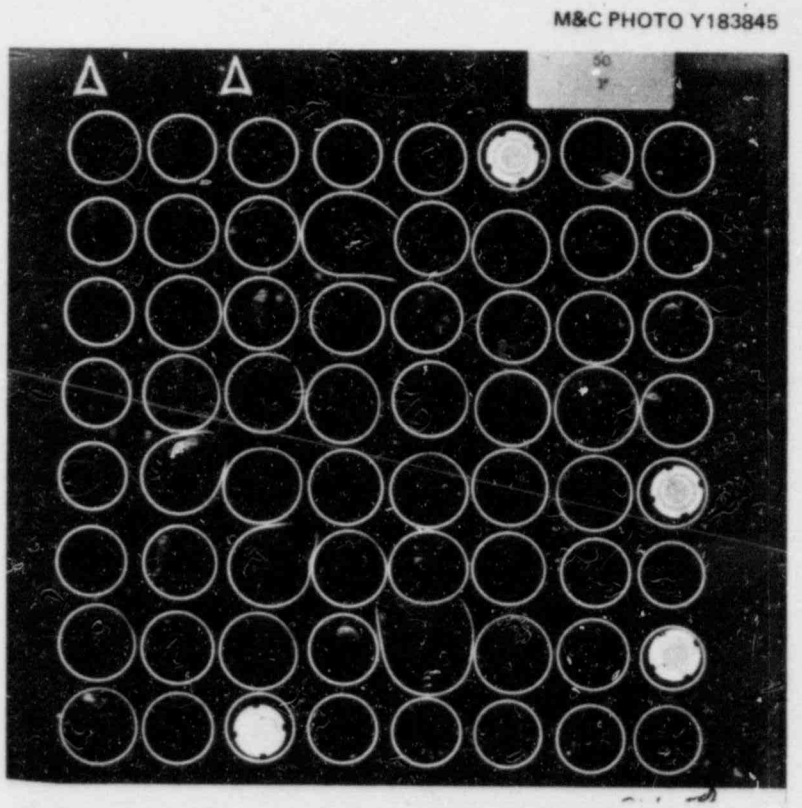

Fig. 68. Section at 24.6-cm elevation.

M&C PHOTO Y183846

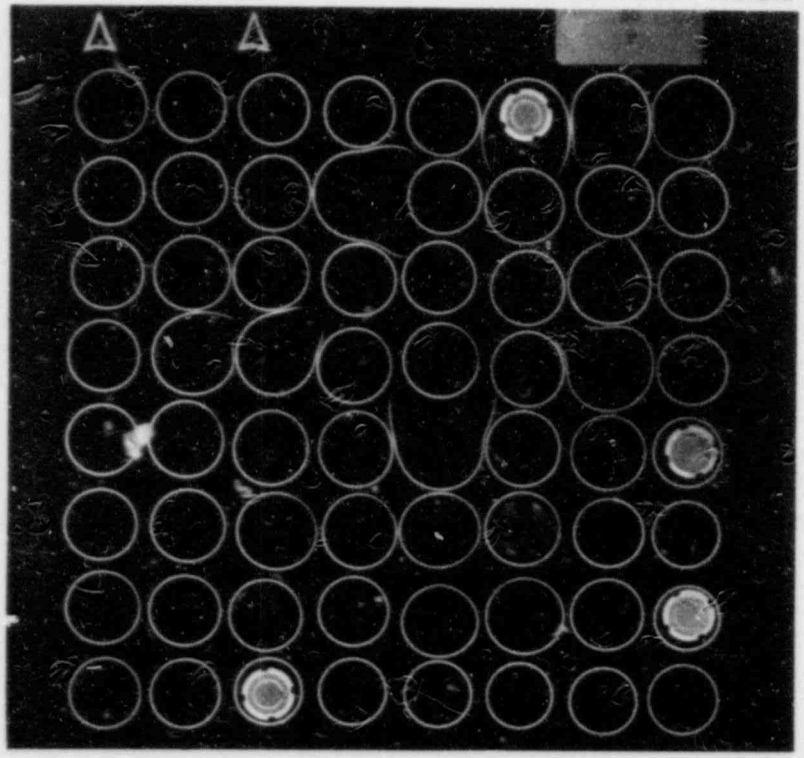

Fig. 69. Section at 26.1-cm elevation.

M&C PHOTO Y183847

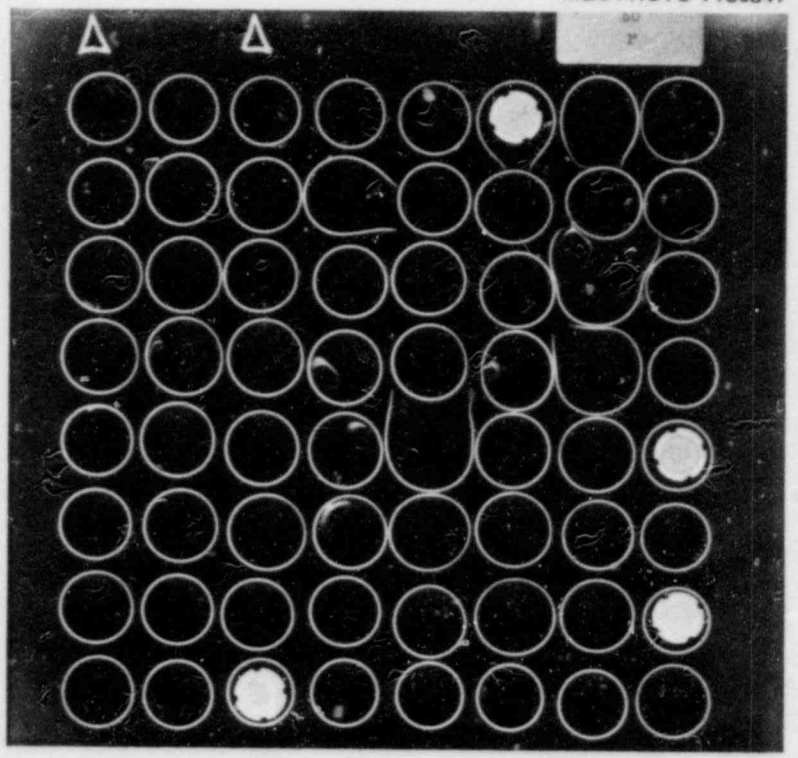

Fig. 70. Section at 27.5-cm elevation.

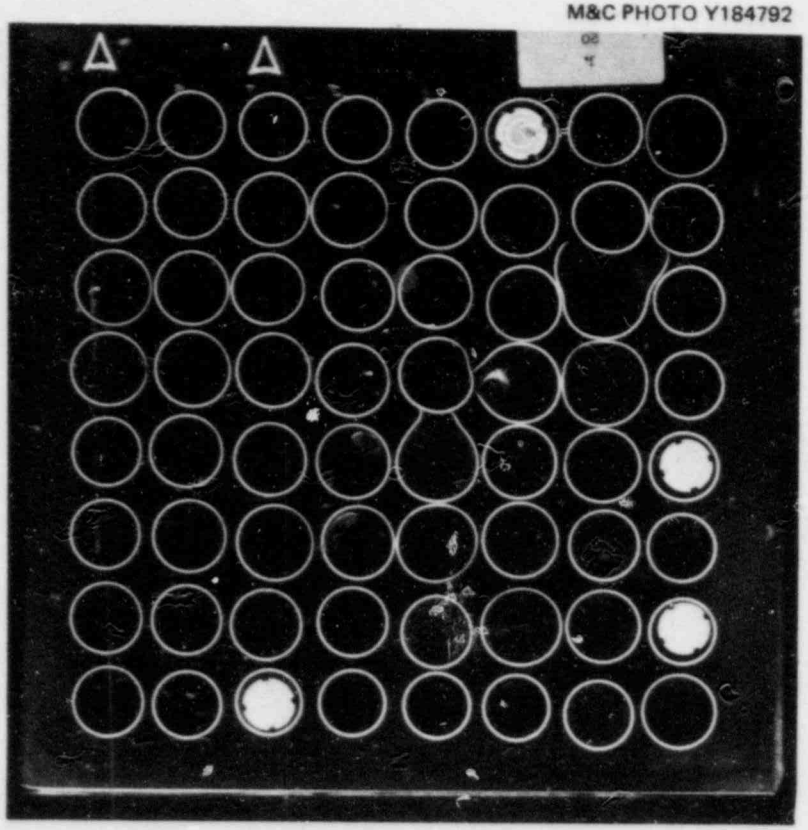

Fig. 71. Section at 27.9-cm elevation (reversed image to show correct tube positions).

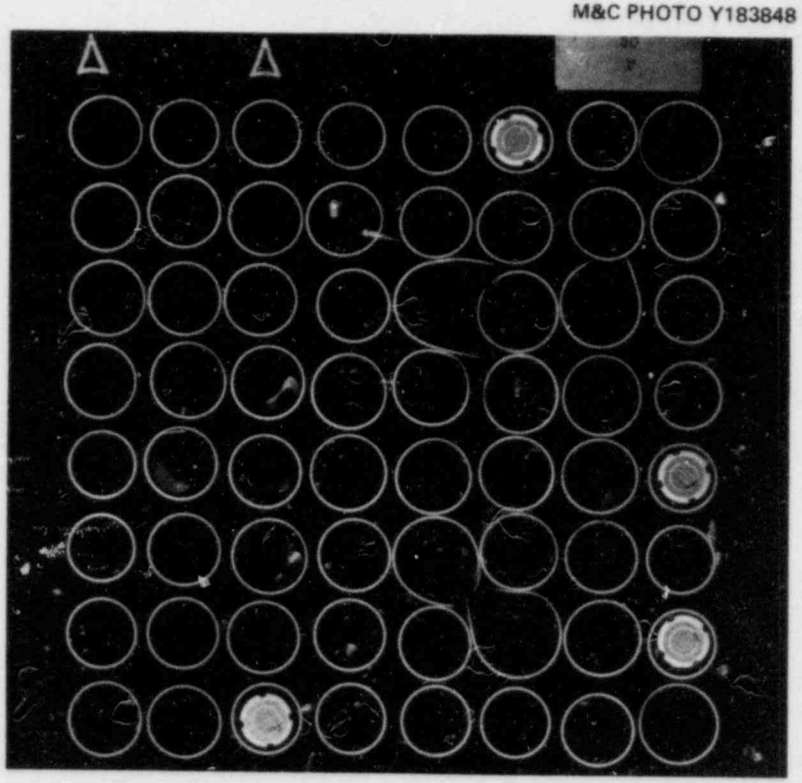

Fig. 72. Section at 29.5-cm elevation.

ORNL–PHOTO 3499–82

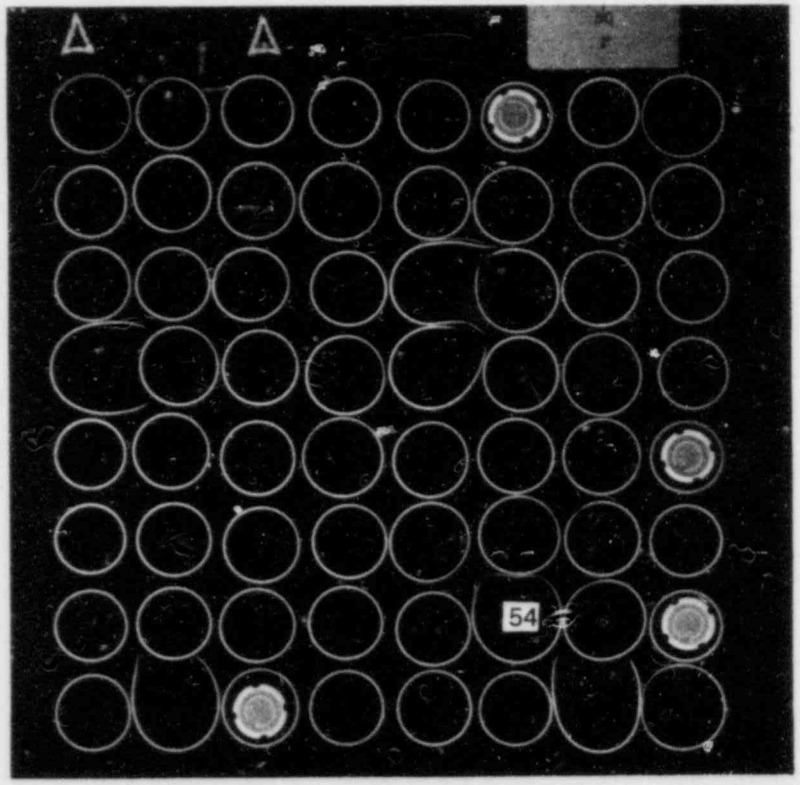

Fig. 73. Section at 31.0-cm elevation.

ORNL–PHOTO 3500–82

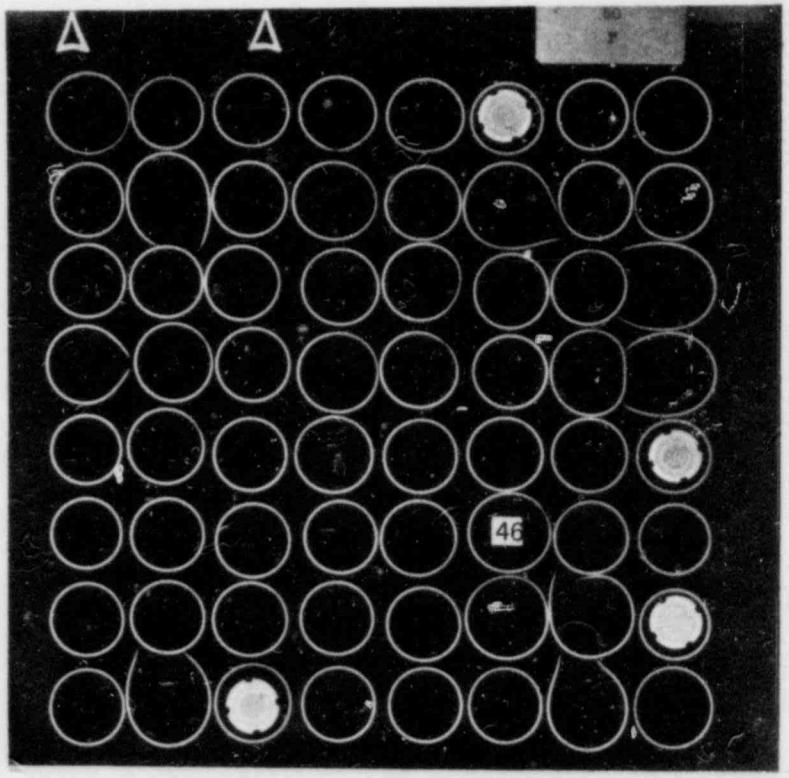

Fig. 74. Section at 32.4-cm elevation.

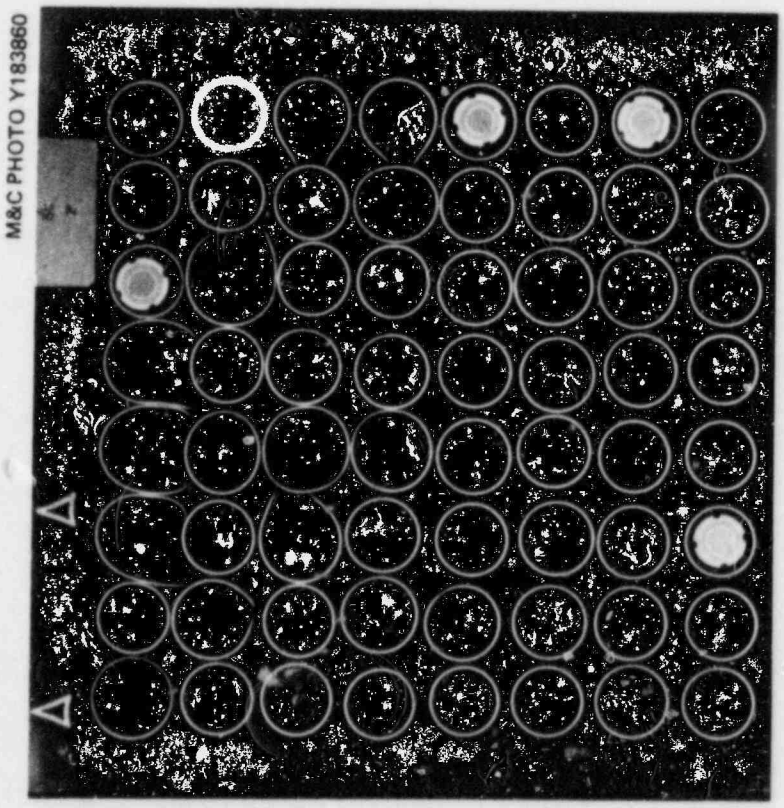

Fig. 75. Section at 33.8-cm elevation.

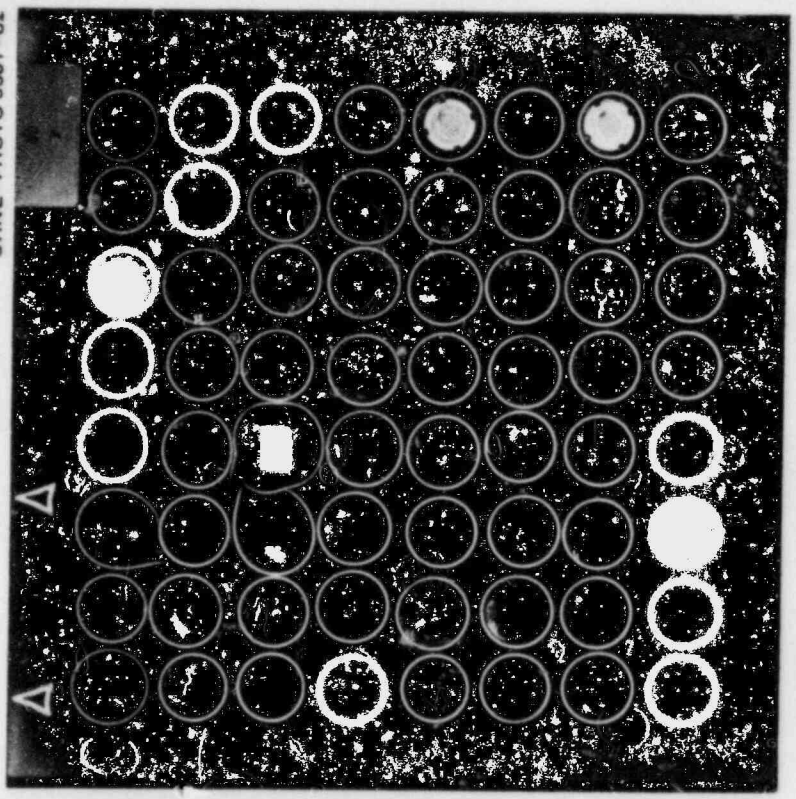

Fig. 76. Section at 35.2-cm elevation.

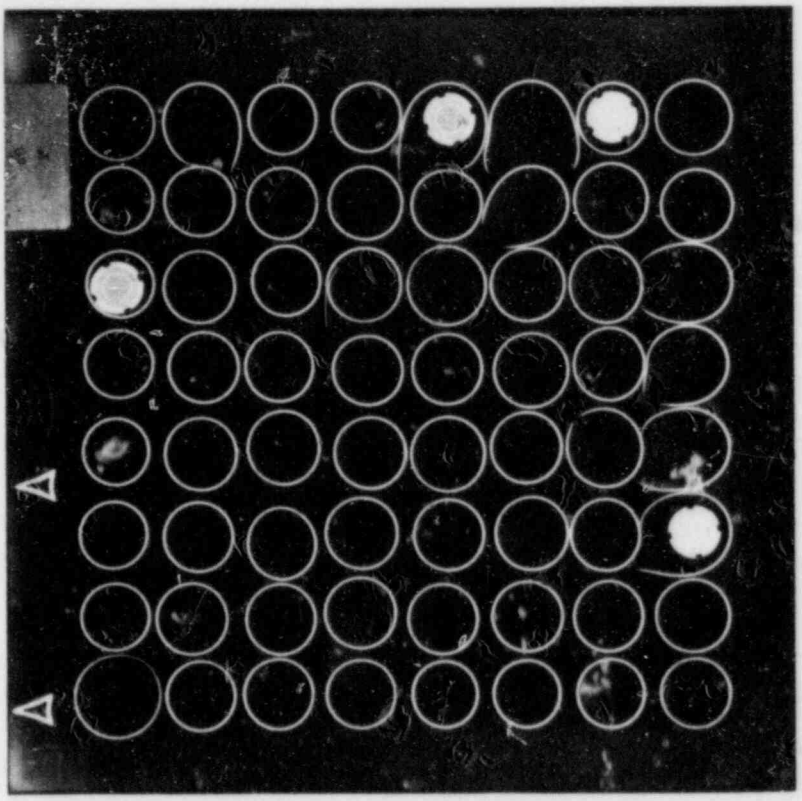

Fig. 78. Section at 38.4-cm elevation.

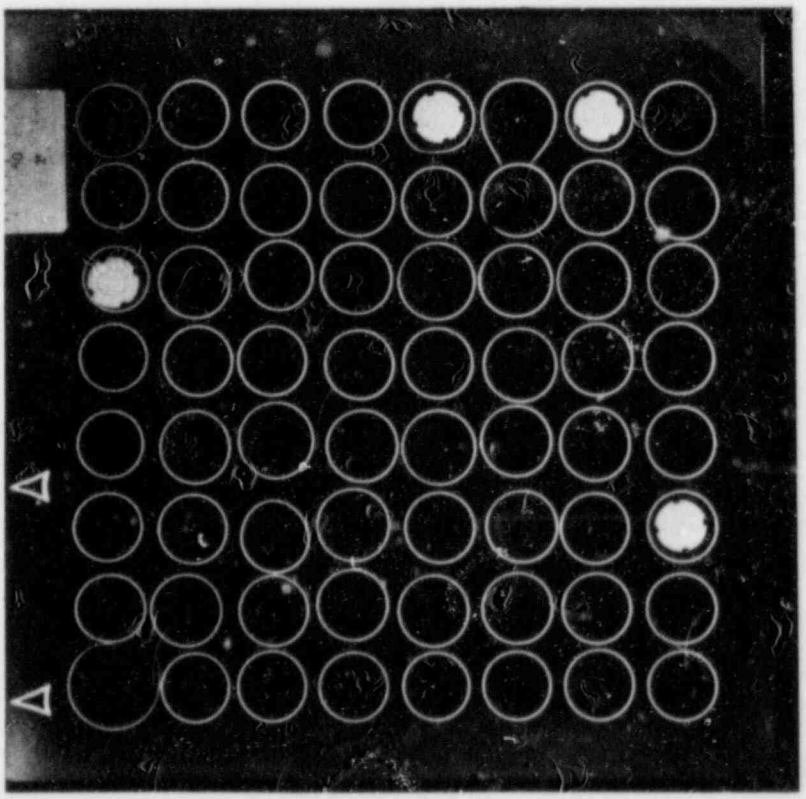

Fig. 77. Section at 37.0-cm elevation.

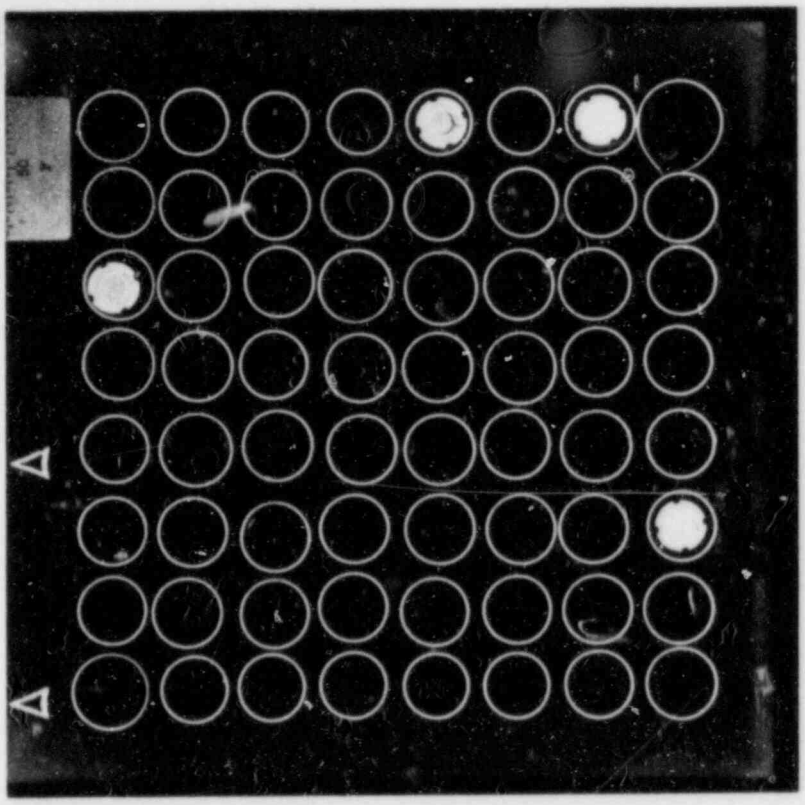

Fig. 80. Section at 41.8-cm elevation.

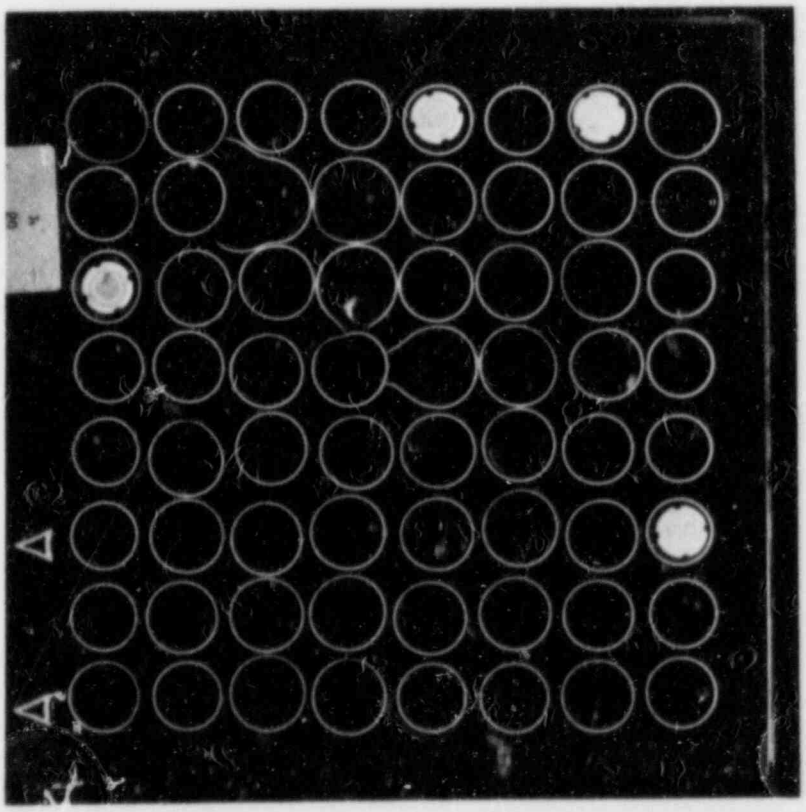

Fig. 79. Section at 39.8-cm elevation.

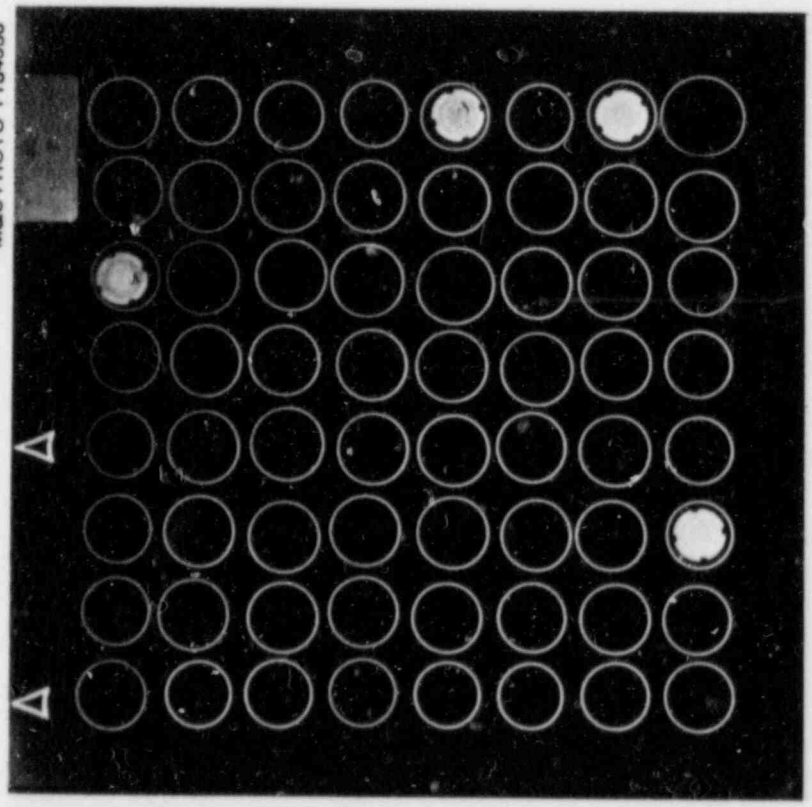

Fig. 81. Section at 43.6-cm elevation.

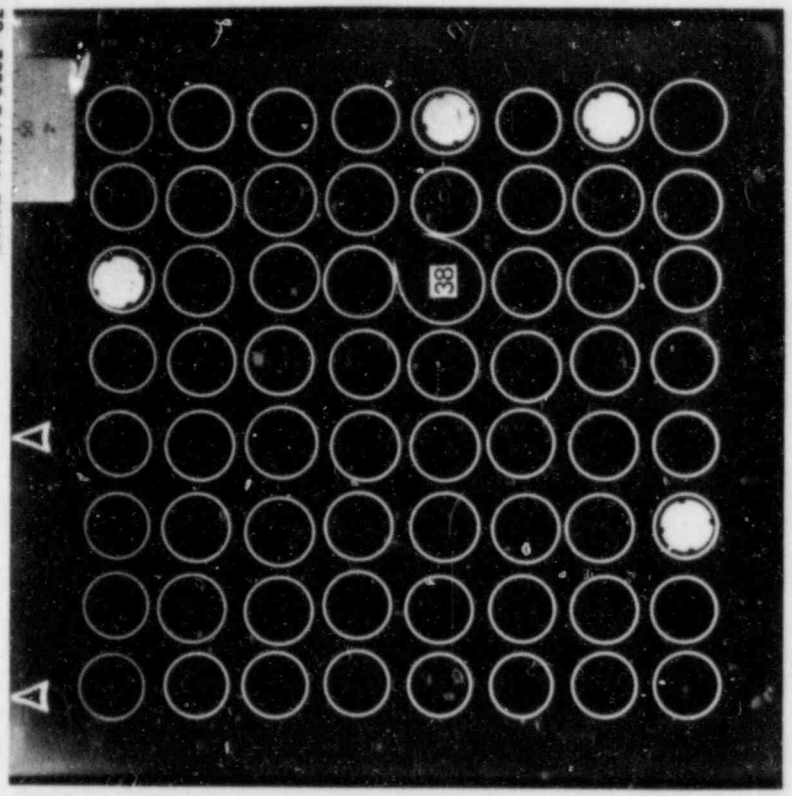

Fig. 82. Section at 45.3-cm elevation.

M&C PHOTO Y184349

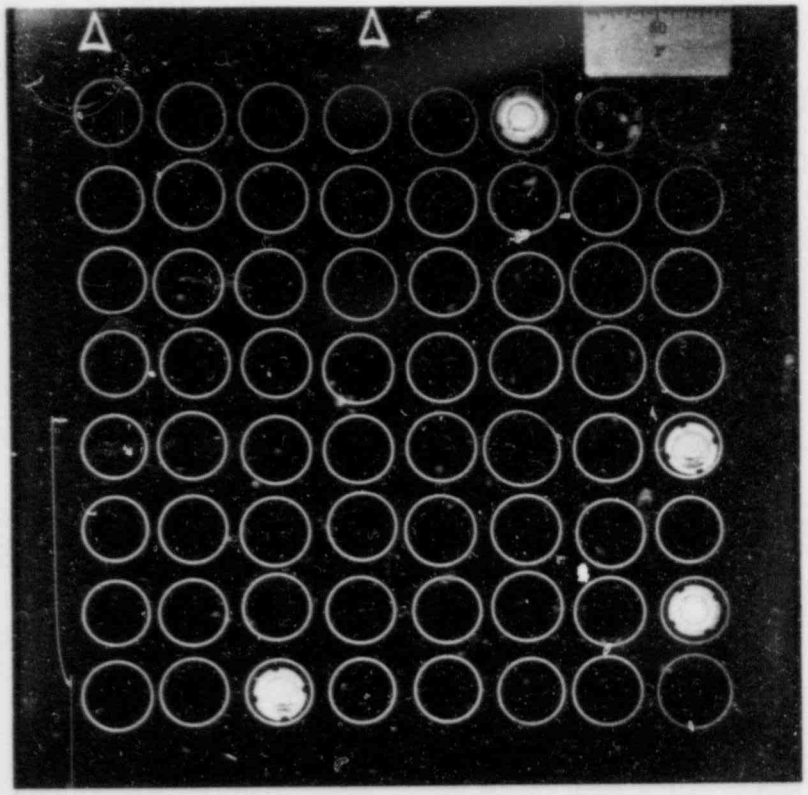

Fig. 83. Section at 46.9-cm elevation.

M&C PHOTO Y184354

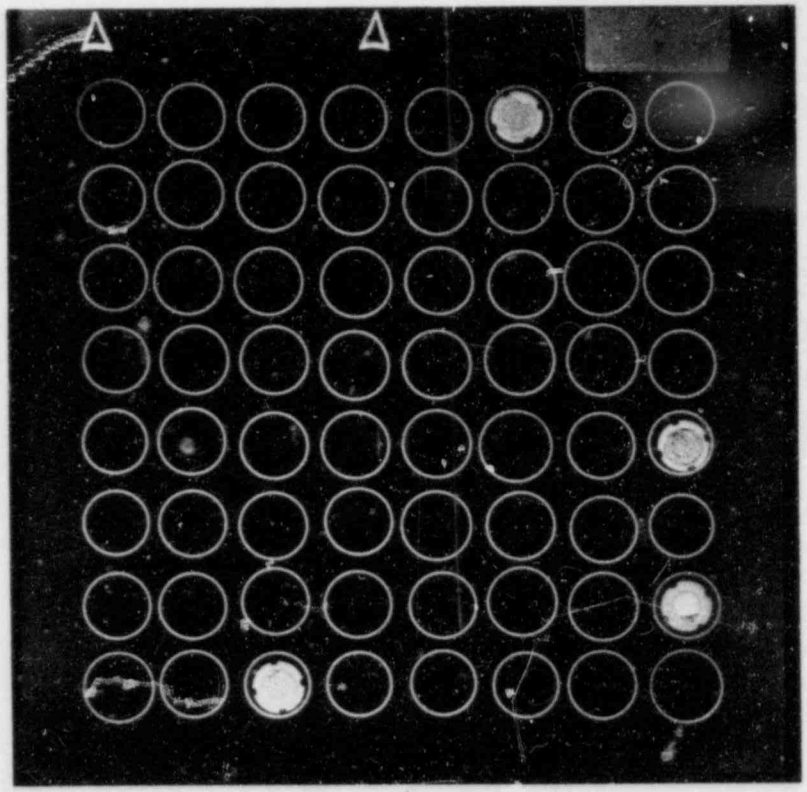

Fig. 84. Section at 48.4-cm elevation.

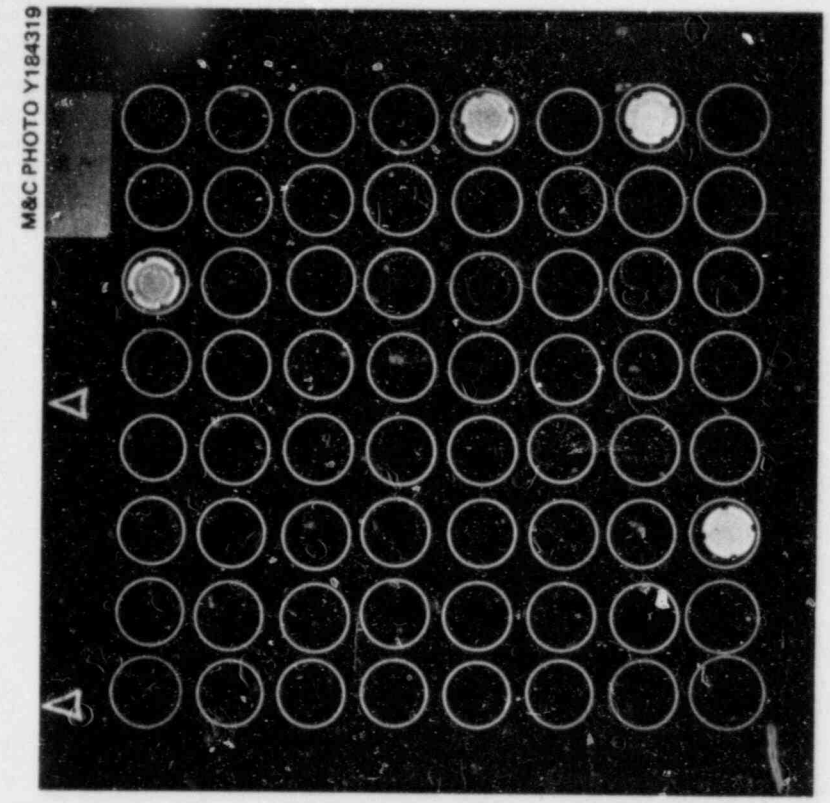

Fig. 86. Section at 51.6-cm elevation.

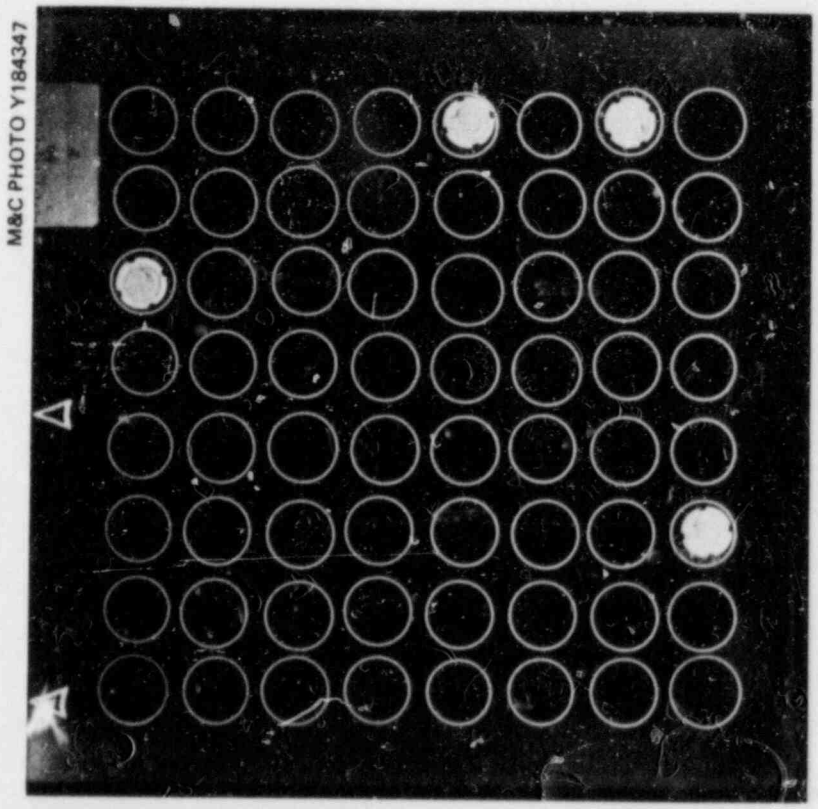

Fig. 85. Section at 50.0-cm elevation.

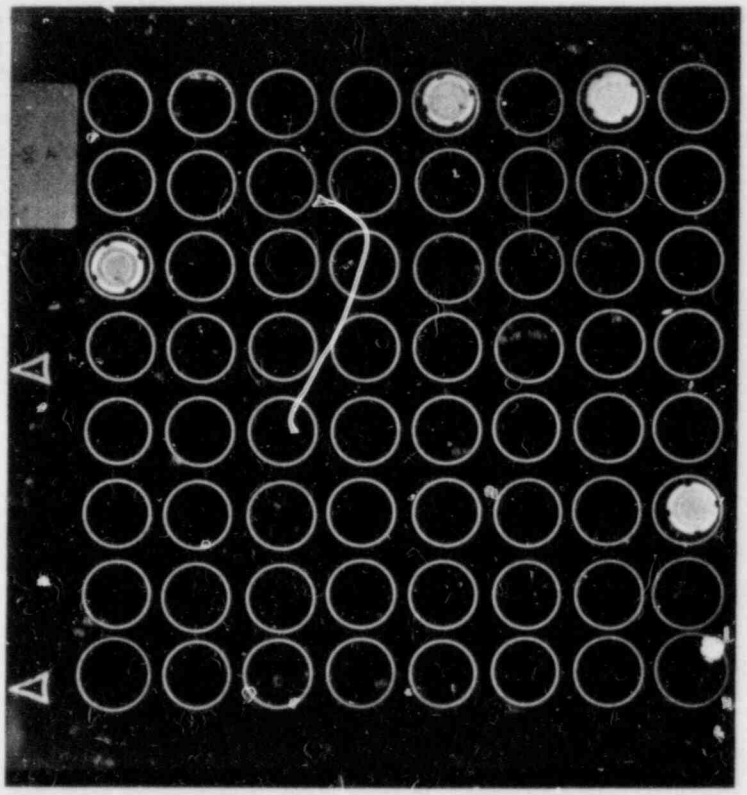

Fig. 88. Section at 54.8-cm elevation.

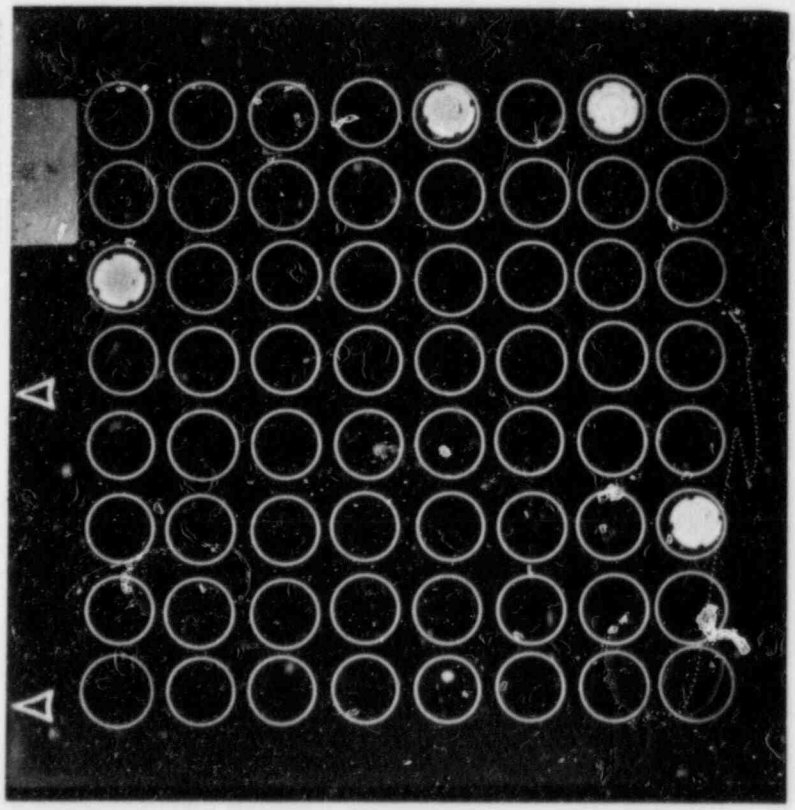

Fig. 87. Section at 53.2-cm elevation.

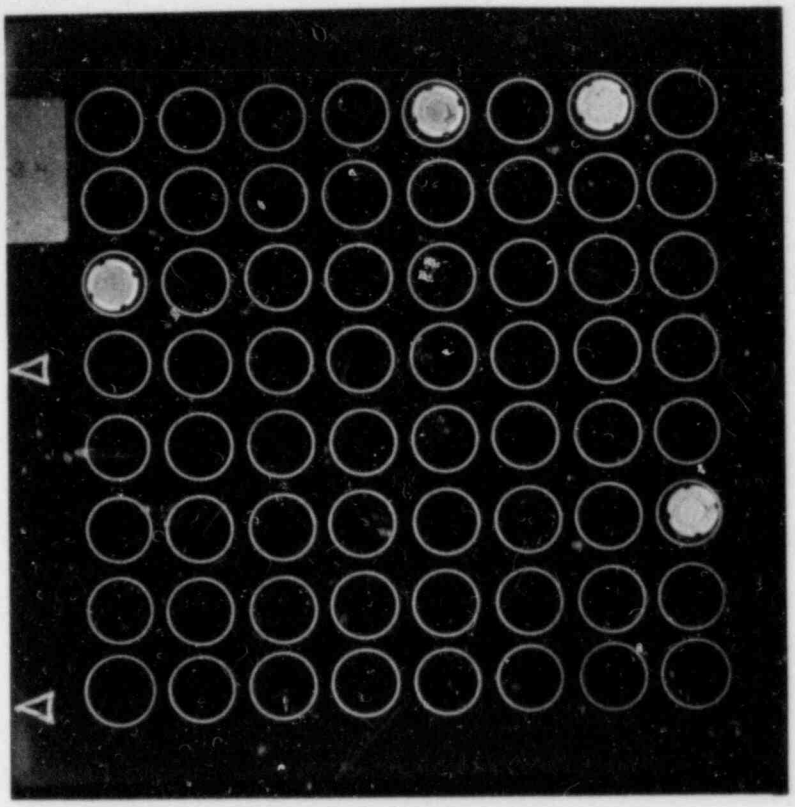

Fig. 90. Section at 58.2-cm elevation.

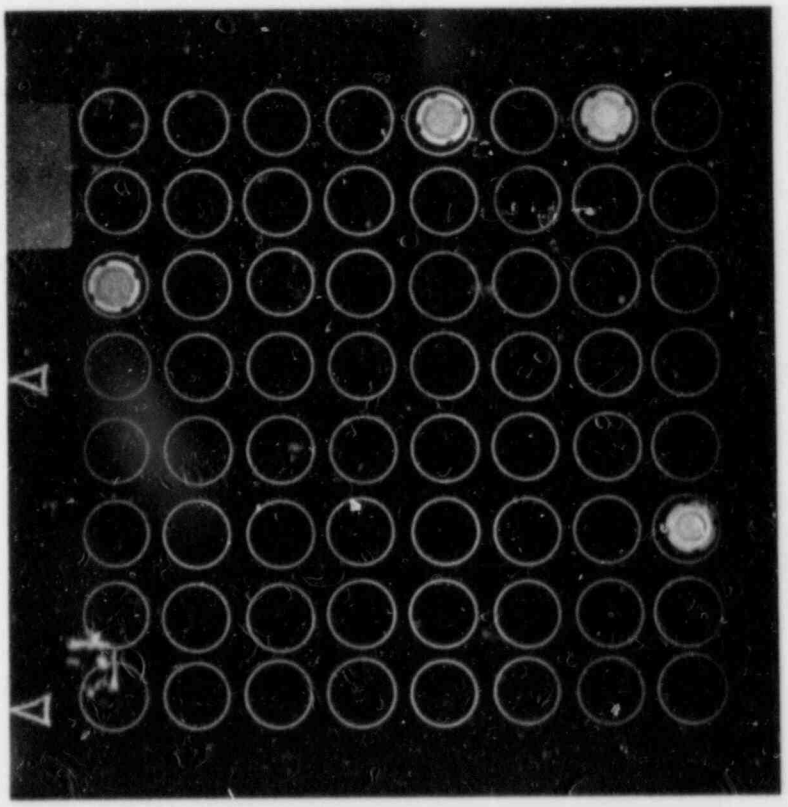

Fig. 89. Section at 56.5-cm elevation.

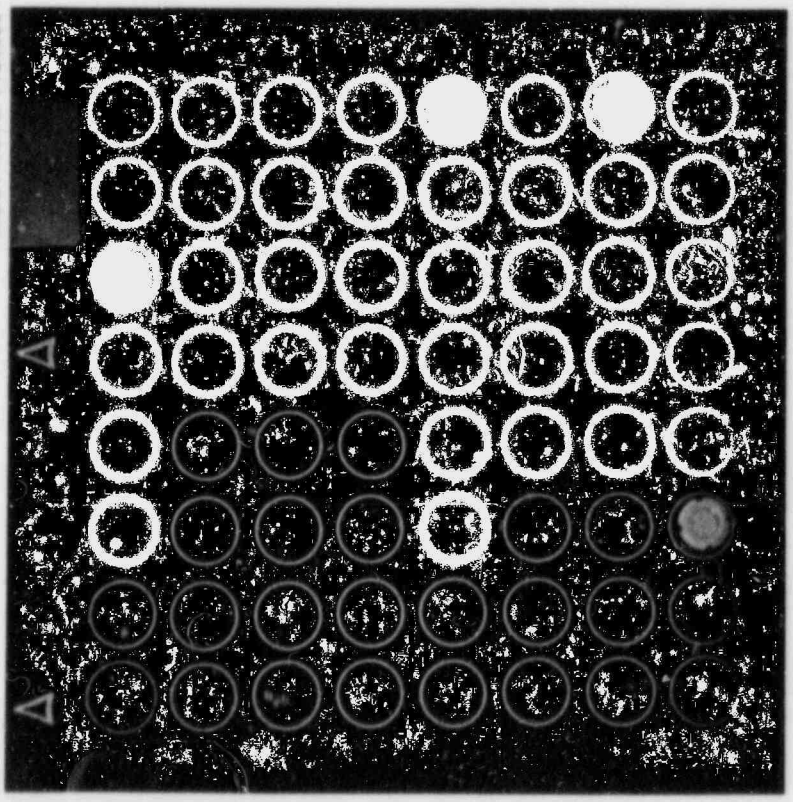

Fig. 91. Section at 60.0-cm elevation.

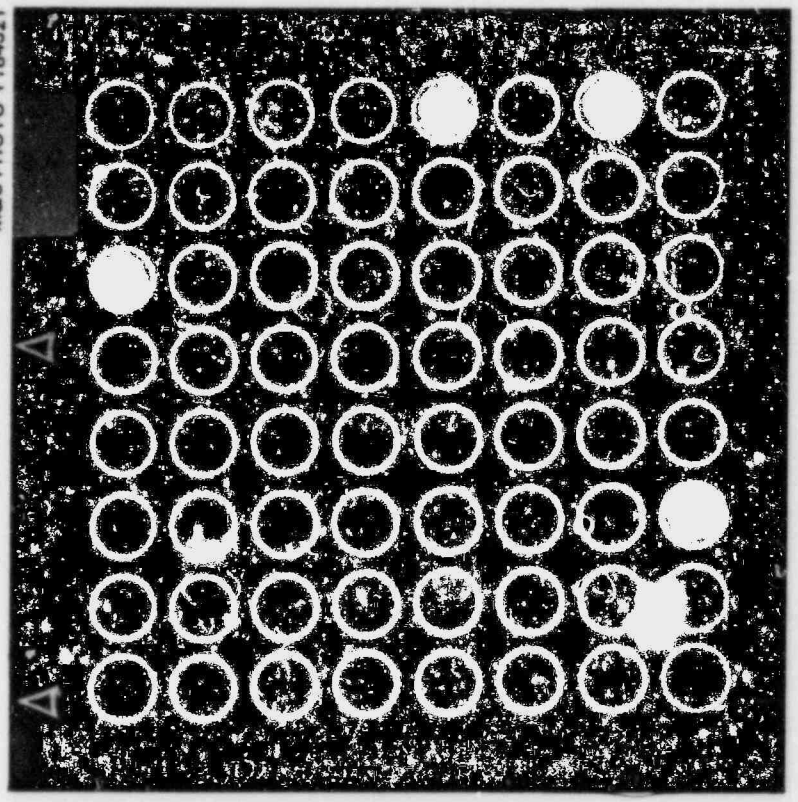

Fig. 92. Section at 61.7-cm elevation.

M&C PHOTO Y184322

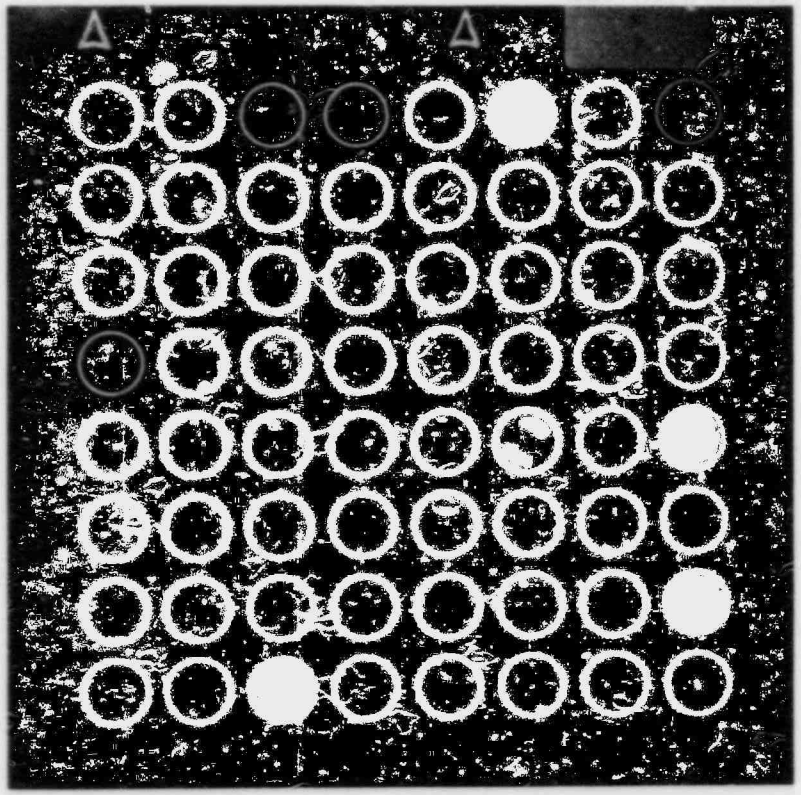

Fig. 93. Section at 63.4-cm elevation.

M&C PHOTO Y184316

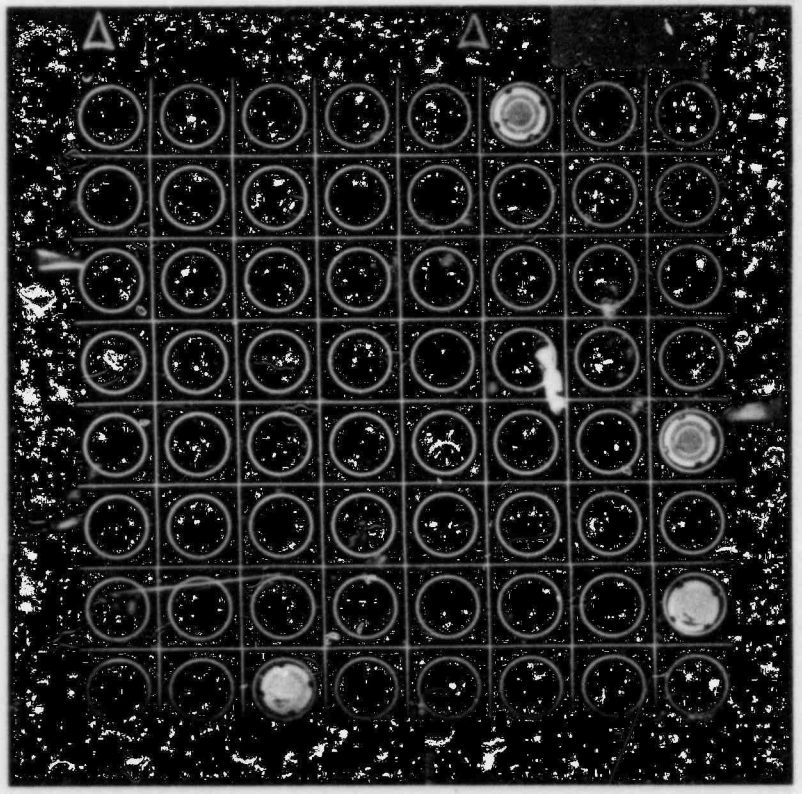

Fig. 94. Section through upper grid at 65.0-cm elevation.

M&C PHOTO Y184323

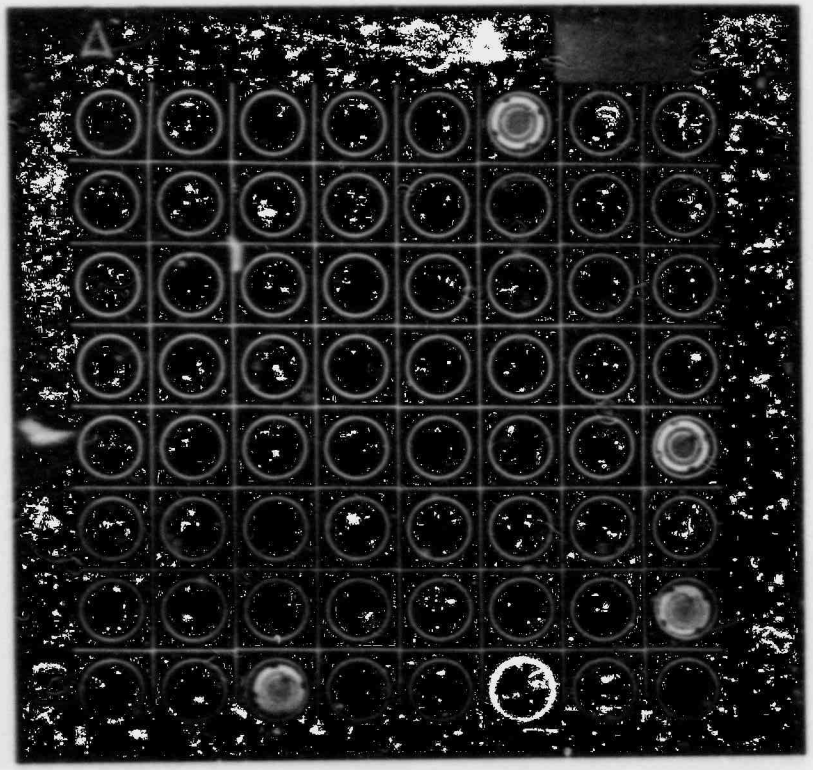

Fig. 95. Section through upper grid at 67.6-cm elevation.

M&C PHOTO Y184589

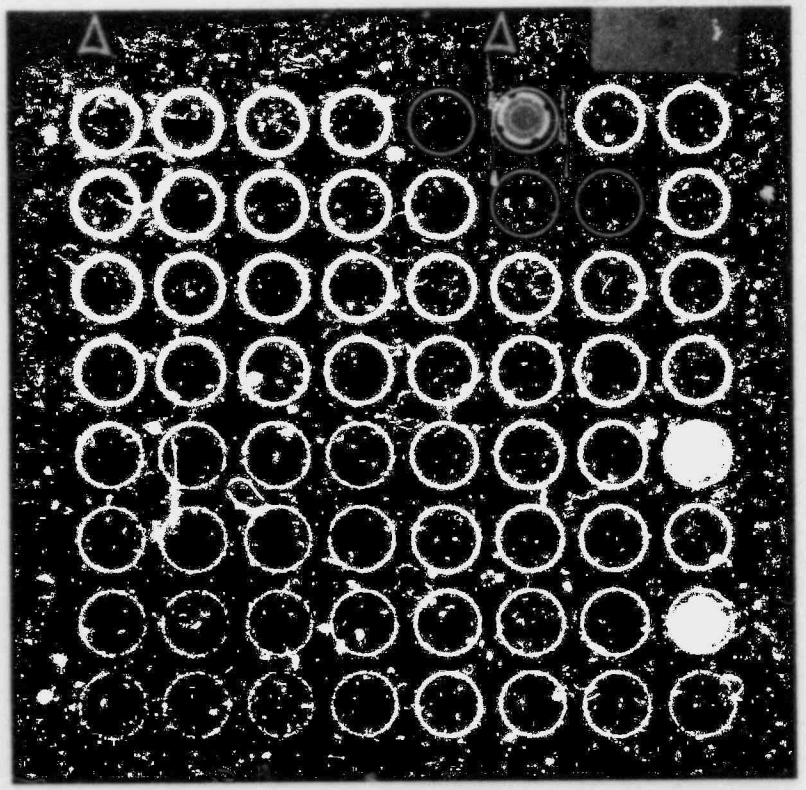

Fig. 96. Section at 69.2-cm elevation.

M&C PHOTO Y184598

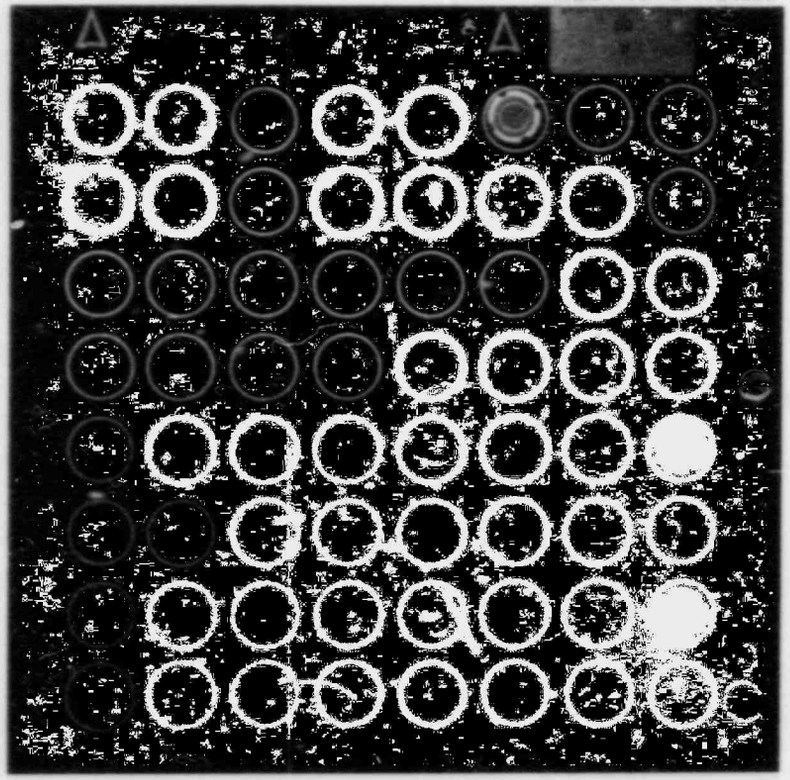

Fig. 97. Section at 71.0-cm elevation.

M&C PHOTO Y184593

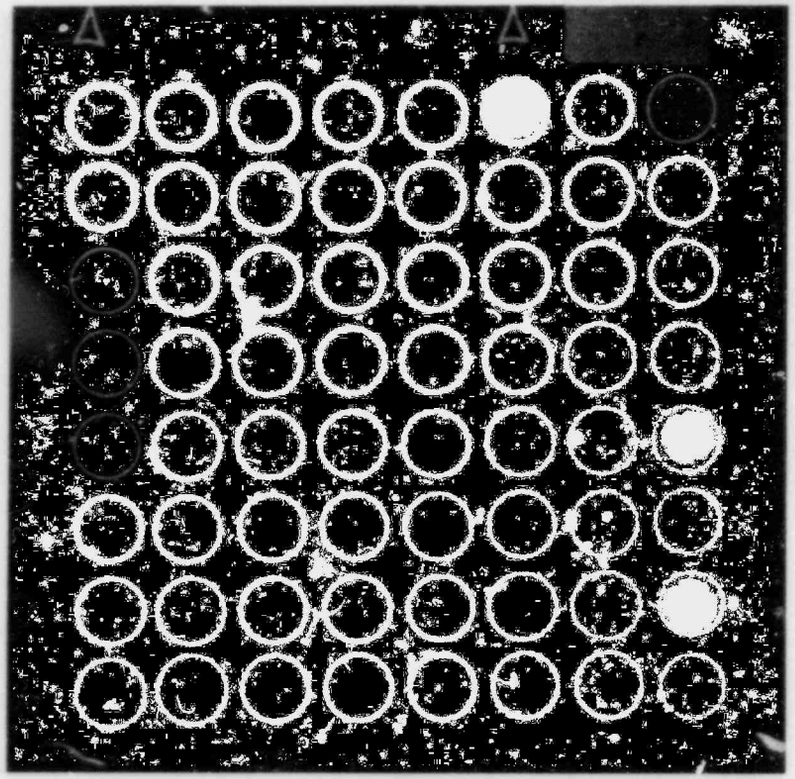

Fig. 98. Section at 72.8-cm elevation.

M&C PHOTO Y184591

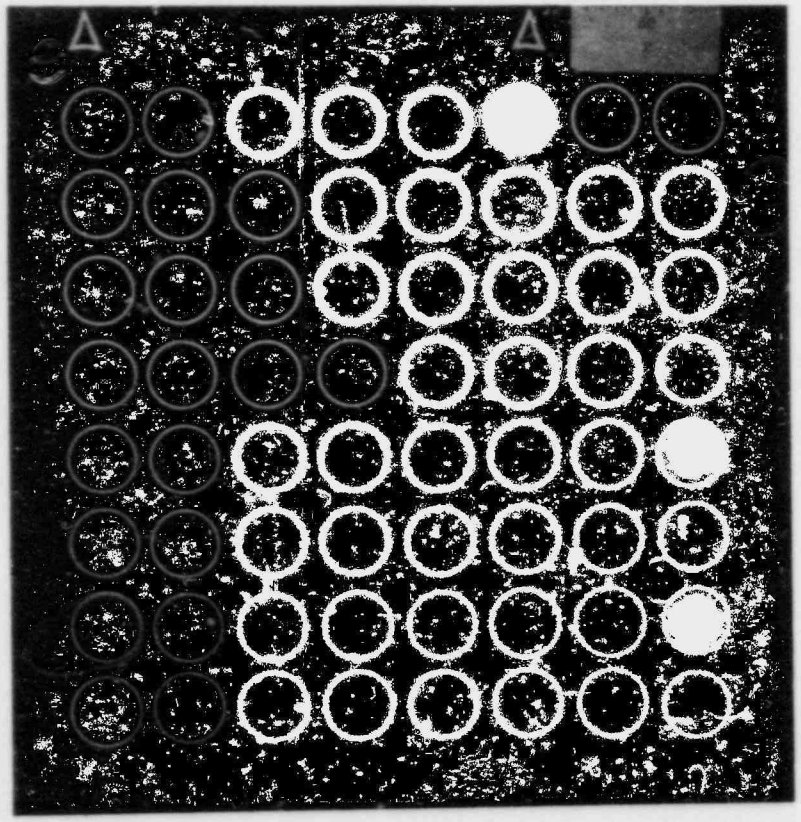

Fig. 99. Section at 74.7-cm elevation.

M&C PHOTO Y184596

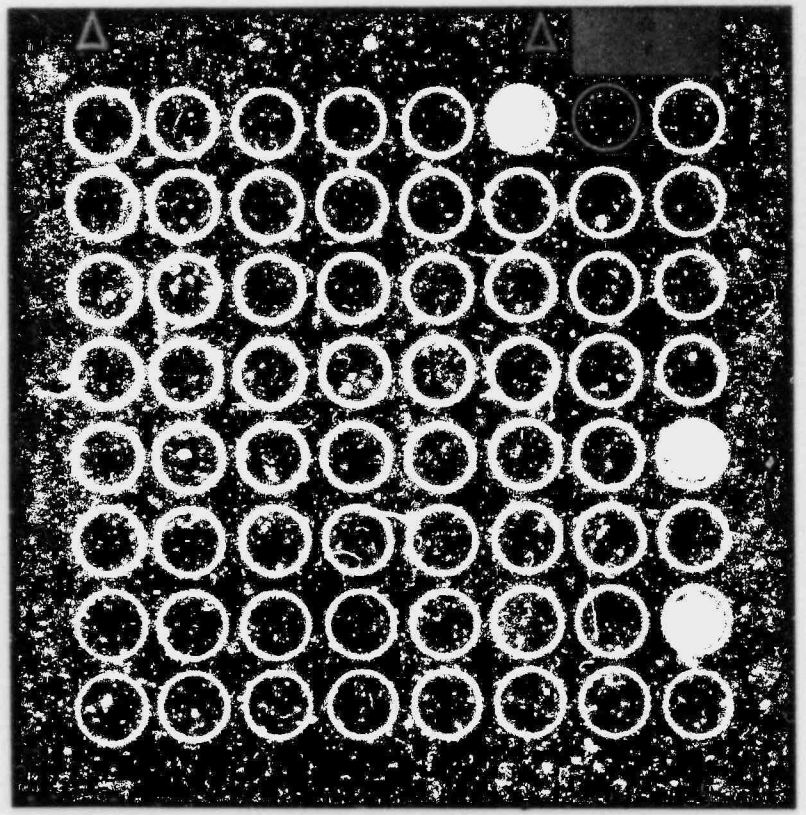

Fig. 100. Section at 76.6-cm elevation.

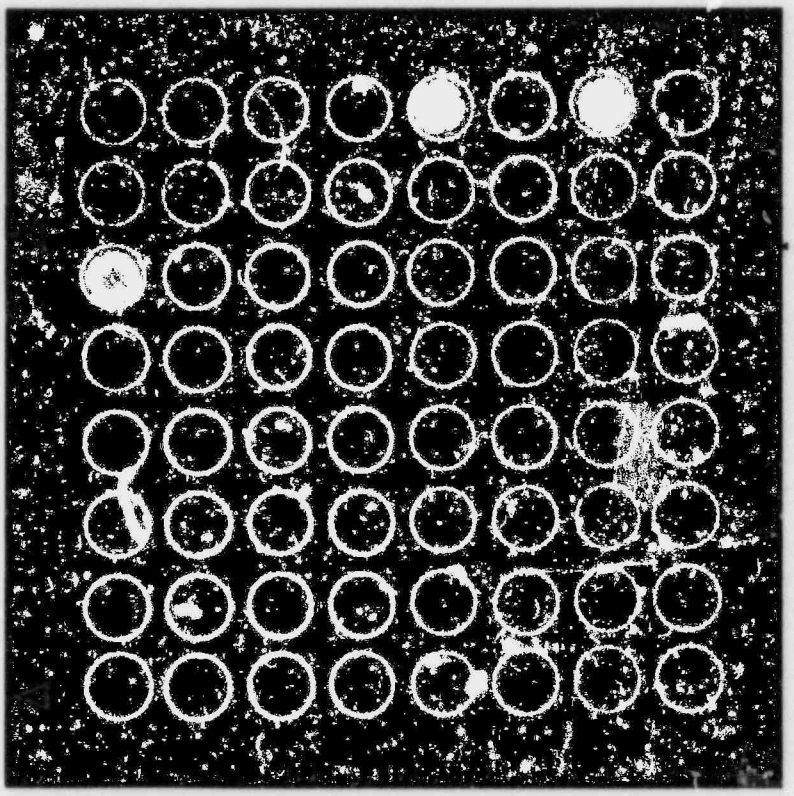

Fig. 102. Section at 80.4-cm elevation.

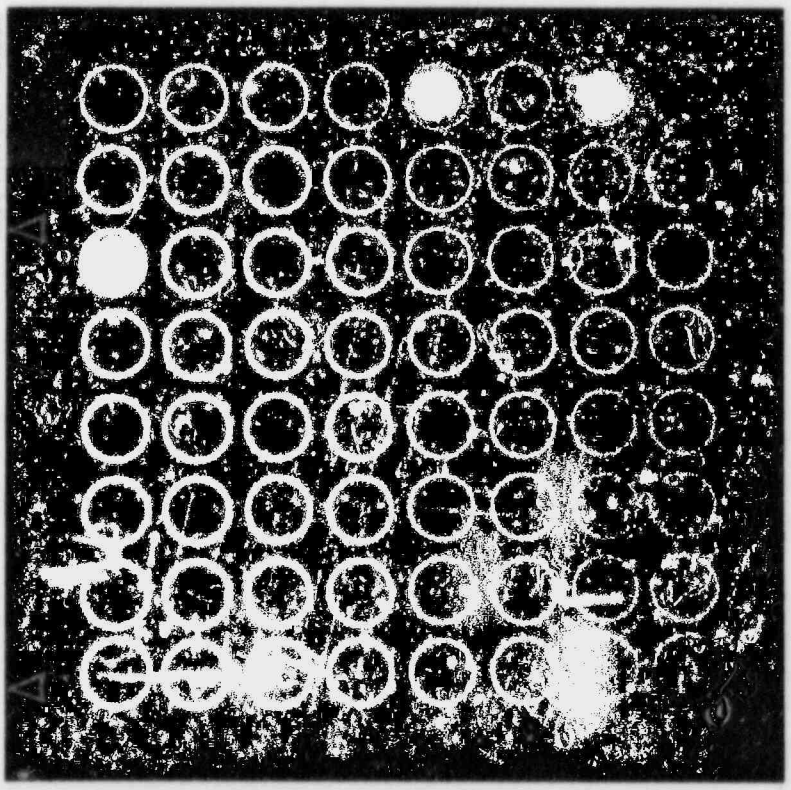

Fig. 101. Section at 78.5-cm elevation.

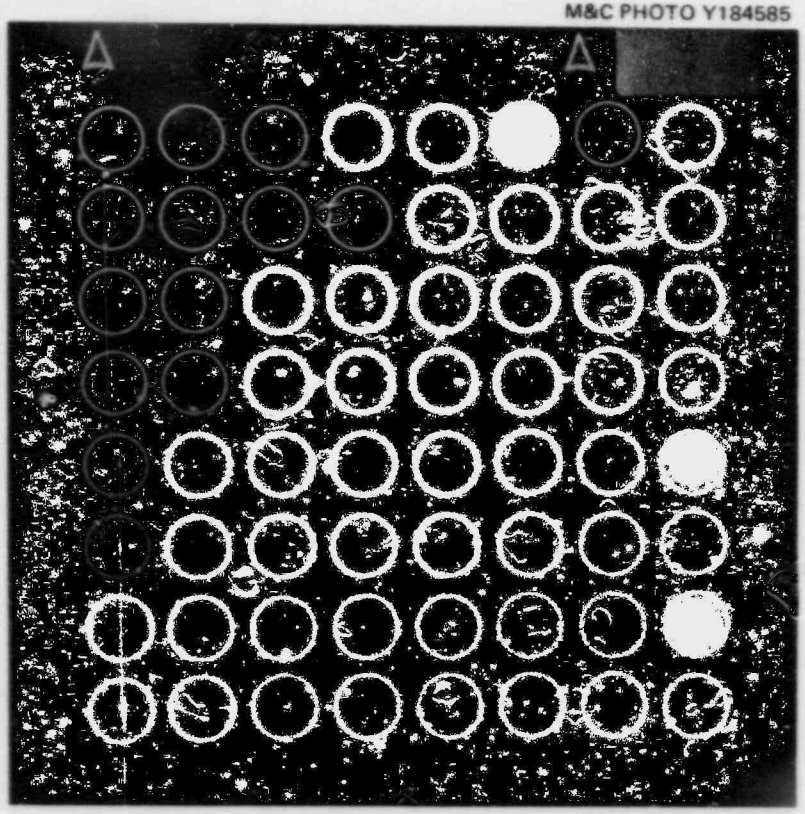

Fig. 103. Section at 82.4-cm elevation.

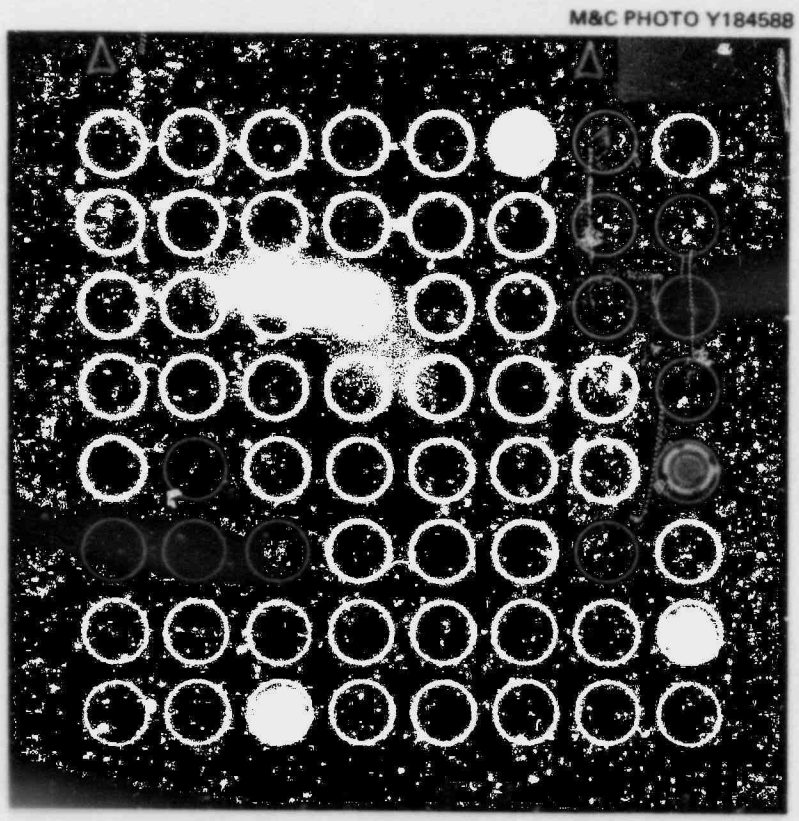

Fig. 104. Section at 84.4-cm elevation.

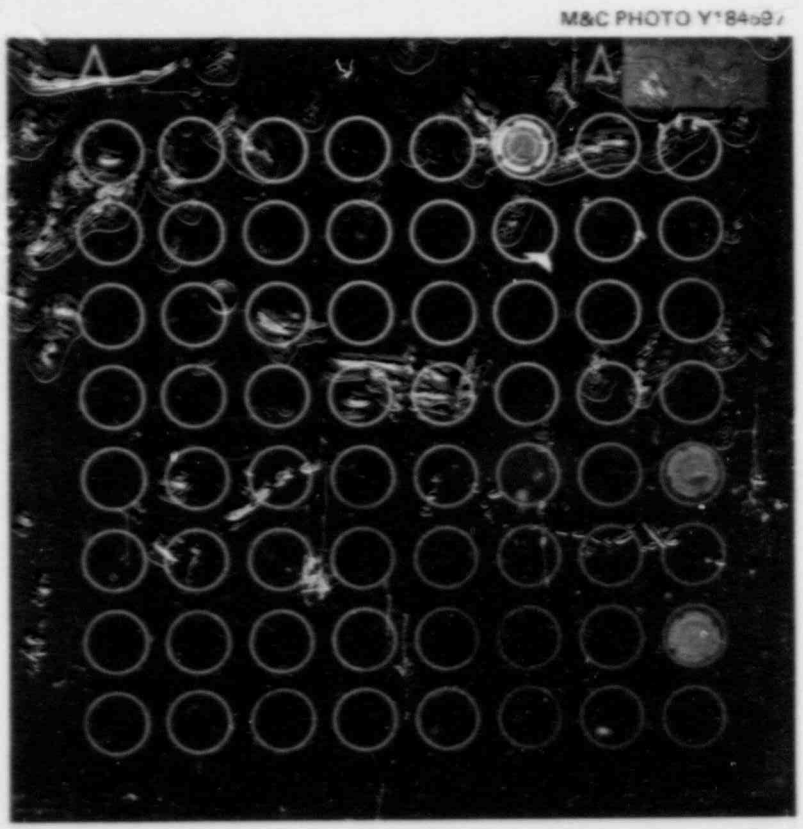

Fig. 105. Section at 86.2-cm elevation.

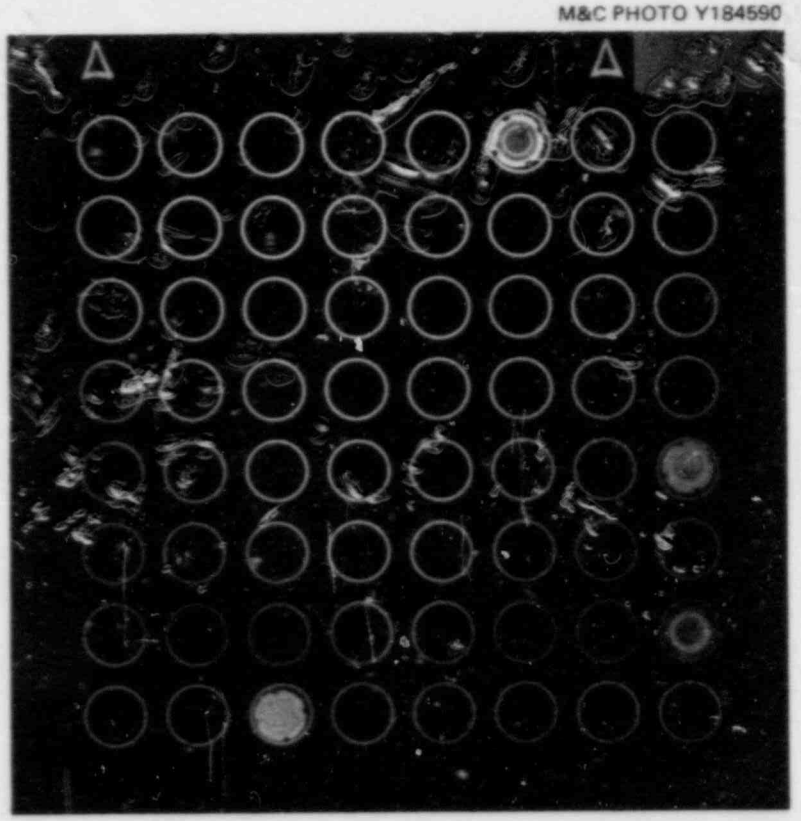

Fig. 106. Section at 88.0-cm elevation.

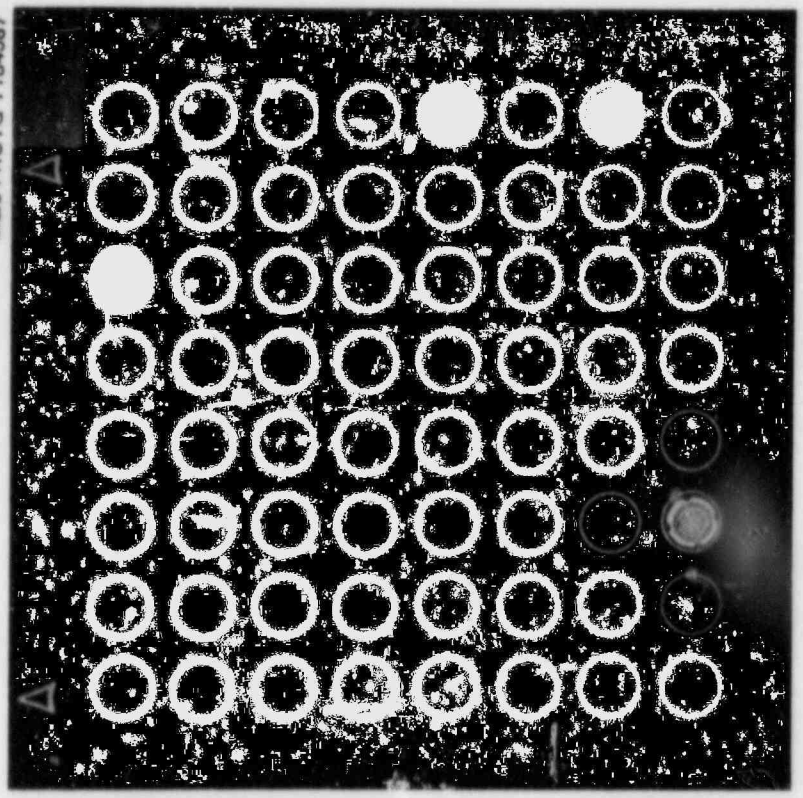

Fig. 108. Section at 91.5-cm elevation.

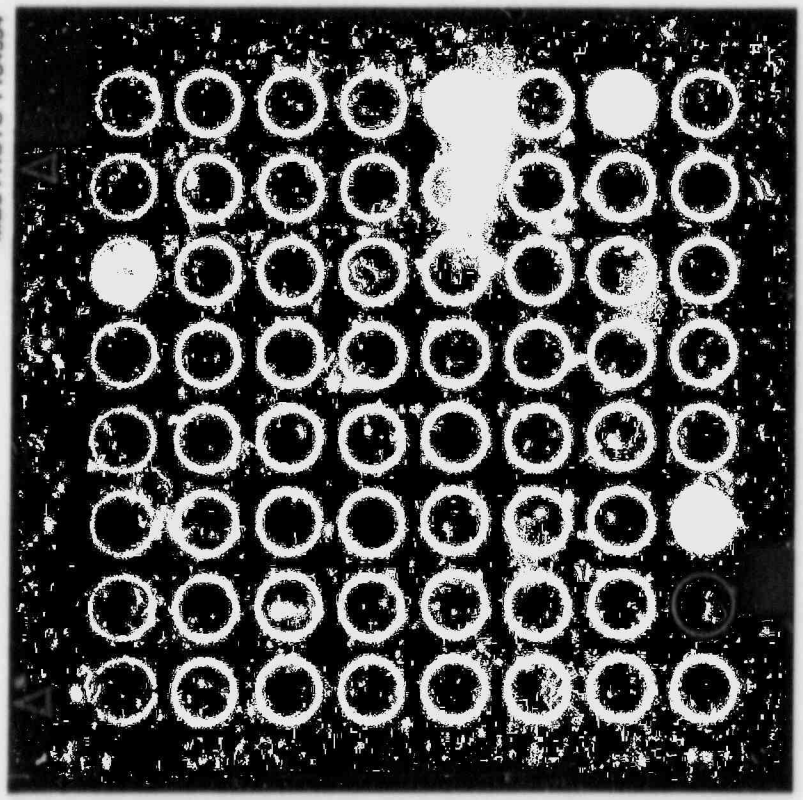

Fig. 107. Section at 89.5-cm elevation.

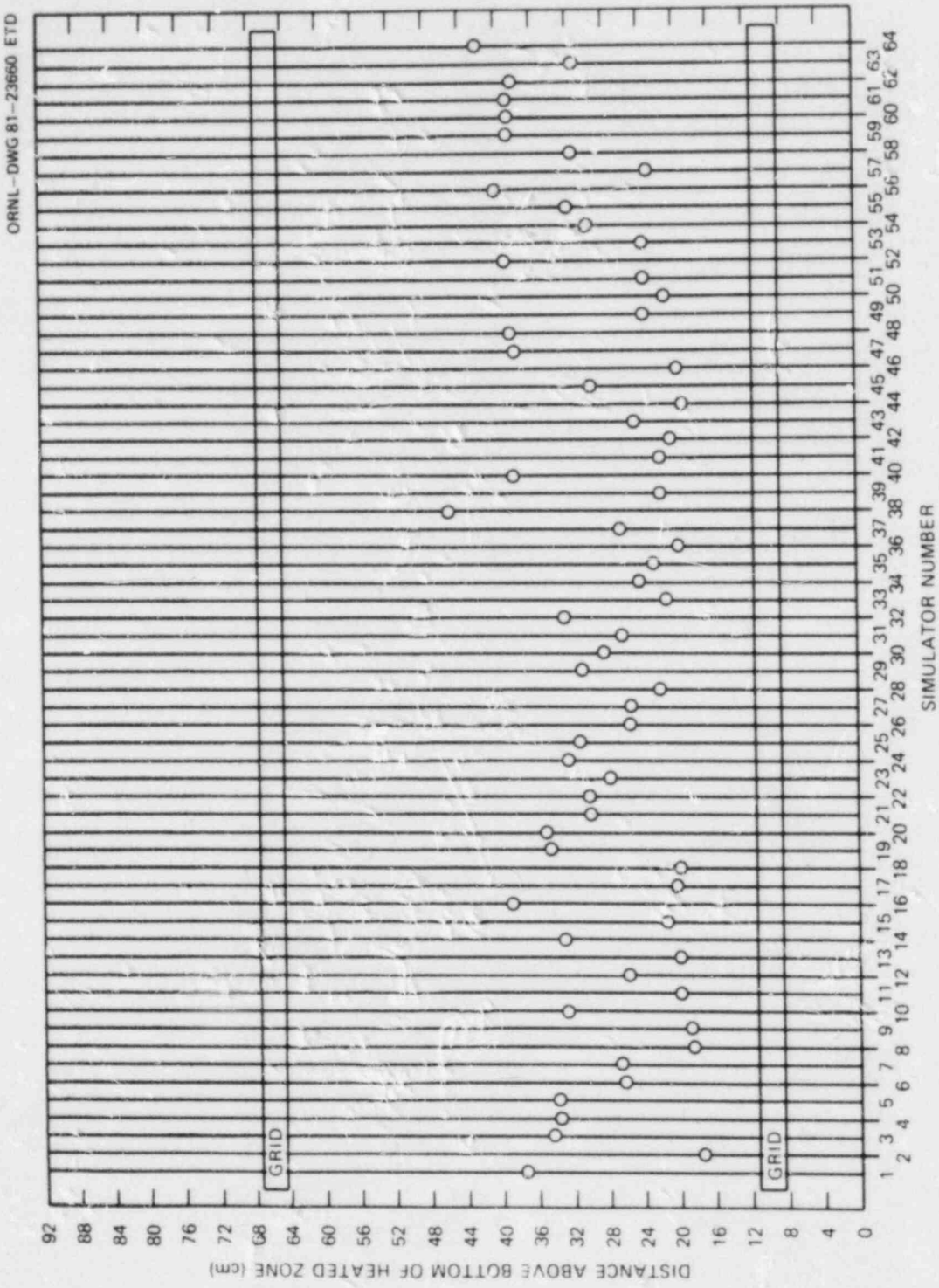

Fig. 109. Approximate burst midpoint elevations.

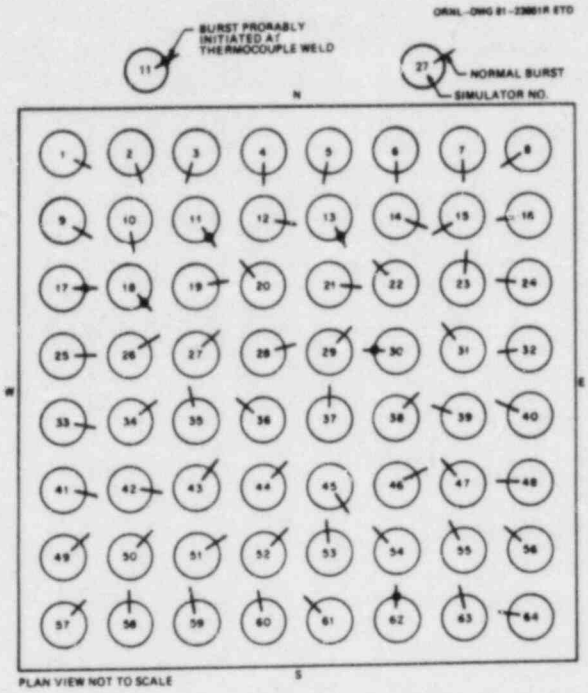

Fig. 110. Approximate burst midpoint orientations.

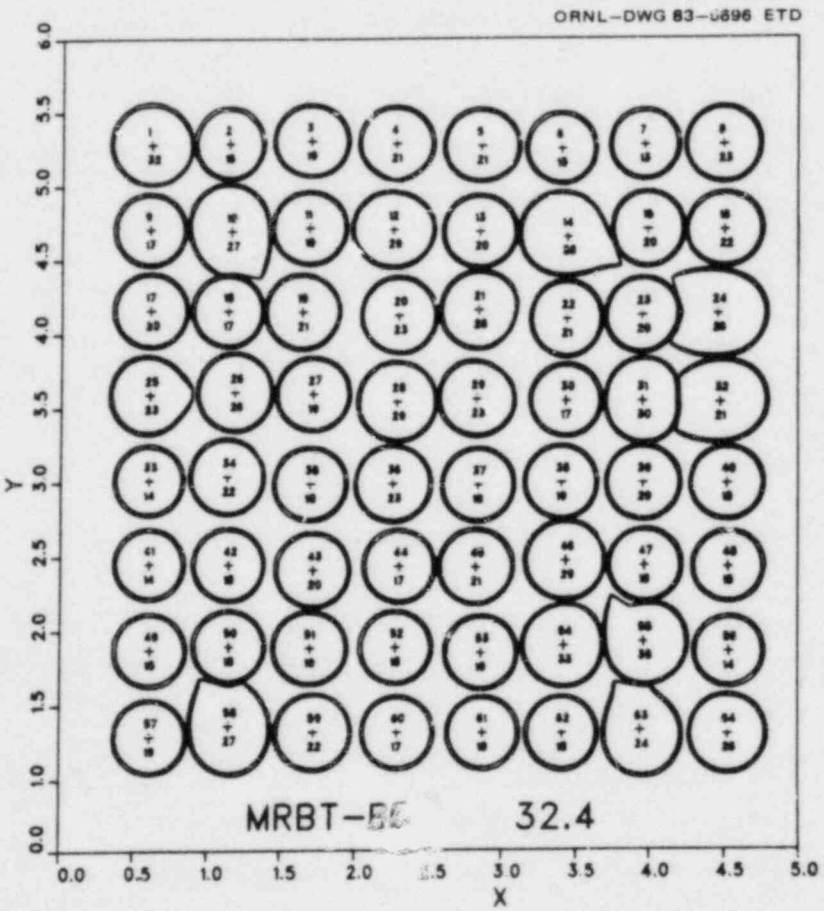

Fig. 111. Example of software reconstruction of photograph in Fig. 74.

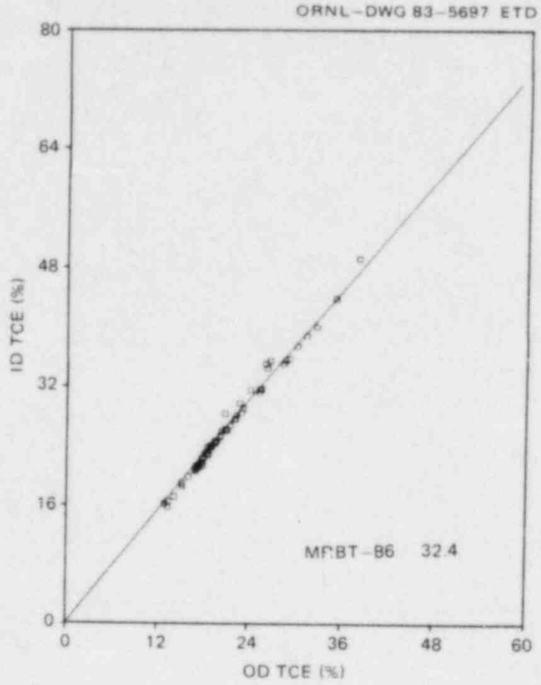

Fig. 112. Example of strain data verification procedure.

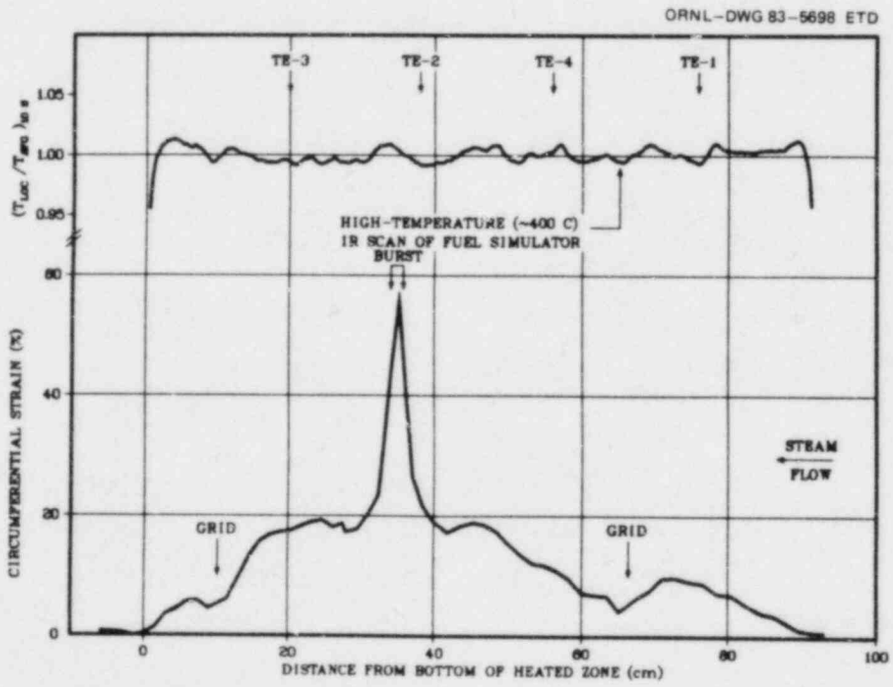

Fig. 113. Deformation profile of tube 0.

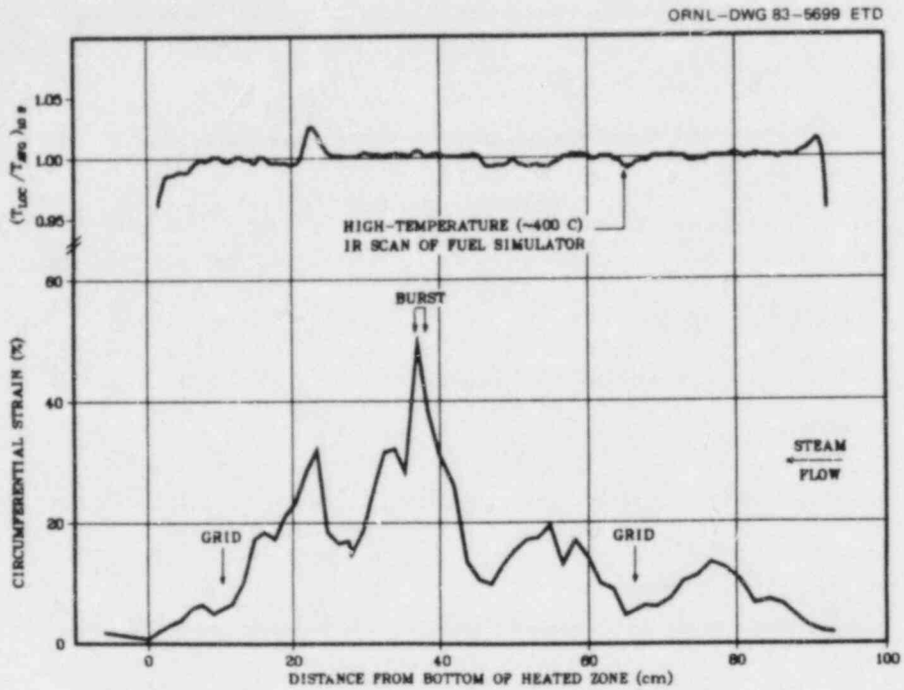

Fig. 114. Deformation profile of tube 1.

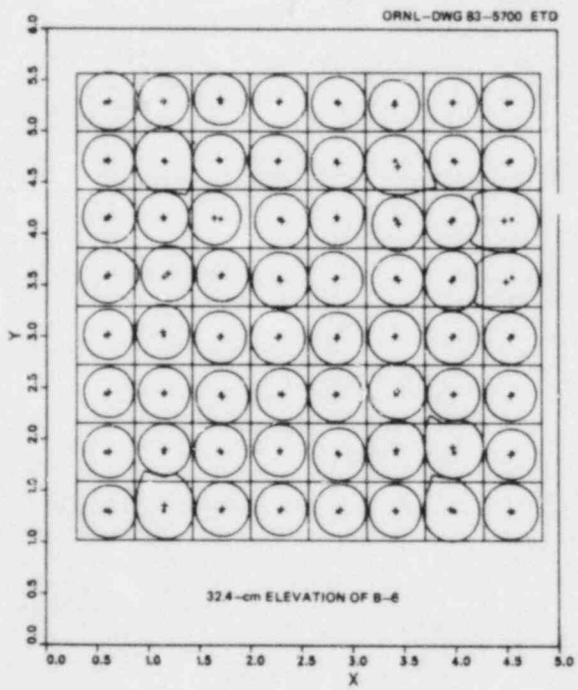

Fig. 115. Example of tube relocation at 32.4-cm elevation.

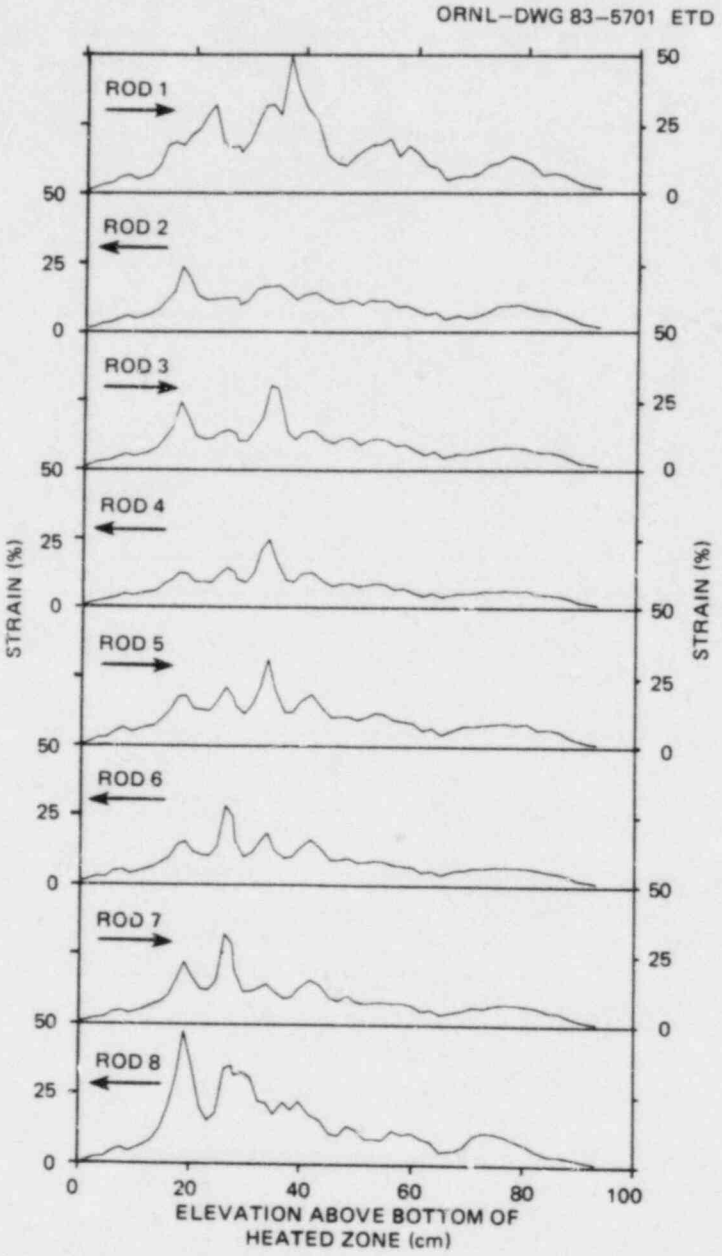

Fig. 116. Comparison of deformation profiles of first layer of tubes on north side of bundle.

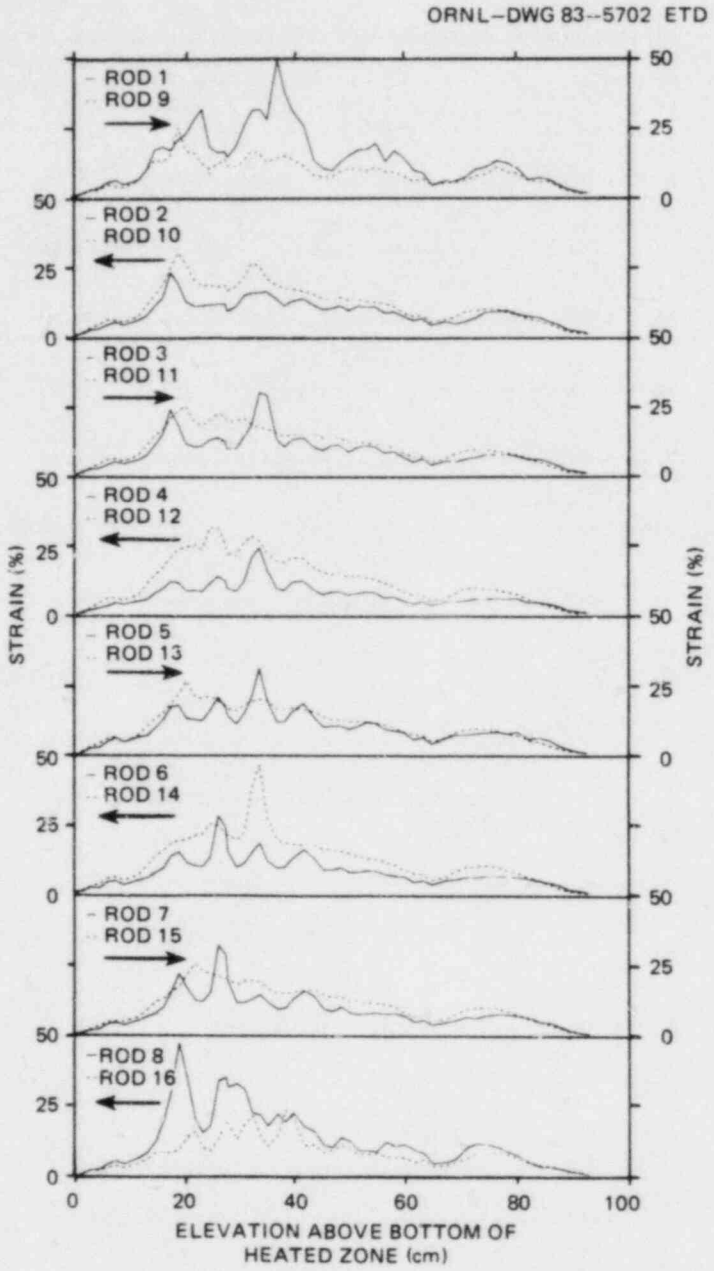

Fig. 117. Comparison of deformation profiles of first and second layers of tubes on north side of bundle.

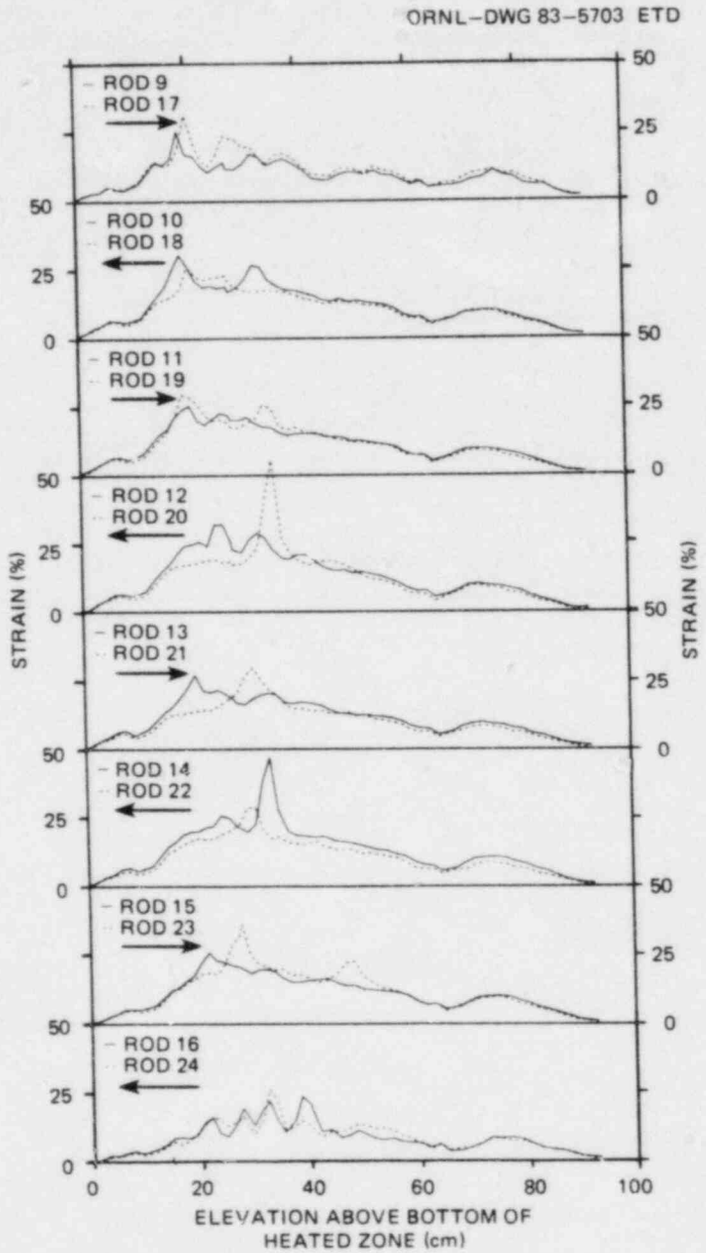

Fig. 118. Comparison of deformation profiles of second and third layers of tubes on north side of bundle.

APPENDIX A

TRANSIENT PRESSURE AND TEMPERATURE PLOTS

Individual pressure (differential) and temperature plots are presented for the simulators as a function of time after power-on in Figs. A-1 through A-64 on sheet 1 of the microfiche enclosures in the pocket attached to the inside back cover of this report. Typical examples of the plots were given in Figs. 36 and 37 to illustrate the type of data available from the microfiche records.

Because cladding temperature measurements were not made on 20 of the 28 simulators in the outer ring of the array (see Fig. 3), we have plotted TAV-10 (characteristic bundle average temperature defined in Sect. 2.1) on the plots for these simulators to give an impression of their temperature as a function of time. No claim is made that TAV-10 is a good measure of the temperature of these simulators; better indications may be available, depending on relative positions in the array, from the fully instrumented neighboring simulators.

Temperatures measured on the four faces of the shroud are plotted in Figs. A-65 through A-68 and compared in Figs. A-69 through A-72 to temperatures measured on simulators in the immediate vicinity.

Transient plots of the inlet steam temperature measurements are given in Fig. A-73 and of the outlet steam temperature measurements in Fig. A-74.

APPENDIX B

MEASURED CONDITIONS AT SELECTED TIMES OF INTEREST

Summary tables of the bundle conditions measured at the times of the individual tube bursts are presented in Tables B-1 through B-64 on sheet 2 of the microfiche enclosures in the pocket attached to the inside back cover of this report. An example was given in Table 6 to illustrate the type, format, and identification of the data available from the microfiche records.

Similar tables, giving summary test conditions over a 200-s time span, are presented in Tables B-65 through B-95. These tables, with 10-s time intervals for the first 120 s, 2-s intervals for the next 40 s, and 5-s intervals for the remaining 40 s, can be used to approximate either the transient of an individual simulator or that of the bundle as a whole from power-on until a few seconds after the last tube burst.

APPENDIX C

GEOMETRIC PARAMETERS OF SECTION PHOTOGRAPHIC DATA

The section photographs were digitized and reduced to tables of geometric parameters that were used for verification of the digitized data and as source files for further processing. For documentary purposes, Tables C-1 through C-61 are reproduced on sheet 3 of the microfiche enclosures in the pocket attached to the inside back cover of this report. An example was given as Table 9 to illustrate the type, format, and identification of the data available from the microfiche records.

APPENDIX D

DEFORMATION PROFILES

The strain matrix (Table 10) was used to generate axial profiles of the circumferential strain in each of the tubes. These are presented in Figs. D-1 through D-64 on sheet 4 of the microfiche enclosures in the pocket attached to the inside back cover of this report. Example plots were presented in Figs. 113 and 114 to illustrate the type and format of the information available from the microfiche records.

APPENDIX E

TUBE CENTROID DISPLACEMENTS AT EACH AXIAL NODE

A least-squares fitting routine was used to minimize the average displacement between the pretest and posttest centroids of the 64 tubes as described in Sect. 4.2.4. The results are presented in Tables E-1 through E-61 on sheet 5 of the microfiche enclosures in the pocket attached to the inside back cover of this report. An example was given in Table 13 to illustrate the type and format of the data available from the microfiche records.

APPENDIX F

PLOTS OF TUBE DISPLACEMENTS AT EACH AXIAL NODE

The least-squares fitting routine that was used to minimize the average displacement between the pretest and posttest centroids of the 64 tubes was combined with the routine that reconstructed the images of the section photographs to produce a plot of the posttest tube locations relative to an imaginary grid at the respective axial node. The plots show, in effect, the permanent displacement of the tubes within their individual unit cells and aid visualization of subchannel flow area restriction. The plots are presented in Figs. F-1 through F-61 on sheet 6 of the microfiche enclosures in the pocket attached to the inside back cover of this report. An example of the plots was depicted in Fig. 115 to illustrate the type and format of the data available from the microfiche records.

NUREG/CR-3460
ORNL/TM-8890
Dist. Category R2, R3

Internal Distribution

1-5. R. H. Chapman
6-10. J. L. Crowley
11. D. S. Griffith
12. D. O. Hobson
13-17. A. W. Longest
18. A. P Malinauskas
19. H. E. Trammell
20. Patent Office
21. Nuclear Safety Information Center
22. Central Research Library
23. Document Reference Section
24-25. Laboratory Records Department
26. Laboratory Records (RC)

External Distribution

27. Office of Assistant Manager for Energy Research and Development, DOE, ORO, Oak Ridge, TN 37830
28. Chief, Fuel Behavior Branch, Office of Nuclear Regulatory Research, Nuclear Regulatory Commission, Washington, DC 20555
29. Chief, Core Performance Branch, Office of Nuclear Reactor Regulation, Nuclear Regulatory Commission, Washington, DC 20555
30. R. Van Houten, Fuel Behavior Branch, Office of Nuclear Regulatory Research, Nuclear Regulatory Commission, Washington, DC 20555
31. G. P. Marino, Fuel Behavior Branch, Office of Nuclear Regulatory Research, Nuclear Regulatory Commission, Washington, DC 20555
32. R. A. Adamson, Mail Code V-03, General Electric Company, Vallecitos Atomic Laboratory, P.O. Box 846, Pleasanton, CA 94566
33. D. L. Burman, Westinghouse Nuclear Fuel Division, P.O. Box 355, Pittsburgh, PA 15230
34. C. E. Crouthamel, Exxon Nuclear, Inc., 2955 George Washington Way, Richland, WA 99352
35. F. J. Erbacher, Project Nukleare Sicherheit, Kernforschungszentrum Karlsruhe, Postfach 3640, 75 Karlsruhe, Federal Republic of Germany
36. M. D. Freshley, Pacific Northwest Laboratories, P.O. Box 999, Richland, WA 99352
37. R. Potter, UKAEA Atomic Energy Research Establishment, Harwell, Didcot, Oxfordshire, OX11 ORA, England
38. D. L. Hagrman, EG&G Idaho, Inc., INEL, Idaho Falls, ID 83401
39. T. Healey, CEGB Berkeley Nuclear Laboratories, Berkeley, Gloucestershire, GL13 9PB, England
40. E. D. Hindle, UKAEA Springfields Nuclear Laboratories, Salwick, Preston, PR4 ORR, England
41. S. Saito, Japan Atomic Energy Research Institute, Tokai-Mura, Naga-Gum, Ibaraki-Ken, Japan
42. T. Howe, EG&G Idaho, Inc., INEL, Idaho Falls, ID 83401
43. S. Kawasaki, Japan Atomic Energy Research Institute, Tokai-Mura, Naga-Gum, Ibaraki-Ken, Japan

44. E. T. Laats, EG&G Idaho, Inc., INEL, Idaho Falls, ID 83401
45-46. W. Lowenstein, Electric Power Research Institute, 3412 Hillview Avenue, P.O. Box 10412, Palo Alto, CA 94304
47. A. L. Lowe, Babcock and Wilcox Company, P.O. Box 1260, Lynchburg, VA 24505
48. R. Duffey, Electric Power Research Institute, 3412 Hillview Avenue, P.O. Box 10412, Palo Alto, CA 94304
49. H. Rininsland, Projekt Nukleare Sicherheit, Kernforschungszentrum Karlsruhe, Postfach 3640, 75 Karlsruhe, Federal Republic of Germany
50. P. A. Smerd, Combustion Engineering, Inc., 1000 Prospect Hill Road, Windsor, CT 06093
51. W. Spencer, EG&G Idaho, Inc., INEL, Idaho Falls, ID 83401
52-53. Technical Information Center, DOE, Oak Ridge, TN 37830
54-438. Distribution as shown for NRC categories R2 and R3 (NTIS-10)

☆U.S. GOVERNMENT PRINTING OFFICE: 1983-746-018/4073

NRC FORM 335 (11-81) U.S. NUCLEAR REGULATORY COMMISSION

BIBLIOGRAPHIC DATA SHEET

1. REPORT NUMBER (Assigned by DDC)
NUREG/CR-3460
ORNL/TM-8890

4. TITLE AND SUBTITLE (Add Volume No., if appropriate)
Experiment Data Report for Multirod Burst Test (MRBT) Bundle B-6

2. (Leave blank)

3. RECIPIENT'S ACCESSION NO.

7. AUTHOR(S)
R. H. Chapman, A. W. Longest, and J. L. Crowley

5. DATE REPORT COMPLETED
MONTH: June YEAR: 1984

9. PERFORMING ORGANIZATION NAME AND MAILING ADDRESS (Include Zip Code)
Oak Ridge National Laboratory
Post Office Box X
Oak Ridge, TN 37830

DATE REPORT ISSUED
MONTH: July YEAR: 1984

6. (Leave blank)

8. (Leave blank)

12. SPONSORING ORGANIZATION NAME AND MAILING ADDRESS (Include Zip Code)
Division of Accident Evaluation
Office of Nuclear Regulatory Research
U.S. Nuclear Regulatory Commission
Washington, DC 20555

10. PROJECT/TASK/WORK UNIT NO.

11. FIN NO.
B0120

13. TYPE OF REPORT
Topical

PERIOD COVERED (Inclusive dates)

15. SUPPLEMENTARY NOTES

14. (Leave blank)

16. ABSTRACT (200 words or less)

A reference source of MRBT bundle B-6 test data is presented with minimum interpretation. The primary objective of this 8 x 8 multirod burst test was to investigate cladding deformation in the alpha-plus-beta-Zircaloy temperature range under simulated light-water-reactor (LWR) loss-of-coolant accident (LOCA) conditions. B-6 test conditions simulated the adiabatic heatup (reheat) phase of a LOCA and produced very uniform temperature distributions. The fuel pin simulators were electrically heated (average linear power generation of 1.42 kW/m) and were slightly cooled with a very low flow (Re ~ 1-0) of low-pressure superheated steam. The cladding temperature increased from the initial temperature (330°C) to the burst temperature at a rate of 3.5°C/s. The simulators burst in a very narrow temperature range, with an average of 930°C. Cladding burst strain ranged from 21 to 56%, with an average of 31%. Volumetric expansion over the heated length of the cladding ranged from 16 to 32%, with an average of 23%. The average burst strain and the average volumetric expansion for the interior simulators were only slightly greater than the averages for the exterior simulators. The coolant channel flow area reduction was modest, with a maximum of 39% for the entire 8 x 8 array, 43% if based on the interior 6 x 6 array, and 45% if based on the central 4 x 4 array. As expected, no evidence of rod-to-rod mechanical interaction effects was observed.

17. KEY WORDS AND DOCUMENT ANALYSIS

Zircaloy
Nuclear fuel cladding
Bundle burst tests
Loss-of-coolant accident simulation
Fuel pin simulators
Flow blockage

17a. DESCRIPTORS

Tubes
Deformation
Rod-to-rod interactions
Boundary conditions

17b. IDENTIFIERS/OPEN-ENDED TERMS

18. AVAILABILITY STATEMENT
Unlimited

19. SECURITY CLASS (This report)
Unclassified

21. NO. OF PAGES

20. SECURITY CLASS (This page)
Unclassified

22. PRICE
$